Controlling Photon Emission from Nitrogen Vacancy Centers in Diamond

by

Vinodh Raj Rajagopal Muthu

A thesis
presented to the University of Waterloo
in fulfillment of the
thesis requirement for the degree of
Master of Applied Science
in
Electrical and Computer Engineering (Quantum Information)

Waterloo, Ontario, Canada, 2021

Author's Declaration

I hereby declare that I am the sole author of this thesis. This is a true copy of the thesis, including any required final revisions, as accepted by my examiners.

I understand that my thesis may be made electronically available to the public.

Abstract

In this thesis we investigate two domains of control over the photonic emission from NV centers. In the first part of the thesis, which focuses on emission control in the spatial domain, we will be exploring the design of a nanophotonic structure that would be able to control the directionality of photon emission from NV centers. We will be using the inverse design methodology known as adjoint optimization to design the structure. Furthermore we will present FDTD simulations to assess the performance of the designed structure and compare its performance with existing structures. We then present some preliminary experimental results from a confocal microscopy setup we built in our lab.

In the second part of the thesis, which focuses on emission control in the spectral domain, we investigate the potential of using single NV centers for photon conversion between the microwave and optical regimes. The conversion between the microwave photons, that couple to superconducting qubits, and optical photons, that are used in long range communication and memories, is an important component in realizing an extended quantum network. In our proposed scheme, we explore the use of Λ system in NV centers coupled to optical and microwave cavities as a platform for efficient conversion between the microwave and optical regimes. We present analytical and numerical simulations to identify the required characteristics of the system to achieve high conversion efficiencies.

Acknowledgements

My masters journey was filled with unexpected challenges, including a global pandemic. I would like to take this time to acknowledge all the people who have supported me and made this a worthwhile journey.

First, I would like to thank my supervisor, Prof. Michal Bajcsy, for giving me the opportunity to work in his lab both as an undergraduate and as a master's student. I am thankful to him for teaching me the research process, and for introducing me to the plethora of knowledge and resources available in IQC. There are several other people in IQC that have made my master's journey a memorable one. I would like to thank my research partner Supratik Sarkar for all the support and encouragement he has provided me both inside and outside of work. These past two years would've definitely been a very different experience without him and I am very grateful for his friendship. I would also like to thank Dr. Behrooz Semnani for his mentorship on one of my master's projects. Working with him was truly an enriching learning experience which expanded my research horizons. Thank you also to Dr. Rubayet Al Maruf for teaching me the ins and outs of lab work with such great patience. I would also especially like to thank Steve Weiss for all of his sage wisdom and timely advice. In addition, I would also like to thank the rest of my group mates: Paul Anderson, Sai Sreesh Venuturumilli, Sema Kuru for their support.

I was also very fortunate to meet a lot of wonderful people in Waterloo outside of IQC that have made my Canadian experience an amazing one. First and foremost I would like to thank David and Nancy Matthews for providing me with a "home away from home". I will always be grateful to them for making me feel so welcome in Waterloo and for creating a loving and supportive environment. I would also like thank my past and present housemates, Lane, Brad, Ian, Turner, Randy, and Tracy, who have been a blast to live with. I would also especially like to thank Marie, Ben and Matthew for their companionship and emotional support, especially during the pandemic. Furthermore, a big thank you to all my friends from back home in Malaysia: Yasodharan, Amir, Harshini, Nandiniy, Linesha, Zhen Meng, Hoon Heng, Gareb, and Kirthana for their constant support despite our distance. I am especially grateful to Yasodharan for his friendship and for our weekly 'catch-up' sessions which never failed to lift my spirits up.

Finally and most importantly, I would like to thank my parents and sister. My parents, and the sacrifices they've made, are the reason I am the person I am today. I am eternally grateful to my parents for their unconditional love, and for always encouraging me to pursue my interests. Thank you to my father, Rajagopal, for showing me the importance of integrity, and for imbuing in me a sense of curiosity and interest in science. Thank you to my mother, Vasanthi, for teaching me the importance of maintaining inter-personal connections and cultivating great relationships – the significance of which can sometimes be lost in the world of science and engineering. I am also blessed to have an amazing sister, Vinitha, who has always been there for me through all my ups and downs. She has been a constant source of support through all the uncertainties, and I am lucky to call her a friend. I am forever grateful to have been blessed with an amazing and supportive family.

Dedication

I would like to dedicate this thesis to my loving parents and sister.

Table of Contents

List of Tables

List of Figures

Chapter 1

Introduction

Max Planck's theoretical explanation of blackbody radiation formulated in 1900, together with Albert Einstein's 1905 paper on the discrete quantized nature of light paved the way to our current understanding of the fundamental theory in physics known as quantum mechanics. Early demonstrations of the exotic properties of quantum mechanics such as superposition and entanglement [10] raised the question of whether "quantum resources" could be exploited for useful applications. This brought forth many exciting avenues of research such as quantum information and computing, quantum metrology, and secure quantum communications, all of which can be broadly categorized as quantum technologies. When selecting potential systems to be used in quantum technology applications, there are two criteria that need to be considered: control and scalability [11]. Control is achieved in systems such as single atom/trapped ion experiments where the system is maximally isolated from environmental effects [12]. Single atom platforms however are not particularly scalable. In the aspect of scalability, solid state systems are superior due to the possibility of on chip integration as well as the availability of established nanofabrication techniques and tools from the semiconductor industries. One such solid state platform that has gained traction in the past few years are Nitrogen Vacancy (NV) centers embedded in diamonds. Due to atom like properties and attractive qualities such as long coherence times, whilst also being embedded in a solid state material, NV centers have been used in several quantum technology applications.

Having selected a viable system, which in our case are NV centers, an important subsequent avenue to explore would be the control over the photon emission from said system. Indeed, control over the quantum state of light in systems lies central to the implementation of several useful quantum technology applications such as metrology, communication and information processing [13]. In this thesis we will be exploring the potential of two photonic quantum technology applications involving the control over the photonic emission from NV centers. We begin the thesis with Chapter 2 with a brief introduction to NV centers and review a few of their basic properties.

1.1 Design of Nanophotonic Structures for Directional Control of NV Center Emission

In Part I of this thesis we investigate the design of nanophotonic structures to control the directionality of photon emission from NV centers embedded near the surface in bulk diamonds. The control over the emission directionality from NV centers is vital for several applications such as on-demand single photon generation [14], nanoscale magnetometry [15, 16], study of spin interactions and entanglement [17, 18, 19], and quantum information processing [20]. Specifically, we use an inverse design tool known as adjoint optimization to design the nanophotonic structure. In Chapter 3 we start by looking at the use of classical antenna formulations to describe the emission from quantum emitters. In Chapter 4 we look at the theory behind the inverse design methodology known as adjoint optimization. We review how adjoint optimization can be used to design photonic structures with user defined electromagnetic responses. Finally, in Chapter 5 we look at the design of a nanophotonic structure using adjoint optimization to control the emission profile from NV centers. We will perform simulations to quantitatively compare the performance of the adjoint optimized structure to existing structures in controlling the emission directionality from NV centers. Furthermore, we present some preliminary experimental results from a confocal microscope setup to observe the fluorescence from NV centers and conclude with future directions of the project.

1.2 Microwave to Optical Domain Transducer with Single NV Centers

In Part II of the thesis we investigate the potential of using a single NV center for efficient photon conversion between microwave and optical regimes. In this project we aim to develop a quantum interface between microwave and optical photons. This is an essential component in realising a hybrid quantum network where photons as information carriers need to be converted between microwave domain, where they interact with superconducting circuits [21], and optical domain, which allows long-distance communication, high-efficiency detection, and storage in a quantum memory [22, 23]. We investigate the potential of microfabricated devices with integrated optical and microwave cavities coupled to a single NV centre – which we model as a three-level Λ-type quantum emitter – to efficiently convert microwave photons into optical photons. We present analytical and numerical simulation results that explore the required characteristics of the microwave and optical cavities to achieve high conversion efficiency between the microwave and optical regimes. In Chapter 6, we first outline the framework with which we will investigate the conversion between the microwave and optical regimes using NV centers. We present two definitions of the conversion efficiency which we will be exploring. In the first intrinsic definition of the conversion efficiency, we ask the question: *If we can get a microwave photon into microwave cavity, what cavity parameters would maximize the output optical photons?*. In second, extrinsic, definition of the conversion efficiency we ask the question: *For every microwave photon incident on the microwave cavity, what cavity parameters would maximize the output optical photons?* . In Chapter 6 we use analytical and Monte-Carlo simulations of the system to explore the first conversion efficiency definition in different cavity regimes and identify the required parameters for the maximum conversion efficiency. In Chapter 7 we continue the analysis from the previous chapter and explore the second conversion efficiency definition in different cavity regimes and identify the required parameters for the maximum conversion efficiency. Finally we will conclude with a discussion on the system limitations and discuss existing optical and microwave cavities that satisfy the required system parameters to achieve maximal conversion efficiency.

Chapter 2

NV Centers

2.1 Introduction

A nitrogen vacancy (NV) center in diamond is a point defect in diamond lattice where a carbon atom is replaced with a nitrogen atom, whilst the carbon atom adjacent to it is vacant [24]. NV centers can either exist as NV^0 or as NV^-. In NV^0 the three adjacent dangling carbon atoms contribute 3 bond electrons and the nitrogen atom contributes two valence electrons. The addition of one extra electron to that results in the formation of the negatively charged NV^- with six electrons in total (Figure 2.1). Although the NV^0 state has been observed to be the preferred charge state formed at the surface (<200nm) of the pure diamonds through annealing [25], it is the negatively charged NV^- that is formed deeper within the diamonds that have been extensively studied due to it attractive spin and optical properties [26]. Furthermore NV^- is the preferred state that exists dominantly in natural diamonds [27]. Due to the long electron spin coherence times in NV centers [28, 29], the ease of microwave rotations[30], optical readout and manipulation [31], and the ability control the geometric position via ion implantation [32, 33], NV centers offer an excellent platform for applications in quantum metrology [34, 35, 29, 36, 37], quantum information [38, 39] and in quantum networks [40, 41, 18]. In this chapter we will look at the basic properties of NV^- centers, including how they can be used as a Λ system in optical experiments. The Λ configuration consists of one excited state and two ground state sublevels. Furthermore, we will also briefly discuss the theory behind confocal microscopy, which is the primary way in which fluorescence from NV centers is experimentally observed.

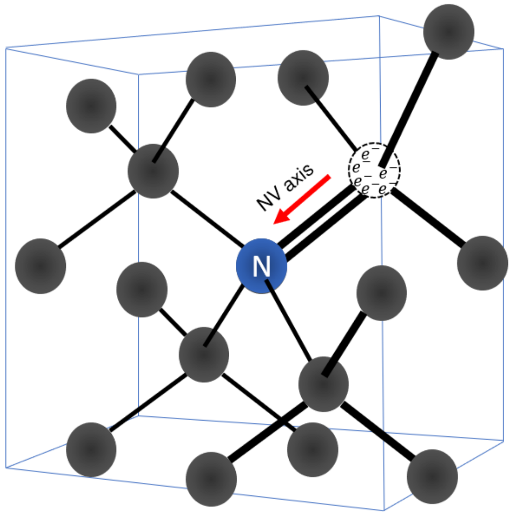

Figure 2.1: In the diamond lattice, NV centers are formed by the substitution of a carbon atom with a nitrogen atom and the vacancy of the adjacent atom. This results in the contribution of the three dangling bond electrons from the neighbouring carbon atoms, two from the nitrogen atom, and one additional electron. The total of six electrons results in the formation of the NV$^-$.

2.2 Basic Properties

The NV$^-$ center's electronic structure consists of a ground and excited spin triplet states, $^2A_3$ and ^3E, and the singlet states $^1A_1$ and ^1E as seen in Figure 2.2. The ground triplet state is well studied and documented thoroughly through electron spin resonance (ESR) [42, 43], Raman heterodyne [44], and optically detected magnetic resonance (ODMR) experiments [45]. The ground triplet state is split into the spin levels $m_s = 0$ and the levels $m_s = \pm 1$ levels by 2.87GHz. The dipole transition between the ground spin triplet and excited spin triplet states corresponds to the 637nm Zero Phonon Line (ZPL) emission band. This ZPL emission and the 2.87GHz ground spin triplet splitting is characteristic of a NV$^-$ center and is typically used in identifying the presence of a defect. The excited state ^3E, is associated with six excited sates corresponding to two states for the $m_s = 0$, and the four levels A_1, A_2, and E (2 levels) corresponding to the spin values of $m_s = \pm 1$ [46]. External strain and temperature may cause perturbations that shift or mix the excited triplet levels even further [27].

At low temperatures (T =2K) the triplet and singlet dipole transitions correspond to 637nm and 1043nm respectively. These transitions between the distinct electronic states

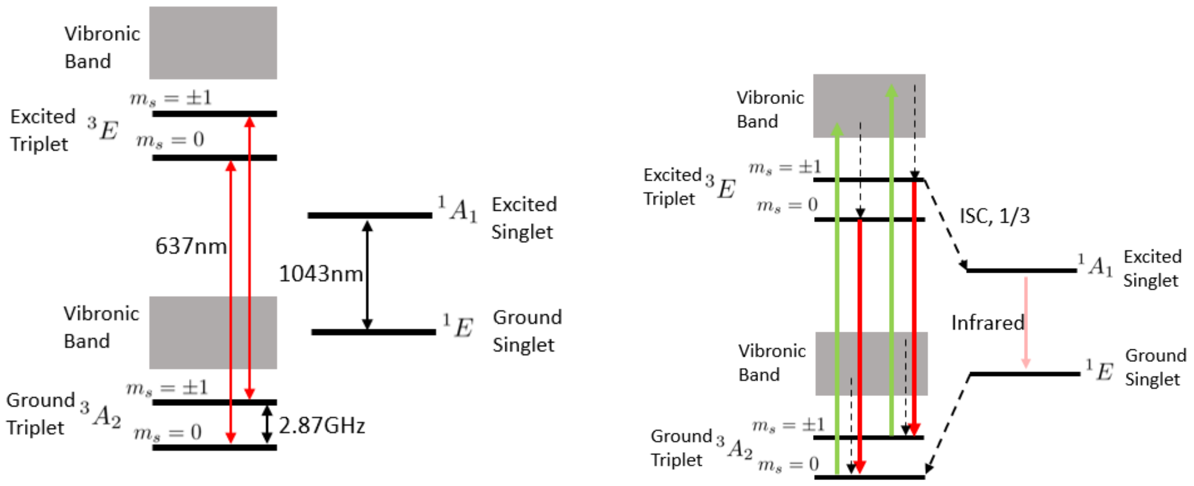

(a) (b)

Figure 2.2: a) The electronic structure of an NV center showing the ground and excited triplet and singlet states, and the vibronic bands. The resonant decay from the excited state results in the ZPL, whilst non resonant decay to the vibronic bands above the ground triplet contribute to the phonon sidebands in the NV spectrum. b) The NV centers can be excited with an above resonant energy pulse (green) to the vibronic bands from which they decay to the excited triplet state ^3E by emitting phonons. From the excited triplet state in spin state $m_s = 0$, the NV decays to the ground triplet state $^3A_2$ via a transition in the optical regime. If the excited state begins in the $m = \pm 1$ spin state, infrared decay through due to Inter-System Crossing (ISC) occurs with a probability of 1/3.

contribute to what is known as the Zero Phonon Line (ZPL) [47]. At room temperatures however these transitions are broadened due to phonon-assisted processes as seen in Figure 2.3a. In addition to the electronic excited states, there exists a band of vibronic states above the electronic triplet states. When the NV center is in the excited state ^3E, the NV center can either decay resonantly through the ZPL, or it can decay to the vibronic bands above the ground state $^3A_2$ from which it relaxes into the electronic ground triplet states through phonon relaxations. These transitions involving the vibronic band result in the phononic side bands (PSB) appearing at higher wavelengths (above the ZPL) due to emission, and at lower wavelengths due to absorption [24, 27]. As can be seen in Figure 2.3a only $\sim 3\%$ of the fluorescence from an NV^- is emitted into the ZPL. One of the main difficulties in working with NV centers is the large spectral inhomogeneity that arises due to the phonon side bands. This is because only the ZPL emission is what is useful for most applications as the emission from the non-ZPL spectrum dephases very quickly [48]. By coupling the NV centers to a cavity however, it has been shown that the ZPL emission can be enhanced by ~ 4 times [2, 49]. Similarly as can be seen in Figure 2.2b, the NV center can be excited with an above resonant energy (wavelength of 532nm) into the vibronic bands above the excited state, from which it relaxes into the excited states through phonon relaxations.

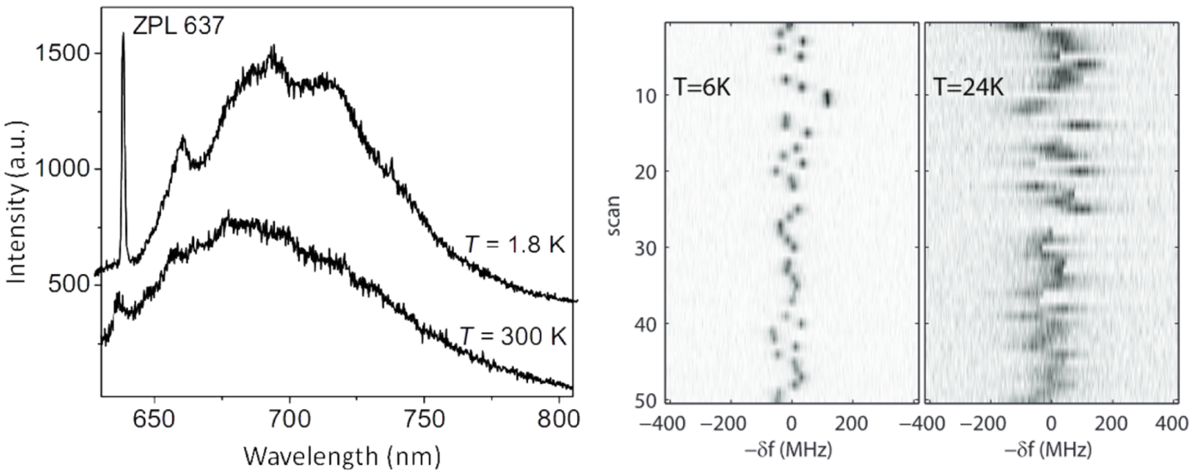

(a)

(b)

Figure 2.3: a) Fluorescence spectrum of a NV^- at room temperature (T=300K) and low temperatures (T = 1.8K). As can be seen approximately only 3% of the spectrum is emitted in the Zero Phonon Line(ZPL). Figure adapted from Reference [1]. b) Photoluminescence excitation (PLE) measurements of a single NV center in a CVD diamond excited at ZPL (632nm) while the photoluminescence is collected from the phonon sidebands repetaed over many scans. The z-axis represents the photoluminescence intensity, the x axis is the detuning from the excitation frequency, and the y-axis is the scan number. Figure adapted from [2]

When in the excited state with spin level $m_s = 0$, the NV center decays to the ground state via a fluorescence in the optical transition as seen in Figure 2.3a. However if the NV center begins in the excited state with spin level $m_s = \pm 1$, there is a 2/3 probability that the system will decay with the fluorescence in the optical transition and 1/3 probability that the excited triplet state will decay to the excited singlet state via inter-system crossing (ISC). The excited singlet state then decays to the ground singlet state emitting into the infra-red regime. The lifetime of the singlet states is 300ns [24]. Furthermore, the NV axis (Figure 2.1), which lies perpendicular to the optical dipole axis, is aligned along the $\langle 111\rangle$ axis. Which means in (100) oriented diamonds the NV lies at angle of 54.7^o with respect to the surface normal. Thus in a (111)-oriented diamond the optical dipole lies perpendicular to the surface normal [50].

2.3 Lambda System

In addition, NV centers can also form Λ configurations which can be used in applications such as Stimulated Raman adiabatic passage (STIRAP) [51], or, in our case, as an interface for microwave to optical photon conversion. Although the ground triplet of the NV center is well studied and documented, due to the uncertainty surrounding the excited triplet level structure, there doesn't exist one well defined Λ system that can be studied [4]. There exists several Λ systems that can picked from for different uses. One way to form a Λ system in the NV center is by applying a magnetic field along the NV axis to lift the degeneracy in the ground triplet states to split the spin states $m_s = \pm 1$. For a magnetic field strength of 117G at a cryogenic temperature of 8K, this splitting between the $|+1\rangle$ and $|-1\rangle$ state is 655MHz. A Λ system can then be formed from the excited state ${}^3E$ and the pair from the ground state triplet $|+1g\rangle$, and $|-1_g\rangle$ [3], with spin preserving transitions between the lower $|+1g\rangle$, and $|-1_g\rangle$ levels and the excited level $|{}^3E\rangle$ as seen in Figure 2.4a.

Alternatively due to factors such as strain, a Λ system exists in NV centers at zero magnetic field as well due to the symmetry breaking in the excited state $|{}^3E\rangle$ [4, 46, 52]. This results in the formation of a closed Λ system with the excited state $|{}^3E\rangle$ and ground states $|0\rangle$ and $|\pm 1\rangle$ as seen in Figure 2.4b [53, 4]. The ground triplet state is stable and has a long lifetime of $\sim$ 7.5ms [54, 55, 56, 57] and the excited state triplet of the NV center has a lifetime of $\sim$ 12ns at cryogenic temperatures. NV centers are also beneficial in that ground state NV center spins have a long transverse decay time T_2, approaching $\sim$ 2.4ms [15, 55, 57]. As can be noted from the photoluminiscence emission (PLE) measurement from Figure 2.3b, the linewidth of the $|{}^3E\rangle \leftrightarrow |0g\rangle$ transition is broadened with a width of $\sim$ 100MHz [2]. This spectral diffusion is due to a phonon assisted population decays between the E_y and E_x sublevels in the excited $|{}^3E\rangle$ state. This broadening scales as T^5 with the temperature till 100K. However at room temperatures and below room temperatures, this population transfer is at a rapid pace that only an averaged $|{}^3E\rangle$ can be observed. Thus for the purposes of our study we take into account this broadening as a transverse decay of the excited state.

The $|0_g\rangle \leftrightarrow |\pm 1_g\rangle$ in the Λ system can be addressed with a microwave field whilst the remaining two transitions can be coupled with optical fields. This Λ system in NV centers

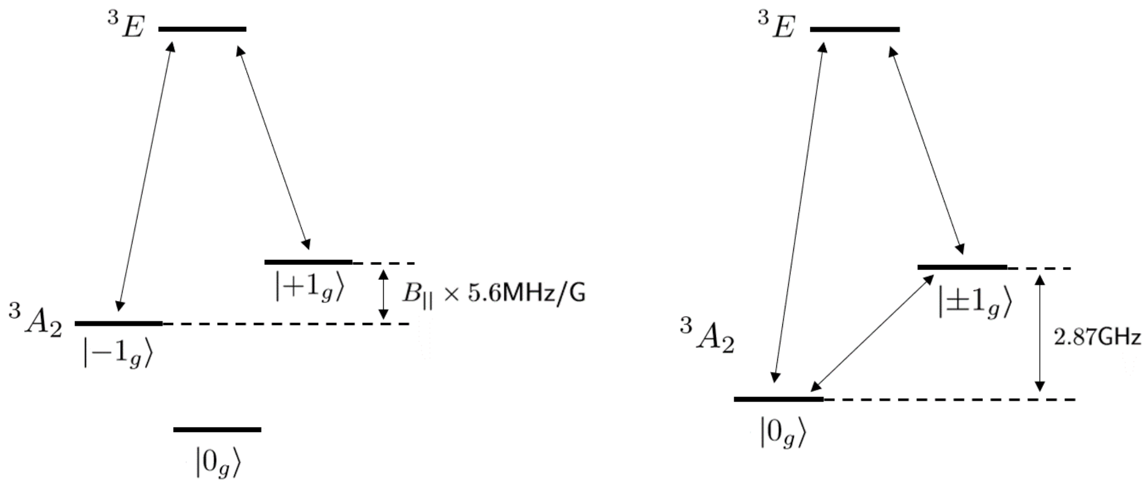

(a) (b)

Figure 2.4: The various Λ systems that can be formed in an NV center.a) Λ system formed by lifting the degeneracy of ±1 states in the ground triplet. This results in a splitting between the two ground states of $B_{||} \times 5.6MHz$ [3]. b) Due to natural strains within an NV center a Λ system can be formed in the presence of zero magnetic field with the ground triplet states and the excited state [4].

can then be used for the conversion between optical and microwave photons as we will see in Part II of the thesis.

2.4 Confocal Microscopy

The primary method used to experimentally observe fluorescence from NV center is the use of confocal microscopy. In this section we will briefly go over the theory behind confocal microscopy. Confocal microscopy, which was developed by Marvin Minsky in 1988 [58], is based upon the principle of conjugate planes in ray optics. When an optical system is used to image a point source, the plane at which the image is formed is said to be conjugate with the plane on which the point source is located. In confocal microscopy the image is constructed in a "point-by-point" manner wherein a single point on the sample is illuminated with incident light, and only the light emerging from the point of interest is captured, whilst the light that is scattered from unwanted sources on the sample is blocked. To achieve this, a pinhole is placed on the image plane such that the light rays from the *point of the interest* on the source plane intersect at the pinhole. As such light that is scattered from other locations are blocked by the barrier and not detected. The pinhole is said to be on the conjugate plane to the point source plane, or the image is *confocal* with the *point of interest*. As can be seen in Figure 2.5, in a system that comprises of two convex lenses, only rays from the red circle, *the point of interest*, intersect at the pinhole on the image plane and forms an image that is in focus. Light emanating from the off axis sources (purple cross) have images that are formed on the image plane but are blocked by the barrier and thus doesn't get through the pinhole. Light emanating from the sources that are on the axis but not on the source plane (blue cross) have images that are formed either before or after the image plane with the pinhole, thus the light that passes through the pinhole has a low intensity.

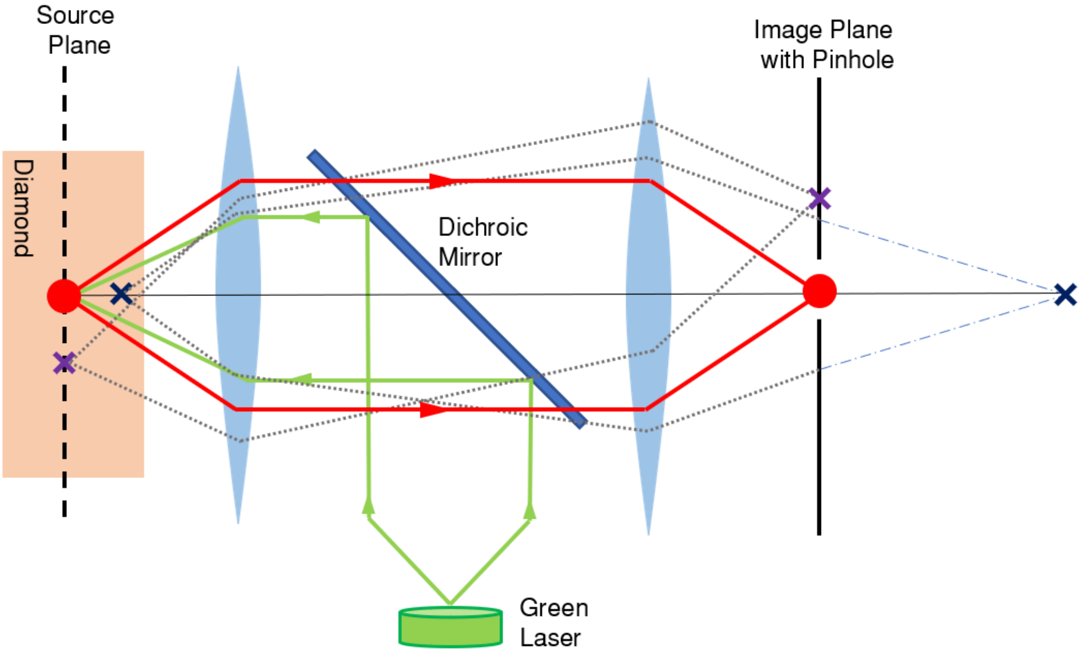

Figure 2.5: The principle of confocal microscopy to image NV centers in diamonds with two convex lenses. The source plane and the image plane are on conjugate planes. The conjugate point of the point of interest (red circle) is imaged at the pinhole, while all other conjugate points are blocked on the source plane. The dichroic mirror reflects the NV excitation green light whilst allows the fluoresced red light from the NV centers to pass.

Either by moving the sample or using scanning optics, different *points of interest* can be focused an imaged through the pinhole, thus reconstructing a complete image of the sample. To study NV centers, the technique that used is known as fluorescence confocal microscopy, wherein the excitation and emission wavelength of light is different [24, 27]. For NV centers specifically, as noted in Figure 2.2b, green light of wavelength 532nm is used to excited the NV centers, and red light of wavelength 637nm in ZPL is emitted. The microscope setup makes use of a dichroic mirror that reflects the green light and transmits the red light. The transmitted light is then collected to form an image of the NV center on a camera or for spectral or photon statistics measurements.

Part I

Design of Nanophotonic Structures for Directional Control of NV Center Emission

Chapter 3

Optical Antennas

3.1 Introduction

In this chapter we will look at the quantum and classical formalism of an emitter, and provide motivation as to why in certain contexts it would be beneficial to treat a quantum emitter as a classically radiating dipole antenna. The purpose of this is to provide background for understanding the results presented in Chapter 5, wherein we shall explore how we can control the photonic emission pattern from NV centers using sub-wavelength nanophotonic structures. The control over the emission directionality of photons from quantum emitters is an important challenge in experiments involving light-matter interactions. One method of studying the emission directionality from quantum emitters is to treat the emitters as classical dipole antennas. We can then adapt the formulations used in classical antenna formulations to study the system. Such formulations offer an advantageous approach, as they have been extensively explored and have a well established toolbox of design parameters such as directivity and front to back ratio. An optical antenna as defined by Novotny [59], is any device that is able to control free propagating radiation into localized fields. Thus an antenna can either be a macroscopic device that is driven by an electrical current, or a nanophotonic structure that is fed by a quantum emitter. In this chapter we will start with the description of a two level quantum emitter and show that by using the Local Density of States formalism, we can seamlessly describe the emitter as a classical electric dipole. Once we can describe an emitter with a classical dipole, we will show how we can use antenna formalism such as directivity and front to back ratio to study the emission from a quantum emitter.

3.2 QED Formalism Approach

Unlike typical antennas that are fed by electric currents, optical antennas are fed by the radiation from localized emitters. Thus a formalism for the enhancement of electromagnetic radiation due to an optical antenna is required. Although typically isolated single emitters such as atoms are treated quantum mechanically, we show in the discussion below that the spontaneous decay of a two level emitters can be simplified to a purely classical picture of Green's function via the local density of electromagnetic states (LDOS) formalism.

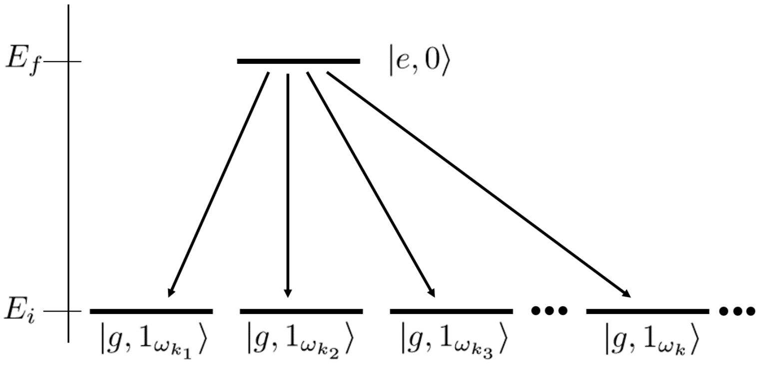

Figure 3.1: Transitions from the initial state $|e,0\rangle$ to the final states $|g,1_{\omega_{\mathbf{k}}}\rangle$, where E_i (E_f) is the energy of the initial (final) state. The states describe the emitter and field system where $|e\rangle$ ($|g\rangle$) is the excited (ground) state of the emitter while $|0\rangle$ is the zero photon state and $|1_{\omega_{\mathbf{k}}}\rangle$ is the one photon state in the mode $\mathbf{k}$

Since spontaneous decay of atom is a quantum mechanical process we begin with a fully quantum treatment of the system. We consider a system which consists of a two level quantum emitter in the presence of a field, treating it in the Heisenberg picture. The initial state and final states of the combined emitter and field system is given by:

$$\begin{aligned} |i\rangle &= |e,0\rangle \\ |f\rangle &= |g,1_{\omega_{\mathbf{k}}}\rangle \end{aligned} \tag{3.1}$$

where $|e\rangle$ and $|g\rangle$ are the excited and ground state of the two level emitter respectively, $|0\rangle$ is the zero photon state and $|1_{\omega_{\mathbf{k}}}\rangle$ is the one photon state with mode $\mathbf{k}$. The final states have the same energy and only differ by the mode **k**. The mode **k** does not refer to the wavevector here, instead it denotes the specific mode of the radiating field which in itself is described together by the wavevector and the polarization vector of the radiating field.

The decay rate of the total system from an initial state,$|i\rangle$, to the final state, $|f\rangle$, is described by Fermi's golden rule [59]:

$$\gamma = \frac{2\pi}{\hbar^2} \sum_f |\langle f| \hat{H}_I |i\rangle|^2 \delta(E_f - E_i) \tag{3.2}$$

where the summation includes the possible final states and the delta function ensures energy conservation. In the dipole approximation the interaction Hamiltonian H_I between the emitter and the field is described as:

$$\hat{H}_I = -\hat{\mathbf{p}}.\hat{\mathbf{E}} \tag{3.3}$$

where $\hat{\mathbf{p}}$ is the transition dipole moment of the two level emitter and $\hat{\mathbf{E}}$ is the quantized electric field operator. The transition dipole moment operator of the two level emitter, $\hat{\mathbf{p}}$, is represented as:

$$\hat{\mathbf{p}} = \mathbf{p}(|e\rangle \langle g| + |g\rangle \langle e|) \tag{3.4}$$

where $\mathbf{p}$ is the transition dipole moment or the dipole matrix element. The electric field operator $\hat{\mathbf{E}}(\mathbf{r_0}, t)$ at position $\mathbf{r_0}$ is defined as:

$$\begin{aligned}\hat{\mathbf{E}}(\mathbf{r_0}, t) &= \sum_{\mathbf{k'}} (\mathbf{E}^{+}_{\mathbf{k'}}(\mathbf{r_0})\hat{a}_{\mathbf{k'}}(t) + \mathbf{E}^{-}_{\mathbf{k'}}(r_0)\hat{a}^{\dagger}_{\mathbf{k'}}(t)) \\ &= \sum_{\mathbf{k'}} (\mathbf{E}^{+}_{\mathbf{k'}}(\mathbf{r_0})\hat{a}_{\mathbf{k'}}(0)e^{-i\omega_{\mathbf{k'}}t} + \mathbf{E}^{-}_{\mathbf{k'}}(r_0)\hat{a}^{\dagger}_{\mathbf{k'}}(0)e^{i\omega_{\mathbf{k'}}t})\end{aligned} \tag{3.5}$$

where $\hat{a}_{\mathbf{k'}}(0)$ and $\hat{a}^{\dagger}_{\mathbf{k'}}(0)$ are the field annihilation and creation operators respectively, while the summation is done over all the $\mathbf{k'}$ field modes. The complex fields $\mathbf{E}^{+}_{\mathbf{k'}}(\mathbf{r_0})$ and $\mathbf{E})^{-}_{\mathbf{k'}}(\mathbf{r_0})$ are spatially dependant, and denote the positive and negative frequency components of the complex electric field such that $\mathbf{E}^{+}_{\mathbf{k'}}(\mathbf{r_0}) = (\mathbf{E}^{-}_{\mathbf{k'}}(r_0))^*$. The action of the operator $\hat{\mathbf{p}}.\hat{\mathbf{E}}$ on the initial state $|i\rangle$ results in:

$$\hat{\mathbf{p}}.\hat{\mathbf{E}}\,|i\rangle = \mathbf{p}.\sum_{\mathbf{k'}}\mathbf{E}^{-}_{\mathbf{k'}}(\mathbf{r_0})e^{i\omega_{\mathbf{k'}}t}\,|g, 1_{\omega_{\mathbf{k'}}}\rangle \tag{3.6}$$

due to the action of the annihilation operator $\hat{a}_{\mathbf{k'}}(0)$ on the initial state. The action of the state $\langle f|$ on this results in:

$$\langle f|\,\hat{\mathbf{p}}.\hat{\mathbf{E}}\,|i\rangle = \mathbf{p}.\sum_{\mathbf{k'}}\mathbf{E}^{-}_{\mathbf{k'}}(\mathbf{r_0})e^{i\omega_{\mathbf{k'}}t}\langle g, 1_{\omega_{\mathbf{k}}}|g, 1_{\omega_{\mathbf{k'}}}\rangle \tag{3.7}$$

In a similar fashion:

$$\langle i|\,\hat{\mathbf{p}}.\hat{\mathbf{E}}\,|f\rangle = \mathbf{p}.\sum_{\mathbf{k'}}\mathbf{E}^{+}_{\mathbf{k'}}(\mathbf{r_0})e^{-i\omega_{\mathbf{k'}}t}\langle g, 1_{\omega_{\mathbf{k'}}}|g, 1_{\omega_{\mathbf{k}}}\rangle \tag{3.8}$$

Substituting these definitions of the $\hat{\mathbf{E}}$ and $\hat{\mathbf{p}}$ into Eq: 3.2, and invoking the orthogonality of the radiation modes, the decay rate of the system from $|i\rangle$ to $|f\rangle$ with the non vanishing terms can be reduced to:

$$\gamma = \frac{2\pi}{\hbar^2}\sum_{\mathbf{k}}(\mathbf{p}.\mathbf{E}^{+}_{\mathbf{k}}\mathbf{E}^{-}_{\mathbf{k}}.\mathbf{p})\delta(\omega_{\mathbf{k}} - \omega_0) \tag{3.9}$$

where $\omega_0 = (E_e - E_g)/\hbar$, with E_e and E_g being the energy of the excited and ground states of the emitter. The complex electric fields can then be expressed in terms of the normal modes $\mathbf{u_k}$ as:

$$\begin{aligned}\mathbf{E}^{+}_{\mathbf{k}}(\mathbf{r_0}) &= \sqrt{\frac{\hbar\omega_{\mathbf{k}}}{2\epsilon_0}}\mathbf{u_k}(\mathbf{r_0})\\ \mathbf{E}^{-}_{\mathbf{k}}(\mathbf{r_0}) &= \sqrt{\frac{\hbar\omega_{\mathbf{k}}}{2\epsilon_0}}\mathbf{u_k}(\mathbf{r_0})^*\end{aligned} \tag{3.10}$$

The spatially dependant normal modes, $\mathbf{u}(\mathbf{r_0})_{\mathbf{k}}$, are eigenfunctions of the time independent electric field wave equation:

$$\nabla \times \nabla \times \mathbf{u_k}(\mathbf{r_0}) - (\frac{\omega_{\mathbf{k}}}{c})^2\mathbf{u_k}(\mathbf{r_0}) = 0 \tag{3.11}$$

Furthermore, the normal modes are functions that are orthonormal to each other. Using the expression of the electric field operator in terms of the normal modes, the decay rate of the system from $|i\rangle$ to $|f\rangle$ can be expressed as:

$$\begin{aligned}\gamma &= \frac{2\omega_0}{\hbar\epsilon_0}|\mathbf{p}|^2\sum_{\mathbf{k}}(\hat{\mathbf{n}}_{\mathbf{p}}\cdot\mathbf{u}_{\mathbf{k}}(\mathbf{r_0})\mathbf{u}^*_{\mathbf{k}}(\mathbf{r_0})\cdot\hat{\mathbf{n}}_{\mathbf{p}})\delta(\omega_{\mathbf{k}}-\omega_0)\\ &= \frac{2\omega_0}{3\hbar\epsilon_0}|\mathbf{p}|^2\rho_p(\mathbf{r}_0,\omega_0)\end{aligned} \tag{3.12}$$

where the outer product of the normal modes is $\rho_p(\mathbf{r}_0,\omega_0)$, which is known as the partial local density of states.

3.2.1 Local Density of States

The partial local density of states is expressed as:

$$\rho_p(\mathbf{r}_0,\omega_0) = 3\sum_{\mathbf{k}}(\hat{\mathbf{n}}_{\mathbf{p}}\cdot\mathbf{u}_{\mathbf{k}}(\mathbf{r_0})\mathbf{u}^*_{\mathbf{k}}(\mathbf{r_0})\cdot\hat{\mathbf{n}}_{\mathbf{p}})\delta(\omega_{\mathbf{k}}-\omega_0) \tag{3.13}$$

where $\mathbf{n_p}$ is the unit vector in the direction of $\mathbf{p}$. As can be noted the partial local density of states is a function of the classical field normal modes, $\mathbf{u_k}$. Since the outer product of the normal modes $\mathbf{u_k}(\mathbf{r_0})\mathbf{u}^*_{\mathbf{k}}(\mathbf{r_0})$ is a 3x3 matrix, if we average the partial local density of states over over the three different axis orientations of $\mathbf{n_p}$, we arrive at the *total* local density of states:

$$\rho(\mathbf{r}_0,\omega_0) = \sum_{\mathbf{k}}|\mathbf{u_k}(\mathbf{r_0})|^{\mathbf{2}}\delta(\omega_{\mathbf{k}}-\omega_0) \tag{3.14}$$

The *total* local density of states is essentially the total number of electromagnetic modes that are present in a unit volume at a given frequency ω_0. However as shown earlier, in practice the *partial* LDOS has more significance as it is directly related to the spontaneous decay rate, γ, which is dependant on the orientation of the dipole of the emitter. In free space the *total* LDOS and *partial* LDOS are equal to each other and take the value of:

$$\rho_0 = \frac{\omega_0^2}{\pi^2c^3} \tag{3.15}$$

which refers to the density of states encountered in blackbody radiation, which leads to the well known result of the spontaneous free space decay rate of an emitter:

$$\gamma_0 = \frac{\omega^3|\mathbf{p}|^2}{3\pi\epsilon_0\hbar c^3} \tag{3.16}$$

3.2.2 Green's function

The outer product of the normal modes can also be represented by the system's dyadic Green's function, $\overleftrightarrow{\mathbf{G}}$ as [60, 59]:

$$\rho_p(\mathbf{r}_0,\omega_0) = \frac{6\omega_0}{\pi c^2}\left[\hat{\mathbf{n}}_{\mathbf{p}}\cdot \mathrm{Im}\left\{\overleftrightarrow{\mathbf{G}}(\mathbf{r}_0,\mathbf{r}_0,\omega_0)\right\}\cdot\hat{\mathbf{n}}_{\mathbf{p}}\right] \tag{3.17}$$

In classical electromagnetic theory the dyadic Green's function $\overleftrightarrow{\mathbf{G}}(\mathbf{r},\mathbf{r}_0,\omega_0)$, is a 3x3 matrix which essentially describes the field at location $\mathbf{r}$ due to the emitter at $\mathbf{r}_0$. The electric field produced by a dipole can be described with the Green's functions as:

$$\mathbf{E}(\mathbf{r}) = \frac{\omega_0^2}{c^2\epsilon_0}\overleftrightarrow{\mathbf{G}}(\mathbf{r},\mathbf{r}_0,\omega_0)\,\mathbf{p} \tag{3.18}$$

where each column in the $\overleftrightarrow{\mathbf{G}}$ matrix describes the electric field components of a dipole aligned along that specific axis. The components of the dyadic Green's function is solved by starting with the electric field wave equation:

$$\nabla\times\nabla\times\mathbf{E}(\mathbf{r}) - \frac{\omega_0}{c^2}\mathbf{E}(\mathbf{r}) = i\frac{\omega_0}{c^2\epsilon_0}\mathbf{j}(\mathbf{r}) \tag{3.19}$$

where $\mathbf{j}(\mathbf{r})$ is the current density at position $\mathbf{r}$. The current density due to a dipole source located at location $\mathbf{r_0}$is given by:

$$\mathbf{j}(\mathbf{r}) = -i\omega_0\boldsymbol{\mu}\delta(\mathbf{r}-\mathbf{r}_0) \tag{3.20}$$

From the above two equations we can thus solve for the dyadic Green's function by solving the wave equation:

$$\nabla\times\nabla\times\overleftrightarrow{\mathbf{G}}(\mathbf{r},\mathbf{r}_0,\omega_0) - \frac{\omega}{c^2}\overleftrightarrow{\mathbf{G}}(\mathbf{r},\mathbf{r}_0,\omega_0) = \overleftrightarrow{\mathbf{I}}\delta(\mathbf{r}-\mathbf{r}_0) \tag{3.21}$$

where $\overleftrightarrow{\mathbf{I}}$ is the unit tensor (which is the 3x3 identity matrix). Now that we have a general idea of the dyadic Green's function, we can return back to out discussion of the partial LDOS. Once again averaging over the different dipole orientations of the dipole, $\mathbf{n}_p$ we arrive at the *total* local density of states expressed in the form of the Green's function [60, 59] :

$$\rho(\mathbf{r}_0, \omega_0) = \langle \rho_p(\mathbf{r}_0, \omega_0) \rangle = \langle \mathbf{n}_p \cdot \overleftrightarrow{\mathbf{G}}(\mathbf{r}_0, \mathbf{r}_0, \omega_0) \cdot \mathbf{n}_p \rangle = \frac{2\omega_0}{\pi c^2} \mathrm{Im} \left\{ \mathrm{Tr}[\overleftrightarrow{\mathbf{G}}(\mathbf{r}_0, \mathbf{r}_0, \omega_0)] \right\} \tag{3.22}$$

where Tr is the trace of the Green's dyadic tensor function. The total LDOS, ρ, thus refers to the total number of electromagnetic modes present in per unit volume per unit frequency at a given point, $\mathbf{r}_0$. If we look at it from the classical frame, $\overleftrightarrow{\mathbf{G}}(\mathbf{r}_0, \mathbf{r}_0, \omega_0)$ is the field at $\mathbf{r}_0$ previously emitted by the quantum emitter, that has been reflected back towards to the position of the emitter. This is an important result as we can see how the emission of a two level quantum emitter can be essentially described purely in the classical frame with classical electromagnetic fields.

It can thus be seen how the surrounding medium influences the spontaneous emission rate of an emitter by modifying the local density of states in which the emitter is located in. This characteristic effect of the surrounding environment on the spontaneous emission rate of emitters is captured in the ratio between the spontaneous decay rate, γ, and the spontaneous decay rate of the emitter in vacuum, γ_0, which is known as the Purcell factor $(\frac{\gamma}{\gamma_0})$[61]. The value of the Purcell factor thus is a measure of how much the environment or structure in which the emitter is embedded in modifies the emitter's radiative properties. Now that we have a basic understanding of the quantum mechanical description of a two level emitter interacting with a field, we will proceed to see how this can be equated to a classical dipole description.

3.3 Classical Antenna Power Approach

We will now see how the quantum mechanical description of a two level emitter can be described by classically radiating dipole antenna. This translation from the quantum mechanical description of a two level emitter to a radiating dipole can be done with the Green's function. As we saw above the Green's function Green's function $\overleftrightarrow{\mathbf{G}}(\mathbf{r}, \mathbf{r}_0, \omega_0)$, essentially describes the electric field at a point $\mathbf{r}$ by a dipole $\boldsymbol{\mu}$, located at some point $\mathbf{r}_0$, oscillating harmonically at a frequency of ω_0:

$$\mathbf{E}(\mathbf{r}) = \frac{\omega_0^2}{c^2\epsilon_0}\overleftrightarrow{\mathbf{G}}(\mathbf{r}, \mathbf{r}_0, \omega_0)\,\boldsymbol{\mu} \tag{3.23}$$

In electromagnetic theory the current density of an oscillating dipole $\boldsymbol{\mu}$ can be represented as:

$$\mathbf{j}(\mathbf{r}) = -i\omega_0\boldsymbol{\mu}\delta(\mathbf{r} - \mathbf{r}_0) \tag{3.24}$$

The power dissipated by this classical dipole is defined by Poynting's theorem from classical electromagnetic theory as [59]:

$$P = -\frac{1}{2}\int_V \mathrm{Re}\{\mathbf{j}^*.\mathbf{E}\}dV \tag{3.25}$$

where V is the volume occupied by the dipole, $\mathbf{j}$ is current density generated in the region V due to the oscillating dipole, and $\mathbf{E}$ is the electric field. Since the current density of the dipole is a delta function at the position $\mathbf{r}_0$, the power integral above can be expressed as:

$$P = \frac{\omega_0}{2}\mathrm{Im}\{\mu^*.\mathbf{E}(\mathbf{r}_0)\} \tag{3.26}$$

where $\mathbf{E}(\mathbf{r}_0)$, is the electric field at the position of the dipole $\mathbf{r}_0$. By substituting the expression for the electric field in terms of the Green's function from Equation 3.23, we arrive at:

$$P = \frac{\omega_0^3|\mu|^2}{2c^2\epsilon_0}[\mathbf{n}_\mu \cdot \mathrm{Im}\{\overleftrightarrow{\mathbf{G}}(\mathbf{r}, \mathbf{r}_0, \omega_0)\} \cdot \mathbf{n}_\mu] \tag{3.27}$$

where $\boldsymbol{\mu} = \mu\mathbf{n}_\mu$, with $\mathbf{n}_\mu$ being the unit vector in the direction of the dipole moment. This allows us to directly represent the power emitted by a classical dipole as a function of the LDOS from Equation 3.17 as:

$$P = \frac{\pi\omega_0^2}{12\epsilon_0}|\mu|^2\rho_p(\mathbf{r}_0, \omega) \tag{3.28}$$

Since the power emitted by a classical dipole oscillating harmonically can be represented by the LDOS, this gives us a direct connection to the spontaneous emission rate of a two level quantum emitter (Equation 3.12):

$$\frac{P}{\gamma} = \frac{|\mu|^2}{|\langle g| \hat{\mathbf{p}} |e\rangle |^2} \frac{\hbar\omega_0}{4} \tag{3.29}$$

where the ratio between the power emitted by a classically radiating dipole and the transition rate of a two level quantum emitter can be directly expressed as a ratio of the classical dipole moment μ, and the transition dipole moment $\hat{\mathbf{p}}$. In other words, the field of quantum emitter and a classically radiating dipole differs only by a factor. Thus by using the LDOS formalism, we can connect the emission pattern of a two level quantum emitter and a classical dipole antenna. Making this connection provides us with a supply of a wide array of features from the toolbox of classical antenna formalism to study the emission from quantum emitters by modelling them as classical dipole antennas. One example of this includes the use of impedance matching by representing the resistance of quantum emitters Z, as a function of the LDOS:

$$\mathbf{Re}\{Z\} = \frac{P}{I^2} = \frac{\pi\rho_p}{12\epsilon_0} \tag{3.30}$$

This circuit formalism of describing quantum emitters has been extended by Krasnok, *et al*, in Reference [62]. However for the purposes of this thesis we will restrict ourselves to adopting the tools of directivity and front to back ratio from classical antenna theory to study the emission pattern from quantum emitters.

3.4 Directivity

When discussing the control of emission of radiation from emitters, it is also important to consider the angular distribution of the radiation. In classical antenna theory this is characterized by the directivity, D, of the antenna. To derive this, we start by describing the normalized angular power density, $p(\theta, \phi)$ of radiation as:

$$\int_0^{\pi} \int_0^{2\pi} p(\theta, \phi) sin\theta d\phi d\theta = P_{rad} \tag{3.31}$$

where P_{rad} is the total power radiated by the emitter. The directivity, D, is a measure of the ratio between angular power density of the antenna, $p(\theta, \phi)$, and the power density of an isotropic radiator that radiates power evenly around a 4π solid angle:

$$D(\theta, \phi) = \frac{4\pi}{P_{rad}} p(\theta, \phi) \tag{3.32}$$

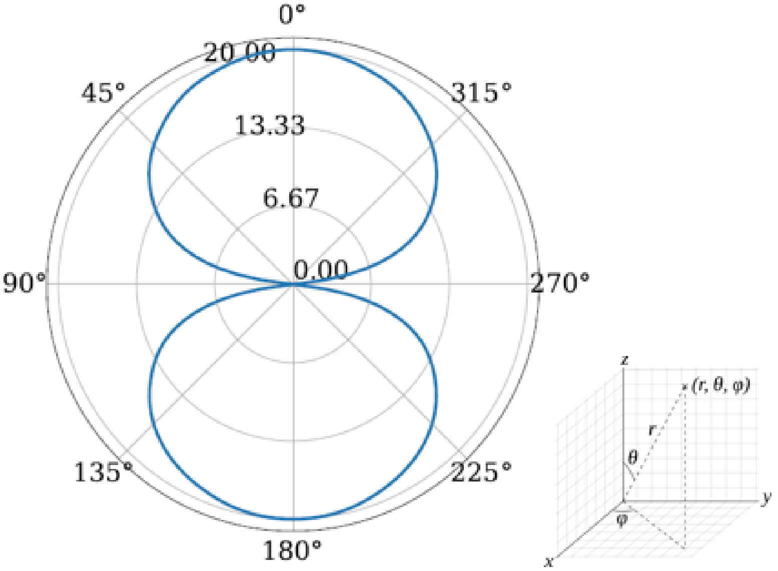

Figure 3.2: Normalized directivity plot of a electric dipole aligned along the x axis. The concentric circles refer to the power in dB. The angular coordinates are measured along the θ axis. The front and back lobes are associated with the forward and backward emissions of the antenna at elevation angle $\theta = 0^o$ and $\theta = 180^o$ respectively. The angular axis in the directivity plot denotes the elevation angle in a spherical coordinate system, and the radial axis denotes the directivity value in decibels (dB). Inset: Spherical coordinates used to the describe dipole emission.

The values of the directivity, D, is usually measured in decibels (dB). As we would see in Chapter 5, in the simulation results, the directivity pattern allows one to gain better knowledge of the angular emission pattern of a given structure. As an example, Figure 3.2 shows the directivity plot a dipole positioned along the x-axis, wherein the front and back lobes are associated with the emission of the dipole are at $\theta = 0^o$ and $\theta = 180^o$ respectively. The radial axis denote the directivity values at each angle and the angular axis denotes the elevation angle θ. Another measure of an antenna performance is the Front to Back ratio (FBR). The front to back ratio is the ratio between the power gain of the antenna in the forward propagating fields and the backward propagating fields from an antenna defined as:

$$FBR = D(\theta = 0) - D(\theta = 180^o) \tag{3.33}$$

A positive FBR indicates that the antenna is preferentially emitting in the intended forward direction and a negative FBR indicates that it is preferentially emitting in the backwards direction. Thus in designing a directional antenna, it would be ideal to design an antenna wherein it has a large positive FBR value.

Chapter 4

Inverse Design

4.1 Introduction

In this chapter, we will look at the theoretical framework for understanding the inverse design methodology used in Chapter 5. This methodology allows one to design nanophotonic structures that produce a specified electromagnetic response.

All of electromagnetic theory is condensed into the four succinct equations known as Maxwell's equations. The electromagnetic response and the propagation of the fields through any structure can thus be fully defined by solving the Maxwell's equations with the appropriate boundary conditions. This is the basis of the *forward* design methodology used in most nanophotonic problems: *for a given structure, what would be the expected electromagnetic response?*. In certain contexts however, it is much more beneficial to ask the *inverse* design question: *for a user defined electromagnetic response, what would be the required geometry?*. Answering this question would allow one engineer designs that are more efficiently suited to solving the problem at hand.

However, one caveat in trying to solve the inverse problem is that, unlike the forward problem, there doesn't exist one unique solution. Furthermore, sometimes for a given field response, there might not even exist a geometry to produced the desired output due to the demands of physical reality. These issues can be circumvented by instead framing the inverse problem as an optimization problem, wherein we look for the geometry that would most closely produce the desired electromagnetic response. Inverse design then becomes an optimization problem where we try to optimize a certain *figure of merit* (FOM) constrained to the Maxwell's equations. Or, in other words, what geometry, described by the spatially varying permitivity (ϵ) and permeability (μ) of the structure, would maximize the desired FOM. In recent years, the use of inverse design methodologies for photonic design has become prevalent and has included the use of deep learning networks [63] and linear regression models such as gradient descent [64, 65]. In our work, we focus on the use of a gradient descent optimization model known as adjoint optimization that is used to calculate the gradients of the FOM as a function of the design parameters. We will theoretically show how the use of the adjoint optimization will greatly improve computational efficiency in solving the inverse design problem, as opposed to a brute force method.

For the purposes of gaining an intuitive understanding of the process of adjoint optimization we will assume that the material of the structure is non-magnetic ($\mu = \mu_0$), and we will also assume that the fields are time harmonic. For a more comprehensive discussion on the adjoint optimization technique please refer to Owen Miller's PhD thesis [66].

4.2 Adjoint Optimization

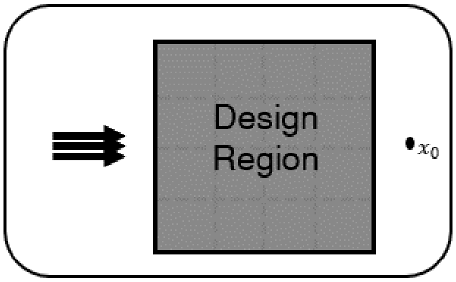

Figure 4.1: The initial setup of the design problem to intuitively understand the process of adjoint optimization. We have a field that is incident on the design region, or the region over which we intend to optimize a structure such that the *figure of merit* (FOM) is maximized at the point x_0. The background permitivity of the design region is assumed to be ϵ_1.

As discussed above, the inverse design problem can be re-framed as an optimization problem that can be solved iteratively using linear regression models such as the gradient ascent or descent methodology. The gradient ascent (descent) method is an optimization algorithm in which the local maximum (minimum) of a function is reached by iteratively moving in (away from) the direction of the steepest gradient at each point in the function [67]. This can be understood in the electromagnetic design context with a simple two dimensional example as shown in Figure 4.1. The problem can be posed as follows: *what geometry within the design region, with a background permitivity of* ϵ_1*, would maximize the electric field intensity,* $|E(x_0)|^2$*, at the position* x_0*[66]?*. The FOM can then written as:

$$FOM = |E(x_0)|^2 \tag{4.1}$$

Following from this, the gradient, or the change in the FOM, subject to a change in the geometry in the design region can be expressed as:

$$\delta(FOM) = |E_{new}(x_0)|^2 - |E_{old}(x_0)|^2 \tag{4.2}$$

where $|E_{new}(x_0)|^2$ is the electric field intensity at x_0 after a change in geometry in the design region, and $|E_{old}(x_0)|^2$ is the electric field intensity at x_0 before the geometry change was made. The change in geometry for simplicity can be modelled by splitting the design region into a grid with N number of points, and placing small dielectric inclusions with a permittivity ϵ_2 and volume V at different points, x_n, on the grid. The change in the FOM due to the inclusion can be represented as:

$$\begin{aligned}
\delta(FOM) &= |E_{old}(x_0) + \delta E(x_0)|^2 - |E_{old}(x_0)|^2 && \text{(4.3a)}\\
&= E_{old}(x_0)\delta\overline{E(x_0)} + \overline{E_{old}(x_0)}\delta E(x_0) + |\delta E(x_0)|^2 && \text{(4.3b)}\\
&\approx 2\text{Re}\left\{\overline{E_{old}(x_0)}\delta E(x_0)\right\} && \text{(4.3c)}
\end{aligned}$$

where in the the last step the higher order terms can be ignored in the limit that the dielectric inclusion is small ($V \to 0$) which is also known as *linearization*. Linearization allows for complex non-linear electromagnetic design problems to be modelled and solved with linear regression as long as the change in geometry in each iteration is small. Furthermore taking the limit, $V \to 0$, allows for any arbitrary topology or shape to be approximated. The naive straightforward approach to optimizing the FOM would be to use a brute force method. As shown in Figure 4.2, this might done by placing a dielectric inclusion at every possible point, x_n, on the grid one-by-one. The geometry is updated by keeping the geometry with the largest gradient, $\delta(FOM)$, and in the next iteration the process is repeated by placing an inclusion in every possible point on the new geometry. As can be seen right away this is a computational exhaustive process as $N + 1$ simulations are required within each iteration.

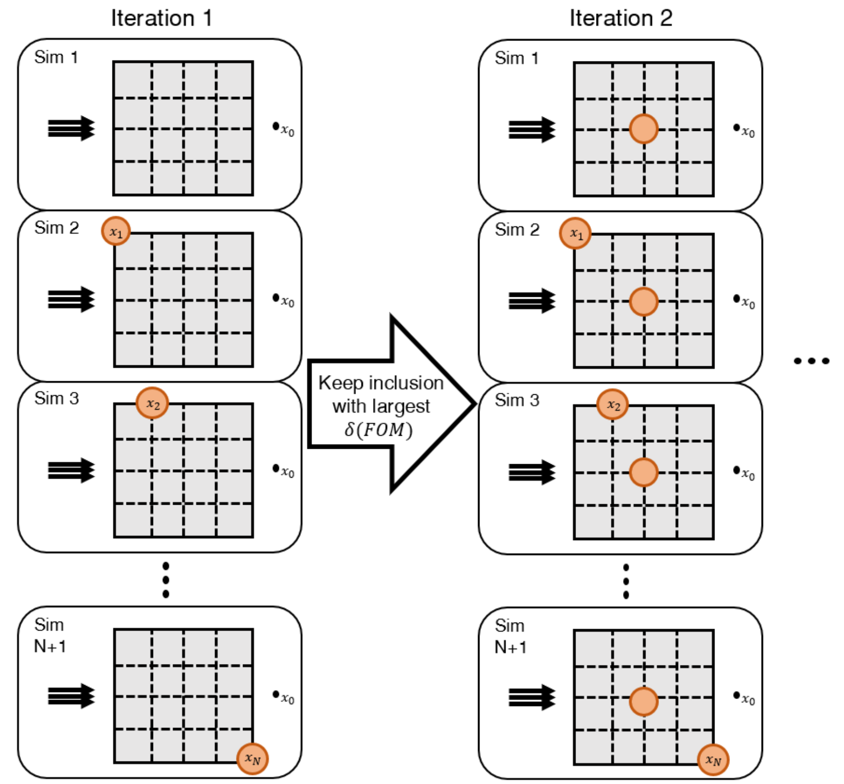

Figure 4.2: The setup for brute force optimization. The optimization begins with no inclusions within the design region. Within iteration, a simulation is performed with an inclusion at each possible position on the grid x_n. The inclusion with the largest increase in the FOM is kept and the second iteration is begun. The process is repeated until the best solution is found wherein there is no longer an increase in the FOM.

As we shall see, by utilizing the reciprocity of Maxwell's equations of electromagnetism, this process can be reduced to performing only two simulations in each iteration. For any dielectric inclusion placed at a point, x_n, on the grid, there is an induced dipole moment, p_{ind}, on that inclusion due to the old electric field, $E_{old}(x)$ (since for $V \rightarrow 0$, $E_{new}(x_n) = E_{old}(x_n)$)[68]:

$$p_{ind} \approx \alpha(\epsilon_2, V) E_{old}(x_n) \tag{4.4}$$

where α is the polarizability of the inclusion which is given by the Claussiu-Mosotti factor [68] according to the shape of the inclusion [1]. The polarizability of the inclusion is a function of the volume,V, and the permitivity, ϵ_2, of the inclusion. As we saw in the previous chapter, the electric field due to a dipole can be expressed with the Green's function (3.18). Using this formalism, the change in the electric field at x_0 due to the dielectric inclusion at x can then represented as:

$$\delta E(x_0) = G(x_0, x_n) p_{ind}(x_n) \tag{4.5}$$

where the Green's function, $G(x_0, x_n)$, is the field at point x_0 due to a dipole with unit amplitude at point x_n [59] (where for simplicity we have dropped the normalization factor seen in Equation 3.18). Furthermore, in this case we are referring to the scalar Green's function as opposed to the dyadic Green's function we saw in the previous chapter. The FOM gradient due to the dielectric inclusion at point x_n can then represented as:

$$\begin{aligned} \delta(FOM)_{x_n} &= 2\mathrm{Re}\left\{\overline{E_{old}(x_0)} G(x_0, x_n) p_{ind}(x_n)\right\} \\ &= 2\mathrm{Re}\left\{\overline{E_{old}(x_0)} G(x_0, x_n) \alpha E_{old}(x_n)\right\} \end{aligned} \tag{4.6}$$

From Equation 4.6, the terms $\overline{E_{old}(x_0)}$ and $p_{ind}(x_n)$ can be determined from a single *forward* simulation. By invoking the reciprocity of the Maxwell's equation, the Green's function can be written as: $G(x_0, x_n) = G(x_n, x_0)$. Or in the other words, the field at x_0 due to a unit dipole at x_n, is equal to the field at x_n due to a unit dipole at x_0. Using this symmetry, the FOM gradient can now be written as:

$$\delta(FOM)_{x_n} = 2\mathrm{Re}\left\{G(x_n, x_0)\alpha\overline{E_{old}(x_0)} E_{old}(x_n)\right\} \tag{4.7}$$

where the first three terms $G(x_n, x_0)\alpha\overline{E_{old}(x_0)}$ can be interpreted as the field at x_n due to a dipole at x_0 with amplitude $\alpha E_{old}(x_0)$. We define this field as the *adjoint* field:

$$E_{adj}(x_n) = G(x_n, x_0)\alpha\overline{E_{old}(x_0)} \tag{4.8}$$

Using this definition of the adjoint fields, E_{adj}, the FOM gradient can now be expressed as:

---

[1] Before the optimization begins, the shape of the inclusion is selected and fixed. This shape is then used throughout the optimization process

$$\delta(FOM)_{x_n} = E_{adj}(x_n)E_{old}(x_n) \tag{4.9}$$

As we can see very quickly, this greatly reduces the computation required to determine the FOM gradient. At each iteration to determine the FOM gradient due to an inclusion with a polarizability α, a *forward* simulation is performed to calculate the $E_{old}(x_n)$ at all possible potential points at which the dipole inclusion could be placed, x_n. In a second *adjoint* simulation, a dipole with amplitude $\alpha\overline{E_{old}(x_0)}$ (the value of which was determined from the *forward* simulation) is driven from the position x_0. From this second simulation the adjoint field, $E_{adj}(x_n)$, at all possible potential positions, x_n, due to a dipole at x_0 with amplitude $\alpha\overline{E_{old}(x_0)}$ can be calculated. Hence with this optimization technique, at each iteration, the inclusion which results in the largest FOM gradient can be determined simply from two simulations (*forward* and *adjoint*) as opposed to the $N + 1$ simulations required if a brute force method is used [66].

For the sake of intuitive understanding in the simple two dimensional problem above, all the fields were scalar and the FOM was only dependant on the electric field. The same approach can be extended to three dimensions to include vector fields with the FOM being an arbitrary function of both electric and magnetic fields. Although this extension is non trivial, the general theory remains the same. The FOM gradient due to a change in the geometry, $\mathcal{G}$, at $\mathbf{x_n}$ is represented as:

$$\delta(FOM)_{\mathbf{x_n}} = 2\text{Re}\left\{\int_{\mathcal{G}} \mathbf{P_{ind}}(\mathbf{x_n}).\mathbf{E_{adj}}(\mathbf{x_n})d^3\mathbf{x_n}\right\} \tag{4.10}$$

where $\mathbf{P_{ind}}(\mathbf{x_n})$, is the induced polarization density due to a change in geometry, $\mathcal{G}$, and $\mathbf{E_{adj}}(\mathbf{x_n})$ is adjoint field[2]. As was before, in the general case, the use of adjoint optimization results in the requirement of only 2 simulations per iteration to identify the largest gradient of the FOM [66]: one *forward* simulation to identify all the possible induced polarization densities, $\mathbf{P_{ind}}(\mathbf{x_n})$, and one *adjoint* simulation to identify the adjoint field, $\mathbf{E_{adj}}(\mathbf{x_n})$. The induced polarization density, $\mathbf{P_{ind}}(\mathbf{x_n})$, is calculated in a different manner for a topological and shape variation, which we will see in the next section.

4.3 Topology vs Shape Variation

The change in geometry of a design structure can be done through a shape variation or a topological variation as seen in Figure 4.4. We will briefly see what the differences between

---

[2] Here the adjoint field is in units of dipole moment as the polarizability α is absorbed into P_{ind}

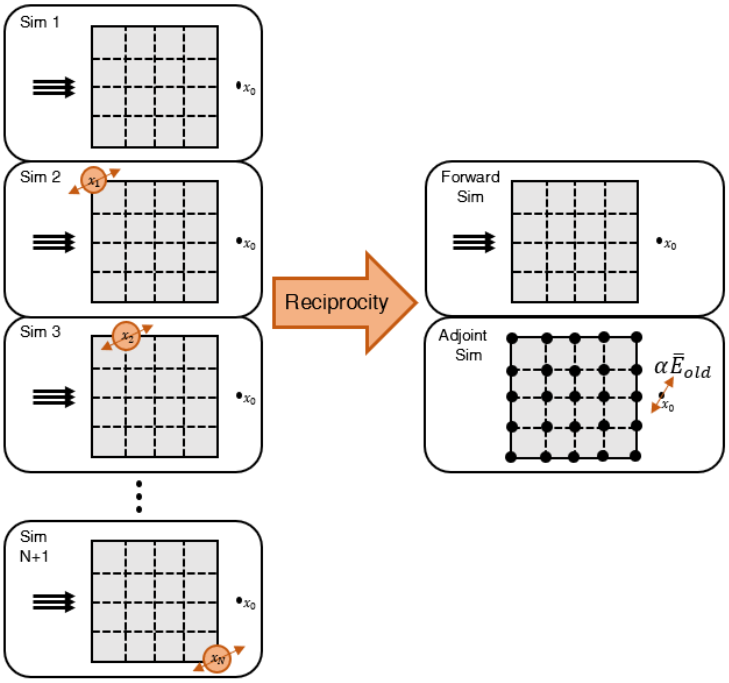

Figure 4.3: Adjoint optimization setup wherein by representing each inclusion as a dipole, the $N+1$ simulations in each iteration can be reduced to only two simulations per iteration by using the reciprocity of electromagnetic theory. One forward simulation and one adjoint simulation is required in each iteration to calculate the change in the FOM, $\delta(FOM)$. From the forwad simulation, the $E_{old}(x_n)$ at all possible points, x_n, is calculated. From the adjoint simulation, a dipole with amplitude $\alpha\overline{E_{old}}$ is driven from x_0 thus the $E_{adj}(x_n)$ at possible points x_n can be calculated.

them are.

4.3.1 Topology Variation

If the design region is split into a grid, and dielectric inclusion of an arbitrary permitivity is included at specific points on the grid, then the topology of the design is said to be changed as seen in Figure 4.4a. If the inclusion is a dielectric with a permitivity ϵ_2, placed in a region where the background permitivity is ϵ_1, the induced polarization due to the inclusion in Equation 4.10 is given by:

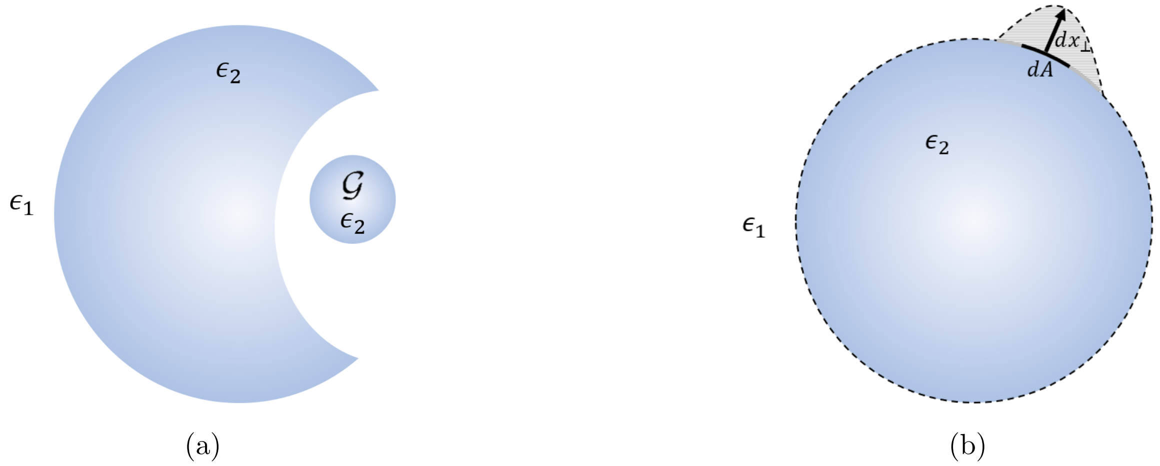

(a) (b)

Figure 4.4: a) Topology variation wherein the change in the geometry $\mathcal{G}$, is due to an inclusion with an arbitrary permittivity included anywhere within the design region. b) Shape variation wherein the change in the geometry, $\mathcal{G}$, is due to a change in the boundary of the initial structure. The permittivity of the structure within the boundary is fixed throughout the optimization process.

$$\mathbf{P_{ind}}(\mathbf{x}) = \alpha \mathbf{E}(\mathbf{x}) \tag{4.11}$$

where α is the polarizability which is defined by the Claussiu-Mosotti factor [68] according to the shape of the inclusion. The change in the FOM at each iteration is expressed by substituting this into Equation 4.10:

$$\delta(FOM)_{x_n} = 2\text{Re}\left\{\int_{\mathcal{G}} \alpha \mathbf{E}(\mathbf{x_n}).\mathbf{E_{adj}}(\mathbf{x_n}) d^3\mathbf{x_n}\right\} \tag{4.12}$$

In the limit that the size of the inclusion goes to zero, the above integral can be approximated as:

$$\delta(FOM)_{x_n} = 2V\text{Re}\left\{\alpha \mathbf{E}(\mathbf{x_n}).\mathbf{E_{adj}}(\mathbf{x_n})\right\} \tag{4.13}$$

where V is the volume of the inclusion. Hence with topology changes due to inclusion, the adjoint optimization design process in each iteration would go as follows: i) Simulate the forward fields $\mathbf{E}(\mathbf{x_n})$ and adjoint fields $\mathbf{E_{adj}}(\mathbf{x_n})$ over the design region. ii) Add an inclusion at the point in the design region at which $\delta(FOM)$ is maximized.

4.3.2 Shape Variation

With the shape variation the structure is defined with fixed boundaries with a specific permitivity within the boundary, $\epsilon_{in} = \epsilon_2$, and a different permitivity outside the boundary, $\epsilon_{out} = \epsilon_1$. The boundary of the structure can be changed as shown in Figure 4.4b. Figure 4.4b shows the cross-sectional area of a three dimensional shape, where the shaded region is the change in volume due to the changing boundary. The change in the FOM due to this volumetric change can be written as:

$$\delta(FOM)_{x_n} = 2\text{Re}\left\{\int\int \mathbf{P_{ind}}(\mathbf{x_n}).\mathbf{E_{adj}}(\mathbf{x_n})dx_{\perp}dA\right\} \tag{4.14}$$

where dA is the differential area element on the surface and $dx_{\perp}$ is the the differential length element normal to the surface area. In the limit that deformation size goes to zero, the change in FOM can be written as:

$$\delta(FOM)_{x_n} = 2\text{Re}\left\{\int \mathbf{P_{ind}}(\mathbf{x_n}).\mathbf{E_{adj}}(\mathbf{x_n})\delta_{x_{\perp}}(\mathbf{x_n})dA\right\} \tag{4.15}$$

where $\delta_{x_{\perp}}$ is the size of the deformation in the normal direction at each point on the grid, x_n. The induced polarization, $\mathbf{P_{ind}}(\mathbf{x_n})$, is given by:

$$\mathbf{P_{ind}}(\mathbf{x_n}) = (\epsilon_2 - \epsilon_1)\mathbf{E_{new}}(\mathbf{x_n}) \tag{4.16}$$

where $\mathbf{E_{new}}(\mathbf{x_n})$ is the electric field due to the new shaped with the deformed boundary related to the electric field of the original shape non-trivially. For a full treatment on this see Reference [66]. Equation 4.15, thus gives us a way to identify the change in FOM due to a boundary change.

The change in the boundary of a structure is usually done by first defining the boundary by defining it as a *spline*: a piecewise polynomial function. Incremental changes to the structure can then be made by incrementally moving different sectors in the spline. However this is computationally costly and not effective. Instead a more efficient way to perform this would be to use something known as a level set function [69] where the boundary is embedded into a signed function, $\mathcal{LS}$, such that for all coordinates within the boundary the function is negative and for all points on the boundary are zero. For instance, the level set function of a two dimensional circle centered at $(0, 0)$ with radius R can be represented as:

$$\mathcal{LS}_{circle} = \sqrt{x^2 + y^2} - R \tag{4.17}$$

Using a level set function allows for easier tracking and storing of the boundary conditions and the permitivities associated with the shape. The level set function is initialized with:

$$\mathcal{LS}(\mathbf{x}(t), t) = 0 \tag{4.18}$$

where $\mathbf{x}(t)$ are all the points on the initial boundary at time, $t = 0$. The boundary is then changed continuously and the level set function is continuously updated according to the time derivative:

$$\frac{\delta(\mathcal{LS})}{\delta t} + \frac{d\mathbf{x}}{dt}.\nabla\mathcal{LS} = 0 \tag{4.19}$$

where $\frac{d\mathbf{x}}{dt}$ is velocity normal to the boundary of the shape. Keeping track of incremental changes in the level set function is computationally more efficient than keeping track of individual boundary points and updating them constantly. Thus in the circle example, the change in the shape boundary would be an incremental change defined by the velocity, and the level set function is constantly updated. Using the level set technique is one way in which computational efficiency can be improved over using a spline to keep track of boundary conditions when performing shape variation optimization. For an in depth analysis of extending this to any arbitrary shape see Reference [69].

Chapter 5

Directional Control of Photon Emission from NV Centers with Adjoint Optimization

5.1 Introduction

The control over the emission directionality of photons from quantum emitters is an important challenge in experiments involving light-matter interactions. Efficient collection of photons from emitters is an important aspect that needs to be addressed for use in applications such as single photon sources [14], sensing/metrology [15, 16] and quantum information processing[20, 18].

For a given emitter to be used in any useful manner, extracting the spontaneously emitted photons in an efficient manner is vital for applications involving communication, metrology, or information processing. For an emitter in positioned free space, the photon emission from the emitter is isotropically emitted in the entire 4π solid angle. Theoretically, to collect all the photons from this free space emitter, detectors would have to be placed in the entire 4π solid angle around the emitter. As we can see very quickly that this is not an efficient approach at all. Thus we can see there is a need to be able to control the emission directionality of the photon emission from free space emitters. If this emitter was instead embedded in a solid state material, as is the case with quantum dots and colour centers, there is an added constraint that needs to be addressed. This is because for solid state emitters, majority of the photon emission is scattered back into the material due to the large refractive index mismatch at the boundary between the material and free space.

For instance, in diamonds, the photon extraction efficiency from NV centers is greatly hindered due to the total internal reflection at the vacuum-diamond interface. This results in a requirement for additional 'guiding' structures to allow for efficient photon extraction from the solid state emitter into free space for to be utilized in any useful manner.

Some of the structures that have been previously used to address this issue include nano-pillars [70, 50, 71, 72], solid immersion lenses [73, 8, 74, 75] and bullseye gratings [76, 77, 78]. Here in our work, we investigate the use of the inverse design methodology, seen in Chapter 4, as a potential framework to design a structure for the efficient control over the directionality of radiation from an embedded solid state emitter. We will be specifically looking at the control of fluorescence from NV centers, the properties of which we looked at in Chapter 2. In particular, by treating the emitter as an individual dipole antenna, the system can be studied in the framework of antenna formulations. Such formulations offer an advantageous approach, as they have been extensively explored and have a well established toolbox of design parameters such directivity and front to back ratio as seen in Chapter 3. In this chapter we briefly go over the need for photon emission control in NV centers, existing design structures, and the use of inverse designed structure for NV center emission control. This work was done together with Supratik Sarkar. The project was influenced and guided by Dr. Behrooz Semnani and the experimental setup was possible due to the tremendous help provided by Dr. Rubayet Al Maruf.

5.2 Emission Control

For all the advantages that NV centers present that was discussed, one important constraint in collecting the fluorescence/photo-luminescence out of NV centers is the total internal reflection of light at the diamond-air interface due to the large refractive index mismatch ($n_{\text{diamond}} \approx 2.4$). The Fresnel reflection coefficient for normal incidence between diamond and air is:

$$r = \frac{n_{diamond} - n_{air}}{n_{diamond} + n_{air}} = 0.41 \tag{5.1}$$

Furthermore total internal reflection occurs at any incidence angle above the critical angle, $\theta_c = 23.6^o$. To understand quantitatively the emission from NV centers embedded in a bare diamond slab we perform a Finite-Difference Time-Domain (FDTD) simulation. As seen in Chapter 3 we can represent the NV center as a radiating electric dipole. Furthermore as we saw in Chapter 2, the optical dipole axis of the NV center is perpendicular

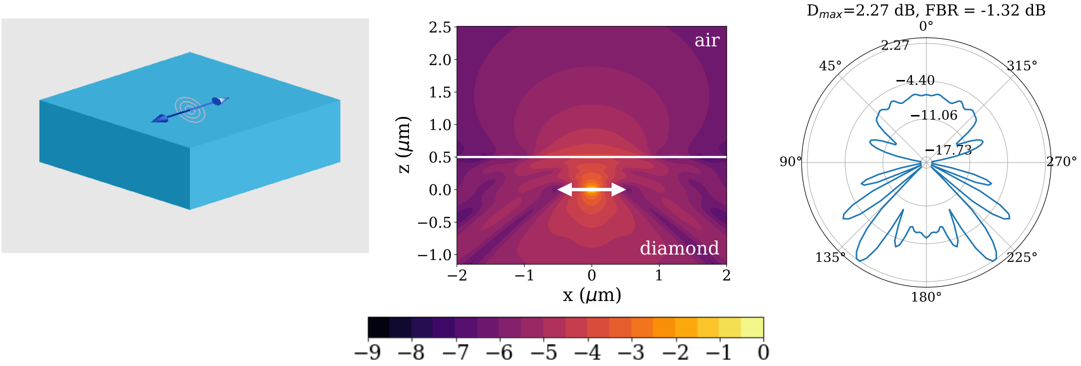

Slab | $log_{10}(|E|^2/|E_{max}|^2)$ | Directivity

Figure 5.1: Structure, simulated normalized electric field intensity (log scale), and directivity plots of bare slab with an embedded horizontal dipole. The angular axis in the directivity plot denotes the elevation angle in a spherical coordinate system, and the radial axis denotes the directivity value in decibels (dB).

to the NV axis (Figure 2.1) which lies along the $\langle 111 \rangle$ axis. This means in a (111) oriented diamond crystal the NV center can be modelled as a horizontal dipole embedded in a dielectric with a refractive index of $n_{\text{diamond}} \approx 2.4$. To model the emission from an NV center it is important to select the best orientation of the dipole axis.

Even though the most commonly available diamond samples are (100) diamonds which are cut along $< 100 >$ crystal axis, the NV centers formed in these samples are not efficient for use in photon extraction applications. This is because as we saw in Chapter 2, in (100) oriented diamonds, the NV axis lies at an angle of 54.7^o to the surface normal. It has been reported that the photon collection efficiency is maximized when the dipole axis is oriented perpendicular to the surface normal [50] as is the case with (111) surface diamonds. The reason for this can be understood by referring back to the directivity pattern of the dipole emission in Figure 3.2. For a dipole oriented along the x-y plane, the fields are maximized along the z-axis, thus it becomes easier to control the photon emission from a horizontal dipole. Furthermore, single NV centers formed in (111) diamonds have also shown to have more attractive properties, such as longer spin coherence times, than single NV centers formed in (100) diamonds [79, 80]. As such we proceed to understand the field emission pattern from a horizontal dipole embedded in a (111) sample.

Figure 5.1 shows the FDTD simulation of the electric field and the far field directivity of a NV center, modelled as a horizontal dipole, embedded at a depth of 0.5μm below the surface of a (111) diamond slab. The emission spectrum of the dipole is modelled like the spectrum of an NV center at room temperature (Figure 2.3a) centered around a wavelength of ∼680nm. As can be seen in the simulation in Figure 5.1, majority of the emitted field is scattered back into the diamond. The maximum upward directivity of the emission is -6.74dB with a FBR of -1.32dB. This means that the emission is preferentially emitted backwards. The upward scattered light into the air is not directional with most of the upward emission into air scatted within the whole upwards half angle of 90^o (Numerical Aperture(NA) = 1).

Since majority of the emission from the NV center is reflected back into the diamond due to total internal reflection, there exists a need to design structures to control the emission. Some of the existing dielectric designs that are used to control the emission profile of solid state emitters can be broadly categorized into three main design structures which include vertical nano-pillars [70, 50, 71, 72], solid immersion lenses [73, 8, 74, 75], and two dimensional bullseye structures [76, 77, 78]. To understand how each of these structures perform we will briefly look at the simulations of the existing structures.

Bullseye

Bullseye structures, as seen in Figure 5.2, are concentric circles of a fixed periodicity etched around around the emitter. These high contrast bullseye gratings work on the basis of Distributed Bragg Reflectors (DBR) with the periodicity of the structure satisfying the second order Bragg condition ($a = \lambda/n$) where $\lambda \approx 680nm$. Light extraction with circular Bragg gratings have been demonstrated in light emitting diodes [78], vertically emitting lasers [81], and for out of plane coupling of waveguide modes [82]. The Bragg gratings provide strong horizontal confinement of light from the emitter due to partial reflections at each period of the grating. Preferential emission in the vertical direction is then achieved by reducing the index contrast in the collection side interface compared to backward interface. For instance in the structure used in Reference [76], photon emission is preferentially emitted into a glass base due to the lower index contrast of the diamond-glass interface as opposed to the diamond-air interface. However with just the bare bullseye structure with no additional guiding elements, the field is not preferentially emitted into the air layer with as the FBR of the structure -4.94dB as seen in Figure 5.2. However due to the tight horizontal confinement provided by the high contrast bullseye structure, there is a greater horizontal field confinement of the fields compared to the directivity of the slab in Figure 5.1. We can note from the directivity plot that majority of the upward and backward radiation is confined within a half angle of 45^o (NA = 0.7).

Bullseye	$log_{10}(\|E\|^2/\|E_{max}\|^2)$	Directivity
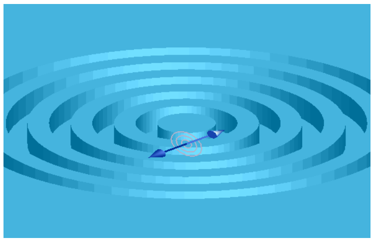	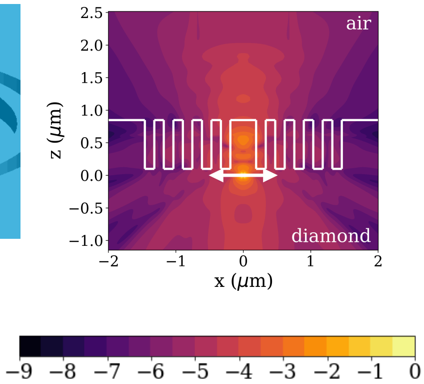	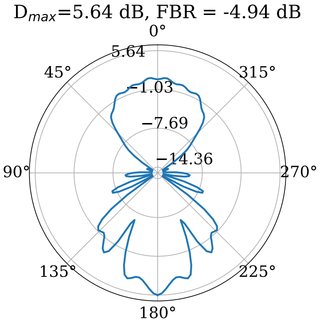

Figure 5.2: Structure, simulated normalized electric field intensity (log scale), and directivity plots of a 2D bullseye pattern with a horizontal dipole embedded at its focus point. The angular axis in the directivity plot denotes the elevation angle in a spherical coordinate system, and the radial axis denotes the directivity value in decibels (dB).

Solid Immersion Lenses

Solid Immersion Lenses (SILs) are semi-spherical structures with the radiating horizontal dipole placed at the focus. Figure 5.3 shows the FDTD simulation results of a SIL with a radius of $2.5\mu m$ [73]. SILs function by reducing total internal reflection at the diamond-air interface by providing a surface that is normal to all rays radiating spherically outward from the dipole. This in effect reduces total internal reflection thus maximizing the collection of upward radiating field. As can bee seen in the directivity plot in Figure 5.3, the maximum upward directivity is 4.71dB with a positive front to back ratio of 3.80dB. However as can been seen the directivity plot, the SIL isn't not great at focusing the emission as the upward propagating field is confined within the whole upward half angle of 90^o (NA = 1). This reduces the maximum achievable forward directivity as the SIL doesn't provide any structural design that allows for specific focusing of upward propagating fields.

Solid Immersion Lens — $log_{10}(|E|^2/|E_{max}|^2)$ — Directivity

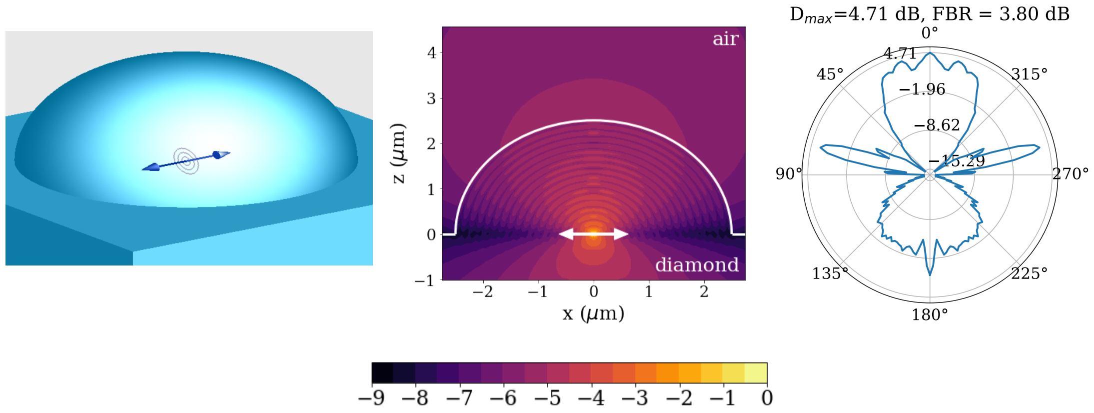

Figure 5.3: Structure, simulated normalized electric field intensity (log scale), and directivity plots of a solid immersion lens with a horizontal dipole embedded at its focus point. The angular axis in the directivity plot denotes the elevation angle in a spherical coordinate system, and the radial axis denotes the directivity value in decibels (dB).

Nanopillars

Nanopillars structures are cylindrical shaped extrusions on the surface of the diamond with the horizontal dipole placed in the center of the cylinder. Nanopillars function as a waveguide wherein the dipole couples to the fundamental mode of the waveguide (HE_{11})[70]. This waveguide mode guides the upward emitting field from the dipole and couples it the radiating modes in the the air with minimal reflection at the interface. Figure 5.4 shows the FDTD simulation results of a dipole embedded within a nanopillar with a radius of $0.23\mu m$. The field has a maximum upward directivity of 3.66dB, however the upward field is scattered over the total upward half angle of 90^o (NA = 1). The FBR of the nanopillar is -3.19dB, which means that the dipole emits preferentially in the backwards direction. Improvements on the nanopillar structures have been made by tapering the nanopillar towards to the tip which ensures that all waveguide coupled fields are maximally emitted at the tip of the waveguide [71] however the control of the emission mode of the structure cannot be achieved with the nanopillar structure.

Several other design structures of emission control from solid state emitters exist which include different permutations of the above described structures[8, 83], however arbitrary

Nano-Pillars	$log_{10}(\lvert E\rvert^2/\lvert E_{max}\rvert^2)$	Directivity

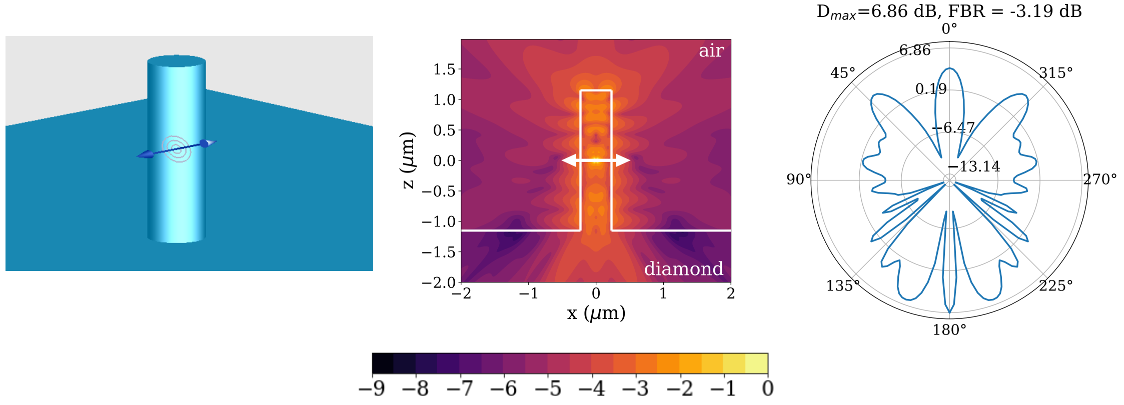

Figure 5.4: Structure, simulated normalized electric field intensity (log scale), and directivity plots of a nano-pillar structure with a horizontal dipole embedded at its focus point. The angular axis in the directivity plot denotes the elevation angle in a spherical coordinate system, and the radial axis denotes the directivity value in decibels (dB).

control of the field pattern is not attainable with any of the above described dielectric structures.

5.3 Adjoint Optimized Structure

To have arbitrary control of the field pattern of NV centers, we can make use of inverse design tool, known as adjoint optimization, that we discussed in Chapter 4. To do that let us first look at the initial setup to the optimization problem that we intend to solve.

Intial Setup

We intend to design a two dimensional grating structure that would be able to efficiently couple light emitted by the NV center to free space with a large FBR and a narrow upward half angle emission. In addition to that we would like to see if we can design a nanophotonic structure that would be able to control the output propagating mode profile such that it can directly couple to a fiber placed above the surface of the diamond. This would allow for the design of an integrated device that can be used to extract photons out of an NV center without the need for additional bulky optics. As such the optimization problem can be framed as follows: *For a horizontal dipole, corresponding to a NV center embedded in (111)-oriented diamond, positioned at a distance of* $0.5um$ *below the surface of diamond, what two dimensional pattern etched on the diamond surface would maximize the upwards directional coupling to a fiber of radius, r=0.7µm, positioned* $2\mu m$ *above the surface of the diamond)?*

The initial setup is presented in Figure 5.5. Since we intend to work with two dimensional structures, due to the ease of fabrication, we begin with the two dimensional bullseye grating as our initial guess. The optimization region is set to have a footprint of $3\mu m \times 3\mu m$, with a periodicity of $282nm$ corresponding to the second order Bragg condition, and an etch depth of $0.3\mu m$ [76]. A cylindrical silicon fiber ($n_{silicon} \approx 1.44$) of radius 0.7µm is placed at a distance of $2\mu m$ above the surface of the diamond, well beyond the distance at which the fields from a bare bullseye structure tends to zero. Now from this setup, we set the *figure of merit* (FOM) to be the overlap integral between the upward propagating fields from the structure and the fundamental mode of the fiber at the surface of the fiber, $\mathbf{S}$:

$$FOM = \frac{|\int(\mathbf{E} \times \overline{\mathbf{H_m}.} + \overline{\mathbf{E}} \times \mathbf{H_m}).d\mathbf{S}|^2}{\int \mathrm{Re}\{\mathbf{E_m} \times \overline{\mathbf{H_m}}\}.d\mathbf{S}} \tag{5.2}$$

where $\mathbf{E}$ and $\mathbf{H}$ are the electric and magnetic fields from the structure at $\mathbf{S}$, and $\mathbf{E_m}$ and $\mathbf{H_m}$ are the electric and magnetic fields of the fundamental mode of the fiber.

Adjoint Optimization Tool

For the performing the inverse design operation we use the Python based adjoint optimization package, LumOpt [65, 84], together with the electromagnetic simulation application Lumerical FDTD Simulation. The Automation API is used to interface between Python optimization process and the and Lumerical simulations. Since we are interested in an arbitrarily shaped structure with no fixed boundaries, we use topology optimization (see Figure 4.4). Figure 5.6a shows an overview of the optimization process. The initial geometry is first defined in Lumerical FDTD, and the optimization constraints and cutoff values are defined in Python. Once the optimization process is begun, in each iteration a forward simulation with the dipole source, and an adjoint simulation with the adjoint source (fundamental mode source) at the fiber tip is performed in Lumerical. The results are then exported to Python wherein the max[$\delta(FOM)$] for each topological geometric inclusion is

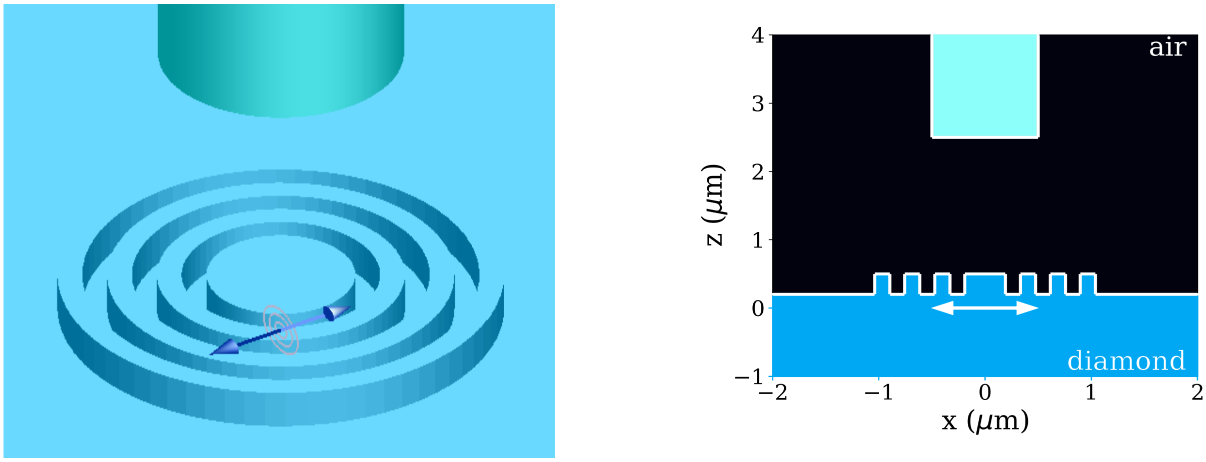

(a) (b)

Figure 5.5: The initial structure that is used to begin the optimization process. The structure is initialized with a a bullseye structure with a periodicity corresponding to the second order Bragg condition ($p = \lambda/n$), with a horizontal dipole embedded 500nm below the surface of the diamond. A silicon fiber is placed $2\mu m$ above the and the figure of merit to be optimized is the overlap between the fields of the structure and the fundamental mode of the fiber.

calculated. If the change in the max[$\delta(FOM)$] between each iteration is below the defined cutoff region, the optimization process is exited, otherwise the geometry is updated as a function of the max[$\delta(FOM)$] according to the optimizer chosen, which in our case is the L-BFGS method, to update the index profile of the structure.

Optimized structure

The FOM of the structure is calculated at each iteration and plotted in Figure 5.6b. As can be observed, the optimization process is stopped when the change in the FOM, $\delta(FOM)$, is relatively constant over a number of iterations. The final optimized structure, which provides the maximum overlap between the output fields from the structure and the fundamental mode of the fiber placed above the structure, is shown in Figure 5.7.

With the adjoint optimized structure we then perform FDTD simulation to analyze the performance of the structure. As can be seen in the FDTD forward field simulation in Figure 5.8a, the optimized structure is able to direct the emission from the dipole source in a highly directional manner. The far field directivity plot in Figure 5.8b shows that the

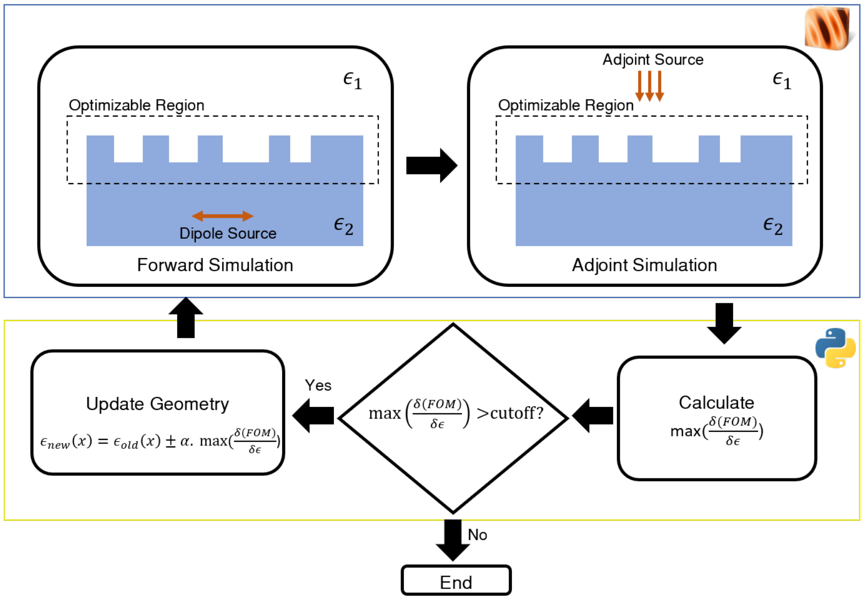

(a)

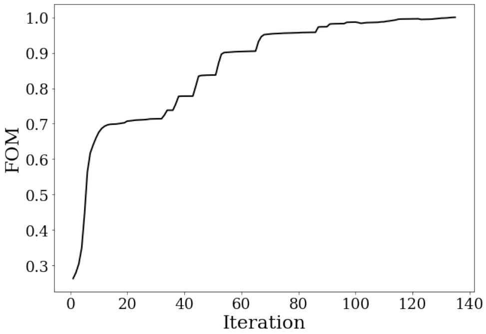

(b)

Figure 5.6: a)The flowchart representing the implementation of the inverse design process. The forward and adjoint simulations are performed with the FDTD solver from the Lumerical suite, and the results are exported to Python using the Automation API. The derivative of the figure of merit, $\delta(FOM)$, is calculated in Python and if $\delta(FOM) >$ cutoff the geometry of the structure is updated and the process continues until the $\delta(FOM) <$ cutoff. b)Normalized FOM plot as a function of the iteration number in the inverse design process.

structure has a maximum upward directivity of 7.323dB, which is ∼3dB larger than the fields from a solid immersion lens. Thus we see that by optimizing the structure to have

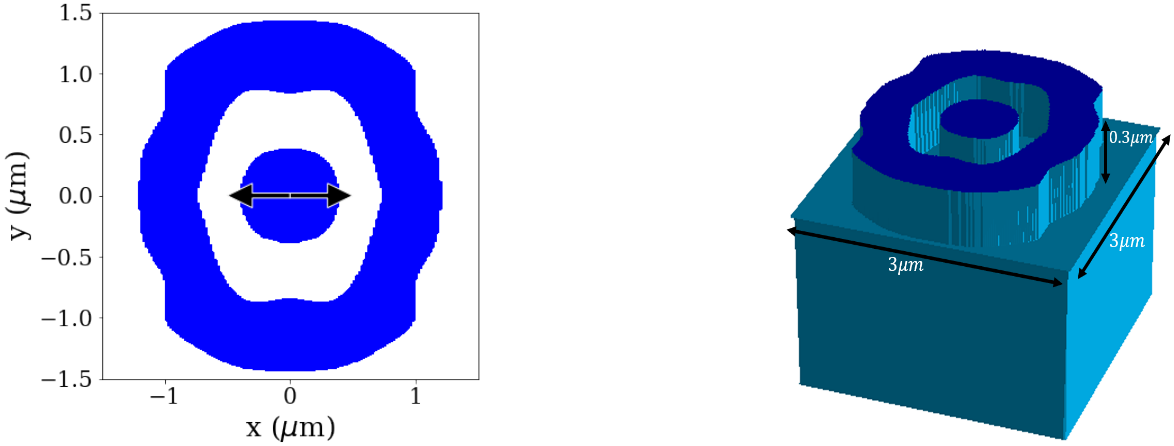

(a) (b)

Figure 5.7: a) Index profile of the structure designed with adjoint optimization with the horizontal dipole, where the colored blue indicates the diamond and the white space indicate the etched region. b) Isometric view of the adjoint optimized structure.

maximal overlap with a fiber, we were able to increase the forward directivity to $\sim$ 14dB larger than that of a rectangular slab. We note that with the adjoint optimized structure we are able to collect $\sim$ 8 more power within a NA of 0.7 compared to a an NV center embedded in a rectangular slab. This signature can be used in a confocal microscopy setup to validate the efficacy of the fabricated structure. Furthermore all of the upward emitting fields from structure is confined within a upward half angle of 45^o (NA $= 0.7$). In addition to that the FBR of the optimized structure is 4.71dB which shows that the dipole emission is preferentially upwards. This shows the the adjoint optimized structure is able to control the emission from the embedded dipole in a highly directional manner whilst providing a maximum upward directivity compared to the other structures that were previously discussed. Figure 5.8c shows the far field emission profile of the structure, showing that the optimized structure performs as intended by producing a emission field profile that has a maximum overlap with the fundamental mode of a fiber of radius $0.7\mu m$. This means that the field emitted from the structure is able to maximally couple to a fiber placed above the structure without any additional guiding structures. This, in principle, means that the complexity of the experimental setup required to image the fluorescence and collect photons out of the NV centers embedded beneath the structure can be greatly reduced. Howev . This design methodology offers a promising step forward in producing a tightly integrated device which includes the fabricated structure packaged together with

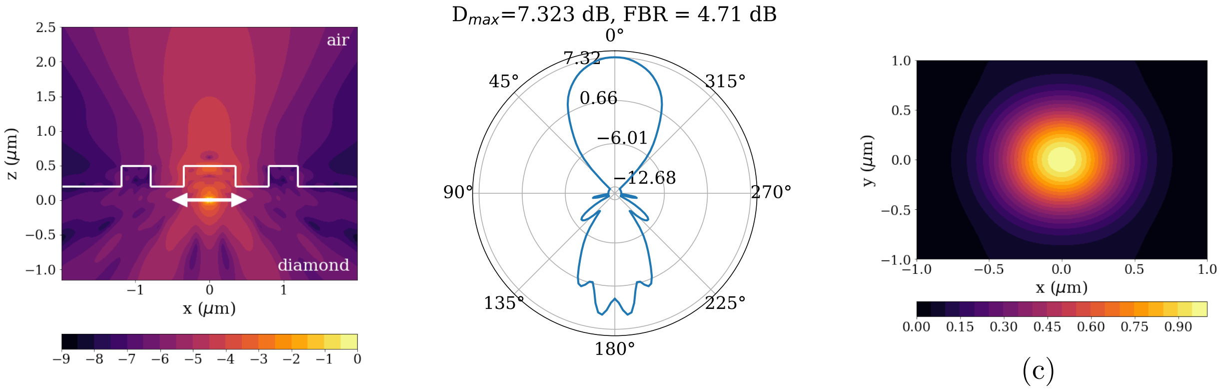

(a)

(c)

(b)

Figure 5.8: a) Simulated normalized electric field intensity (log scale) from the dipole within the inverse designed structure. b) Directivity plot of the inverse designed structure. The angular axis in the directivity plot denotes the elevation angle in a spherical coordinate system, and the radial axis denotes the directivity value in decibels (dB). c) Simulated normalized electric field intensity ($log_{10}(|E|^2/|E_{max}|^2)$) of the far field emission profile from the optimized structure.

a single mode fiber that can be used to excite the NV center and collect the fluorescence from the NV center without the need of any additional optical components.

5.4 Sensitivity Analysis

To understand how the emission performance of the structure is affected by the position of the NV center relative to the structure, we perform two sensitivity analysis: emission sensitivity and excitation sensitivity.

5.4.1 Emission Sensitivity

An emission sensitivity analysis was performed to calculate the sensitivity of the structure's emission performance with respect to the spatial position of the embedded dipole or the NV center. Using the reciprocity of electromagnetic fields, the structure was illuminated from above (at the location with the fiber 2μm above the surface of the structure) with the fundamental mode source of the fiber. Figure 5.9 shows the two dimensional normalized field plots (second row) and the one dimensional normalized field plots across the horizontal coordinates and the depth from the surface of the structure (third row). Due to reciprocity, the field strength at each location indicates the relative overlap of the emission field with the output fundamental mode, if the dipole was placed in that location. As can be noted, the performance of the structure has a high sensitivity to the lateral position of the NV center. The structure has an intended peak performance for a dipole placed at $x = y = 0$ at a depth of $z = 0.5\mu m$ with a full-width half maximum of 200nm and 160nm across the x and y dimensions respectively. For a diamond sample with a concentration of 5ppb (1ppb $= 180\mu m^{-3}$), which is typically used in sensing applications, the average distance between each NV center is $\sim 103.4nm$. Thus with a diamond of 5ppb concentration, this would mean there is a reduction in the emission from the background emitters that are not positioned directly in the intended position. With respect to the depth of the NV, the performance of the structure peaks steeply at the intended depth of $0.5\mu m$. With further increase in the depth of the dipole, the structure's performance decreases more gradually compared to the lateral x and y position of the dipole.

5.4.2 Excitation Sensitivity

To observe fluorescence from the NV centers, the NV centers in a confocal microscopy setup are excited with an above resonant energy source with a wavelength of 532nm as seen in Figure 2.2. To observe the focusing capabilities of the structure at for excitation light at a wavelength of $\lambda = 532nm$, perform a simulation of the structure illuminated from the above with a plane wave. Figure 5.10 shows the two dimensional normalized field plots (first row) and the one dimensional normalized field plots across the horizontal coordinates and the depth from the surface of the structure (second row). As seen in x and y axis field plots from Figure 5.10, the structure successfully focuses the fields at the location of the NV center ($x = y = z = 0$) with a full-width half maximum of 160nm and 140nm across the x and y dimensions respectively.. Thus with a diamond of 5ppb concentration, with average NV center separation of $\sim 103.4nm$, this would mean there is a reduction in the excitation from the background emitters that are not positioned directly in the intended position. With regards to the depth of the illumination, although the illumination intensity is not maximised at the dipole position at a depth of $0.5\mu m$, the illumination is large enough to excite an NV. Furthermore, even if an NV located at the maximized depth of $0.65\mu m$ is excited, the fluorescence from the emitted structure will be suppressed as we saw previously in Figure 5.9.

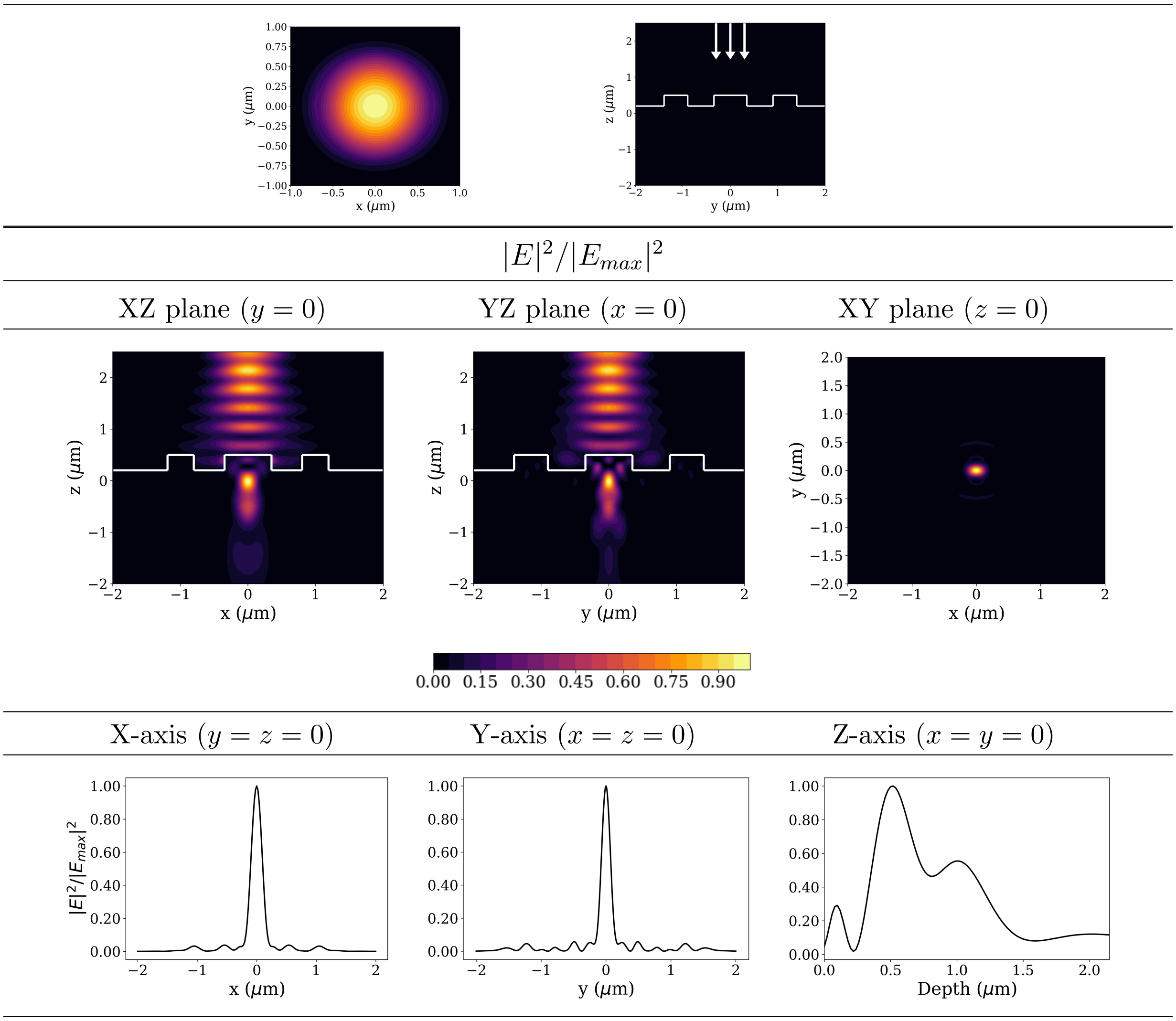

Figure 5.9: The simulated electric field intensity of the structure when illuminated from above with the intended fundamental mode source corresponding to the spectrum of an NV center at room temperature. Due to the reciprocity of electromagnetism, the strength of the fields in the structure correspond to the sensitivity of the output of the fields to the relative position of the dipole within the structure. First row: Fundamental mode source used to illuminate the structure from 2μm above the surface of the structure. Second row: Two dimensional normalized field plots. Third row: One dimensional normalized field plots across the horizontal coordinates(x and y) and the depth within the structure.

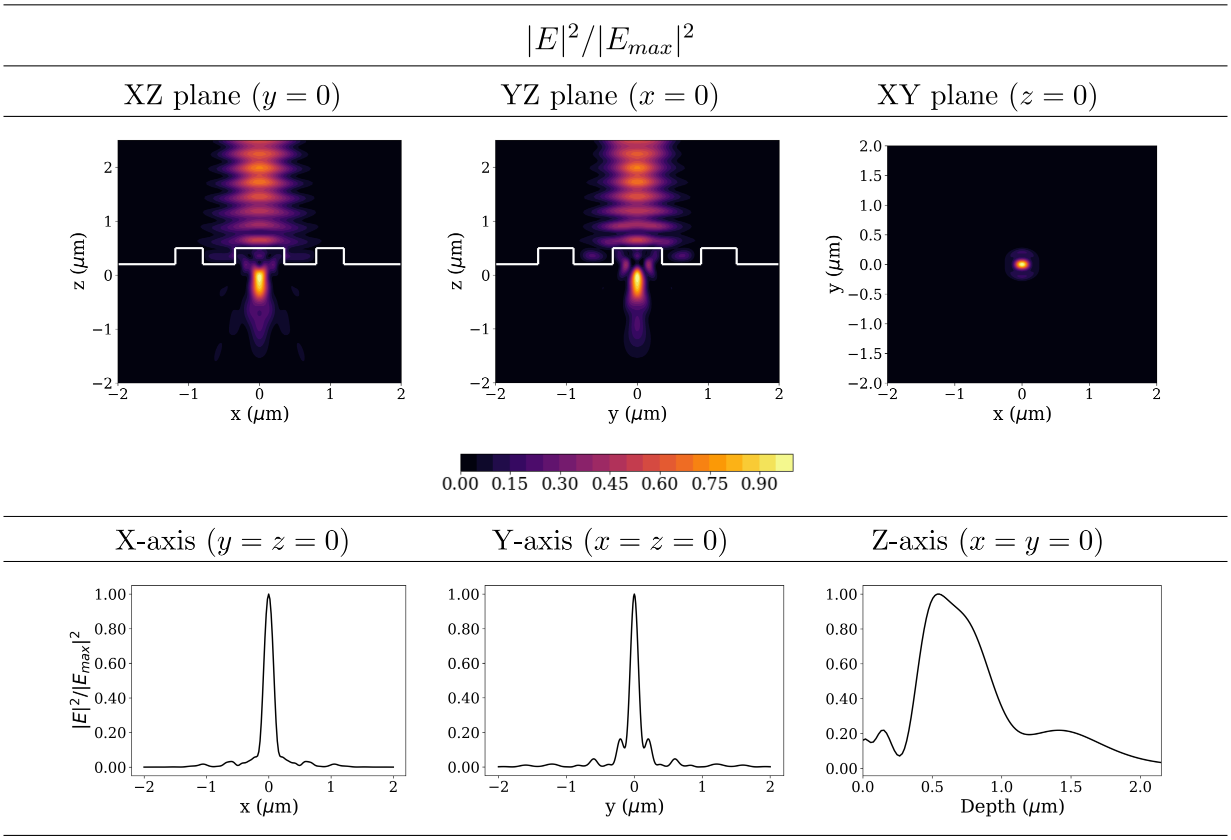

$|E|^2/|E_{max}|^2$

XZ plane ($y = 0$) YZ plane ($x = 0$) XY plane ($z = 0$)

X-axis ($y = z = 0$) Y-axis ($x = z = 0$) Z-axis ($x = y = 0$)

Figure 5.10: The simulated electric field intensity of the structure when illuminated from above with a fundamental mode corresponding to a wavelength of 532nm. The electric field strength within the structure correspond to the excitation strength of the NV centers at that position. As can be seen the structure is able to focus the excitation light to the intended NV center location thus reducing the contributions from background NV centers. First row: Two dimensional normalized field plots. Second row: One dimensional normalized field plots across the horizontal coordinates(x and y) and the depth within the structure.

5.5 Confocal Microscopy Setup

To observe the fluorescence out of the diamond structures we use a confocal microscopy setup, the theory of which was covered in Chapter 2. As discussed, the confocal microscopy setup allows us to observe images of the NV centers at specific depths of interest whilst blocking out the images formed different depths. Figure 5.11 shows the schematic of the experimental setup used in the lab to observe fluorescence from NV centers. Although we have optimized the structure for a fiber mode, as we noted above, with the adjoint optimized structure we are able to collect ~ 8 more power within a NA of 0.7 compared to a an NV center embedded in a rectangular slab. This signature can be used of the adjoint optimized structure can be used to characterize the fabricated structure.

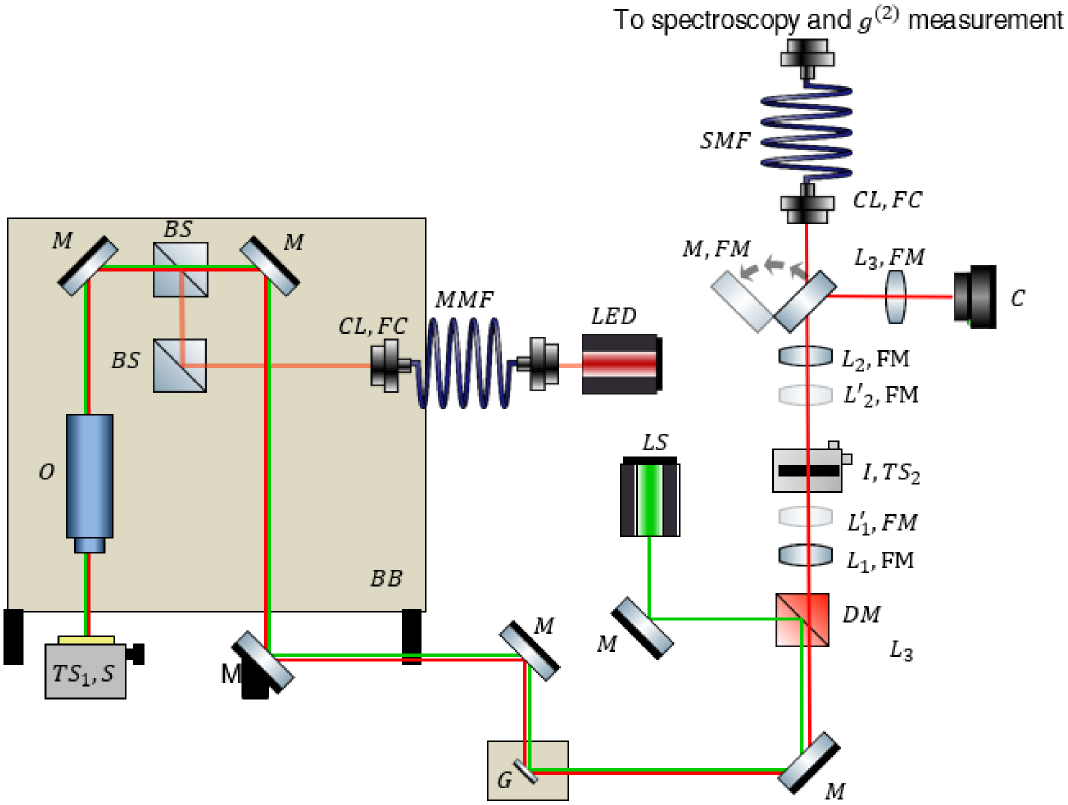

Figure 5.11: The confocal microscopy setup used to observe fluorescence from the NV centers in the diamond sample. The corresponding component names have been listed in Table 5.1.

Component	**Manufacturer**	**Part**	**Diagram**
Laser	Sprout	Sprout-G	LS
Fiber-coupled red LED	Thorlabs	M625F2	LED
Diamond sample	Applied Diamond Inc	$<$ 1ppm, $<$ 5ppb, (111) orientation	S
Translation stage	Thorlabs Machifit	MBT616D LD-60-LM	TS_1 TS_2
Galvo mirror	Thorlabs	GVSM002-US	G
Objective	Mitutoyo	MY 100X-806	O
CMOS camera	Edmund Optics	EO-5012M	C
Dichroic mirror	Semrock	LM01-552-25	DM
Flip Mount	Thorlabs	TRF90	FM
Mirrors	Newport	10D620ER.2	M
Lens	Thorlabs	AC254-200-A AC254-100-A AC254-200-A AC254-100-A AC254-35-A	L_1 L_1' L_2 L_3 L_3'
90-10 Beam splitter	Thorlabs	BSN10	BS
Iris	Thorlabs	ID25Z	I
Single mode patch cable	Thorlabs	P1-630A-FC-2	SMF
Multi mode patch cable	Thorlabs	M76L02	MMF
Vertical Breadboard	Thorlabs	MB12	BB
Fiber Coupler Lens	Thorlabs	C220TMD-A	CL

Table 5.1: Experimental components for confocal scanning microscopy of NV centers

Objective

The objective used in the confocal microscopy setup is a infinity corrected Mitutoyo MY 100X-806 model. It is important that when working with NV centers the objective have a magnification of $> 80\times$[24]. The Mitutoyo MY 100X-806 is a dry objective with a numerical aperture(NA) of 0.7 and a working distance of 6mm. Furthermore the objective is also infinity corrected, which means the light from the sample that exits through the back aperture of the objective forms a collimated infinity parallel beam before reaching the tube lens (L_1). This means that the magnification of the objective does not change even if the distance between the objective lens and the tube lens is changed. Furthermore this also means placing optical elements such as mirrors or filters between the objective lens and the tube lens wouldn't shift the position of the image formed. From the objective specification, the magnification provided by the objective is thus $m = 100 \times \frac{f_1}{200\text{mm}}$. The effective focal length of the objective is $f_{objective} = \frac{f_{designtube}}{m} = 200\text{mm}/100 = 2\text{mm}$. To produce a diffraction limited spot on the sample, the excitation light should fill the back aperture of the objective. The back aperture of the objective $d_{\text{aperture}} = 2 \times f_{\text{objective}} \times NA = 2 \times 2\text{mm} \times 0.7 = 2.8\text{mm}$. The objective has a working distance of 6mm and the Field of View(FOV) of the microscope in mm is given by, $FOV = 24/m_{objective}$.

The total linear magnification of the microscope is calculated as follows:

$$\begin{aligned} m_{total} &= m_{objective} \times m_{telescope} \\ &= (100 \times \frac{f_1}{200mm}) \times \frac{f_3}{f_2} \end{aligned} \tag{5.3}$$

where f_1, f_2, and f_3 and the focal lengths of the lenses in L_1, L_2, and L_3 respectively in Figure 5.11. As can be noted from Figure 5.11, the lenses L_1 (L_1') and L_3 (L_3') are placed on flip mounts(FM), and by switching between different configurations of L_1 or L_1', and L_2 or L_3', different magnifications of the microscope can be achieved as summarized in Table 5.2.

Magnification, m_{total}	f_1**(mm)**	f_2**(mm)**	f_3**(mm)**
50	200	200	25
100	200	200	50
100	100	200	100
100	50	200	200

Table 5.2: Summary of magnifications for different lens configurations.

Wave Propogation

To model the propagation of the fluorescence from the NV center to the detector so as to determine the positions of the lenses in relation to the iris and camera, we make use of a Gaussian Wave propagation method used in Reference [24] with the ABCD matrix approach. We employed the methodology introduced in Reference [85] wherein the beam profile is evolved with two real rays using the ABCD ray matrix method.

In ray optics the ABCD matrix method allows us to model the effect of various optical elements on the path of a ray. The rays are represented as a column vector $\begin{pmatrix} x \\ \theta \end{pmatrix}$ where x is the distance of the ray from the optical axis and θ is the angle between the ray and the optical axis. The effect of the propagation through air and thin lenses are then modelled with the ABCD matrices as:

$$M_{air} = \begin{pmatrix} 1 & d \\ 0 & 1 \end{pmatrix} \tag{5.4a}$$

$$M_{lens} = \begin{pmatrix} 1 & 0 \\ -\frac{1}{f} & 1 \end{pmatrix} \tag{5.4b}$$

where d is the propagation distance through air, and f is the focal length of the lens.

Although a simple ray optics approach wouldn't suffice to model Gaussian beam propagation, the Arnaud method introduced in Reference [85] offers a bridge to model Gaussian beams with the ABCD matrix approach. In general the intensity distribution of a Gaussian or a TEM$_{00}$ wave is defined as:

$$I(r, z) = I_0 \left(\frac{w_0}{w(z)} \right)^2 exp \left(\frac{-2r^2}{w(z)^2} \right) \tag{5.5}$$

with

$$I_0 = \frac{2P}{\pi w_0^2} \tag{5.6}$$

where w_0 is the beam waist, P is the total power in the beam, r is the radial distance orthogonal to the optical axis of the beam, z is the distance along the optical axis, and $w(z)$ is known as the beam radius or the distance from the optical axis at which the intensity of the Gaussian beam reduces to $\frac{1}{e^2}$. The beam radius can be expressed as:

$$w(z) = w_0 \sqrt{1 + \left(\frac{\lambda z}{\pi w_0^2} \right)^2} \tag{5.7}$$

where λ is the wavelength of the beam. The profile of the beam expressed by $w(z)$ is hyperbolic in nature as can be seen in Figure 5.12. The entire beam profile of the Gaussian beam can be defined by two rays ξ and η at $z = 0$ where:

$$\xi = \begin{pmatrix} 0 \\ \frac{\lambda}{\pi \theta_0} \end{pmatrix} \tag{5.8a}$$

$$\eta = \begin{pmatrix} w_0 \\ 0 \end{pmatrix} \tag{5.8b}$$

where the asymptotic angle $\theta_0 = \frac{\lambda}{\pi w_0}$. The beam radius can then be computed from the x components of the column matrices ξ and η as $w(z) = \sqrt{\xi_x^2 + \eta_x^2}$. The evolution of the Gaussian beam radius through the optical components can now be computed by action of the ABCD matrices corresponding to the optical elements on the two rays ξ and η.

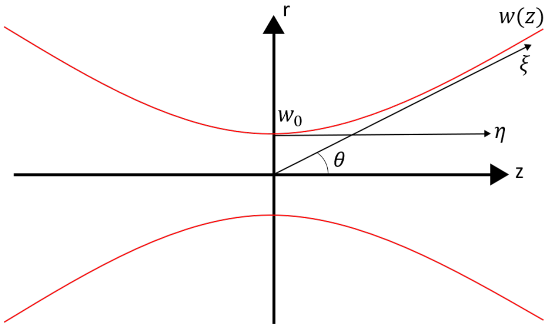

Figure 5.12: The profile of a Gaussian beam.

Using the wave propagation ray tracing method listed above the, the beam radius of the system is plotted to identify where the iris and the camera should be located. In Figure 5.13 we plot the Gaussian beam propogation through the system for the lenses with focal lengths of $f_1 = 100mm$, $f_2 = 200mm$, and $f_3 = 200mm$.

Galvo Mirrors

To perform fine scanning over the sample we use the two axis galvo GVSM002-US from Thorlabs. We built a manual scan circuit (see Appendix C) to control the individual galvo mirror angles with a resolution of 1V/^{o}.

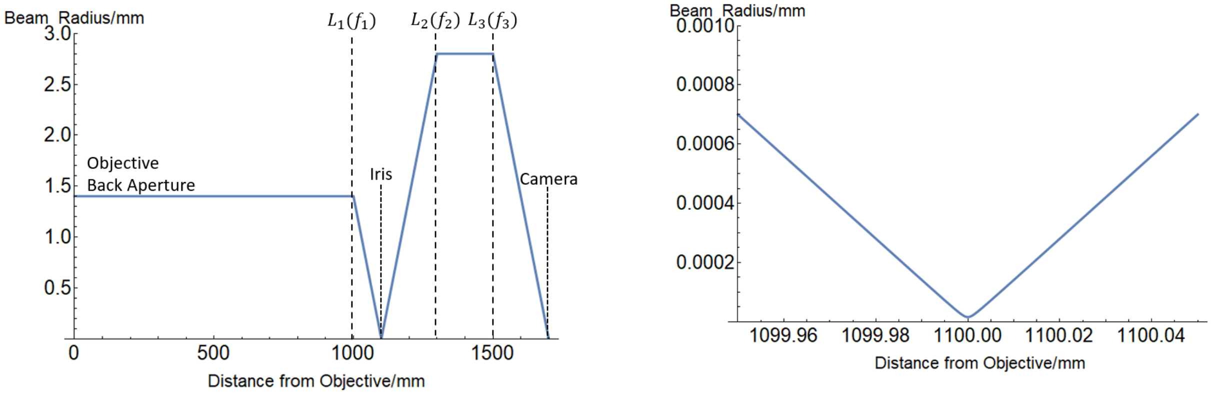

(a)

(b)

Figure 5.13: a) The beam radius evolution of the fluorescence collected by the objective as it propagates from the back aperture of the objective to the camera. Focal lengths used in this plot are $f_1 = 100mm$, $f_2 = 200mm$, and $f_3 = 200mm$. b) Close up of bream radius plot at position of iris.

Dichroic Mirror

To perform spatial separation of the excitation laser light of 532nm and emission light from the NV center of ∼680nm, we use the dichroic mirror Semrock LM01-552-25. The filter has a reflectance of $96-99\%$ for wavelengths <552nm and has a transmittance of $94-95\%$ for wavelengths >552nm.

Diamond Sample

The sample of the diamond we use for the experiment are pure type IIa diamonds with NV center concentration of 1ppm(1ppm = 1.80×10^{17}cm^{-3}) and <5ppb (1ppb = $180\mu m^{-3}$). The diamonds were purchased from Applied Diamonds Inc. and are cut along the (111) axis wherein the optical dipole axis is horizontal with respect to the surface of the diamond.

Camera and Fiber Coupler

The fluorescence from the objective can be collected in the camera C, for imaging purposes or be coupled to the fiber coupler FC, for spectral and $g^{(2)}$ measurement purposes, by switching the mirror mounted on to the flip mount(M, FM) to change the path of the beam.

5.5.1 Microscope Results

Once the microscope was built we captured some preliminary images for calibration of the image. We used a silicon wafer with a standard dose test design patterned on it with Electron Beam Lithography. Some of the images taken for microscope calibration are presented in Figure 5.14.

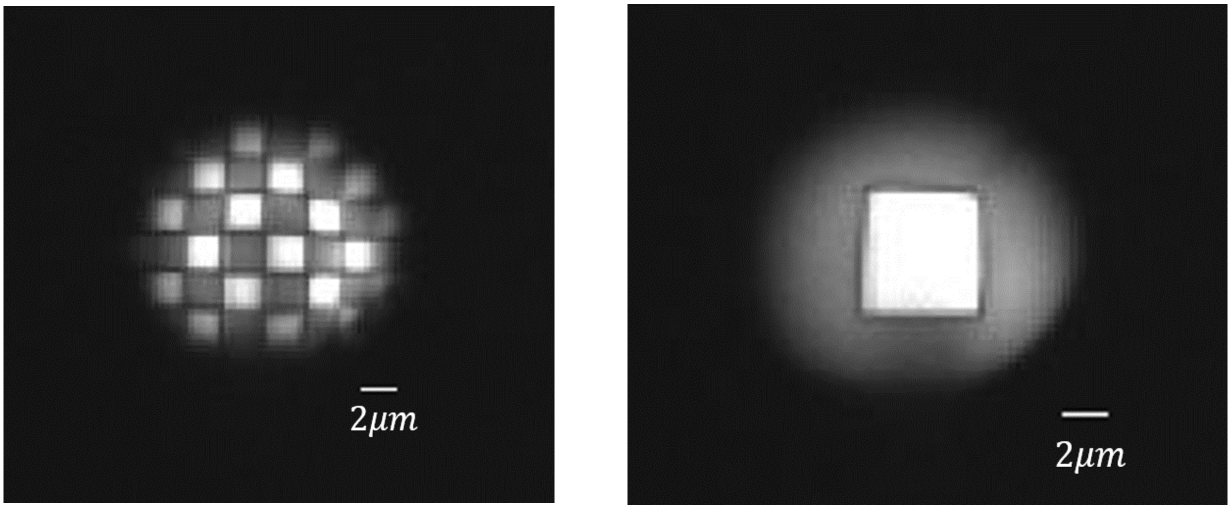

(a) (b)

Figure 5.14: a) Image of a standard JEOL EBL dose test wafer. The size of the individual square in the checkerboard pattern is $2.5\mu m \times 2.5\mu m$. b) Image of a standard JEOL EBL dose test wafer. The size of the individual square in the checkerboard pattern is $5.7\mu m \times 6.4\mu m$. 50x magnification was used in both images.($f_1 = 100mm, f_2 = 200mm, f_3 = 100mm$)

We then tried to look for NV centers within a diamond sample from Element Six with a concentration of <200ppm using the confocal microscope setup. Figure 5.15 shows some of the images that were produced. Figure 5.15a shows the image of the sample captured with just a red LED for illumination. This shows us the image of the surface of the diamond sample. When the green excitation laser ($\lambda = 532$nm) with a power of 7μm, was turned on a bright spot appears in the image as seen in Figure 5.15b. This bright spot with the radius of $\sim 0.8\mu m$ is a suspected image of the NV center fluorescence. Figure 5.15c shows the image of the sample with the red illumination LED turned off. The presence of the NV center can be confirmed by performing a spectral measurement of the emitted fluorescence.($f_1 = 100mm, f_2 = 200mm, f_3 = 100mm$)

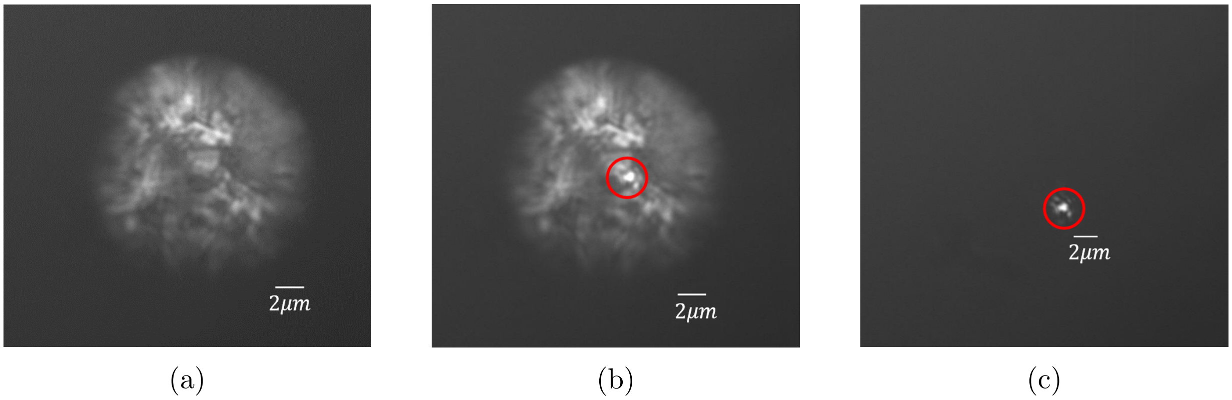

(a) (b) (c)

Figure 5.15: a) Image of diamond sample with red LED. Image shows reflections off of the diamond surface b) Image of diamond sample with red LED and green excitation laser turned on. The red circle indicates the suspected fluorescence from NV center. c) Image of diamond sample with only green excitation laser turned on.

5.6 Conclusion and Outlook

As we have seen in the simulations presented above, by using adjoint optimization we can design subwavelength structures that are able to control the directionality of photo emission from NV centers. We saw that with the adjoint optimized structure the maximum forward directivity was 7.323dB whilst all forward emission was confined to a 45^o (NA = 0.7) upward half angle. As discussed above this directivity was not achievable with any of the other bare structures that currently exist. A further advantage of using the inverse approach includes the possibility to shape the output mode of the NV center emission. In our case above we were able to design a structure that produces an output mode that overlaps with the fundamental mode of a fiber without the need of additional bulky optical elements. This design approach is a promising step forward in designing an integrated device with a single mode fiber that can be used to both excite the NV centers and collect fluorescence and single photons from the NV centers. We also have assembled a confocal microscopy setup capable of observing and collecting NV center emission and presented some preliminary images that we observed with the microscope.

Although the structure proposed above is advantageous in several aspects, there are still avenues for further improvements. As is the case with any optimization problem, since there doesn't one unique solution, the output of the results is only as good as the initial starting point and constraints placed on it. To further enhance the upward emission of the from the NV center, the initial optimization structure could include mirror like structures on the backward emitting face of the device. The addition of metallic mirror structures could also be used to further improve the Purcell enhancement of the device. Furthermore to optimize for the parameters of the structure including the depth of the NV center, and thickness of the grating, a combination of particle swarm optimization and adjoint optimization can be combined in a back and forth fashion wherein the depth/thickness is optimized via particle swarm and the topology of the 2D grating is optimized via adjoint optimization [86].

On the experimental side of things one of the first steps to be taken would be to fabricate the proposed design above. There exists literature on the standard process to be followed for the fabrication of the structure on diamond samples [70, 76, 50, 87, 88, 89]. One of the main fabrication challenges to be overcome would be spin-coating of the small diamond samples which would result in large edge bead. One approach to overcome this would be to etch a recess of the appropriate size in a silicon wafer and attaching the sample to the recess with vacuum bonding. With the sample flush with the surface of the silicon wafer, the edge bead effects will be minimized. It is also important to note that once the diamond sample is etched, the quality of the shallow NV centers are drastically reduced, but this can be overcome by annealing the sample post etching. Another approach that could be considered instead of randomized fabrication of the structures over a randomly distributed population of NV centers, would be the deterministic implantation of the NV centers over fabricated structures via ion implantation [32, 33]. In addition to the fabrication challenges in the design of the experimental setup, the galvo and the camera could be integrated to a single control and monitoring station to automate the scanning and imaging of over the samples. This can be achieved by implementing the galvo on a DAQ (data acquisition) platform. The results presented in this chapter opens up a whole avenue for designing structures with arbitrary output field patterns that can be used in several different applications.

While working on this project we became aware of two recent works that use inverse design to design structures for photon extraction from NV centers [90, 91]. In both papers the authors use adjoint optimization to control the extraction of photons from an NV center embedded in diamond with a two dimensional grating structure designed with topology optimization. The authors in Reference [91], proposed a design for a silicon grating placed above the surface of the diamond. The FOM used to design the structure, in this case, was the photon extraction efficiency at the surface of the diamond. This efficiency was defined as the ratio between the photon extraction with and without the grating structure. Furthermore, this paper also performed a two dimensional optimization of the grating thickness before a three dimensional optimization was performed to design the grating. This resulted in a reported upward half angle confinement of 30^o. However this work did not perform any mode shaping of the upward propagating emission from the NV centers. In a similar manner in Reference [90], a gallium phosphide grating structure was designed to control the emission from NV centers. Here, the authors used two different FOMs to test the photon collection enhancement. Total flux collection and local density of states (LDOS) were used as the two different figures of merit. It was shown that higher photon collection was achievable only by optimizing the flux collection, as Purcell factor enhancement by optimizing the LDOS was not achievable with a purely dielectric structure. This result validates the approach we took in optimizing the field collected above the diamond. Furthermore, the authors of the paper also fabricated the structure and used ion implantation to position the NV centers at precise locations below the structure. However in this paper no mode shaping of the emission of the NV centers was performed. Furthermore in both the papers, the enhancement was done with a NV center in a (100) diamond. As shown in Reference [50], a larger enhancement of the output flux can be done with a horizontal dipole embedded in a (111) diamond. The progress made in both the papers give us confidence and validates our approach that using adjoint optimized grating structures for photon extraction is a step in the right direction.

Part II

Microwave to Optical Domain Transducer with Single NV Centers

Chapter 6

Microwave to Optical Domain Conversion I

6.1 Introduction

The development of superconducting qubits, that operate at gigahertz frequencies, for quantum information processing applications have been rapidly evolving in recent years [92, 93]. However microwave photons, that couple to superconducting qubits, are unusable in long range networks as microwave photons suffer from losses due to noise in the environment. As can be seen from the spectral radiance plot of blackbody radiation in Figure 6.1, for temperatures T≤300K, there is large component of background radiation at microwave gigahertz frequencies. This interference with the background radiation is the primary reason why microwave photons are unusable for long range communications. Optical photons, that operate at hundreds of terahertz frequencies, on the other hand have low transmission losses over long distances and have been used to make long lived quantum memories [22, 23, 9]. Hence there is a need for a quantum interface between microwave and optical photons. This component is essential in realising a scalable hybrid quantum network where information needs to be efficiently interfaced between superconducting microwave circuits, for quantum information processing, and optical photons, for communication and memories. Currently there exists several theoretical and experimental proposals for the microwave to optical frequency conversion. These include nanomechnical oscillators [5, 94, 95, 96, 97], non-linear crystals modulators [98, 99, 100, 6], Rydberg gases, and more recently the use of rare earth doped crystals [101, 102, 103, 104].

In the nanomehanical or optomechanical approach (Figure 6.2a) [5, 94, 95, 96, 97],

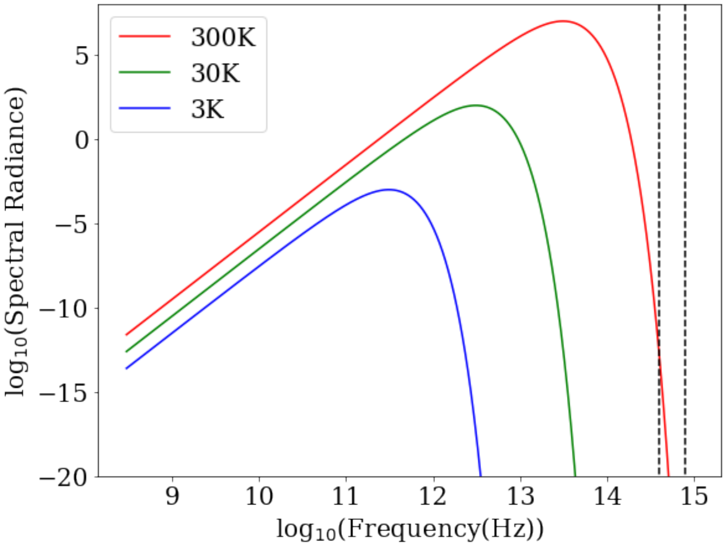

Figure 6.1: Blackbody spectral radiance plot for different temperatures against frequency. The dotted black line shows the frequency band of visible light. The spectral radiance is the emissive power per unit area, per solid angle for different frequencies ($W.sr^{-1}.m^{-3}$).

a mechanical resonator, such as a membrane, that couples to both the microwave and optical modes is used to interface between a optical cavity and a microwave cavity. The mechanical resonator is positioned between the optical and microwave cavity in such a way that it is coupled to both the microwave and optical cavities which results in effective coupling between the microwave and optical domains via the vibrational modes. This coupling is done via radiation pressure wherein there is an exchange of momentum between the mechanical membrane and the electromagnetic field. These methods of frequency conversion have shown to exhibit quantum conversion efficiencies of ~ 0.1 [5]. However one of the downsides of using the nanomechanical approach is achieving a low noise in the output which requires the mechanical resonator to be cooled down to its ground state. Cooling down of the resonator can be however quite challenging to reduce vibrational noise at the single-quantum level.

In the second approach [98, 99, 100, 6], a microwave field is used to modulate the refractive index of the optically transparent material non-linear materials (Figure 6.2b). This results in the formation of symmetric sidebands produced around the optical carrier frequency with one sideband at the microwave frequency. One of the symmetric sideband can be removed by manipulation of the transmission spectrum of the resonator, however quantum conversion has been demonstrated to ~ 0.01 [98]. The main challenge with this

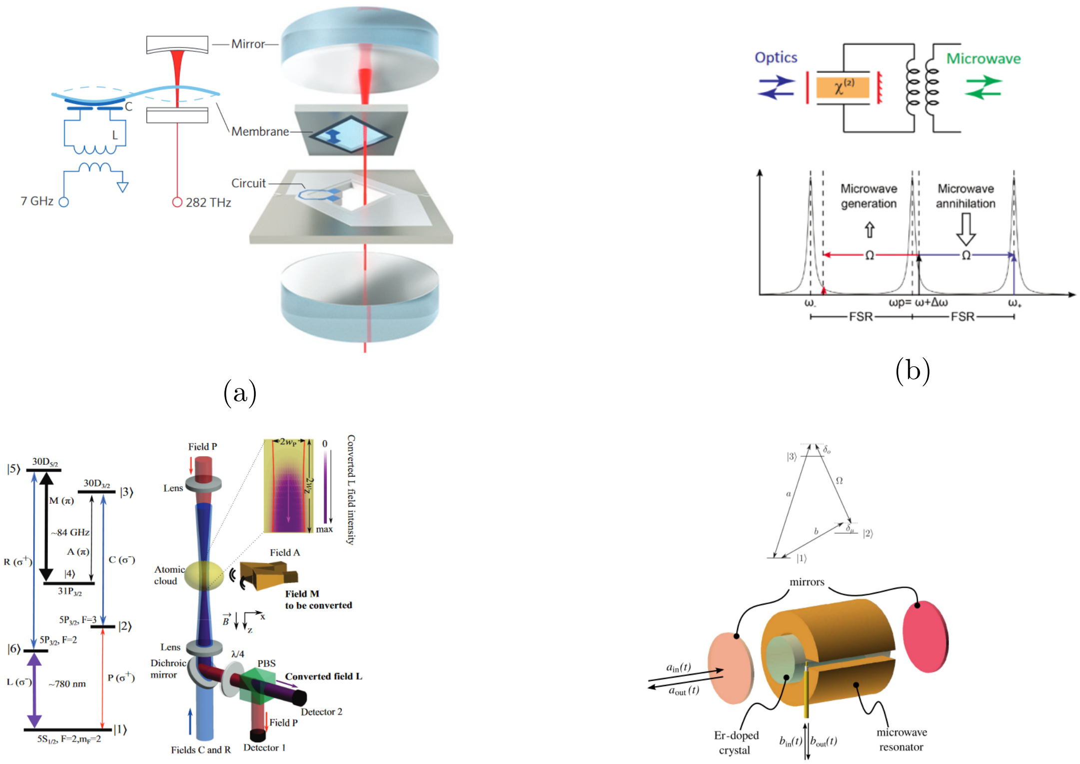

(a)

(b)

(c)

(d)

Figure 6.2: a) In the optomechanical approach for frequency conversion, a mechanical resonator such is coupled to both the optical and microwave cavities thus allowing allowing for an effective coupling between both the microwave and optical cavities. Figure adapted from Reference [5] b) In the nonlinear materials approach, a microwave pump is used to modulate the refractive index of a non-linear material, such that symmetric sidebands around the optical pump frequency is produced. The down-converted sideband can be suppressed by detuning the optical carrier frequency from resonance. Figure adapted from [6, 7]. c)Ensembles of Rubidium atoms, in the Rydberg state, are used in a six-wave mixing scheme to convert photons in the microwave transition (M) to photons in the optical transition (L). Figure adapted from Reference [8] d) In the rare-earth materials approach, ensembles of Λ systems based on rare-earth ions doped into glass-like materials are used as an interface between the optical and microwave photons. By coherently driving the microwave transition ($|1\rangle \leftrightarrow |2\rangle$) and one optical transition ($|2\rangle \leftrightarrow |3\rangle$) and optical field is produced in the other optical transition ($|1\rangle \leftrightarrow |3\rangle$). Figure adapted from Reference [9]

approach is producing non-linearities that are high enough for the conversion between the microwave and optical frequency domains, and also in ensuring that the conversion is single sideband.

In the Rydberg gasses approach [105, 106], ensembles of cold trapped atoms, such as rubidium, are used together with several pumps that coherently couple to the multiple transitions, allowing for the conversion from microwave to optical regime. Figure 6.2c, shows a one such scheme which uses a six wave mixing process to convert the the microwave photons in the M transition to converted photons in the L transition. Frequency conversion using Rydberg states in rubidium atoms was demonstrated to achieve maximum conversion efficiencies of ~ 0.05 [105].

The final more recent approach in microwave to optical domain conversion involves the use of ensembles of Λ-system quantum emitters based on rare-earth ions doped into glass-like materials [101, 102, 103, 104] as a medium that couples to both the optical and microwave cavities (Figure 6.2d). Rare earth materials, such as $\mathrm{Er}^{3+} : \mathrm{Y_2SiO_5}$, are attractive due to narrow inhomogenous broadening of the microwave and optical transitions and long coherence times. The approach involves the use of a Λ system which has a microwave frequency transition and two optical frequency transitions. By coherently driving the microwave and one of the optical transition, an optical field is produced in the other optical transition. Although no conclusive demonstrations have been reported some preliminary results in proof-of-concept experiments have shown this methodology to produce conversion efficiencies of 10^{-4} [101] with aims of achieving experimental conversion efficiencies of > 0.3 [104]. One of the main downsides in using spin ensembles for the conversion between the microwave and optical domains are the losses in the system due to collective spin decoherence.

Conversion Scheme	**Demonstrated Conversion Efficiency**
Optomechanical Resonator	~ 0.1 [5]
Nonlinear Materials	~ 0.01 [98]
Rydberg Gases	~ 0.05 [105]
Rare-Earth Ions	$\sim 10^{-4}$ [101]

Table 6.1: Summary of conversion efficiency schemes and the experimentally demonstrated conversion efficiencies

In this work, we investigate the potential of micro-fabricated devices with integrated optical and microwave cavities that use individual three-level solid-state emitters. We will be exploring the potential of using the three level Λ configuration in single NV centers coupled to a microwave and optical cavity for efficient conversion between the microwave and optical regimes. The long spin-coherence times, and well defined transitions that correspond to the microwave and optical frequency regimes make NV centers a viable candidate to investigate in the conversion schemes. Furthermore, the solid-state nature of NV centers make it more attractive due to the potential of scalability and on-chip integration. We will explore a similar scheme for frequency conversion as used in the rare-earth ion approach. We propose the use of the Λ system in single NV centers which has a microwave frequency transition and two optical frequency transitions as an interface between an optical and microwave cavity. By coherently driving the microwave cavity and one optical transition, an output field is produced in the optical cavity. The goal of this work is to identify the microwave and optical cavity parameters that would maximize the conversion between the input microwave field and the output optical field.

In this chapter, we begin by briefly looking at the cavity dynamics of a two level emitter coupled to a cavity to get a basic understanding of the dynamics of an emitter coupled to a cavity. In Section 6.3, we will introduce the proposed model which we intend to study in which a Λ-system is coupled to a microwave and optical cavity. Based on the proposed model, in Section 6.4 we then present two definitions for the conversion efficiency between the microwave and the optical regimes: A) an intrinsic definition and B) a extrinsic definition for the conversion. The analysis in this chapter will be focused on understanding the conversion efficiency of the former kind. In Section 6.5, we perform analytical non-Hermitian approximations of the ground state and first manifold of the system to get an intuitive understanding of the system dynamics. In Section 6.6 we employ the Python based QuTIP package [107, 108] to investigate via Monte-Carlo simulations the intrinsic conversion efficiency of the system with: a i) weak continuous drive microwave field and ii) with a single microwave photon. The QuTIP package is an computational physics package that is used to simulate the dynamics of open quantum systems.

The Python codes used to perform the simulations in this chapter have been attached in Appendix E.

6.2 Two-Level Emitter in a Cavity

Before we begin looking into the three level Λ system coupled to two cavities, in this section we will very briefly go over the dynamics of a two level system resonantly coupled to a cavity. Studying the dynamics of a two level emitter in a cavity will serve as a sanity check

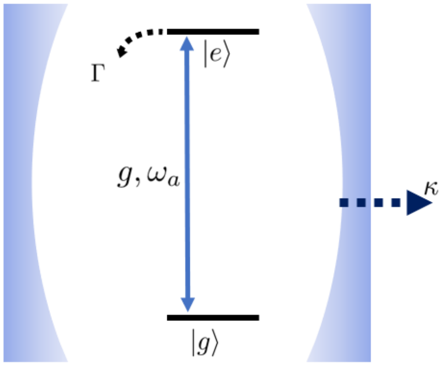

Figure 6.3: Two level emitter coupled to a cavity.

to understand the results we obtain from the three level Λ system. The dynamics of cavity with a single atom emitter inside the cavity is described by the Hamiltonian:

$$H = H_o + H_{int} \tag{6.1}$$

where

$$H_o/\hbar = \omega_a |e\rangle\langle e| + \omega_c a^\dagger a \tag{6.2a}$$

$$H_{int} = -\hat{d} \cdot \hat{E} \tag{6.2b}$$

where $|e\rangle$ and $|g\rangle$ are the excited and ground states of the emitter respectively, a is the annihilation operator of the cavity mode, ω_e is the $|g\rangle \leftrightarrow |e\rangle$ transition frequency, ω_a is the cavity mode frequency, $\hat{E}$ is the electric field operator, and d is the atomic dipole moment operator. With the second field quantization, we can express the electric field in the cavity in terms of the annihilation and creation operators in the Heisenberg picture as:

$$\hat{E} = \vec{\zeta} E(\vec{r}) \sqrt{\frac{\hbar\omega_c}{2V_{mode} max\{\epsilon(\vec{r})|E(\vec{r})|^2\}}} (a e^{-i\omega_c t} + a^\dagger e^{i\omega_c t}) \tag{6.3}$$

where $E(\vec{r})$ is the spatially dependent electric field within the cavity, $\vec{\zeta}$ is the unit polarization vector of the electric field, $\epsilon(\vec{r})$ is the permitivity at position $\vec{r}$ in the cavity, V_{mode} is cavity mode volume, and ω_c is cavity resonance frequency. The mode volume of the cavity V_{mode} is given as:

$$V_{mode} = \frac{\iiint_V \epsilon(\vec{r})|E(\vec{r})|^2 dV}{max\{\epsilon(\vec{r})|E(\vec{r})|^2\}} \tag{6.4}$$

where $E(\vec{r})$ is the electric field at position r within the cavity. The dipole operator in the Heisenberg picture can be expressed as:

$$\hat{d} = -\vec{\mu}d_{eg}(|g\rangle\langle e| e^{-i\omega_a t} + |e\rangle\langle g| e^{i\omega_a t}) \tag{6.5}$$

where $\vec{\mu}$ is the unit vector in the direction of the dipole orientation, and d_{eg} is the atomic dipole matrix element. With these above two definitions, we can write the interaction Hamiltonian as:

$$H_{int} = \vec{\mu}d_{eg} \cdot \vec{\zeta}E(\vec{r_A})\sqrt{\frac{\hbar\omega_c}{2V_{mode}max\{\epsilon(\vec{r})|E(\vec{r})|^2\}}}(ae^{-i\omega_c t} + a^\dagger e^{i\omega_c t})(|g\rangle\langle e| e^{-i\omega_a t} + |e\rangle\langle g| e^{i\omega_a t}) \tag{6.6}$$

where $\vec{r_A}$ is the position of the emitter. We can note that the interaction Hamiltonian contains both fast oscillating terms $e^{\pm(\omega_a+\omega_c)t}$, and slow oscillating terms $e^{\pm(\omega_a-\omega_c)t}$. Here we can invoke the rotating wave approximation (RWA) to ignore the fast oscillating terms under the assumption that $|\omega_a - \omega_c| << \omega_a + \omega_c$, which means that the fast oscillating terms average to zero over long times where only the slowly varying dynamics of the system is considered. Returning back to the time independent Schrodinger picture, the interaction Hamiltonian can be written as:

$$H_{int}/\hbar = g(\vec{r_A})(a|e\rangle\langle g| + a^\dagger|g\rangle\langle e|) \tag{6.7}$$

where we define the position dependent field-atom coupling rate $g(\vec{r_A}) = g_0\Psi(\vec{r_A})cos(\xi)$, with

$$g_0 = d_{eg}\sqrt{\frac{\omega_c}{2\epsilon_M\hbar V_{mode}}} \tag{6.8a}$$

$$\Psi(\vec{r_A}) = \frac{E(\vec{r_A})}{|E(\vec{r_M})|} \tag{6.8b}$$

$$cos(\xi) = \vec{\mu} \cdot \vec{\zeta} \tag{6.8c}$$

where r_M is the position within the cavity where the electric field intensity is maximum, ϵ_M is the dielectric constant at that position, and ξ is the angle between the unit dipole vector $\vec{\mu}$ and the unit polarization vector $\vec{\zeta}$. Unless otherwise stated, we focus on the idealized case where $\Psi(\vec{r_A}) = 1$, and $cos(\xi) = 1$ such that $g = g_0$. This corresponds to the emitter placed at the field maximum of the cavity mode and the emitter's dipole moment aligned with the mode polarization. The coupling rate g refers to the rate at which the cavity mode couples to the emitter, and the value $2g$ is known as the one photon Rabi frequency, as we shall see below. It can be noted that g is proportional to the dipole moment of the emitter and inversely proportional to the mode volume of the cavity. Thus with a large atomic dipole moment and low mode volumes of the cavity, there is strong coupling between the emitter and the cavity. Putting the initial and interaction Hamiltonian terms together, the Hamiltonian of the two-level emitter in a cavity, otherwise known as the Jaynes-Cummings Hamiltonian, (Figure 6.3) in the rotating wave approximation can now be written as:

$$H/\hbar = \omega_e \left|e\right\rangle \left\langle e\right| + \omega_a a^\dagger a + g(a \left|e\right\rangle \left\langle g\right| + a^\dagger \left|g\right\rangle \left\langle e\right|) \tag{6.9}$$

In this study we assume that the cavity mode is on resonance with the two level emitter, $\omega_e = \omega_a$. The losses of the system include the cavity field decay rate, κ, and the atomic decay rate, Γ. The cavity field decay rate, κ, refers to the rate at which photons are lost from the cavity, whereas the atomic decay rate Γ refers to the spontaneous emission rate of the atom which includes decay into non-cavity modes and non-radiative decay. Throughout this thesis, to observe the open system dynamics of a given system, we use the Monte-Carlo solver provided by the QuTIP package to perform the simulations.

6.2.1 Monte-Carlo Solver

Here we will very briefly describe the Monte-Carlo solver from the QuTIP package, which is used to simulate the different systems in this thesis. In quantum optics, the open system dynamics of a quantum state is described by the quantum master equation [109]:

$$\frac{d\rho}{dt} = -\frac{i}{\hbar}[H, \rho] + \sum_k (\hat{C}_k \rho \hat{C}_k^\dagger - \frac{1}{2}\hat{C}_k^\dagger \hat{C}_k \rho - \frac{1}{2}\rho \hat{C}_k^\dagger \hat{C}_k) \tag{6.10}$$

where ρ is the time dependent density matrix of the state, H is the Hamiltonian of the system, and $\hat{C}_k$ are the collapse operators describing the loss terms of the system. For the case with the two level emitter coupled to a cavity, these collapse operators are:

$$\hat{C}_1 = \sqrt{\kappa_o} a, \tag{6.11a}$$

$$\hat{C}_2 = \sqrt{\Gamma} \left| g \right\rangle \left\langle e \right| , \tag{6.11b}$$

The collapse operator $\hat{C}_1$ describes the decay of the cavity field modes with decay rate κ. The collapse $\hat{C}_2$ describes the spontaneous emission decay of the emitter from the excited state $|e\rangle$ to the ground state $|g\rangle$ with a decay rate Γ. The state evolution can thus be derived by iteratively solving the quantum master equation. However, keeping track of the state density matrix of the system for individual time steps requires a lot of computational processing and memory. This is a very inefficient way to solve the state evolution, especially when the system is large consisting of several atomic states and with multiple cavity modes. A more efficient way to simulate the dynamics of the system is to use the Monte-Carlo, or quantum trajectory, approach for the state evolution [110]. Here the time evolution of the state is described by the Schrodinger equation with the effective non-Hermitian Hamiltonian:

$$H_{eff} = H - \frac{i\hbar}{2} \sum_k \hat{C}_k^\dagger \hat{C}_k \tag{6.12}$$

In addition to the time evolution via the Schrodinger equation, the system is monitored continuously at each time step δt, where a system collapse may take place with a certain probability. For instance if the environmental measurements register a quantum jump via the spontaneous emission of the emitter, the wave function undergoes a jump to the state described by:

$$|\psi(t + \delta t)\rangle = \frac{\hat{C}_2 |\psi(t)\rangle}{\sqrt{\langle\psi(t)| \hat{C}_2{}^\dagger \hat{C}_2 |\psi(t)\rangle}} \tag{6.13}$$

where the probability of collapse is:

$$P_2(t) = \frac{\langle\psi(t)| \hat{C}_2{}^\dagger \hat{C}_2 |\psi(t)\rangle}{\delta t \sum_k \hat{C}_k^\dagger \hat{C}_k} \tag{6.14}$$

This is extended to all collapse operators included in the system $\hat{C}_k$. This stochastic process is repeated over a number of times, or trajectories, and the final state of the system is averaged over the total number of quantum trajectories. Thus the Monte-Carlo approach is essentially a stochastic way of solving the master equation. In this thesis we use the Monte-Carlo solver provided by the QuTIP package. As mentioned above, QuTIP is a Python based computational physics package that has inbuilt functions that can be used to simulate the dynamics of open quantum systems. The advantage of using the Monte-Carlo approach over solving the master equation, is that only the state vector of the system is required to be stored in the computers memory, as opposed to the entire density matrix. As mentioned previously, this is especially advantageous for large systems. For instance, for a system with a Hilbert space of size n, the master equation solver requires n^2 computations, while the Monte-Carlo solver requires only n computations.

Although for the system consisting of a two-level emitter coupled to a cavity the overhead cost of averaging over multiple stochastic trajectory calculations does not offer any specific advantage, since we will be working with larger systems in the subsequent sections, we use the Monte-Carlo solver here as well for the sake of consistency and as a form of sanity check. In QuTIP, we set up the simulation by first defining the Hilbert space of the system. This Hilbert space is the tensor product of the Hilbert space of the two level emitter and the Hilbert space of the cavity. In our case this results in a vector space of dimension $2 + N$, where N is the size of the cavity mode Hilbert space. Although ideally in a physical system $N \to \infty$, to perform numerical simulations we have to truncate the Hilbert space. This truncation should be done such that N is large enough to produce physically meaningful results, whilst also being small enough that the simulation time isn't too long. In the simulations in this thesis, we set $N = 7$, as for any manifold level $N < 7$ the system evolution was not accurate, while for $N > 7$ the simulation time was long.

The atomic and annihilation operators of the system are then defined in the Hilbert space as matrices. For instance the cavity mode annihilation operator, a, is defined as:

$$a = I_2 \otimes \begin{pmatrix} 0 & \sqrt{1} & 0 & \cdots & 0 \\ 0 & 0 & \sqrt{2} & \cdots & 0 \\ \dots & \dots & \dots & \ddots & \dots \\ 0 & 0 & 0 & \cdots & \sqrt{N} \\ 0 & 0 & 0 & \cdots & 0 \end{pmatrix} \tag{6.15}$$

and the atomic operator $|e\rangle\langle e|$ is defined as:

$$|e\rangle\langle e| = \begin{pmatrix} 1 & 0 \\ 0 & 0 \end{pmatrix} \otimes I_N \tag{6.16}$$

where I_n is the n dimensional identity matrix, and $\otimes$ is the tensor product. We extend this methodology to define the collapse operators $\hat{C}_k$. These operators can then be used to construct the Hamiltonian of the system (Equation 6.9). Furthermore we set the number of trajectories to be $n_{traj} = 500$. This value was chosen because the errors in the simulation scale as $1/n_{traj}$, and for $n_{traj} = 500$ we get good accuracy. The Hamiltonian and the initial state vector are then fed to the Monte-Carlo solver (*mcsolve*) in QuTIP, along with the collapse operators to simulate the time evolution of the of the system.

Now that we've introduced the solver we use, let us begin simulating the system. Before we start introducing losses into the system, lets observe what happens in a perfectly lossless system ($\kappa = 0, \Gamma = 0$) by using the Monte-Carlo solver. In a perfectly lossless system, this reduces to solving the Schrodinger equation:

$$\frac{d}{dt} |\psi(t)\rangle = \frac{1}{i\hbar} H |\psi(t)\rangle \tag{6.17}$$

The system is initialized with the emitter in the excited state with no photons in the cavity, $\psi(0) = |e, 0\rangle$.

As can be noted from Figure 6.4, in a lossless system we observe oscillations known as Rabi between the between the states $|e, 0\rangle$ state and the $|g, 1\rangle$. The expectation value $\langle a^\dagger a\rangle$ is the probabilistic expected value of the photon number in the cavity, and the expectation value $\langle |e\rangle \langle e|\rangle$ is the probabilistic expected value that the emitter is in the excited state $|e\rangle$. In general for photon number n, these oscillations occur at a frequency of $2g\sqrt{n+1}$, between the $|e, n\rangle$ and $|g, n+1\rangle$ states. Now we see why $2g$ is known as the single photon Rabi frequency.

From here we can introduce losses into the system to observe the dynamics of a lossy system. Here we would like to explore two regimes of the system: namely the strong coupling regime, where $g > \kappa, \Gamma$, and the weak coupling regime , $g < \kappa, \Gamma$.

6.2.2 Strong Coupling Regime

In the strong coupling regime, the coupling of the atom to the cavity modes is at a much higher rate than the atomic and cavity decay rates. Since the rate of the coupling constant is larger than the rate at which either the atom or the cavity modes can decay, Rabi oscillations occur in the system. The condition for the strong coupling regime is given as: $\frac{g}{\kappa} >> 1$ and $\frac{g}{\Gamma} >> 1$. To observe the transient dynamics of the system, we initialize the system in the $|e, 0\rangle$ state with the atom in the excited state and with no photons in the cavity and we evolve the state with the Hamiltonian in Equation 6.9 together with the

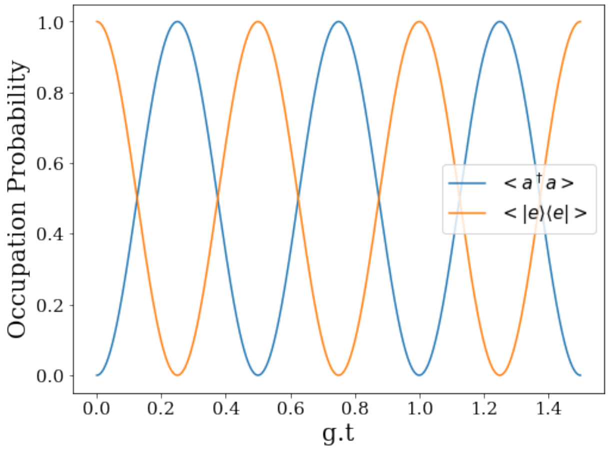

Figure 6.4: Transient response of a two level emitter coupled to a cavity with parameters $\kappa = 0$, and $\Gamma = 0$.

collapse operators defined in Equation 6.11. Figure 6.6a shows the transient response of a strongly coupled cavity to an atom. As can be seen when the system is evolved, we observe Rabi oscillations as we did before in the lossless system. In general for photon number n, these oscillations occur at a frequency of $2g\sqrt{n+1}$, between the $|e,n\rangle$ and $|g,n+1\rangle$ states. However, in the system with losses we observe that the oscillations are damped at a rate of $\frac{\kappa+\Gamma}{2}$.

Figure 6.5 shows the energy manifolds of the system on resonance $\omega_a = \omega_c$. The states $|g,n+1\rangle$ and $|e,n\rangle$ are known as the bare states and the states $|\pm,n+1\rangle$ are known as the dressed states. With atom is not coupled to the cavity, the bare states of the system are the eigenstates of the Hamiltonian. When the interaction Hamiltonian is turned on and the system is strongly coupled ($\frac{g}{\kappa} >> 1$ and $\frac{g}{\Gamma} >> 1$), the new eigenstates of the system are the dressed states. The dressed states of the system are expressed as:

$$|\pm,n+1\rangle = \frac{|e,n\rangle \pm |g,n+1\rangle}{\sqrt{2}} \tag{6.18}$$

As can be6.5, the energy splitting between the dressed states in the nth manifold is $2g\sqrt{n+1}$. This splitting between the dressed states is characteristic of the strong coupling regime. The splitting between the dressed states in the first manifold can be observed by looking at the transmission spectrum of the system by driving the cavity with a classical field. We define the cavity drive term of the Hamiltonian as:

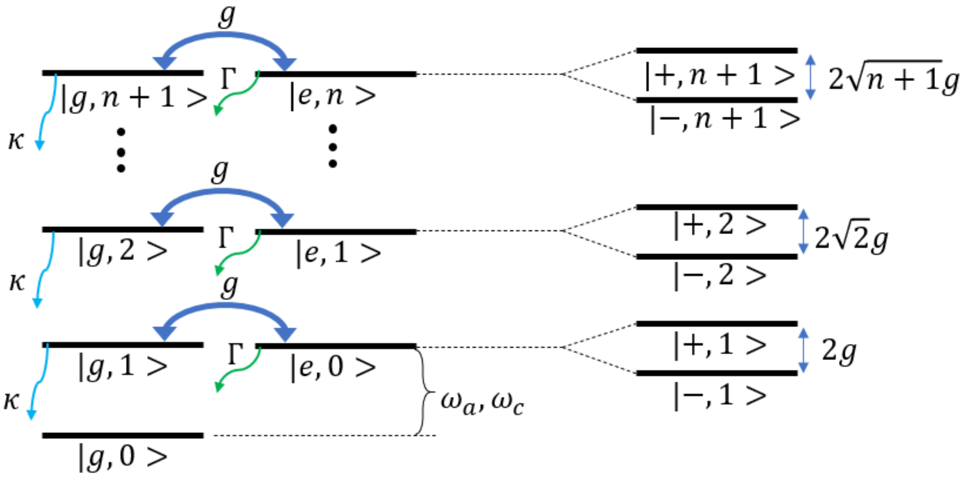

Figure 6.5: The left ladders represent the uncoupled states of the system with $\omega_c = \omega_a$. When the atom and the cavity are strongly coupled, the eigenstates of the system are the dressed states shown in the right most ladder.

$$H_{drive}/\hbar = \sqrt{\kappa}\varepsilon e^{-i\omega_d t}a^{\dagger} + \sqrt{\kappa}\varepsilon^{*}e^{i\omega_d t}a \tag{6.19}$$

where ω_d is the frequency of drive and the drive term ε is given by:

$$\varepsilon = \sqrt{\frac{P}{\hbar\omega_d}} \tag{6.20}$$

where P is the power of the laser used to drive the cavity. The addition of this term to Equation 6.9 results in a time dependant Hamiltonian. We can however get rid of the time dependence of the Hamiltonian by transforming from the static lab frame to a rotating frame of the laser. This transformation can be done applying a time dependent unitary operator, U, to the Hamiltonian such that the rotated Hamiltonian is given by:

$$\mathcal{H} = U^{\dagger}HU + i\frac{dU^{\dagger}}{dt}U = \mathcal{H}_o + \mathcal{H}_{int} + \mathcal{H}_{drive} \tag{6.21}$$

where

$$U = e^{i\omega_d t(a^\dagger a + |e\rangle\langle e|)} \tag{6.22}$$

The transformed Hamiltonian is :

$$\mathcal{H}/\hbar = \Delta_e |e\rangle\langle e| + g(a|e\rangle\langle g| + a^\dagger |g\rangle\langle e|)\Delta_c a^\dagger a + \sqrt{\kappa}(\varepsilon a^\dagger + \varepsilon^* a) \tag{6.23}$$

where the detunings $\Delta_e = \omega_e - \omega_d$ and $\Delta_c = \omega_c - \omega_f$. We can now observe the splitting between the dressed states with a weak drive $|\varepsilon|^2 = 0.01g$ and plotting the steady state transmission of the system. The steady state transmission, T, of the system is defined defined as:

$$T = \frac{\langle a^\dagger a\rangle\kappa}{|\varepsilon|^2} \tag{6.24}$$

where $\langle a^\dagger a\rangle$ is the expectation value of photons in the cavity at steady state. The term $\langle a^\dagger a\rangle\kappa$ refers to the rate at which the photons are exiting the cavity, and the term $|\varepsilon|^2$ refers to the rate at which the photons are incident on the cavity laser power P. Thus the transmission T describes the ratio between the photons exiting the cavity and the photons incident on the cavity. The steady state transmission of the system with weak drive ($|\varepsilon|^2 = 0.01g$) is plotted in Figure 6.6b with the detuning $\Delta = \omega_d - \omega_a$ ($\omega_a = \omega_c$). These transmission peaks, also known as the polariton peaks, are split by $2|g|$ in the first manifold [111] as can be seen in Figure 6.6b.

6.2.3 Weak Coupling Regime

In the weak coupling regime, the coupling of the atom to the cavity mode is at a much lower rate than the atomic and cavity field decay rates. The condition for the weak coupling regime is given as: $\frac{g}{\kappa} << 1$ and $\frac{g}{\Gamma} << 1$. To observe the dynamics of the system we simulate the non-Hermitian Hamiltonian described in Equation 6.12 in the weak coupling regime. Figure 6.7a shows the transient response of a weakly coupled cavity to an atom. The system is initialized in the $|e, 0\rangle$ state with the atom in the excited state and no photons in the cavity. As can be noted in Figure 6.7a, when the system is evolved, we don't observe any oscillations between in the system as the atom-cavity system doesn't have enough time to couple coherently before the dissipation in the system occurs. We once again plot the steady state transmission of the system T by driving the system with a weak drive ($|\varepsilon|^2 = 0.01g$). We observe that in the weak coupling regime the eigenstates, are

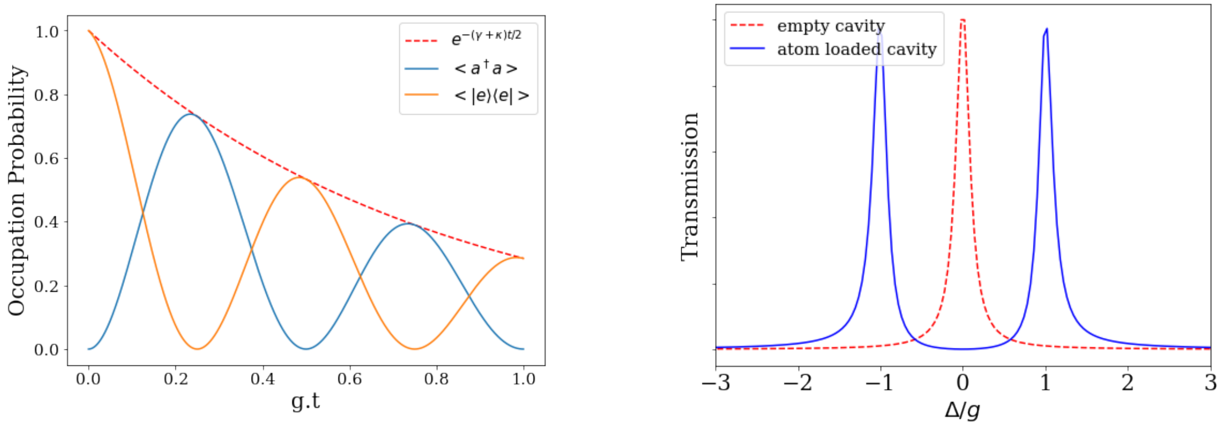

(a)

(b)

Figure 6.6: a) Transient response of a two level emitter coupled to a cavity with parameters $\kappa = 0.1g$, and $\Gamma = 0.1g$. b) Transmission spectrum of the transmission through an empty cavity and a strongly coupled atom loaded cavity when weakly excited. Δ is the detuning between the excitation frequency and the cavity-atom system.

not split and transmission occurs mainly on resonance with $\Delta = 0$. Figure 6.7b shows the transmission spectrum of the a weakly coupled system. The transmission linewidth of the loaded cavity is slightly larger than the transmission profile of an empty cavity, however as with the empty cavity, maximum transmission through the cavity occurs at a detuning of zero, or when the excitation frequency is resonant with the system.

A special case of the weakly coupled system, also known as the Purcell regime, occurs when $\kappa > g >> \Gamma$. In this regime, there exists no Rabi oscillations or transmission spectrum splitting as we previously saw, but due to the presence of the cavity, the decay rate of the atom is modified. This can be observed by looking at the transient response of the system in the Purcell regime as seen in Figure 6.7c. The atom decays at an enhanced rate of $2|g|^2/\kappa$ due to the coupling between the cavity and the atom. This enhanced decay rate of atoms coupled to cavities are used to increase the rate of spontaneous emission rate of emitters. For instance the spontaneous emission rate of the ZPL transmission in NV centers can be increased by coupling the NV center to a cavity resonant with the ZPL [49]. Figure 6.7d shows the transmission spectrum of the system in the Purcell regime when driven with a weak drive ($|\varepsilon|^2 = 0.01g$). We note that there exists a dip in the transmission when the the detuning $\Delta = 0$. This can be explained by observing the energy manifold diagram in Figure 6.5. When $\kappa > g >> \Gamma$, the eigenstates of the system are the bare states seen on the left of the diagram in Figure 6.5. When the system is driven resonantly

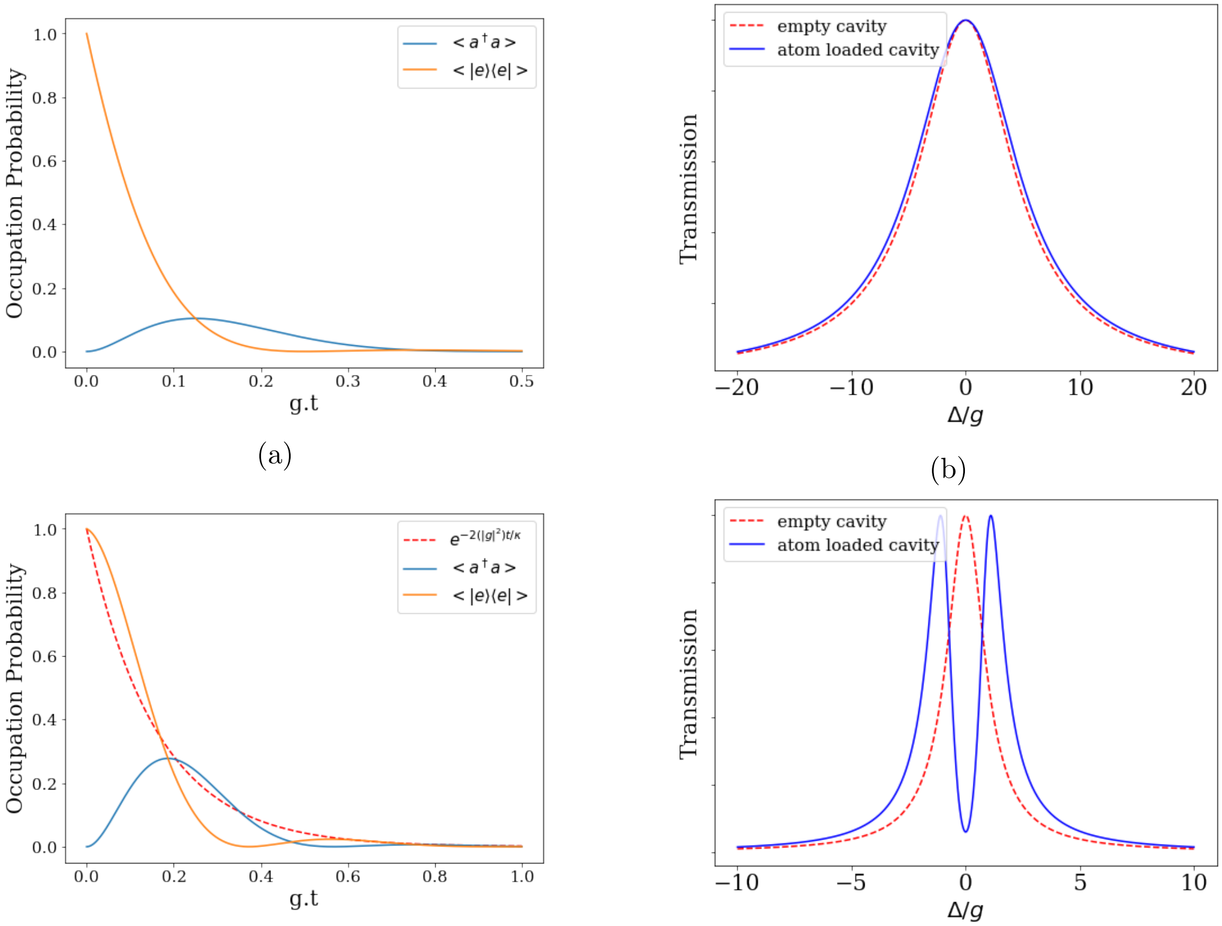

(a)

(b)

(c)

(d)

Figure 6.7: a) Transient response of a two level emitter coupled to a cavity with parameters $g = 2\pi$,$\kappa = 10g$, and $\Gamma = 10g$. b) Transmission spectrum of the transmission through an empty cavity and a weakly coupled atom loaded cavity when weakly excited with excitation rate $|\varepsilon|^2 = 0.01g$. Δ is the detuning between the excitation frequency and the cavity-atom system. c) Transient response of a two level emitter coupled to a cavity with parameters $\kappa = 2g$, and $\Gamma = 0.1g$. The decay rate of the atom is $2|g|^2/\kappa$ due to the presence of the cavity. d) Transmission spectrum of the transmission through an empty cavity and a weakly coupled atom loaded with parameters $\kappa = 10g$, and $\Gamma = 0.1g$ when weakly excited with excitation rate $|\varepsilon|^2 = 0.01g$. Δ is the detuning between the excitation frequency and the cavity-atom system.

with a weak drive such that only the bare states in the first manifold are accessed, a transition occurs between the level $|g,0\rangle$ and the level $|g,1\rangle$. However this transition can occur via two pathways: $|g,0\rangle \rightarrow |g,1\rangle$ or $|g,0\rangle \rightarrow |g,1\rangle \rightarrow |e,0\rangle \rightarrow |g,1\rangle$. The probability amplitudes of these two allowed transition pathways interference destructively resulting in a transparency window at resonance. This phenomenon can be observed in a large number of systems and is termed cavity induced transparency [112], or electromagnetically induced transparency [113]. We can observe looking at the steady state transmission spectrum of the system in Figure 6.7d. We note that there exists a dip in the transmission spectrum at a detuning of $\Delta = 0$.

6.3 Proposed System

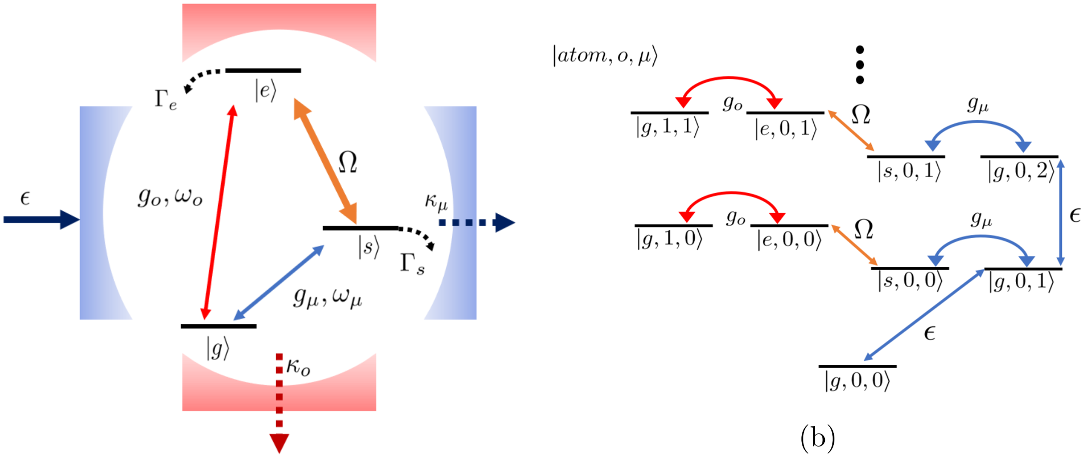

(b)

(a)

Figure 6.8: a) Schematic of the proposed model consisting of a three level closed Λ system coupled to a microwave cavity and an optical cavity. The $|g\rangle \leftrightarrow |s\rangle$ transition is coupled to the microwave cavity (g_μ,κ_μ), and the $|s\rangle \leftrightarrow |e\rangle$ transition is coupled to the optical cavity (g_o,κ_o). The levels $|s\rangle$ and $|e\rangle$ are coupled with a classical field with a frequency of ω_Ω and a driving rate Ω. In the case where the microwave field is due to a classical drive, the microwave cavity is driven by a weak classical field at a frequency of ω_d and a driving rate ε. b) Ground, first, and second manifold of the three Λ system coupled to a microwave and optical cavity with coupling rates g_μ and g_o respectively. The basis states represented are the atomic state, optical photon and the microwave photon respectively.

Now that we have a basic understanding of the cavity dynamics of a two-level emitter, we turn out attention to the proposed system that we intend to study for inter-photon conversion. The system consists of a three level Λ emitter that is coupled to two cavities corresponding to the microwave ($|g\rangle \leftrightarrow |s\rangle$) and the optical frequency transitions ($|g\rangle \leftrightarrow |e\rangle$) respectively as seen in Figure 6.8a. An external monochromatic classical electric field given by $E(t) = E_0 e^{-\imath\omega_\Omega t} + E_0^* e^{\imath\omega_\Omega t}$ is used to drive the $|s\rangle \leftrightarrow |e\rangle$ transition. As was before this interaction Hamiltonian in the dipole approximation is given by Equation 6.2b, where the dipole operator in the Heisenberg picture is given by:

$$d = -d_{se}(|e\rangle\langle s| e^{-i\omega_{se}t} + |s\rangle\langle e| e^{i\omega_{se}t}) \tag{6.25}$$

where d_{se} is dipole matrix element between $|s\rangle \leftrightarrow |e\rangle$ transition, and ω_{se} is the transition frequency. Thus the interaction Hamiltonian between the classical drive and the $|s\rangle \leftrightarrow |e\rangle$ transition can be written as:

$$H_{se} = d_{se}(|e\rangle\langle s| e^{-i\omega_{se}t} + |s\rangle\langle e| e^{i\omega_{se}t})(E_0 e^{-\imath\omega_\Omega t} + E_0^* e^{\imath\omega_\Omega t}) \tag{6.26}$$

Once again we notice that this Hamiltonian contains both fast oscillating terms $e^{\pm(\omega_{se}+\omega_\Omega)t}$, and slow oscillating terms $e^{\pm(\omega_{se}-\omega_\Omega)t}$. Here we can invoke the rotating wave approximation (RWA) to ignore the fast oscillating terms under the assumption that $|\omega_{se}-\omega_\Omega| << \omega_{se}+\omega_\Omega$, which means that the fast oscillating terms average to zero over long times where only the slowly varying dynamics of the system is considered. This is also under the assumption that the drive field is a weak probe such that, $\frac{d_{se}E_0}{\hbar} << \omega_{se}$. Thus Hamiltonian H_{se} in the Schrodinger picture can be written as:

$$H_{se} = \hbar(\Omega e^{-i\omega_\Omega t}|e\rangle\langle s| + \Omega^* e^{i\omega_\Omega t}|s\rangle\langle e|) \tag{6.27}$$

where the Rabi frequency $\Omega = \frac{d_{se}E_0}{\hbar}$.

With this system, the proposed conversion efficiency scheme is as follows: by introducing a microwave field into the microwave cavity, and by coherently driving the $|s\rangle \leftrightarrow |e\rangle$ transition with the Rabi drive Ω, we expect an optical field to be produced in the optical cavity. The optical photons decaying out of the optical cavity is then said to be the frequency converted photons. We can now describe the dynamics of the the system depicted in Figure 6.8a by the Hamiltonian:

$$H = H_o + H_{int} \tag{6.28}$$

where in the rotating wave approximation,

$$H_o/\hbar = \omega_s \left|s\right\rangle \left\langle s\right| + \omega_e \left|e\right\rangle \left\langle e\right| + \omega_o a^\dagger a + \omega_\mu b^\dagger b, \tag{6.29a}$$

$$\begin{aligned} H_{int}/\hbar =& g_\mu(b \left|s\right\rangle \left\langle g\right| + b^\dagger \left|g\right\rangle \left\langle s\right|) + g_o(a \left|e\right\rangle \left\langle g\right| + a^\dagger \left|g\right\rangle \left\langle e\right|) \\ &+ (\Omega e^{-i\omega_\Omega t} \left|e\right\rangle \left\langle s\right| + \Omega^* e^{i\omega_\Omega t} \left|s\right\rangle \left\langle e\right|), \end{aligned} \tag{6.29b}$$

where a and b are the annihilation operators for the optical and microwave cavity modes respectively, Ω is the Rabi frequency of the classical field coupling the levels $\left|s\right\rangle$ and $\left|e\right\rangle$ without injecting any photons into the cavities. Furthermore ω_e (ω_s) is atomic frequency of the $\left|g\right\rangle \leftrightarrow \left|e\right\rangle$ ($\left|g\right\rangle \leftrightarrow \left|s\right\rangle$) transition while ω_o (ω_μ) is the optical (microwave) cavity mode frequencies. The field in the microwave cavity couples the levels $\left|g\right\rangle$ and $\left|s\right\rangle$ with a rate of g_μ, and the field in the optical cavity couples the levels $\left|g\right\rangle$ and $\left|e\right\rangle$ with a rate of g_o. In the equations above ω_s and ω_e are the atomic transition frequencies from the level $\left|g\right\rangle$ to the levels $\left|s\right\rangle$ and $\left|e\right\rangle$ respectively, while ω_μ and ω_o are the microwave and optical mode cavity frequencies.

In this work we will explore three ways in which the microwave photons are input into the system: i) classical drive, ii) cavity initial conditions and iii) with a feeder/source cavity. With the classical drive, we drive the system with a continuous classical wave that is defined the Hamiltonian term H_{drive}:

$$H_{drive}/\hbar = \sqrt{\kappa_\mu}\varepsilon e^{-i\omega_d t} b^\dagger + \sqrt{\kappa_\mu}\varepsilon^* e^{i\omega_d t} b \tag{6.30}$$

where κ_μ is the microwave cavity decay rate, and ε is the rate at which the classical field is injected at the microwave cavity with a frequency of ω_d. As we saw in the previous section, the drive term ε can be expressed as:

$$\varepsilon = \sqrt{\frac{P}{\hbar\omega_d}} \tag{6.31}$$

where P is the power of with which the microwave cavity is driven. The term $\sqrt{\kappa_\mu}\varepsilon$ is thus a measure of the rate at which microwave photons enter the microwave cavity. The second way in which the microwave photons can be input into the system is by initializing the microwave cavity into a specific photon state (as we shall see in Section 7.2). The third way in which the microwave photons can enter the system by using a source cavity in a cascaded cavity system [114], that is initialized with a specific photon state, which is then used to feed the target system which consists of system described by the Hamiltonian 6.29 (we will explore this approach in Chapter 7).

If we looked at the case with the classical drive, the addition of the H_{drive} term results in a time dependant Hamiltonian. As we did before in the previous section, we can get rid of the time dependant terms by moving to a rotating frame of a time dependent unitary U :

$$U = \exp{(-it)}[\omega_d(b^\dagger b + |s\rangle\langle s|) + (\omega_d + \omega_\Omega)(|e\rangle\langle e| + a^\dagger a)] \tag{6.32}$$

the Hamiltonian is transformed according to:

$$\mathcal{H} = U^\dagger H U + i\frac{dU^\dagger}{dt}U = \mathcal{H}_o + \mathcal{H}_{int} + \mathcal{H}_{drive} \tag{6.33}$$

with

$$\mathcal{H}_o/\hbar = \Delta_s |s\rangle\langle s| + \Delta_e |e\rangle\langle e| + \Delta_o a^\dagger a + \Delta_\mu b^\dagger b, \tag{6.34a}$$

$$\begin{aligned}\mathcal{H}_{int}/\hbar =& g_\mu(b|s\rangle\langle g| + b^\dagger |g\rangle\langle s|) + g_o(a|e\rangle\langle g| + a^\dagger |g\rangle\langle e|) \\ &+ (\Omega|e\rangle\langle s| + \Omega^* |s\rangle\langle e|),\end{aligned} \tag{6.34b}$$

$$\mathcal{H}_{drive}/\hbar = \sqrt{\kappa_\mu}\varepsilon b^\dagger + \sqrt{\kappa_\mu}\varepsilon^* b \tag{6.34c}$$

where the detunings $\Delta_s = \omega_s - \omega_d$, $\Delta_e = \omega_e - \omega_d - \omega_\Omega$, $\Delta_o = \omega_o - \omega_d - \omega_\Omega$, $\Delta_\mu = \omega_\mu - \omega_d$.

With the proposed system above, the goal of the problem now is to identify the optical (g_o, κ_o) and microwave cavity (g_μ, κ_μ) parameters that optimize the output of optical photons from the optical cavity for a given microwave drive rate ε. In other words we would like to find the required quality factor Q and mode volumes V_{mode} of the microwave and optical that would maximize conversion efficiency. The quality factor of the cavity determines the temporal confinement of light whilst the mode volume determines the spatial confinement of light within the cavity. As we saw earlier the mode volume of the cavity is related to the the coupling constant g. The quality factor of a cavity is calculated as:

$$Q = \frac{\omega}{\kappa} \tag{6.35}$$

where ω is the cavity resonance frequency and κ is the cavity field decay rate.

Now would be a good time to introduce the characteristics of the three level Λ system that we intend to study. We model our quantum emitter on the naturally occurring Λ system in NV centers at zero magnetic field (see Chapter 2). As seen in Figure 6.9, the Λ system is formed from the $|0\rangle$, $|\pm 1\rangle$, $|^3E\rangle$ subspace in the NV center corresponding to the states $|g\rangle$, $|s\rangle$, and $|e\rangle$ in Figure 6.8a. As can be seen from Figure 6.9, the frequencies ω_e and ω_s correspond to the operating regimes of optical terhertz and microwave gigahertz frequencies respectively. Furthermore this Λ system is particularly attractive due to the zero magnetic field operation, as it is reported that superconducting resonators which have high quality factors at zero magnetic fields suffer from losses at non-zero magnetic fields[115].

The population decay rate of the metastable state $|\pm 1_g\rangle$ state is $\Gamma_s = 2\pi \times 21.2\text{Hz}$ [56, 57]. The population decay rate from the excited $|^3E\rangle$ state is $\Gamma_e = 2\pi \times 13.3\text{MHz}$ which is the total spontaneous emission rate including the emission into the phonon side bands. The branching ratio of the excited state $|^3E\rangle$ is:

$$\Gamma_e = \Gamma_{ZPL} + \Gamma_{PSB} + \Gamma_{es} \tag{6.36}$$

where Γ_{ZPL} is the decay into the ground state through the resonant zero phonon line emission, Γ_{PSB} is the non-resonant decay into the ground state via the phonon sidebands, and Γ_{es} is the decay into the metastable $|\pm 1_g\rangle$ state. Here $\Gamma_{ZPL} = 2\pi \times 0.35\text{MHz}$, $\Gamma_{PSB} = 2\pi \times 10.20\text{MHz}$ and $\Gamma_{es} = 2\pi \times 2.66\text{MHz}$ [2]. To take into account the phonon sideband (PSB) decay into the ground state from the excited state, this system can be modelled as a "pseudo" three level system as shown in Figure 6.9. Here the excited state decays to the ground state $|g\rangle$ via the ZPL decay, and to the virtual ground state $|g'\rangle$ via the PSB decay. The virtual state $|g'\rangle$ represents the states in the vibronic bands above the ground triplet through which PSB decay occurs. The virtual state $|g'\rangle$ then decays to the ground state $|g\rangle$ via phonon decay at a rate of $\Gamma_p = 2\pi \times 60$ THz [116].

In addition to the population decays, the coherences of the states also damp at a rate given by the transverse decay rate. The transverse decay rate of the system of the metastable state and excited states are $\gamma_{s\perp} = 2\pi \times 66.3\text{Hz}$ and $\gamma_{e\perp} = 2\pi \times 15.9\text{MHz}$ respectively. The transverse decay rate, $\gamma_\perp$, is related to the population decay rate, Γ, of the transition as [109]:

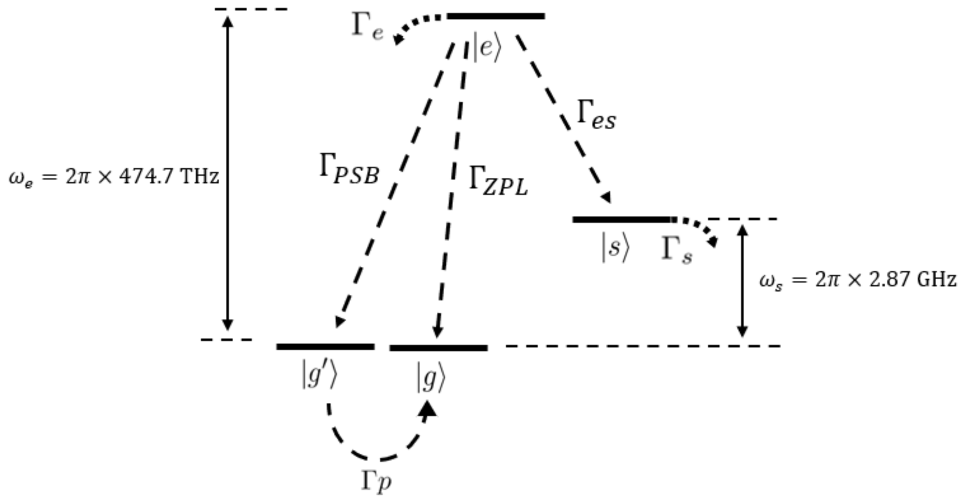

Figure 6.9: The schematic of the pseudo three-level system showing the resonant ZPL and PSB decay. The ground state $|g\rangle$ and the metastable state $|s\rangle$ corresponds to the $|0\rangle$ and $|\pm1\rangle$ state from the ground state triplet state $^3A_2$ in the NV center. The excited state $|e\rangle$ in the Λ system corresponds to the excited state ^3E in the NV center. The excited state $|e\rangle$ decays to the ground state $|e\rangle$ at a rate of $\Gamma_{ZPL} = 2\pi \times 0.35$MHz and the virtual state $|g'\rangle$ at a rate of $\Gamma_{PSB} = 2\pi \times 12.95$MHz. The ground state $|g\rangle$ is then populated from the virtual state $|g'\rangle$ at a decay rate of Γ_p which occurs at a faster rate than the timescales of the other processes involved in the system ($\Gamma_p = 2\pi \times 60$THz)

$$\gamma_\perp = \frac{\Gamma}{2} + \gamma_c \tag{6.37}$$

where γ_c models additional coherence decay in the system due to effects such as dephasing. These additional coherence decays in the metastable state γ_s and the excited state γ_s of the system are:

$$\gamma_s = \gamma_{s\perp} - \frac{\Gamma_s}{2} = 2\pi \times 55.7\text{Hz} \tag{6.38a}$$

$$\gamma_e = \gamma_{e\perp} - \frac{\Gamma_e}{2} = 2\pi \times 9.25\text{MHz} \tag{6.38b}$$

6.4 Conversion Efficiency Definition

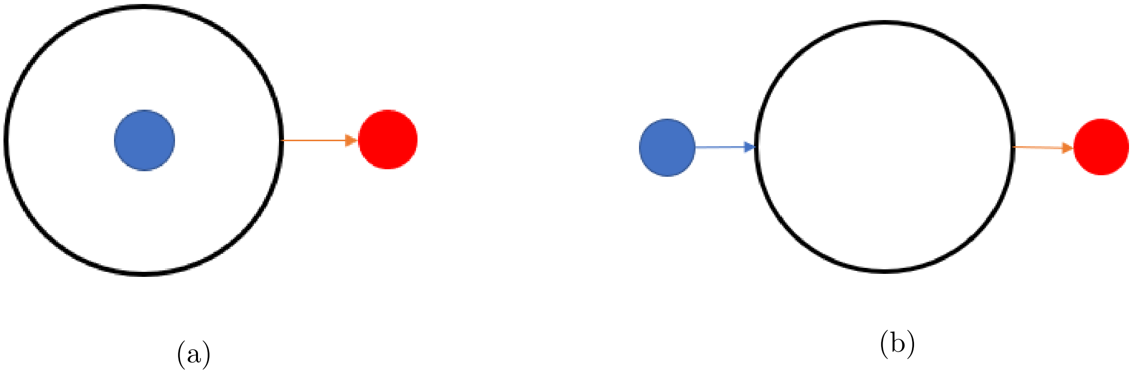
(a)

(b)

Figure 6.10: a) Schematic of the intrinsic conversion efficiency $T^A_{\mu\to o}$ wherein the efficiency is defined as the ratio between the output optical photons (red circle) for every microwave photon (blue circle) initialized within the cavity. b) Schematic of the extrinsic conversion efficiency $T^B_{\mu\to o}$ wherein the conversion efficiency is defined as the ratio between the output optical photons (red circle) for every microwave photon (blue circle) incident on the cavity.

Now that we have setup the initial system, based on the above model it is important to define the conversion efficiency between the microwave and optical photons. We define two versions of the conversion efficiencies in this work. One would be the conversion efficiency in the intrinsic case and the other is a conversion efficiency in a extrinsic case.

In the intrinsic case of the definition, we ask the question: *If we can get a microwave photon into microwave cavity, what cavity parameters would maximize the output optical photons?*. The intrinsic conversion efficiency is defined as:

$$T^A_{\mu\to o} = \frac{\langle a^\dagger a\rangle_{out}}{\langle b^\dagger b\rangle_{cavity}} \tag{6.39}$$

where $\langle a^\dagger a\rangle_{out}$ is the expectation value of the optical photons decaying out of the optical cavity, and $\langle b^\dagger b\rangle_{cavity}$ is the expectation value of the microwave photons in the microwave cavity that is input into the cavity. In the continuous drive regime, $\langle a^\dagger a\rangle_{out}$ would be the rate at which optical photons decay out of the optical cavity, and $\langle b^\dagger b\rangle_{cavity}$ would be the rate at which microwave photons enter the due to the H_{drive} term. When we instead input microwave photons by initializing the microwave cavity with a a specific photon number n, $\langle a^\dagger a\rangle_{out}$ is the total number of optical photons that decay out of the optical cavity and $\langle b^\dagger b\rangle_{cavity}$ would be n.

In the second extrinsic definition of the conversion efficiency we ask the question: *For every microwave photon incident on the microwave cavity, what cavity parameters would maximize the output optical photons?* . The extrinsic conversion efficiency is defined as:

$$T^{B}_{\mu\to o} = \frac{\langle a^{\dagger}a\rangle_{out}}{\langle b^{\dagger}b\rangle_{in}} \tag{6.40}$$

where $\langle a^{\dagger}a\rangle_{out}$ is the expectation value of the optical photons decaying out of the optical cavity, and $\langle b^{\dagger}b\rangle_{in}$ is the expectation value of the microwave photons incident on the microwave cavity. In the continuous drive regime, $\langle a^{\dagger}a\rangle_{out}$ would be the rate at which optical photons decay out of the optical cavity and $\langle b^{\dagger}b\rangle_{in}$ would be the rate at which microwave photons are incident on the cavity due to the H_{drive} term. When we instead input microwave photons using a feeder cavity with a a specific photon number n, $\langle a^{\dagger}a\rangle_{out}$ is the total number of optical photons that decay out of the optical cavity and $\langle b^{\dagger}b\rangle_{in}$ would be n. In this chapter we analyze the conversion efficiency of the intrinsic type, $T^{A}_{\mu\to o}$, and in the subsequent Chapter 7 we explore the conversion efficiency of extrinsic type, $T^{B}_{\mu\to o}$. By observing the results from the ideal case, we would be able to understand the results in the non-ideal case.

6.5 Approximate Analytical Solution

In order to understand an intuitive picture of the system we perform an analytical approximation. An estimate of the conversion from the injected microwave photon to the optical photon output is obtained by analyzing the non-Hermitian Hamiltonian describing the transition of the system between the ground and first manifolds as seen in Figure 6.8b. In the analytical approximation we treat the system as purely three level Λ system without the virtual state $|g'\rangle$. We can absorb some of the loss terms from the collapse operators from the the non-Hermitian Hamiltonian used in the Monte-Carlo simulations (from Equation 6.12) and analytically solve the Hamiltonian:

$$\bar{\mathcal{H}}^{(1)} = \bar{\mathcal{H}}^{(1)}_{o} + \mathcal{H}_{int} + \mathcal{H}_{drive} \tag{6.41}$$

where

$$
\begin{aligned}
\bar{\mathcal{H}}_o^{(1)}/\hbar = &- (i\frac{\gamma_{s\perp}}{2} - \Delta_s) \left|s\right\rangle \left\langle s\right| - (i\frac{\gamma_{e\perp}}{2} - \Delta_e) \left|e\right\rangle \left\langle e\right| \\
&- (i\frac{\kappa_o}{2} - \Delta_a)a^\dagger a - (i\frac{\kappa_\mu}{2} - \Delta_b)b^\dagger b
\end{aligned}
\tag{6.42}
$$

where the complex terms $\frac{i\gamma_{s\perp}}{2} \left|s\right\rangle \left\langle s\right|$, and $\frac{i\gamma_{e\perp}}{2} \left|e\right\rangle \left\langle e\right|$ describe the coherence decays of the $\left|s\right\rangle$ and $\left|e\right\rangle$ respectively, while the complex terms $i\frac{\kappa_o}{2}a^\dagger a$, and $i\frac{\kappa_\mu}{2}b^\dagger b$ describe the cavity field decay of the optical and microwave fields respectively. Assuming the state is described by:

$$
\begin{aligned}
\left|\psi^{(1)}\right\rangle = c_0^{(1)} \left|g,0,0\right\rangle + c_1^{(1)} \left|e,0,0\right\rangle + c_2^{(1)} \left|s,0,0\right\rangle + \\
c_3^{(1)} \left|g,1,0\right\rangle + c_4^{(1)} \left|g,0,1\right\rangle
\end{aligned}
\tag{6.43}
$$

where the state vector $\left|a,o,\mu\right\rangle$ describes the atomic state, optical cavity photon number and the microwave cavity photon number respectively (see Figure 6.8b). We apply the non-Hermitian Hamiltonian to the wave function describing the ground and first manifolds and find a steady state solution of the system in the limit of a weak microwave drive, ε [117] and solve:

$$
i\hbar\frac{d}{dt} \left|\psi^{(1)}\right\rangle = \bar{\mathcal{H}}^{(1)} \left|\psi^{(1)}\right\rangle \tag{6.44}
$$

In the steady state solution, the we set the time derivative $\frac{d}{dt} \left|\psi^{(1)}\right\rangle$ to zero to find the value of $c_3^{(1)}$. Thus the problem is reduced to solving a set of linear equations where we solve for the coefficients $c_n^{(1)}$. In the limit that $|\sqrt{\kappa_\mu}\varepsilon| \to 0$, we set $c_o^{(1)} \approx 1$ and ignore the transitions to higher manifolds such as $\left|g,1,0\right\rangle \to \left|g,1,1\right\rangle$, $\left|e,0,1\right\rangle \to \left|e,1,1\right\rangle$, $\left|s,0,0\right\rangle \to \left|s,1,0\right\rangle$, $\left|s,0,0\right\rangle \to \left|s,0,1\right\rangle$ and $\left|g,0,1\right\rangle \to \left|g,1,1\right\rangle$ couplings. By setting $c_o^{(1)} \approx 1$, we overcome the atom number conservation problem that arises from using the non-Hermitian Hamiltonian. Otherwise all the other coefficients $c_n^{(1)}$ will be zero in steady state. We use the conversion efficiency definition from Equation 6.39 to define the conversion efficiency of the first microwave photon in the cavity to the output optical photon:

$$
T^A_{\mu\to o} = \frac{\langle a^\dagger a\rangle_{out}}{\langle b^\dagger b\rangle_{cavity}} \approx \frac{|c_3^{(1)}|^2\kappa_o}{|\sqrt{\kappa_\mu}\varepsilon|} \tag{6.45}
$$

where $|c_3^{(1)}|^2\kappa_o$ is the rate at which optical photons decay out of the optical cavity ($c_3^{(1)}$ is the expectation value of the state $\left|g,1,0\right\rangle$ where there is one photon in the optical cavity), and $|\sqrt{\kappa_\mu}\varepsilon|$ is the rate at which microwave photons enter the cavity due to the classical drive ε. Thus the conversion efficiency reads as the rate of output optical photons divided by the rate of microwave photons entering the microwave cavity. As a sanity check of the methodology we use, we first perform a similar analysis of the transmission of the first and second photon through single mode cavity with a two level emitter the results of which are plotted in Figure 6.11a and 6.11b. We observe the two polariton peaks in the strong coupling regime due to the dressed states, and a single peak in the weak coupling regime as expected. Furthermore in the strong coupling regime, for small values of κ, the maximum transmission of the first and second photons occur at a detuning of $\Delta/g = 1$. However with increasing κ, the maximum transmission of the first and second photons broaden [117]. For a a two level emitter weakly coupled to a cavity, the maximum transmission occurs at a detuning of $\Delta = 0$. With increasing κ, the transmission peaks of the system broaden as seen in Figure 6.11c and 6.11d. This is in agreement with the dynamics of a two level emitter coupled to a cavity as we saw earlier.

6.5.1 Coupling Regimes

Returning to the Λ system coupled to the two cavities, we perform the analytical approximation for the conversion efficiency of the first photon microwave photon to optical photon. There are 4 limiting case regimes, two for each cavity, of the system that can be explored. Namely the regimes: $g_\mu >> \Gamma_s$, $g_\mu << \Gamma_s$, $g_o >> \Gamma_e$ and $g_o << \Gamma_e$ (where $\Gamma_e = 2\pi \times 13.3\text{MHz}$ and $\Gamma_s = 2\pi \times 21.2\text{Hz}$). Due to the large difference in the values of the of Γ_e and Γ_s, in the limiting case with $g_\mu << \Gamma_s$, the conversion efficiency approaches zero, $T^A_{\mu\to o} \to 0$. The reason for this can be understood by looking at the Fermi's golden rule and referring to Figure 6.8b. The transition probability between the states $|g,0,1\rangle$ and $|s,0,0\rangle$ in the first photon manifold if given by [118]:

$$\Gamma_{|g,0,1\rangle\to|s,0,0\rangle} = \frac{2\pi}{\hbar^2} |\left\langle g,0,1\right| \bar{\mathcal{H}}_{int} \left|s,0,0\right\rangle|^2 \propto |g_\mu|^2 \tag{6.46}$$

where $\bar{\mathcal{H}}_{int}$ is the non-Hermitian interaction Hamiltonian of the first photon manifold from Equation 6.41. As can be noted since the transition probability $\Gamma_{|g,0,1\rangle\to|s,0,0\rangle}$ scales with $|g_\mu|^2$, for $g_\mu << \Gamma_s$, the transition probability $\Gamma_{|g,0,1\rangle\to|s,0,0\rangle}$ is much smaller than the transition probabilities between the other bare states in the first photon manifold (Figure 7.1). This means that very few of the photons that are injected into the microwave cavity are being coupled to the atomic transition and hence the conversion efficiency of the system goes to zero, $T^A_{\mu\to o} \to 0$. Thus it is a necessary condition that the microwave coupling rate,

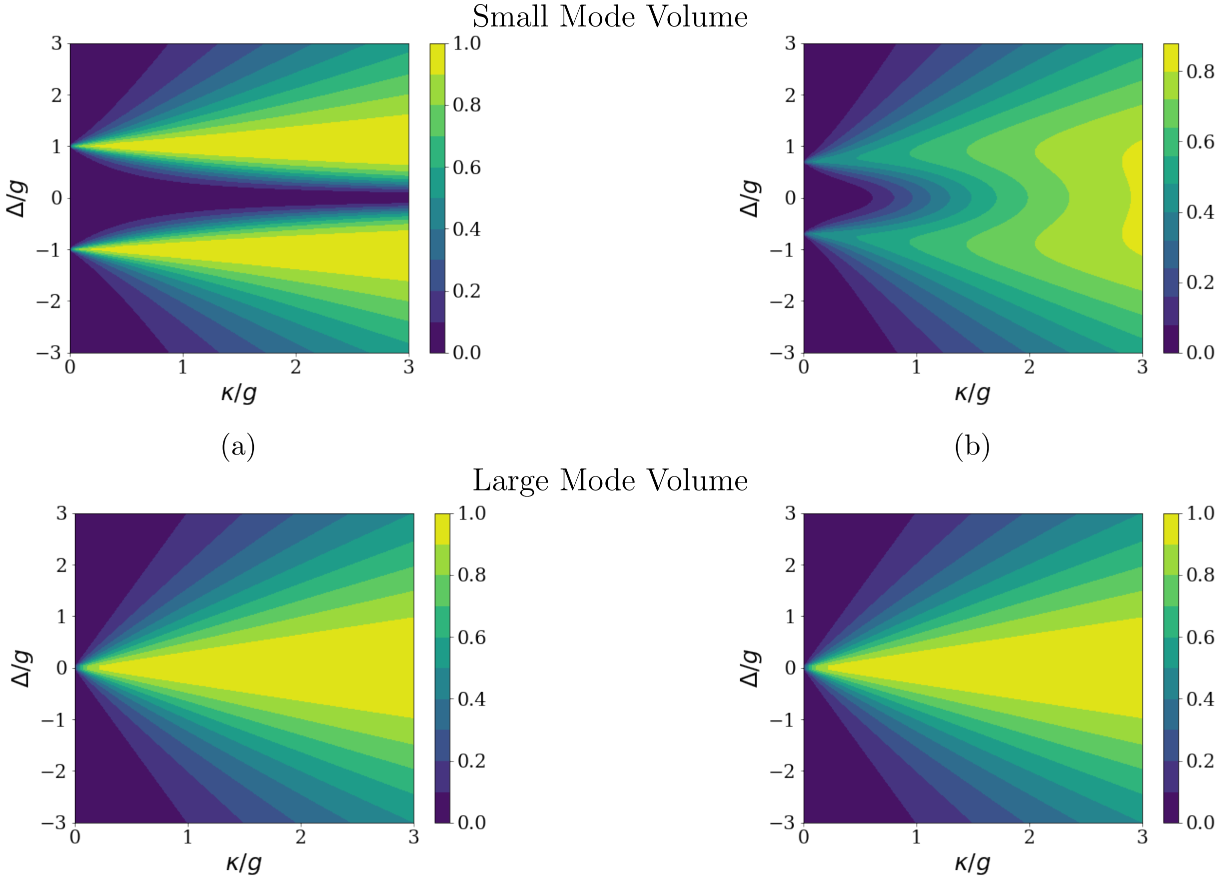

(a) (b)

(c) (d)

Figure 6.11: a) and b) Analytical approximation of the transmission of the first and second photons respectively through a cavity resonantly coupled with a two level emitter. The detunings, $\Delta = \Delta_c = \Delta_{eg}$ and coupling strength, $g = 100\Gamma$, where Γ is the decay rate of the two level emitter. c) and d) Analytical approximation of the transmission of the first and second photons through a cavity resonantly coupled with a two level emitter. The detunings, $\Delta = \Delta_c = \Delta_{eg}$ and with a coupling strength, $g = 0.01\Gamma$, where Γ is the decay rate of the two level emitter.

$g_\mu >> \Gamma_s$, when working with the Λ system in an NV center. With $g_\mu >> \Gamma_s$ we explore the two regimes with optical cavity: $g_o >> \Gamma_e$ and $g_o << \Gamma_e$.

Small Optical Cavity Mode Volume Regime: $g_o >> \Gamma_e$

With the cavity coupling rates $g_0 = 100\Gamma_e$ and $g_\mu = 100\Gamma_s$ (where $\Gamma_e = 2\pi \times 13.3$MHz and $\Gamma_s = 2\pi \times 21.2$Hz), we perform the analytical approximation for constant cavity decay rates $\kappa_\mu = g_\mu$ and $\kappa_o = g_o$, whilst sweeping over the the Rabi coupling rate, Ω, and detunings, Δ $(= \Delta_s = \Delta_e = \Delta_o = \Delta_\mu)$, and κ_o and κ_μ respectively (see Figure 6.12).

$T^A_{\mu\rightarrow o}(\kappa_\mu = \mathbf{g}_\mu)$ $T^A_{\mu\rightarrow o}(\kappa_\mathbf{o} = \mathbf{g_o})$

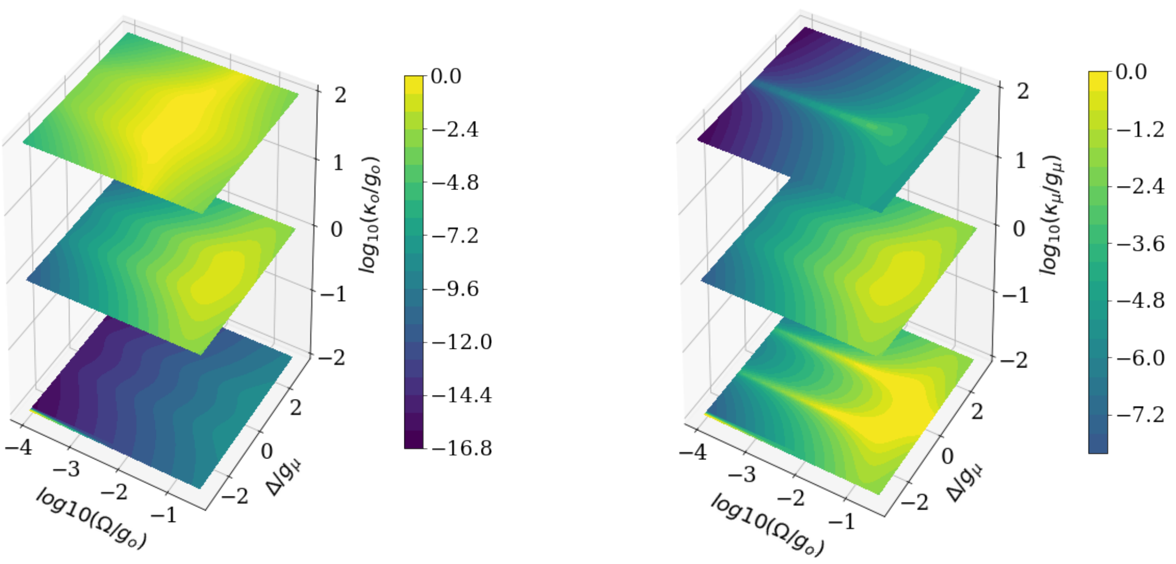

(a) (b)

Figure 6.12: Conversion efficiency ($\log_{10}$ scale) for a constant $\kappa_\mu = g_\mu$ and $\kappa_o = g_o$ sweeping through three different values of κ_o and κ_μ respectively, for $g_o = 100\Gamma_e$ and $g_\mu = 100\Gamma_s$ (where $\Gamma_e = 2\pi \times 13.3$MHz, $\Gamma_s = 2\pi \times 21.2$Hz and $\Delta = \Delta_s = \Delta_e = \Delta_o = \Delta_\mu$). a) The conversion efficiency ($\log_{10}$ scale) for a fixed κ_μ sweeping through three different values of κ_o. As can be observed, as κ_o is increased, the Ω required to achieve maximum conversion efficiency decreases. b)The conversion efficiency for a fixed κ_o sweeping through three different values of κ_μ. With a weak optical cavity maximum conversion efficiency occurs mainly on resonance ($\Delta/g_\mu = 0$) but as κ_μ decreases, additional peaks corresponding to the polariton peaks start appearing at $\Delta/g_\mu = \pm 1$ (polariton peaks).

Some key characteristics of the system can be understood from the analytical plots in Figure 6.12a and Figure 6.12b. It can be noted from Fig. 6.12a, for constant κ_μ, as the value of κ_o is increased, the maximum achievable conversion efficiency increases. Furthermore, as κ_o is increased the value of Ω required to achieve maximum conversion efficiency decreases. These two responses of the system can be attributed to the fact that as the κ_o increases, the optical cavity becomes more leaky allowing for more optical photons to be collected in the output. Furthermore as the optical cavity becomes more leaky, a smaller value of Ω is required for the converted photon to leave the optical cavity within each cycle.

From Fig. 6.12b it can be noted that for a fixed κ_o, as the microwave decay rate, κ_μ is decreased, that is as the microwave cavity gets stronger, the maximum value conversion efficiency occurs at detunings of, $\Delta/g_\mu = \pm 1$ (polariton peaks). As Ω is increased, the peaks at which the maximum conversion efficiency occurs start broadening, thus resulting in a broadened detuning over which the conversion efficiency occurs. This phenomenon is known as power broadening and can be understood if we digress a little and look at a two level emitter that is driven with a Rabi drive Ω as seen in Figure 6.13.

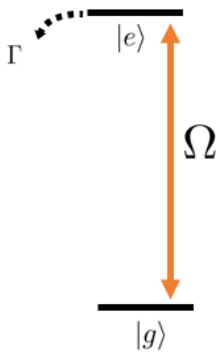

Figure 6.13: Two level emitter driven by a Rabi drive, Ω with decay rate Γ.

Digression: In a two level system with excited state $|e\rangle$ and $|g\rangle$, that is being driven by a Rabi drive Ω, and decay rate Γ, the excited state population of the system in steady state derived from the Optical Bloch equations can be expressed as [109]:

$$\rho_{ee} = \frac{\Omega^2/\Gamma^2}{1 + (\frac{2\Delta}{\Gamma})^2 + 2(\frac{\Omega}{\Gamma})^2} \tag{6.47}$$

where Δ is the detuning. In the weak Rabi drive limit:

$$\rho_{ee} = \frac{\Omega^2/4}{\Delta^2 + (\frac{\Gamma}{2})^2} \tag{6.48}$$

This represents a Lorentizian with a Full Width Half Maximum(FWHM) of Γ with a maximum value of $(\frac{\Omega}{\Gamma})^2 << 1$. In the strong Rabi drive limit, the excited state population is:

$$\rho_{ee} = \frac{\Omega^2/4}{\Delta^2 + (\frac{\Omega^2}{2})} \tag{6.49}$$

In the strong drive limit, this also represents a Lorentzian but has a larger FWHM of $\sqrt{2}\Omega$ with a maximum value of 0.5 as expected for a saturated transitions of a two level system. The absorption line of a two level system for different Rabi drive strengths is plotted in Figure 6.14.

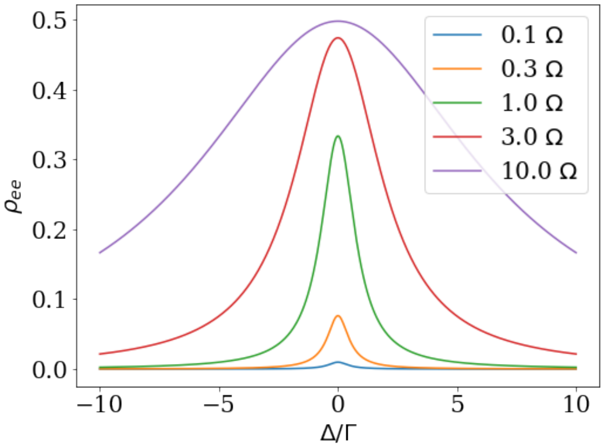

Figure 6.14: Steady state population of the excited state of a two level system with population decay rate Γ, driven by a Rabi drive Ω with a detuning of Δ.

Now returning back to the Λ system, we now understand maximum conversion efficiency can be achieved for the system on resonance for a sufficiently large Ω due to power broadening and manifold mixing. Furthermore we also note from Figure 6.12b that with increasing κ_μ, the conversion efficiency decreases, due to the increase in the leakage of the microwave photons from the microwave cavity.

In order to understand the conversion efficiency dependence on the the parameters κ_o, κ_μ and Ω simultaneously, we sweep over the the three parameters and plot the maximum conversion efficiency for each pair of κ_o and κ_μ, and the corresponding Rabi drive rate, Ω, required to achieve the maximum conversion (Fig. 6.15) with the system on resonance ($\Delta_s = \Delta_e = \Delta_o = \Delta_\mu = 0$).

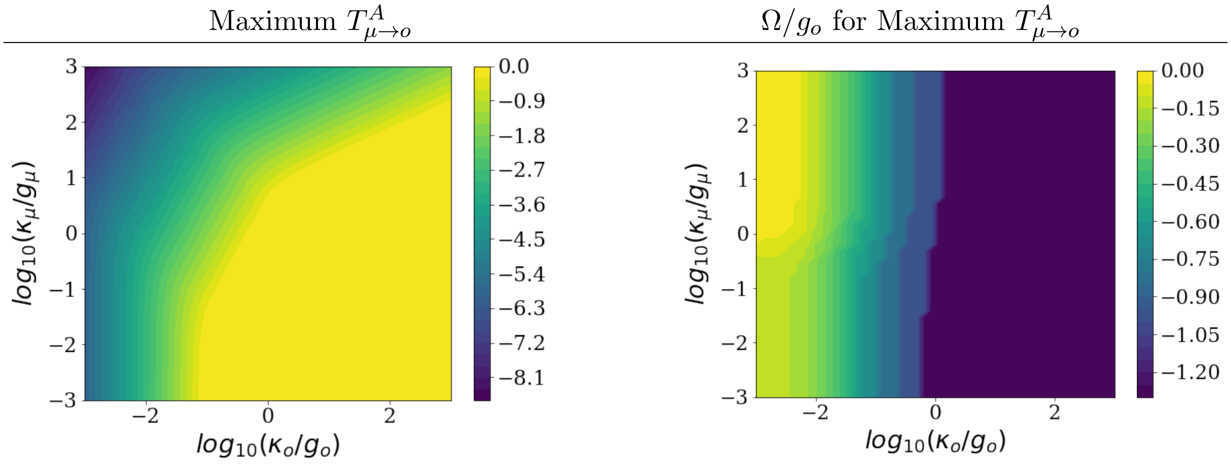

(a) (b)

Figure 6.15: Maximum conversion efficiency ($\log_{10}$ scale) and the corresponding Ω to achieve maximum efficiency for the system for $g_o = 100\Gamma_e$ and $g_\mu = 100\Gamma_s$ (where $\Gamma_e = 2\pi \times 13.3$MHz, $\Gamma_s = 2\pi \times 21.2$Hz), for the system on resonance ($\Delta_s = \Delta_e = \Delta_o = \Delta_\mu = 0$).

As can be noted from the plots in Figure 6.15, as the optical cavity decay rate κ_o is increased the conversion efficiency of the system increases, whilst the required Ω for maximum conversion decreases. This is in agreement with what was observed in Figure 6.12a, wherein with a larger κ_o more photons that are in the $|g, 1, 0\rangle$ are able to leave the cavity before being coupled back into the emitter. Furthermore as the microwave cavity decay rate, κ_μ, is increased there exists a turnaround point at which the conversion efficiency starts decreasing. This is in agreement with what was observed in Figure 6.12b, wherein with the increase in κ_μ the lifetime of the microwave photons in the cavity decreases resulting in fewer photons being converted to optical photons.

Large Optical Cavity Mode Volume Regime: $g_o << \Gamma_e$

We perform a similar analysis as before for the system with the cavity coupling rates $g_0 = 0.01\Gamma_e$ and $g_\mu = 100\Gamma_s$ (where $\Gamma_e = 2\pi \times 13.3$MHz and $\Gamma_s = 2\pi \times 21.2$Hz), for constant cavity decay rates $\kappa_\mu = g_\mu$ and $\kappa_o = g_o$, whilst sweeping over the the Rabi coupling rate, Ω, and detunings, Δ ($= \Delta_s = \Delta_e = \Delta_o = \Delta_\mu$), and κ_o and κ_μ respectively (see Figure 6.16).

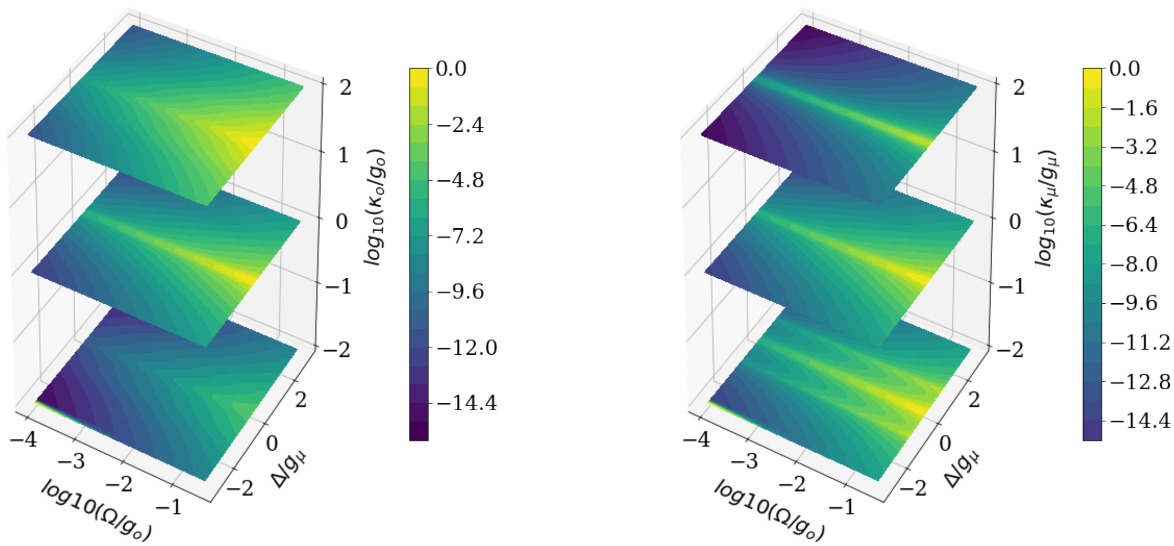

$T^{A}_{\mu\to o}(\kappa_\mu = g_\mu)$ $T^{A}_{\mu\to o}(\kappa_o = g_o)$

(a) (b)

Figure 6.16: Conversion efficiency ($\log_{10}$ scale) for a constant $\kappa_\mu = g_\mu$ and $\kappa_o = g_o$ sweeping through three different values of κ_o and κ_μ respectively, for $g_o = 0.01\Gamma_e$ and $g_\mu = 100\Gamma_s$ (where $\Gamma_e = 2\pi \times 13.3$MHz, $\Gamma_s = 2\pi \times 21.2$Hz and $\Delta = \Delta_s = \Delta_e = \Delta_o = \Delta_\mu$). a) The conversion efficiency for a fixed κ_μ sweeping through three different values of κ_o. b)The conversion efficiency for a fixed κ_o sweeping through three different values of κ_μ. For small κ_μ, maximum conversion efficiency occurs at detunings, $\Delta/g_\mu = \pm 1$ (polariton peaks), whereas as κ_μ is increased, maximum conversion efficiency takes place at detunings, $\Delta/g_\mu = 0$, or when the system is on resonance.

From Figure 6.16a for a constant κ_μ, the conversion efficiency increases with increasing κ_o similar to the trend noted earlier in the previous case (see Figure 6.12a). However due to the lower optical coupling strength, the detuning bandwidth over which maximum conversion occurs is also much narrower and occurs mainly at resonance, $\Delta = 0$. From Figure 6.16b we observe as before that as κ_μ decreases the polariton peaks that are characteristic of a strong cavity start appearing in addition to the single peak on resonance peak due to the weak cavity coupling. However in this case the polariton peaks are much narrower due to the lower g_o. It can also be noted that for a small κ_μ, as Ω is increased the conversion efficiency increases, whilst for large κ_μ the change in Ω results in little to no change in the conversion efficiency. This is due to the fact that as the microwave cavity gets stronger, the lifetime of the microwave photons in the cavity increases, thus as Ω is increased, more and more microwave photons can be converted, whilst for a leaky microwave cavity, regardless of how much Ω is increased, there isn't a change in the expectation value of the output optical photons.

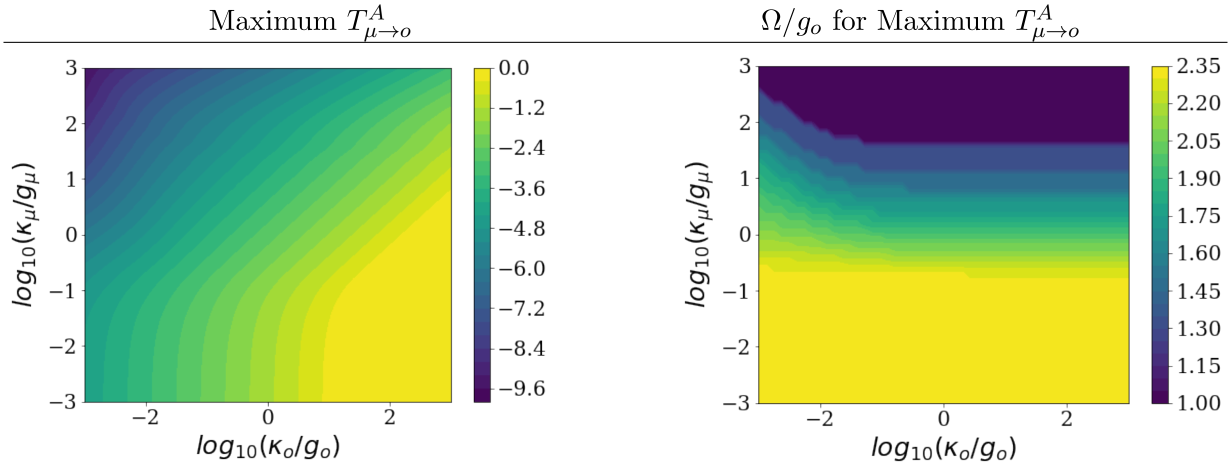
Maximum $T^A_{\mu\to o}$

Ω/g_o for Maximum $T^A_{\mu\to o}$

(a)

(b)

Figure 6.17: Maximum conversion efficiency ($\log_{10}$ scale) and the corresponding Ω to achieve maximum efficiency for the system for $g_o = 0.01\Gamma_e$ and $g_\mu = 100\Gamma_s$ (where $\Gamma_e = 2\pi \times 13.3$MHz and $\Gamma_s = 2\pi \times 21.2$Hz), for the system on resonance ($\Delta_s = \Delta_e = \Delta_o = \Delta_\mu = 0$).

We perform a similar simulation as before and sweep over the values of pair of κ_o, κ_μ and Ω, and plot maximum conversion efficiency for each pair of κ_o and κ_μ, and the corresponding Rabi drive rate, Ω, required to achieve the maximum conversion is plotted (Fig. 6.17) with the system on resonance ($\Delta_s = \Delta_e = \Delta_o = \Delta_\mu = 0$). As before with increasing κ_o, the conversion efficiency increases as more optical photons can leave the cavity before being coupled back to the system. However when compared with Figure 6.15, the required κ_o before which unit conversion efficiency occurs is increased by an order of magnitude. As was noted before, as κ_μ is decreased, the conversion efficiency increases and the required Ω to achieve maximum conversion increases due to the increased lifetime of the microwave photons. However when compared with with Figure 6.15, the required κ_μ to achieve maximum conversion efficiency is decreased by an order of magnitude. This means in the weak optical coupling regime, κ_o is required to be larger and κ_μ is required to smaller than in the strong coupling regime to achieve unit conversion efficiency.

6.6 Monte-Carlo Simulations

6.6.1 Continuous Drive

Although the analytical simulations provide us with a intuitive understanding of the required cavity parameters to achieve maximum conversion, to understand the effects of higher manifolds in the system, we perform Monte-Carlo simulations of the Hamiltonian described in Equation 6.54. We employ the Monte-Carlo Solver from the Python package, QuTIP [107, 108] to perform the simulations. With the Monte-Carlo simulations we also take into the account the fact that only the decay rate via the ZPL emission, $\Gamma_{ZPL} = 2\pi \times 0.35\text{MHz}$, is coupled resonantly to the cavity while the PSB decay – which results in photons emitted in the phonon sideband– from the excited to the ground state is $\Gamma_{PSB} = 2\pi \times 10.2\text{MHz}$ [2]. Thus only a small percentage of the emission from the excited state is resonantly coupled to the ground state $|g\rangle$ via the ZPL whilst the ground state is populated via non resonant decay. We do this by simulating the pseudo three level system that was described in Figure 6.9 using the QuTIP package we introduced in Section 6.2. The effective non-Hermitian Hamiltonian describing the dynamics of the system in the rotating frame is given by:

$$\mathcal{H} = \mathcal{H}_o + \mathcal{H}_{int} + \mathcal{H}_{drive} - \frac{i\hbar}{2}\sum_k \hat{C}_k^\dagger \hat{C}_k, \tag{6.50}$$

with the collapse operators $\hat{C}_k$ defined as:

$$\hat{C}_1 = a_{out} = \sqrt{\kappa_o}a, \tag{6.51a}$$

$$\hat{C}_2 = b_{out} = \sqrt{\kappa_\mu}b, \tag{6.51b}$$

$$\hat{C}_3 = \sqrt{\Gamma_{ZPL}}\,|g\rangle\langle e|\,, \tag{6.51c}$$

$$\hat{C}_4 = \sqrt{\Gamma_{PSB}}\,|g'\rangle\langle e|\,, \tag{6.51d}$$

$$\hat{C}_5 = \sqrt{\Gamma_p}\,|g\rangle\langle g'|\,, \tag{6.51e}$$

$$\hat{C}_6 = \sqrt{\Gamma_s}\,|g\rangle\langle s|\,, \tag{6.51f}$$

$$\hat{C}_7 = \sqrt{\Gamma_{es}}\,|s\rangle\langle e|\,, \tag{6.51g}$$

$$\hat{C}_8 = \sqrt{\gamma_e}\,|e\rangle\langle e|\,, \tag{6.51h}$$

$$\hat{C}_9 = \sqrt{\gamma_s}\,|s\rangle\langle s| \tag{6.51i}$$

where κ_o (κ_μ) is the optical (microwave) cavity decay rate, Γ_s is the population decay rate of the $|s\rangle$ state in the Λ system, γ_e (γ_s) is models additional coherence decays rate of $|e\rangle$ ($|s\rangle$) state, Γ_{ZPL} is the ZPL decay rate, Γ_{PSB} is the PSB decay rate, Γ_{es} is the decay rate from $|s\rangle$ to $|g\rangle$, $|s\rangle$ to the Γp is the decay rate from shelving state $|g'\rangle$ to $|g\rangle$. The operator $\hat{C}_1$ ($\hat{C}_2$) is the optical (microwave) photon decay, $\hat{C}_3$ describes the population decay from the excited state $|e\rangle$ to the ground state $|g\rangle$, $\hat{C}_4$ describes the PSB decay from the excited state $|e\rangle$ to the virtual state $|g'\rangle$, $\hat{C}_5$ describes the population decay from the virtual state $|g'\rangle$ to the ground state $|g\rangle$ through phonon decay, $\hat{C}_6$ describes the population decay from the metastable state $|s\rangle$ to the ground state $|g\rangle$, $\hat{C}_7$ describes the population decay from $|e\rangle$ to $|s\rangle$, and $\hat{C}_8$ ($\hat{C}_9$) describes the additional coherence decay of the state $|e\rangle$ ($|s\rangle$) denoted in Equation 6.38.

The Hamiltonian terms in the rotating frame $\mathcal{H}_o$, $\mathcal{H}_{int}$, and $\mathcal{H}_{drive}$ are defined in Equation 6.34. We define the intrinsic conversion efficiency together with the collapse operator, $a_{out} = \sqrt{\kappa_o}a$ as:

$$T^A_{\mu\to o} = \frac{\int \langle a^\dagger_{out} a_{out}\rangle dt}{\int |\sqrt{\kappa_\mu}\varepsilon| dt} \tag{6.52}$$

in the limit that $|\sqrt{\kappa_\mu}\varepsilon| \to 0$. The term $\langle a^\dagger_{out} a_{out}\rangle$ is the rate at which optical photons decay out of the optical cavity. Thus the integral in the numerator denotes the total optical photons exiting the optical cavity. The term $|\sqrt{\kappa_\mu}\varepsilon|$ is the rate at which microwave photons enter the microwave cavity due to the drive ε. Thus the integral in the denominator describes total microwave photons entering the cavity.

As we did before in Section 6.2.1, we first set up the operators in the Hilbert space of the system. The Hilbert space of the system has a dimension of $4 + N + N$ corresponding to the pseudo-three level emitter (Figure 6.9), and the two cavity modes respectively. The Hilbert space for each cavity mode was truncated at $N = 7$, as for any manifold level $N < 7$ the maximum conversion efficiency saturated at values that were less than one. Although for $N > 7$ we get a unit conversion efficiency, using too large of a Hilbert space results in longer simulation times. The system is initialized in $\psi(0) = |g, 0, 0\rangle$ with the NV center in the ground state with no photons in both the optical and microwave cavities respectively. As we did before in Section6.2.1, we simulate the system by feeding the Hamiltonian and the initial state of the system to the Monte-Carlo solver. The Python codes for this simulation are included in Appendix E.

Small Optical Cavity Mode Volume Regime: $g_o >> \Gamma_e$

We simulate the system with the cavity coupling rates $g_0 = 100\Gamma_e$ and $g_\mu = 100\Gamma_s$ (where $\Gamma_e = 2\pi \times 13.3\text{MHz}$ and $\Gamma_s = 2\pi \times 21.2\text{Hz}$), with the system on resonance ($\Delta_s = \Delta_e = \Delta_o = \Delta_\mu = 0$) by sweeping over the optical and microwave cavity decays rates, κ_o and κ_μ, and the Rabi driving rate, Ω. The maximum conversion efficiency for each pair of κ_o and κ_μ, and the corresponding Rabi drive rate, Ω, required to achieve the maximum conversion is plotted.

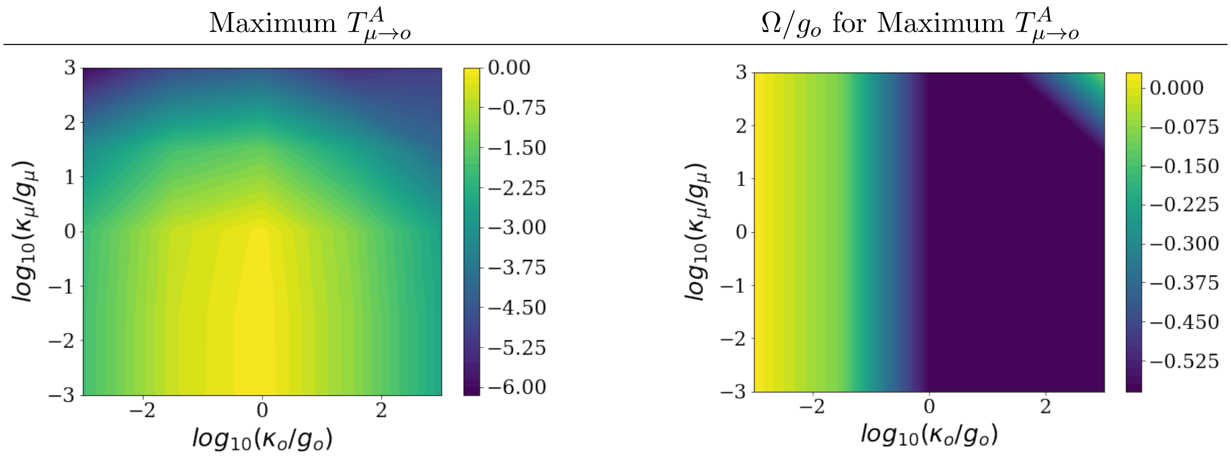
Maximum $T^A_{\mu\to o}$

Ω/g_o for Maximum $T^A_{\mu\to o}$

(a) (b)

Figure 6.18: a) Maximum conversion efficiency ($\log_{10}$ scale) and the corresponding b) Ω to achieve maximum conversion efficiency for the system with $g_\mu = 100\Gamma_s$ and $g_o = 100\Gamma_e$ (where $\Gamma_e = 2\pi \times 13.3\text{MHz}$, $\Gamma_s = 2\pi \times 21.2\text{Hz}$). The system is initialized with the Λ system in the ground state with no photons in the optical and microwave cavities ($\psi(0) = |g, 0, 0\rangle$).

Some key characteristics that can be noted from Figure 6.18. Firstly, when higher manifolds of the system are included, there exists a upper bound on the optical cavity decay rate κ_o for maximum conversion efficiency, as opposed to the analytical approximation of the conversion efficiency of the first photon seen in Figure 6.18. This can be attributed to the fact that in the analytical approximation, only the first and ground manifolds of the system was considered where all the optical cavity decay from the state $|g, 1, 0\rangle$ resulted in being reinitialized again in the ground state $|g, 0, 0\rangle$. However the inclusion of higher manifolds in the simulation results in the increase of decay channels as well. Thus with the higher manifolds, the conversion efficiency starts decreasing as the optical decay rate is increased beyond $\kappa_o \approx 10g_o$. We also note that with increasing κ_o the required Ω to achieve maximum conversion efficiency decreases.

With the microwave cavity parameter, κ_μ, we observe a similar trend in the conversion efficiency as seen in the analytical approximations in Figure 6.18. As the microwave cavity becomes stronger, the conversion efficiency increases due to the increased lifetime of the microwave photons. Unit conversion efficiency occurs for a an optical cavity decay rate of $\kappa_o \sim 10^{-2}g_o - 10^0 g_o$ and microwave cavity decay rate $\kappa_\mu < 10g_\mu$. This corresponds to an optical cavity quality factor ($Q = \omega/\kappa$) of $Q_o \sim 10^6 - 10^8$ and microwave cavity quality factor $Q_\mu > 10^3$.

Large Optical Cavity Mode Volume Regime: $g_o << \Gamma_e$

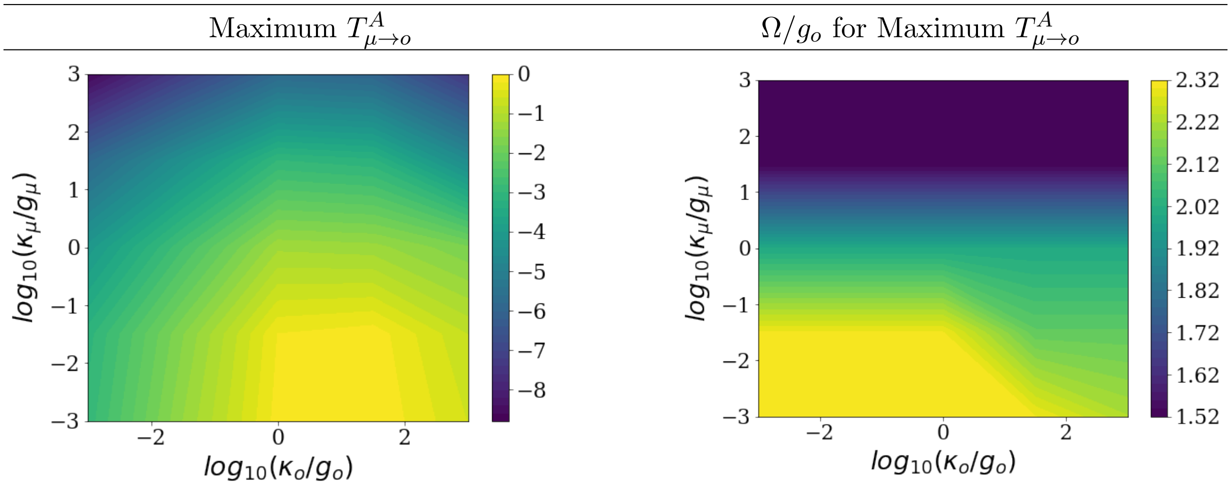

Maximum $T^A_{\mu\to o}$

Ω/g_o for Maximum $T^A_{\mu\to o}$

(a)

(b)

Figure 6.19: a) Maximum conversion efficiency ($\log_{10}$ scale) and the corresponding b) Ω to achieve maximum conversion efficiency for the system with $g_\mu = 100\Gamma_s$ and $g_o = 0.01\Gamma_e$ (where $\Gamma_e = 2\pi \times 13.3\text{MHz}$, $\Gamma_s = 2\pi \times 21.2\text{Hz}$). The system is initialized with the Λ system in the ground state with no photons in the optical and microwave cavities ($\psi(0) = |g, 0, 0\rangle$).

We simulate the system with the cavity coupling rates $g_0 = 0.01\Gamma_e$ and $g_\mu = 100\Gamma_s$ (where $\Gamma_e = 2\pi \times 13.3\text{MHz}$ and $\Gamma_s = 2\pi \times 21.2\text{Hz}$), with the system on resonance ($\Delta_s = \Delta_e = \Delta_o = \Delta_\mu = 0$) by sweeping over the optical and microwave cavity decays rates, κ_o and κ_μ, and the Rabi driving rate, Ω. The maximum conversion efficiency for each pair of κ_o and κ_μ, and the corresponding Rabi drive rate, Ω, required to achieve the maximum conversion is plotted.

In the large optical mode volume regime, from Figure 6.19 we note that as before when higher manifolds of the system is included there exists a upper bound on the optical cavity decay rate κ_o, as opposed to the analytical approximation of the conversion efficiency of the first photon seen in Figure 6.19. Furthermore as we observed in the analytical approximations, in the large optical mode volume regime, the maximum conversion efficiency occurs for a larger κ_o and a smaller κ_μ as compared to the strong coupling regime.. Unit conversion efficiency occurs for an optical cavity decay rate of $\kappa_o \sim g_o - 10^2 g_o$ and microwave cavity decay rate $\kappa_\mu < 10^{-1} g_\mu$. This corresponds to an optical cavity quality factor of $Q_o \sim 10^8 - 10^{10}$ and $Q_\mu > 10^5$.

6.6.2 Single Photon

So far we have seen the conversion efficiency of the system when it is continuously driven with a weak microwave drive. Now we shall explore the conversion efficiency of the system when initialized with a single photon in the microwave cavity. As before, the system dynamics is described by the Hamiltonian $H = H_o + H_{int}$ without the H_{drive} term from Equation 6.29. We go into a rotating frame using the time dependent unitary transformation U:

$$U = \exp{(-it)}[\omega_\Omega(|e\rangle\langle e| + a^\dagger a)] \tag{6.53}$$

where the Hamiltonian is transformed according to:

$$\mathcal{H} = U^\dagger H U + i\frac{dU^\dagger}{dt}U = \mathcal{H}_o + \mathcal{H}_{int} \tag{6.54}$$

with

$$\mathcal{H}_o/\hbar = \omega_s |s\rangle\langle s| + (\omega_e - \omega_\Omega)|e\rangle\langle e| + (\omega_a - \omega_\Omega)a^\dagger a + \omega_\mu b^\dagger b, \tag{6.55a}$$

$$\begin{aligned}\mathcal{H}_{int}/\hbar =& g_\mu(b|s\rangle\langle g| + b^\dagger|g\rangle\langle s|) + g_o(a|e\rangle\langle g| + a^\dagger|g\rangle\langle e|)\\ &+ (\Omega|e\rangle\langle s| + \Omega^*|s\rangle\langle e|),\end{aligned} \tag{6.55b}$$

Once again we define the effective Hamiltonian, H:

$$\mathcal{H} = \mathcal{H}_o + \mathcal{H}_{int} - \frac{i\hbar}{2}\sum_k \hat{C_k}^{\dagger}\hat{C}_k \tag{6.56}$$

with collapse operators $\hat{C}_k$ defined in Equation 6.51. Together with the collapse operator, $a_{out} = \sqrt{\kappa_o}a$, we define the intrinsic conversion efficiency as:

$$T^A_{\mu\rightarrow o} = \int \langle a^{\dagger}_{out}a_{out}\rangle dt \tag{6.57}$$

The term $\langle a^{\dagger}_{out}a_{out}\rangle$ is the rate at which optical photons decay out of the optical cavity. Thus the integral denotes the total optical photons exiting the optical cavity. The system is initialized with one photon in the microwave cavity, $\psi(0) = |g,0,1\rangle$. The Python codes for this simulation are included in Appendix E. Furthermore, as before we would like to explore the case where the system is on resonance with $\omega_e = \omega_o$, $\omega_s = \omega_\mu$, and $\omega_\Omega = \omega_e - \omega_s$.

Small Optical Cavity Mode Volume Regime: $g_o >> \Gamma_e$

We simulate the system with the cavity coupling rates $g_0 = 100\Gamma_e$ and $g_\mu = 100\Gamma_s$ (where $\Gamma_e = 2\pi \times 13.3$MHz and $\Gamma_s = 2\pi \times 21.2$Hz), with the system on resonance ($\Delta_s = \Delta_e = \Delta_o = \Delta_\mu = 0$) by sweeping over the optical and microwave cavity decays rates, κ_o and κ_μ, and the Rabi driving rate, Ω. The system is initialized with one microwave photon $\psi(0) = |g,0,1\rangle$, with the drive term $H_{drive} = 0$. The maximum conversion efficiency for each pair of κ_o and κ_μ, and the corresponding Rabi drive rate, Ω, required to achieve the maximum conversion is plotted.

We can observe from Figure 6.20 a similar trend in the maximum conversion efficiency as we observed in the system with a continuous drive (Figure 6.18). However in the single photon regime, the maximum κ_μ required to achieve unit maximum conversion efficiency, is decreased by an order of magnitude. This means that in the single photon regime the microwave cavity is required to be stronger than in the continuous drive regime to increase the lifetime of the microwave photon. The difference between the drive term turned on and off in Figure 7.6, is due to state ground state $|g,0,0\rangle$ not being excited again to participate in the conversion. Furthermore the range of κ_o over which the unit maximum conversion occurs is narrower. We observe a similar trend in Ω as observed in the continuous drive regime, where with increasing κ_o, the Ω required to achieve maximum conversion decreases. Unit conversion efficiency occurs for a an optical cavity decay rates of $\kappa_o \sim 10^{-1}g_o - g_o$ and microwave cavity decay rates of $\kappa_\mu < g_\mu$. This corresponds to an optical cavity quality factor of $Q_o \sim 10^6 - 10^7$ and $Q_\mu > 10^4$.

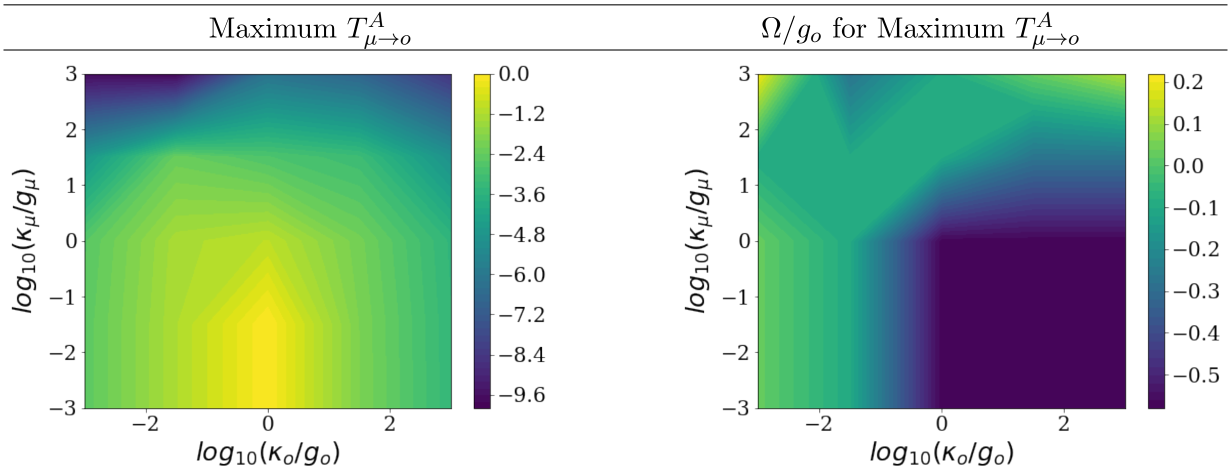
Maximum $T^{A}_{\mu\to o}$

Ω/g_o for Maximum $T^{A}_{\mu\to o}$

(a) (b)

Figure 6.20: a) Maximum conversion efficiency ($\log_{10}$ scale) and the corresponding b) Ω to achieve maximum conversion efficiency for the system with $g_\mu = 100\Gamma_s$ and $g_o = 100\Gamma_e$ (where $\Gamma_e = 2\pi\times 13.3$MHz, $\Gamma_s = 2\pi\times 21.2$Hz). The system is initialized with the Λ system in the ground state with one photon in the microwave cavity and with the drive turned off ($\psi(0) = |g, 0, 1\rangle$)

Large Optical Cavity Mode Volume Regime: $g_o << \Gamma_e$

We perform a similar analysis the system as before with the cavity coupling rates $g_0 = 0.01\Gamma_e$ and $g_\mu = 100\Gamma_s$ (where $\Gamma_e = 2\pi\times 13.3$MHz and $\Gamma_s = 2\pi\times 21.2$Hz), with the system on resonance ($\Delta_s = \Delta_e = \Delta_o = \Delta_\mu = 0$) by sweeping over the optical and microwave cavity decays rates, κ_o and κ_μ, and the Rabi driving rate, Ω. The system is initialized with one microwave photon $\psi(0) = |g, 0, 1\rangle$, with the drive term $H_{drive} = 0$. The maximum conversion efficiency for each pair of κ_o and κ_μ, and the corresponding Rabi drive rate, Ω, required to achieve the maximum conversion is plotted.

In the large optical mode volume regime with a single photon the maximum conversion efficiency and the required Ω to achieve maximum conversion follows the same trend as was observed in Figure 6.18. However in the ranges plotted, the maximum conversion efficiency is 2 orders of magnitude lower than in the continuous drive case. This is also contributed by the fact that the coupling strength g_o is much lower than the atomic decay rate Γ_e thus there is a higher probability of atomic decay before state can be converted to a optical photon. Maximum conversion efficiency occurs for a an optical cavity decay rates of $\kappa_o \sim g_o - 10^1 g_o$ and microwave cavity decay rates of $\kappa_\mu < 10^{-2} g_\mu$. This corresponds to

Maximum $T^A_{\mu\to o}$ | Ω/g_o for Maximum $T^A_{\mu\to o}$

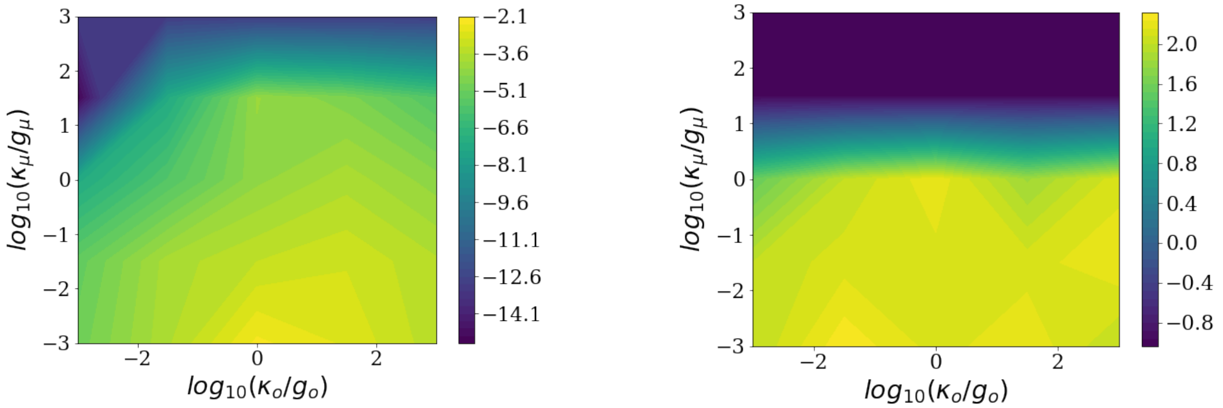

(a) (b)

Figure 6.21: a) Maximum conversion efficiency ($\log_{10}$ scale) and the corresponding b) Ω to achieve maximum conversion efficiency for the system with $g_\mu = 100\Gamma_s$ and $g_o = 0.01\Gamma_e$ (where $\Gamma_e = 2\pi \times 13.3\text{MHz}$, $\Gamma_s = 2\pi \times 21.2\text{Hz}$). The system is initialized with the Λ system in the ground state with one photon in the microwave cavity and with the drive turned off ($\psi(0) = |g, 0, 1\rangle$).

an optical cavity quality factor of $Q_o \sim 10^9 - 10^{10}$ and $Q_\mu > 10^6$.

6.7 Conclusion

Over these past simulations we have been able to identify some of the characteristics of the system to achieve unit conversion efficiency between the microwave and optical regimes using the Λ system. In this chapter we used the intrinsic conversion efficiency definition of the first kind defined in Equation 6.39 where we asked the question: *If we can get a microwave photon into the microwave cavity, what system parameters are required to achieve maximum conversion efficiency?*. We first identified that due to the large discrepancies in the decay rates of the level structure in an NV center, a fundamental requirement of system to achieve maximal conversion efficiency is that the microwave cavity be strongly coupled to the $|g\rangle \leftrightarrow |s\rangle$ transition. Thus in the above simulations the microwave cavity coupling strength was required to be, $g_\mu = 100\Gamma_s = 2\pi \times 2.12\text{kHz}$.

Now with that constraint on the microwave cavity, we explored the small ($g_o = 100\Gamma_e = 2\pi \times 1.33\text{GHz}$) and large ($g_o = 100\Gamma_e = 2\pi \times 133\text{kHz}$) optical cavity mode volume regimes

	Max $T^A_{\mu\to o}$	**Optical Cavity**	**Microwave Cavity**
		Continuous Drive	
Small Mode Volume ($g_o = 100\Gamma_e$, $g_\mu = 100\Gamma_s$)	1	$Q_o \sim 10^6 - 10^8$, $V_o = 0.65(\lambda_a/n)^3$	$Q_\mu > 10^3$, $V_\mu = 10^{-10}(\lambda_b/n)^3$
Large Mode Volume ($g_o = 0.01\Gamma_e$, $g_\mu = 100\Gamma_s$)	1	$Q_o \sim 10^8 - 10^{10}$, $V_o = 6.5 \times 10^7(\lambda_a/n)^3$	$Q_\mu > 10^5$, $V_\mu = 10^{-10}(\lambda_b/n)^3$
		Single Photon	
Small Mode Volume ($g_o = 100\Gamma_e$, $g_\mu = 100\Gamma_s$)	1	$Q_o \sim 10^6 - 10^7$, $V_o = 0.65(\lambda_a/n)^3$	$Q_\mu > 10^4$, $V_\mu = 10^{-10}(\lambda_b/n)^3$
Large Mode Volume ($g_o = 0.01\Gamma_e$, $g_\mu = 100\Gamma_s$)	10^{-2}	$Q_o \sim 10^9 - 10^{10}$, $V_o = 6.5 \times 10^7(\lambda_a/n)^3$	$Q_\mu > 10^6$, $V_\mu = 10^{-10}(\lambda_b/n)^3$

Table 6.2: Summary of the conversion efficiency, $T^A_{\mu\to o}$, and the corresponding optical and microwave cavity parameters for the continuous drive and single photon regimes. ($\Gamma_e = 2\pi \times 13.3$MHz and $\Gamma_s = 2\pi \times 21.2$Hz)

to understand what cavity parameters are required to maximize conversion efficiency. The required cavity parameters for the maximum conversion efficiency in each of the different cases explored above have been summarized in Table 6.2. The transition dipole moments of the NV center corresponding to the $|g\rangle \leftrightarrow |s\rangle$ transition in the Λ system is 3.38×10^{-5} Debye [45] and the transition dipole moments of the NV center corresponding to the $|g\rangle \leftrightarrow |e\rangle$ transition in the Λ system are 0.8Debye [119]. Since in the analysis above we assumed that the cavity was resonant with the atomic transitions, we can calculate the mode volumes and the quality factors of the cavities in the different regimes. These results have been summarized in Table 6.2.

We can note two main characteristics of the conversion efficiency performance from the analysis above. Firstly we note that when we move from the small optical optical mode volume regime to the large optical mode volume regime, to achieve maximum conversion efficiency the required κ_o is increased by an order of magnitude and the required κ_μ is decreased by an order of magnitude. Secondly we see that when we move from the continuous drive to the single photon regime, to achieve maximum conversion efficiency, the required κ_μ is decreased by an order of magnitude. We can also observe from the analysis and from Table 6.2 that in order to achieve maximum conversion efficiency that optical cavity is required to have a strong temporal confinement whilst the microwave cavity is required to have a strong spatial confinement. We will continue this analysis in the next chapter where we will look at the system dynamics with the extrinsic conversion efficiency definition $T^{B}_{\mu \to o}$.

Chapter 7

Microwave to Optical Domain Conversion II

Continuing from study in the previous chapter, in this chapter we will look at the system dynamics with the extrinsic conversion efficiency definition, $T^{B}_{\mu\to o}$ that we defined in Section 6.4. In the previous chapter while working with the intrinsic conversion efficiency definition $T^{A}_{\mu\to o}$, we asked the question: *If we can get a microwave photon into microwave cavity, what cavity parameters would maximize the output optical photons?*. Here we will work with the extrinsic conversion efficiency definition where we ask the question: *For every microwave photon incident on the microwave cavity, what cavity parameters would maximize the output optical photons?*. Once again we will follow a similar analysis procedure as before. In Section 7.1 we perform analytical non-Hermitian approximations of the ground state and first manifold of the system to get an intuitive understanding of the system dynamics. In Section 7.2 we employ the QuTIP package [107, 108] to investigate via Monte-Carlo simulations the extrinsic conversion efficiency of the system with: a i) weak continuous drive microwave field and ii) with a single microwave photon using a cascaded cavity simulation. Finally in Section 7.3 we will discuss some of potential platforms that the system can be integrated onto.

The Python codes used to perform the simulations in this chapter have been attached in Appendix E. The code for the cascaded cavity system used in Section 7.2.2 was written based on an original code written by Jinjin Du in Reference [114].

7.1 Approximate Analytical Solutions

We begin once again with the analytical approximation as we did before to observe the conversion efficiency of the first microwave photon to and optical photon. In the analytical approximation we treat the system as purely three level Λ system without the virtual state $|g'\rangle$.

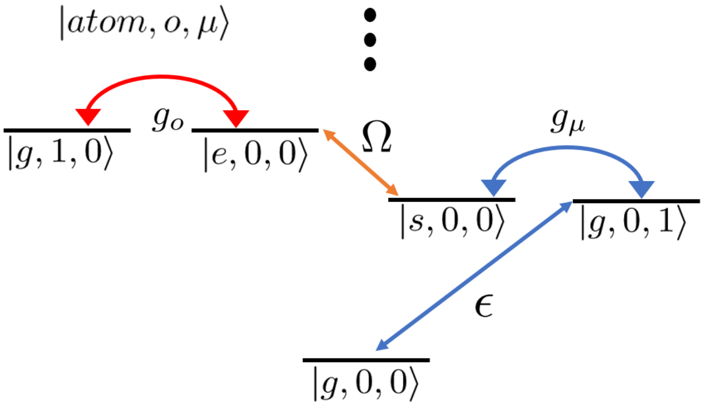

Figure 7.1: Ground state and first manifold of the three Λ system coupled to a microwave and optical cavity with coupling rates g_μ and g_o respectively. The basis states represented are the atomic state, optical photon and the microwave photon respectively.

We follow the approach previously followed in Section 6.5 and look at the non-Hermitian Hamiltonian describing the transition of the system between the ground and first manifolds (see Equations 6.41 - 6.42). We now define the conversion efficiency with a subtle change from Equation 6.45 as:

$$T^B_{\mu\to o} = \frac{\langle a^\dagger a\rangle_{out}}{\langle b^\dagger b\rangle_{in}} \approx \frac{|c_3^{(1)}|^2\kappa_o}{|\varepsilon|^2} \tag{7.1}$$

where $|c_3^{(1)}|^2\kappa_o$ is the rate at which optical photons decay out of the optical cavity ($c_3^{(1)}$ is the expectation value of the state $|g,1,0\rangle$ where there is one photon in the optical cavity), and $|\varepsilon|^2$ is the rate at which microwave photons are incident on the microwave cavity due to the classical drive. Thus the conversion efficiency reads as the rate of output optical photons divided by the rate at which microwave photons are incident on the microwave cavity. We perform the analysis in the weak drive limit, $|\varepsilon|^2 \to 0$

7.1.1 Coupling Regimes

We once again look at the different cavity coupling regimes. As was before due to the large difference in the values of Γ_e and Γ_s, in the limiting case with $g_\mu << \Gamma_s$, the conversion efficiency $T^B_{\mu\to o} \to 0$. This can be understood by referring to Equation 6.46 and referring to Figure 7.1. As can be noted since the transition probability $\Gamma_{|g,0,1\rangle\to|s,0,0\rangle}$ scales with $|g_\mu|^2$, when $g_\mu << \Gamma_s$, the transition probability $\Gamma_{|g,0,1\rangle\to|s,0,0\rangle}$ is much smaller than the transition probabilities between the other bare states in the first photon manifold (Figure 7.1). This means that only few photons that are injected into the microwave cavity are coupled to the atomic transition and hence the conversion efficiency of the system approaches zero, $T^B_{\mu\to o} \to 0$. Thus it is a necessary condition that the microwave coupling rate, $g_\mu >> \Gamma_s$, when working with the Λ system in an NV center. With $g_\mu >> \Gamma_s$ we explore the two optical cavity regimes: $g_o >> \Gamma_e$ and $g_o << \Gamma_e$.

Small Optical Mode Volume Regime: $g_o >> \Gamma_e$

With the cavity coupling rates $g_0 = 100\Gamma_e$ and $g_\mu = 100\Gamma_s$ (where $\Gamma_e = 2\pi \times 13.3\text{MHz}$ and $\Gamma_s = 2\pi \times 21.2\text{Hz}$), we perform the analysis for constant cavity decay rates $\kappa_\mu = g_\mu$ and $\kappa_o = g_o$, whilst sweeping over the the Rabi coupling rate, Ω, and detunings, Δ $(= \Delta_s = \Delta_e = \Delta_o = \Delta_\mu =)$, and κ_o and κ_μ respectively (see Figure 7.2).

Some key characteristics of the system can be understood from the analytical plots in Figure 7.2a and Figure 7.2b. It can be noted from Fig. 7.2a, for constant κ_μ, as the value of κ_o is increased, the maximum achievable conversion efficiency increases. Furthermore, as κ_o is increased the value of Ω required to achieve maximum conversion efficiency decreases. Furthermore as the optical cavity becomes more leaky, a smaller value of Ω is required for the injected microwave photon to be converted within each cycle. These two responses of the system have been previously noted in the earlier conversion efficiency, $T^A_{\mu\to o}$, in Figure 6.12a.

From Fig. 7.2b it can be noted that for a fixed κ_o, as the microwave decay rate, κ_μ is decreased, that is as the cavity gets stronger, the maximum value of the conversion efficiency occurs at, $\Delta/g_\mu = \pm 1$ (polariton peaks). As Ω is increased due to power broadening, the peaks start broadening as well. However as opposed to Figure 6.12b, here the broadened peak widths are narrower. Thus microwave photon injection into the microwave cavity can done on resonance for large Ω. Another main difference that can be noted to be different from the previous conversion efficiency definition is that when κ_μ is too large or too small the maximum conversion efficiency is decreases. There exists a midpoint at which conversion efficiency is maximized. This is due to the fact that when κ_μ is too large, or when the

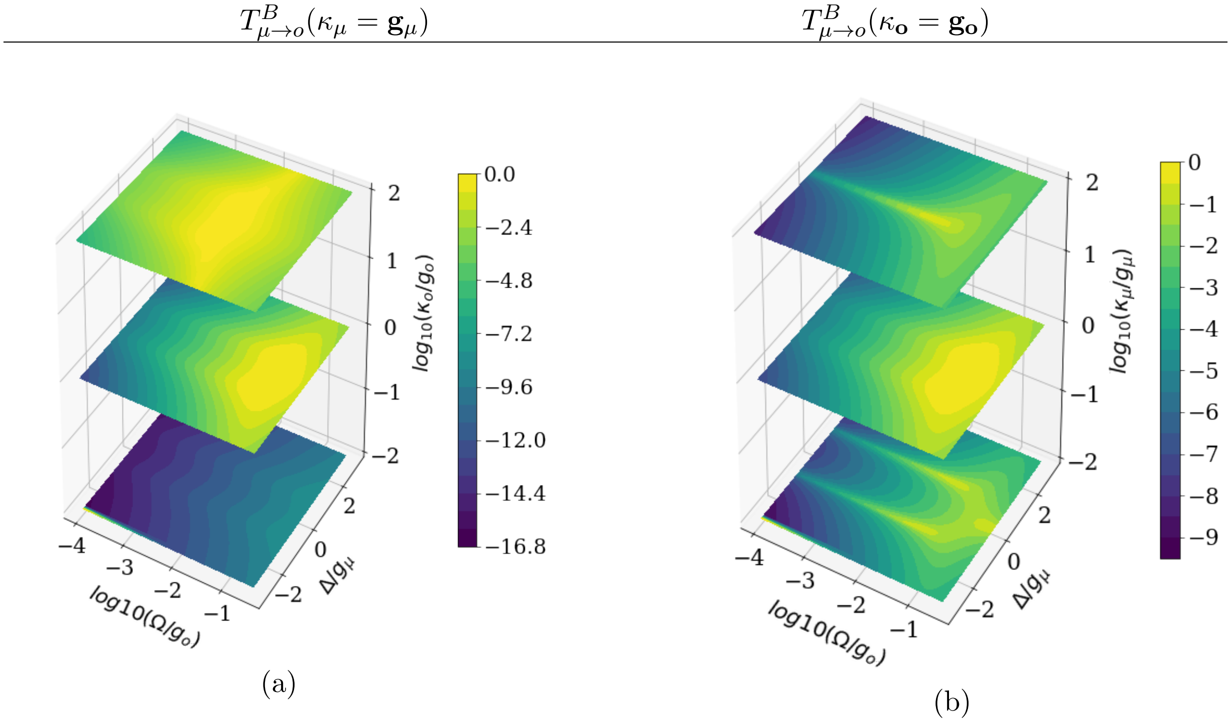

(a)

(b)

Figure 7.2: Conversion efficiency ($\log_{10}$ scale) for a constant $\kappa_\mu = g_\mu$ (a) and $\kappa_o = g_o$ (b) sweeping through three different values of κ_o and κ_μ respectively, for $g_o = 100\Gamma_e$ and $g_\mu = 100\Gamma_s$ (where $\Gamma_e = 2\pi \times 13.3$MHz and $\Gamma_s = 2\pi \times 21.2$Hz and $\Delta = \Delta_s = \Delta_e = \Delta_o = \Delta_\mu$). a) The conversion efficiency for a fixed κ_μ sweeping through three different values of κ_o. As can be observed, as κ_o is increased, the Ω required to achieve maximum conversion efficiency decreases. b)The conversion efficiency for a fixed κ_o sweeping through three different values of κ_μ. For small κ_μ, maximum conversion efficiency occurs at detunings, $\Delta/g_\mu = \pm 1$ (polariton peaks), whereas as κ_μ is increased, maximum conversion efficiency takes place at detunings, $\Delta/g_\mu = 0$, or when the system is on resonance.

cavity is leaky, more and more microwave photons leave the cavity before being coupled to the NV center. However for too small of a κ_μ, when the cavity is strong, it becomes harder to inject microwave photons into the cavity. Thus there exists an ideal value of the microwave cavity decay rate that would allow for maximal injection of microwave photons whilst decreasing photon leakage from the cavity.

In order to understand the conversion efficiency dependence on the parameters κ_o, κ_μ and Ω, we sweep over the the three parameters and plot the maximum conversion efficiency for each pair of κ_o and κ_μ, and the corresponding Rabi drive rate, Ω, required to achieve the maximum conversion (Fig. 7.3) with the system on resonance ($\Delta_s = \Delta_e = \Delta_o = \Delta_\mu = 0$).

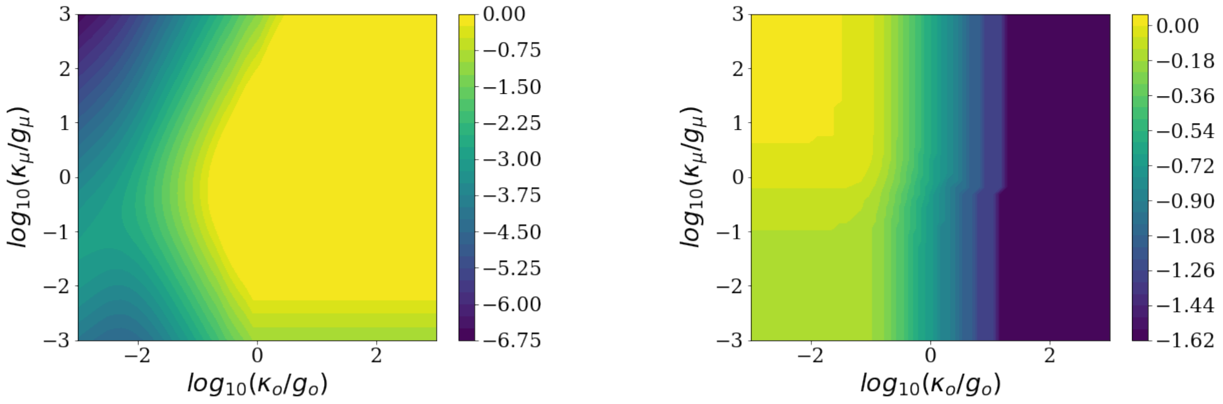
Maximum $T^B_{\mu\to o}$

Ω/g_o for Maximum $T^B_{\mu\to o}$

(a) (b)

Figure 7.3: a) Maximum conversion efficiency ($\log_{10}$ scale) and the corresponding b)Ω to achieve maximum efficiency with $g_o = 100\Gamma_e$ and $g_\mu = 100\Gamma_s$, for a system on resonance ($\Delta_s = \Delta_e = \Delta_o = \Delta_\mu = 0$).

As can be noted from the plots in Figure 7.3, as the optical cavity decay rate κ_o is increased the conversion efficiency of the system increases, whilst the required Ω for maximum conversion decreases. This is in agreement with what was observed in Figure 7.2a and in the previous conversion efficiency definition (Figure 6.15), wherein with a larger κ_o more photons that are in the $|g,1,0\rangle$ are able to leave the cavity before being coupled back into the emitter.

However we notice as opposed to the trend we noticed with $T^A_{\mu\to o}$ in the previous chapter, for κ_μ that is too large or too small, the conversion efficiency starts decreasing. This is in agreement with what was observed in Figure 7.2b, wherein with increased increased κ_μ the injected microwave photons in the state $|g,1,0\rangle$ decay out of the cavity before it can be coupled to the emitter for the conversion to take place, however if the κ_μ is too small the it becomes harder to inject microwave photons into the cavity.

Large Optical Mode Volume Regime: $g_o << \Gamma_e$

We perform a similar analysis as before for the system with the cavity coupling rates $g_0 = 0.01\Gamma_e$ and $g_\mu = 100\Gamma_s$ (where $\Gamma_e = 2\pi\times 13.3$MHz and $\Gamma_s = 2\pi\times 21.2$Hz), for constant cavity decay rates $\kappa_\mu = g_\mu$ and $\kappa_o = g_o$, whilst sweeping over the the Rabi coupling rate, Ω, and detunings, Δ $(= \Delta_s = \Delta_e = \Delta_o = \Delta_\mu =)$, and κ_o and κ_μ respectively (see Figure 7.4).

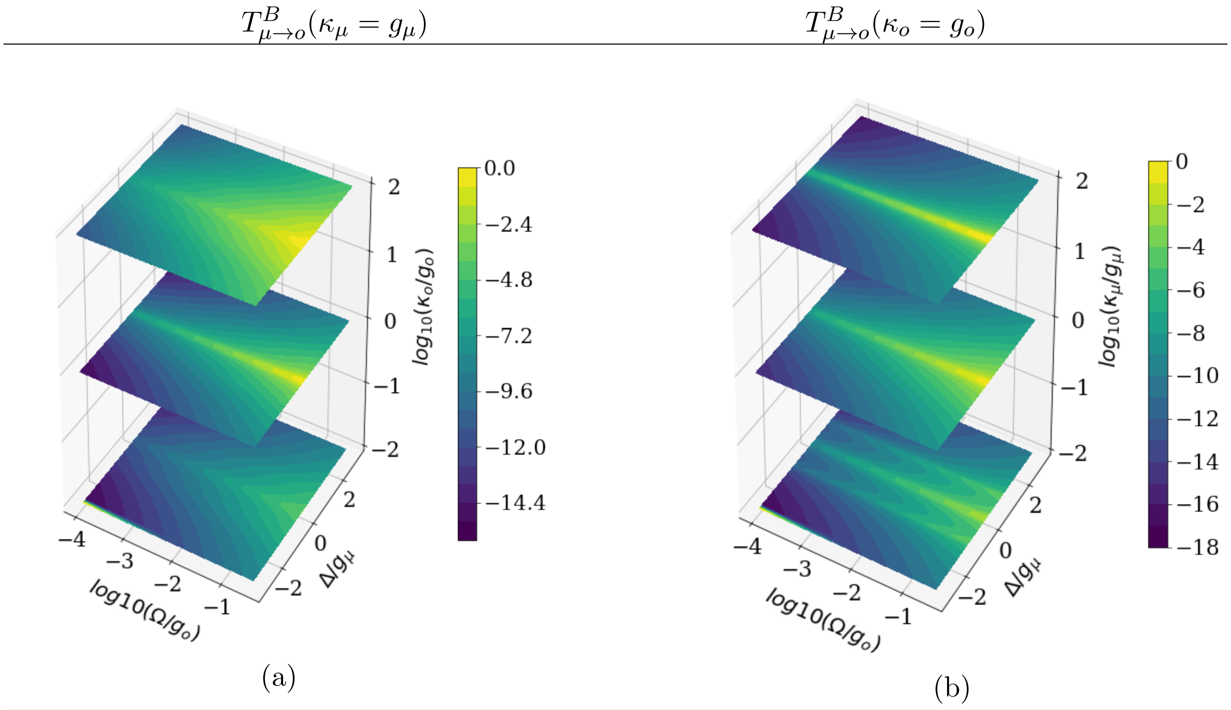
$T^B_{\mu\to o}(\kappa_\mu = g_\mu)$ $T^B_{\mu\to o}(\kappa_o = g_o)$

(a) (b)

Figure 7.4: Conversion efficiency ($\log_{10}$ scale) for a constant $\kappa_\mu = g_\mu$ and $\kappa_o = g_o$ sweeping through three different values of κ_o and κ_μ respectively, for $g_o = 0.01\Gamma_e$ and $g_\mu = 100\Gamma_s$ (where $\Gamma_e = 2\pi \times 13.3$MHz, $\Gamma_s = 2\pi \times 21.2$Hz and $\Delta = \Delta_s = \Delta_e = \Delta_o = \Delta_\mu$). a) The conversion efficiency for a fixed κ_μ sweeping through three different values of κ_o. b) The conversion efficiency for a fixed κ_o sweeping through three different values of κ_μ. With a weak optical cavity maximum conversion efficiency occurs mainly on resonance $(\Delta/g_\mu = 0)$ but as κ_μ decreases, additional peaks corresponding to the polariton peaks start appearing at $\Delta/g_\mu = \pm 1$ (polariton peaks).

From Figure 7.4a for a constant κ_μ, the conversion efficiency increases with increasing κ_o similar to the trend noted earlier in the previous case (see Figure 7.4a). However due to the lower optical coupling strength, the detuning bandwidth over which maximum conversion occurs is also is much narrower and occurs mainly at resonance $\Delta/g_\mu = 0$. From Figure 7.4b as seen before as κ_μ decreases the polariton peaks that are characteristic of a strong cavity start appearing. However as the value of κ_μ is increased the polariton peaks characteristic of a strong cavity start decreasing and maximum conversion efficiency occurs on resonance. We note once again a similar trend that we observed previously in Figure 7.4b where for too large or too small of a κ_μ, the maximum conversion efficiency starts decreasing.

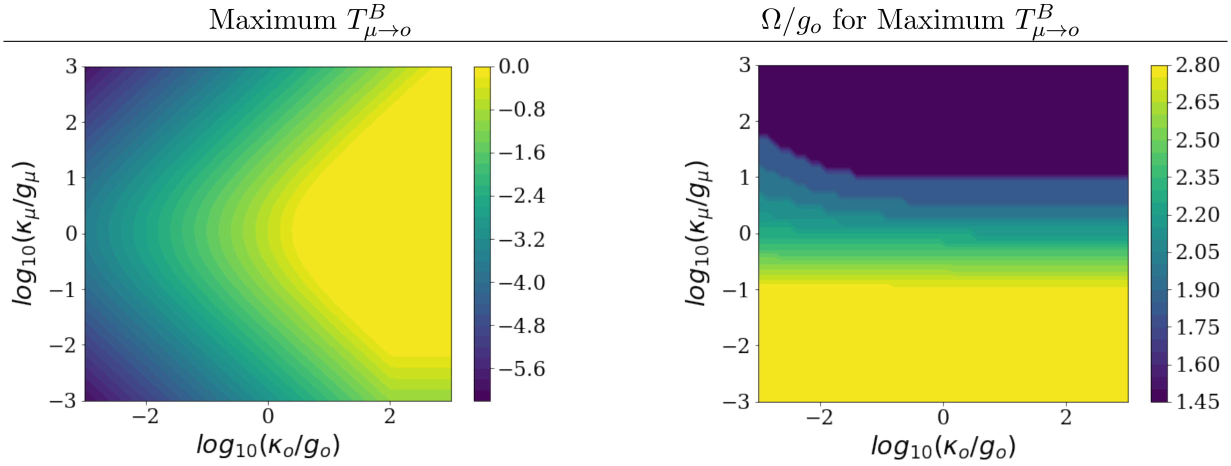

(a) (b)

Figure 7.5: a) Maximum conversion efficiency ($\log_{10}$ scale) and the corresponding b) Ω to achieve maximum efficiency with $g_o = 0.01\Gamma_e$ and $g_\mu = 100\Gamma_s$, for a system on resonance ($\Delta_s = \Delta_e = \Delta_o = \Delta_\mu = 0$).

We perform a similar simulation as before and sweep over the values of κ_o, κ_μ and Ω, and plot the maximum conversion efficiency for each pair of κ_o and κ_μ, and the corresponding Rabi drive rate, Ω, required to achieve the maximum conversion (Fig. 7.3) with the system on resonance ($\Delta_s = \Delta_e = \Delta_o = \Delta_\mu = 0$). As before with increasing κ_o, the conversion efficiency increases as more optical photons can leave the cavity before being coupled back to the system. However as compared with Figure 7.3, the required κ_o before which unit conversion efficiency occurs is increased by an order of magnitude. Furthermore as observed earlier in Figure 7.3, with increasing κ_μ, although more microwave photons can be injected into the cavity, there is a higher probability of microwave photons can leave the cavity before it can be picked up for conversion. On the other hand as with decreasing κ_μ, as the microwave cavity becomes stronger, its becomes harder to inject microwave photons in to the cavity.

7.2 Monte-Carlo Simulations

7.2.1 Continous Drive

To understand the effects of higher manifolds in the system, we once again perform Monte-Carlo simulations to analyse the Hamiltonian as we did in Section 6.6.1. We employ Monte-Carlo Solver from the Python package, QuTIP [107, 108] to perform the simulations. The non-Hermitian Hamiltonian describing the dynamics of the system in the rotating frame is described by Equation 6.50 together with the collapse operators in Equation 6.51. We define the conversion efficiency together with the output operators, $a_{out} = \sqrt{\kappa_o} a$ as:

$$T^B_{\mu \to o} = \frac{\int \langle a^\dagger_{out} a_{out} \rangle dt}{\int |\varepsilon|^2 dt} \tag{7.2}$$

in the limit $|\varepsilon|^2 \to 0$. The term $\langle a^\dagger_{out} a_{out} \rangle$ is the rate at which optical photons decay out of the optical cavity. Thus the integral in the numerator denotes the total optical photons exiting the optical cavity. The term $|\varepsilon|^2$ is the rate at which microwave photons are incident on the microwave cavity due to the classical drive. Thus the integral in the denominator describes total microwave photons incident on the microwave cavity. The system is initialized in $\psi(0) = |g, 0, 0\rangle$ with the NV center in the ground state with no photons in both the optical and microwave cavities respectively. Once again we take into account the decay through the phonon sideband emission as we did in the previous chapter by modelling the NV center as a pseudo-three level system with the virtual state $|g'\rangle$. The Python codes for this simulation are included in Appendix E.

Small Optical Mode Volume Regime: $g_o >> \Gamma_e$

We simulate the system with the cavity coupling rates $g_0 = 100\Gamma_e$ and $g_\mu = 100\Gamma_s$ (where $\Gamma_e = 2\pi \times 13.3\text{MHz}$ and $\Gamma_s = 2\pi \times 21.2\text{Hz}$), with the system on resonance ($\Delta_s = \Delta_e = \Delta_o = \Delta_\mu = 0$) by sweeping over the optical and microwave cavity decays rates, κ_o and κ_μ, and the Rabi driving rate, Ω. The maximum conversion efficiency for each pair of κ_o and κ_μ, and the corresponding Rabi drive rate, Ω, required to achieve the maximum conversion is plotted.

Firstly, as was before in the previous chapter, we note from Figure 7.6, when higher manifolds of the system is included there exists a upper bound on the optical cavity decay rate κ_o, as opposed to the analytical approximation of the conversion efficiency of the

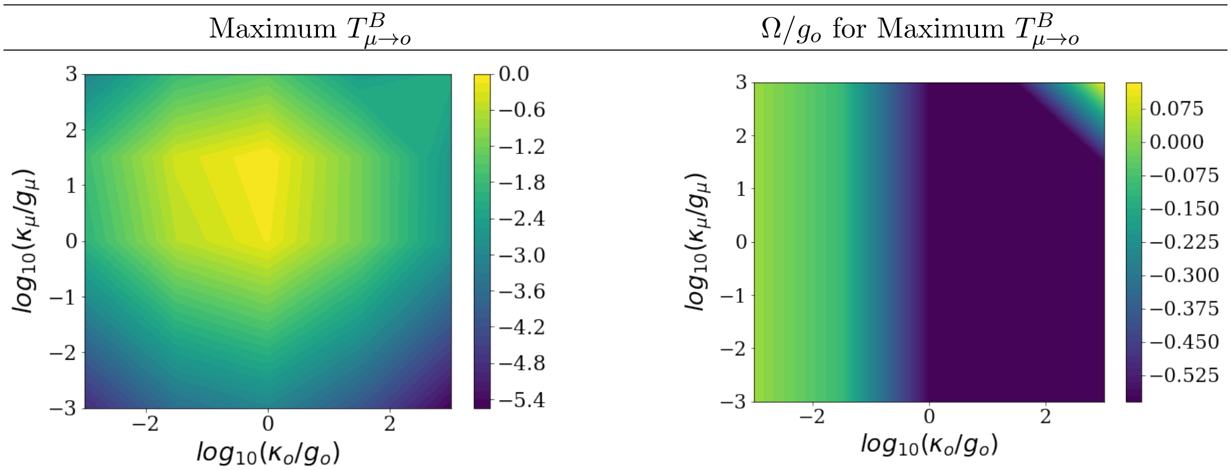

(a) (b)

Figure 7.6: a) Maximum conversion efficiency ($\log_{10}$ scale) and the corresponding b) Ω to achieve maximum conversion efficiency for the system with $g_\mu = 100\Gamma_s$ and $g_o = 100\Gamma_e$ (where $\Gamma_e = 2\pi \times 13.3$MHz, $\Gamma_s = 2\pi \times 21.2$Hz). The system is initialized with the Λ system in the ground state with no photons in the microwave and optical cavities ($\psi(0) = |g, 0, 0\rangle$).

first photon seen in Figure 7.3. Unit conversion efficiency occurs for a an optical cavity decay rate of $\kappa_o \sim 10^{-1}g_o - g_o$. This is the similar range over which we observed maximum conversion in the $T^A_{\mu\to o}$ in Figure 6.18. Across the microwave cavity decay rates, we observe a maximum unit conversion efficiency for $\kappa_\mu \sim g_\mu - 10g_\mu$. These ranges correspond to an optical cavity quality factor of $Q_o \sim 10^6 - 10^7$ and microwave cavity quality factor $Q_\mu \sim 10^2 - 10^4$. We can also note that to achieve maximum conversion efficiency we require the Rabi drive rate, Ω, to be $\sim g_o$.

Large Optical Mode Volume Regime: $g_o << \Gamma_e$

We simulate the system with the cavity coupling rates $g_0 = 0.01\Gamma_e$ and $g_\mu = 100\Gamma_s$ (where $\Gamma_e = 2\pi \times 13.3$MHz and $\Gamma_s = 2\pi \times 21.2$Hz), with the system on resonance ($\Delta_s = \Delta_e = \Delta_o = \Delta_\mu = 0$) by sweeping over the optical and microwave cavity decays rates, κ_o and κ_μ, and the Rabi driving rate, Ω. The maximum conversion efficiency for each pair of κ_o and κ_μ, and the corresponding Rabi drive rate, Ω, required to achieve the maximum conversion is plotted.

In the large optical mode volume regime we observe that the maximum conversion

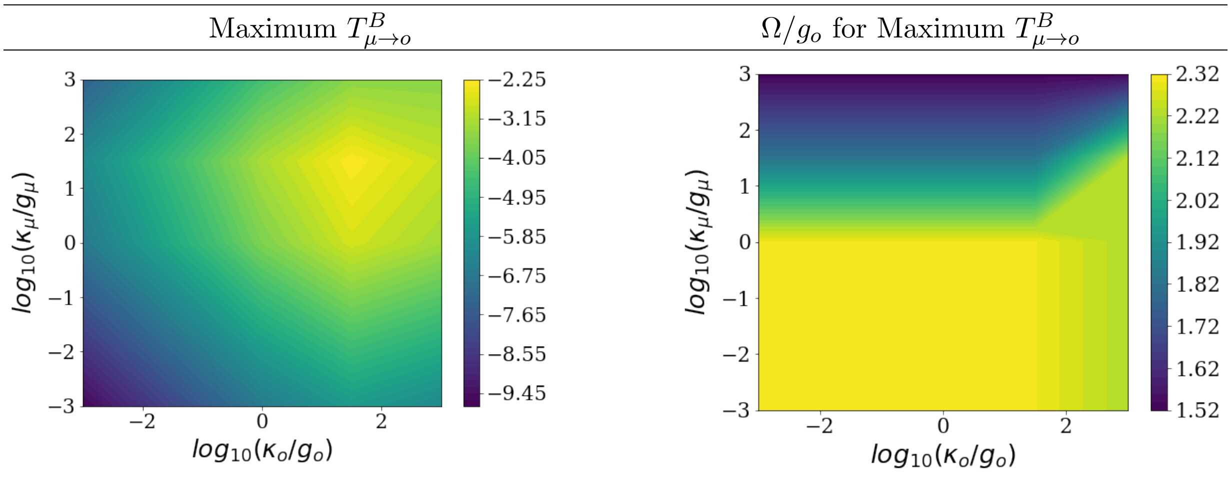

(a) (b)

Figure 7.7: a) Maximum conversion efficiency ($\log_{10}$ scale) and the corresponding b) Ω to achieve maximum conversion efficiency for the system with $g_\mu = 100\Gamma_s$ and $g_o = 0.01\Gamma_e$ (where $\Gamma_e = 2\pi \times 13.3$MHz, $\Gamma_s = 2\pi \times 21.2$Hz). The system is initialized with the Λ system in the ground state with no photons in the microwave and optical cavities ($\psi(0) = |g, 0, 0\rangle$).

efficiency is 2 orders of magnitude lower than in the small optical mode volume regime observed in Figure 7.6. This can be understood by recalling the performance of the intrinsic conversion efficiency $T^A_{\mu\to o}$ from the previous chapter, when moving from the small optical cavity mode volume to the small optical cavity mode volume in Figures 6.18 and 6.19. We observed that in the large optical mode volume regime, the maximum conversion efficiency was shifted lower along the κ_μ axis by an order of magnitude. This was because in the large optical mode volume regime a stronger microwave cavity is required to achieve unit maximum conversion. However with Figure 7.7, we note that a stronger microwave cavity would mean that it becomes harder to inject photons into the cavity. Thus the maximum conversion efficiency is reduced by two orders of magnitude. Maximum conversion efficiency occurs for a an optical cavity decay range of $\kappa_o \sim 10^1 g_o - 10^2 g_o$. This is the similar range over which we observed maximum conversion in the $T^A_{\mu\to o}$ in Figure 6.19. Furthermore maximum conversion occurs across a microwave cavity decay range of $\kappa_\mu \sim 10 g_\mu - 10^2 g_\mu$. This corresponds to an optical cavity quality factor of $Q_o \sim 10^8 - 10^9$ and microwave cavity quality factor, $Q_\mu \sim 10^2 - 10^3$. We understand that when using the conversion efficiency definition $T^B_{\mu\to o}$, we require that both the optical and microwave cavities be strongly coupled to achieve unit conversion efficiency. We can also note that the Rabi drive rate, Ω, follows a similar trend as we noted in the analytical approximations. The required Ω to achieve maximum conversion is $\sim 10^{1.8} g_o$.

7.2.2 Single Photon

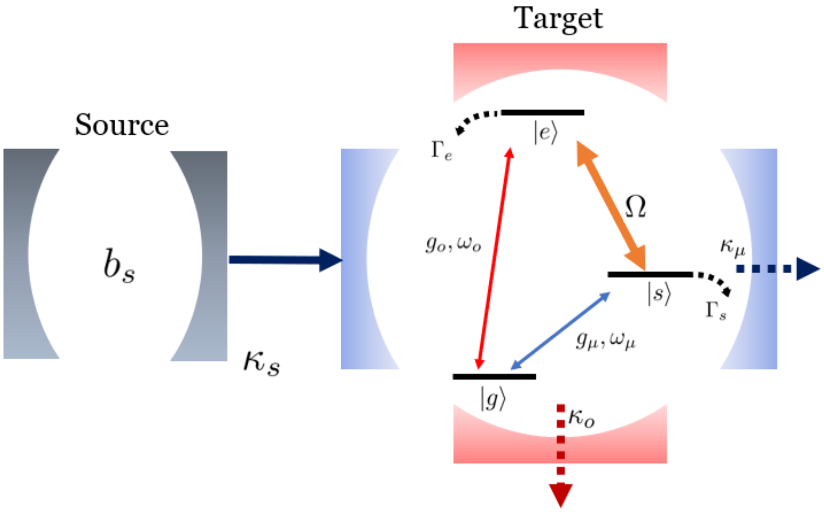

Figure 7.8: Schematics of the model of a cascaded cavity system consisting of a three level closed Λ coupled to an optical and microwave cavity. The source cavity has a decay rate of κ_s which is inversely proportional to the pulse width of the source microwave field. In the target system, the $|g\rangle \leftrightarrow |s\rangle$ transition is coupled to the microwave cavity (g_μ,κ_μ), and the $|s\rangle \leftrightarrow |e\rangle$ transition is coupled to the optical cavity (g_o,κ_o). The levels $|s\rangle$ and $|e\rangle$ are coupled with a classical field with a frequency of ω_Ω and a driving rate Ω. The target microwave cavity is driven by a microwave pulse from the source cavity.

To simulate the conversion efficiency of a single microwave photon incident on the microwave cavity, we make use of a cascaded quantum system as shown in Fig. 7.8 [114, 120]. The source cavity produces a well defined microwave pulse which is incident onto the target microwave cavity. The source cavity here is modelled as a single-sided microwave cavity that has a decay rate of κ_s. The target system is similar to the initial model of the system which consists of a microwave cavity and an optical cavity coupled to the Λ system in an NV center. Following from Equation 6.29, the Hamiltonian of the system is described by:

$$H = H_o + H_{int} + H_{source} \tag{7.3}$$

with

$$H_o/\hbar = \omega_s \left|s\right\rangle \left\langle s\right| + \omega_e \left|e\right\rangle \left\langle e\right| + \omega_o a^\dagger a + \omega_\mu b^\dagger b, \tag{7.4a}$$

$$\begin{aligned} H_{int}/\hbar =& g_\mu(b \left|s\right\rangle \left\langle g\right| + b^\dagger \left|g\right\rangle \left\langle s\right|) + g_o(a \left|e\right\rangle \left\langle g\right| + a^\dagger \left|g\right\rangle \left\langle e\right|) \\ &+ (\Omega e^{-i\omega_\Omega t} \left|e\right\rangle \left\langle s\right| + \Omega^* e^{i\omega_\Omega t} \left|s\right\rangle \left\langle e\right|), \end{aligned} \tag{7.4b}$$

$$H_{source} = \omega_\mu b_s^\dagger b_s \tag{7.4c}$$

where a, b and b_s are annihilation operators of optical, microwave, and the source cavity, respectively. The output modes of the optical and microwave cavity are represented with the input-output formalism [121]. The two output modes for the optical and microwave photons (a and b respectively) are given by:

$$a_{out} = \sqrt{\kappa_o} a \tag{7.5}$$

$$b_{out} = \sqrt{\kappa_\mu} b + \sqrt{\kappa_s} b_s \tag{7.6}$$

In the rotating frame of a time dependant unitary U :

$$U = \exp{(-it)}[\omega_\Omega(\left|e\right\rangle \left\langle e\right| + a^\dagger a)] \tag{7.7}$$

the Hamiltonian is transformed according to:

$$\mathcal{H} = U^\dagger H U + i\frac{dU^\dagger}{dt} U = \mathcal{H}_o + \mathcal{H}_{int} + \mathcal{H}_{source} \tag{7.8}$$

with

$$\mathcal{H}_o/\hbar = \omega_s \left|s\right\rangle \left\langle s\right| + (\omega_e - \omega_\Omega) \left|e\right\rangle \left\langle e\right| + (\omega_a - \omega_\Omega) a^\dagger a + \omega_b b^\dagger b, \tag{7.9a}$$

$$\begin{aligned} \mathcal{H}_{int}/\hbar =& g_\mu(b \left|s\right\rangle \left\langle g\right| + b^\dagger \left|g\right\rangle \left\langle s\right|) + g_o(a \left|e\right\rangle \left\langle g\right| + a^\dagger \left|g\right\rangle \left\langle e\right|) \\ &+ (\Omega \left|e\right\rangle \left\langle s\right| + \Omega^* \left|s\right\rangle \left\langle e\right|), \end{aligned} \tag{7.9b}$$

$$\mathcal{H}_{source}/\hbar = \omega_{\mu} b_s^{\dagger} b_s \tag{7.9c}$$

Using the quantum trajectory simulations [120], the time evolution of the system is described by the Schrodinger equation:

$$i\hbar \frac{d}{dt} |\psi(t)\rangle = \mathcal{H} |\psi(t)\rangle \tag{7.10}$$

Once again we take into the account the phonon sideband decay from the excited state in the target cavity by setting up a pseudo-three level system with a virtual state $|g'\rangle$ as seen in Figure6.9. The non-Hermitian Hamiltonian, H, is given by:

$$\mathcal{H} = \mathcal{H}_o + \mathcal{H}_{int} + \mathcal{H}_{source} - \frac{i\hbar}{2} \sum_k \hat{C_k}^{\dagger} \hat{C}_k \tag{7.11}$$

with collapse operators $\hat{C}_k$ defined as:

$$\hat{C}_1 = a_{out} = \sqrt{\kappa_o} a, \tag{7.12a}$$

$$\hat{C}_2 = b_{out} = \sqrt{\kappa_{\mu}} b + \sqrt{\kappa_s} b_s, \tag{7.12b}$$

$$\hat{C}_3 = \sqrt{\Gamma_{ZPL}} |g\rangle \langle e|, \tag{7.12c}$$

$$\hat{C}_4 = \sqrt{\Gamma_{PSB}} |g'\rangle \langle e|, \tag{7.12d}$$

$$\hat{C}_5 = \sqrt{\Gamma_p} |g\rangle \langle g'|, \tag{7.12e}$$

$$\hat{C}_6 = \sqrt{\Gamma_s} |g\rangle \langle s|, \tag{7.12f}$$

$$\hat{C}_7 = \sqrt{\Gamma_{es}} |s\rangle \langle e|, \tag{7.12g}$$

$$\hat{C}_8 = \sqrt{\gamma_e} |e\rangle \langle e|, \tag{7.12h}$$

$$\hat{C}_9 = \sqrt{\gamma_s} |s\rangle \langle s| \tag{7.12i}$$

where κ_o (κ_{μ}) is the optical (microwave) cavity decay rate, Γ_s is the population decay rate of the $|s\rangle$ state in the Λ system, γ_e (γ_s) is models additional coherence decays rate of $|e\rangle$ ($|s\rangle$) state, Γ_{ZPL} is the ZPL decay rate, Γ_{PSB} is the phonon sideband decay rate, Γ_{es} is the decay rate from $|s\rangle$ to $|g\rangle$, $|s\rangle$ to the Γp is the decay rate from shelving state $|g'\rangle$ to $|g\rangle$. The operator $\hat{C}_1$ ($\hat{C}_2$) is the optical (microwave) photon decay, $\hat{C}_3$ describes the population decay from the excited state $|e\rangle$ to the ground state $|g\rangle$, $\hat{C}_4$ describes the PSB decay from the excited state $|e\rangle$ to the virtual state $|g'\rangle$, $\hat{C}_5$ describes the population decay from the virtual state $|g'\rangle$ to the ground state $|g\rangle$ through phonon decay, $\hat{C}_6$ describes the population decay from the metastable state $|s\rangle$ to the ground state $|g\rangle$, $\hat{C}_7$ describes the population decay from $|e\rangle$ to $|s\rangle$, and $\hat{C}_8$ ($\hat{C}_9$) describes the additional coherence decay of the state $|e\rangle$ ($|s\rangle$) denoted in Equation 6.38.

The Hamiltonian terms in the rotating frame $\mathcal{H}_o$, $\mathcal{H}_{int}$, and $\mathcal{H}_{drive}$ are defined in Equation 6.34. The Hilbert space of the system has a dimension of $4+N+N+N$ corresponding to the pseudo-three level emitter, the target two cavity modes, and the source cavity modes respectively. As before, the Hilbert space for each cavity mode was truncated at $N = 7$, as for any manifold level $N < 7$ the maximum conversion efficiency saturated at values that were less than one for any system configuration used. The system is initialized with the Λ system in the ground state, with zero photons in both the target microwave and optical cavities, and with one photon in the source cavity ($\psi(0) = |g, 0, 0, 1\rangle$).

$$T^B_{\mu\rightarrow o} = \int \langle a^\dagger_{out} a_{out}\rangle dt \tag{7.13}$$

The term $\langle a^\dagger_{out} a_{out}\rangle$ is the rate at which optical photons decay out of the optical cavity. Thus the integral denotes the total optical photons exiting the optical cavity.

To maximize the conversion efficiency the microwave source cavity decay rate should be matched to the target microwave cavity decay rate, $\kappa_s = \kappa_\mu$. This would mean that the photons enter the microwave cavity at the same rate that they are emitted by the source cavity. Furthermore, as before we would like to explore the case where the system is on resonance with $\omega_e = \omega_o$, $\omega_s = \omega_\mu$, and $\omega_\Omega = \omega_e - \omega_s$.

Small Optical Mode Volume Regime: $g_o >> \Gamma_e$

We simulate the system with the cavity coupling rates $g_0 = 100\Gamma_e$ and $g_\mu = 100\Gamma_s$ (where $\Gamma_e = 2\pi \times 13.3$MHz and $\Gamma_s = 2\pi \times 21.2$Hz), with the system on resonance by sweeping over the optical and microwave cavity decays rates, κ_o and κ_μ, and the Rabi driving rate, Ω. The maximum conversion efficiency for each pair of κ_o and κ_μ, and the corresponding Rabi drive rate, Ω, required to achieve the maximum conversion is plotted.

As can be noted from Figure 7.9, we observe that in the single photon regime we observe the similar trend in the conversion efficiency that we observed previously in the continuous drive system in Figure 7.6. However in the single photon regime, the maximum

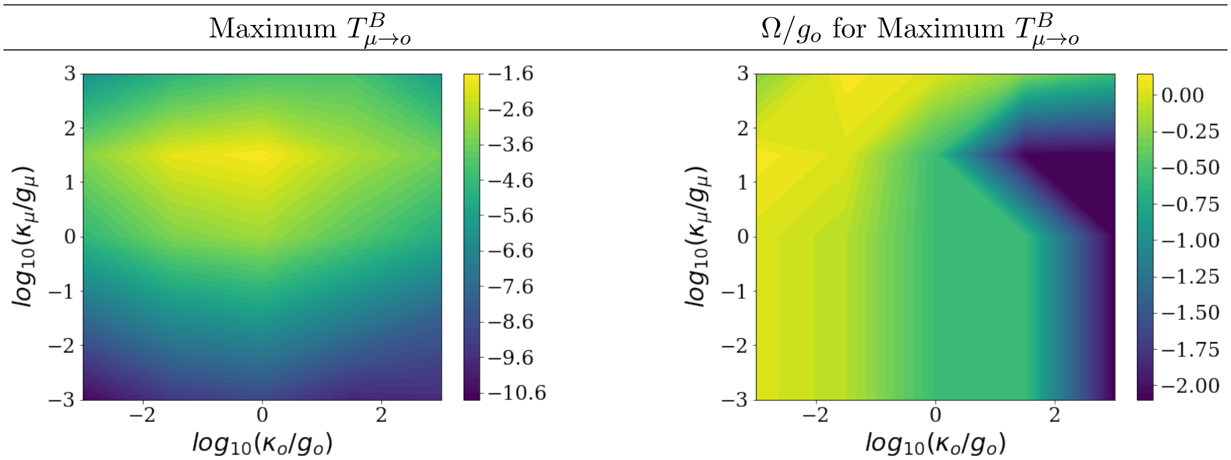

(a) (b)

Figure 7.9: a) Maximum conversion efficiency ($\log_{10}$ scale) and the corresponding b)Ω to achieve maximum efficiency in a cascaded cavity system with $g_\mu = 100\Gamma_s$ and $g_o = 100\Gamma_e$ (where $\Gamma_e = 2\pi \times 13.3$MHz, $\Gamma_s = 2\pi \times 21.2$Hz). The system is initialized with the Λ system in the ground state, with zero photons in both the target microwave and optical cavities, and with one photon in the source cavity ($\psi(0) = |g, 0, 0, 1\rangle$).

achievable conversion efficiency is reduced by 1.6 orders of magnitude. This discrepancy can be understood if we recall the intrinsic conversion efficiency from the previous chapter, $T^A_{\mu\to o}$, and compare the plots between the continuous drive and single photon regimes in Figures 6.18 and 6.20 respectively. We observed that when we moved to the single photon regime, the required κ_μ to allow for unit conversion efficiency was decreased by an order of magnitude. We concluded that in the single photon regime we require the microwave cavity stronger than in the continuous driven system. Bringing our attention back to Figure 7.9, reducing the κ_μ would mean that the rate at which microwave photons enter the cavity would be decreased. Hence the maximum conversion efficiency is decreased compared to the system with a continuous drive. Maximum conversion efficiency occurs for a an optical cavity decay range of $\kappa_o \sim 10^{-1}g_o - g_o$. Across the microwave cavity decay rates, we observe a maximum unit conversion efficiency for $\kappa_\mu \sim 10^1 g_\mu - 10^2 g_\mu$. These ranges correspond to an optical cavity quality factor of $Q_o \sim 10^6 - 10^7$ and microwave cavity quality factor $Q_\mu \sim 10^2 - 10^3$. We also note a similar trend in the required Ω as before in the small optical mode volume regimes. As was the case in continuous drive regime, we note that the required Rabi drive rate for maximum conversion is $\sim g_o$.

Large Optical Mode Volume Regime: $g_o << \Gamma_e$

We simulate the system with the cavity coupling rates $g_0 = 0.01\Gamma_e$ and $g_\mu = 100\Gamma_s$ (where $\Gamma_e = 2\pi \times 13.3\text{MHz}$ and $\Gamma_s = 2\pi \times 21.2\text{Hz}$), with the system on resonance by sweeping over the optical and microwave cavity decays rates, κ_o and κ_μ, and the Rabi driving rate, Ω. The maximum conversion efficiency for each pair of κ_o and κ_μ, and the corresponding Rabi drive rate, Ω, required to achieve the maximum conversion is plotted.

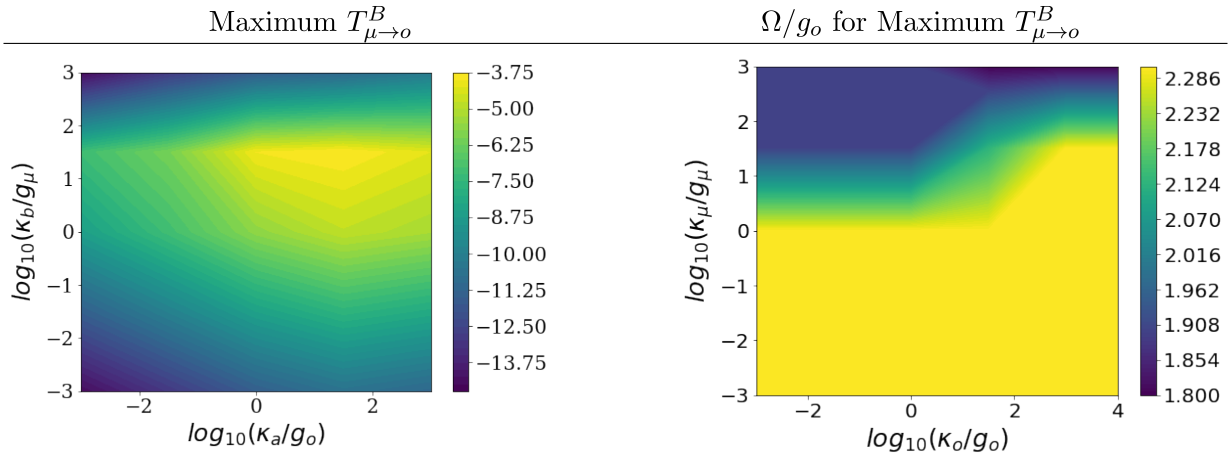
Maximum $T^B_{\mu\to o}$

Ω/g_o for Maximum $T^B_{\mu\to o}$

(a) (b)

Figure 7.10: a) Maximum conversion efficiency ($\log_{10}$ scale) and the corresponding b)Ω to achieve maximum efficiency in a cascaded cavity system with $g_\mu = 100\Gamma_s$ and $g_o = 0.01\Gamma_e$ (where $\Gamma_e = 2\pi \times 13.3\text{MHz}$, $\Gamma_s = 2\pi \times 21.2\text{Hz}$). The system is initialized with the Λ system in the ground state, with zero photons in both the target microwave and optical cavities, and with one photon in the source cavity ($\psi(0) = |g, 0, 0, 1\rangle$).

In the large optical mode volume regime, we note from Figure 7.9 that the maximum achievable conversion efficiency is reduced by $\sim$ 2 orders of magnitude from the small optical mode volume regime. This was similar in what we observed in the continuous drive system in Figures 7.6 and 7.7, wherein when moving from the small optical mode volume regime to the large optical mode volume regime, we observe that there is a drop in the conversion efficiency by approximately two orders of magnitude. In the large optical mode volume regime maximum conversion efficiency occurs for a an optical cavity decay range of $\kappa_o \sim 10g_o - 10^2 g_o$. Across the microwave cavity decay rates, we observe a maximum unit conversion efficiency for $\kappa_\mu \sim 10^1 g_\mu - 10^2 g_\mu$. These ranges correspond to an optical cavity quality factor of $Q_o \sim 10^8 - 10^9$ and microwave cavity quality factor $Q_\mu \sim 10^2 - 10^3$. We also note the Rabi drive rate, Ω, follows a similar trend as was noted in the continuous drive regime.

7.3 Conclusion

7.3.1 System Limitations

In all the analysis we have seen above we note that there are two main limitations with the model that is used above. The first limitation we observe is the fundamental requirement that the microwave cavity have a coupling strength of $g_\mu >> \Gamma_s$. This is due to the nature of the NV center wherein since Γ_s is much smaller than all other transition probabilities, the conversion efficiency, $T^B_{\mu\to o} \to 0$ for $g_\mu << \Gamma_s$. The second limitation that we note with the system is small fraction of the ZPL emission from the excited state ($\Gamma_{ZPL}/\Gamma_e \sim 3\%$). Which means most of the population decay that occurs from the excited state occurs without being coupled directly to the $|e\rangle \to |g\rangle$ transition. This results in fewer optical photons being coupled to the optical cavity thus resulting in a smaller conversion efficiency. Although this ZPL emission can be enhanced in the weakly coupled Purcell regime, as we have seen in the above analysis this regime doesn't result in a large conversion efficiency of the output optical photons when the system is on resonance.

7.3.2 Results Summary

In the above simulations with the constraint that the microwave cavity coupling strength be, $g_\mu = 100\Gamma_s = 2\pi \times 2.12\text{kHz}$, we explored the responses of the system with a strong optical cavity ($g_o = 100\Gamma_e = 2\pi \times 1.33\text{GHz}$) and weak optical cavity ($g_o = 100\Gamma_e = 2\pi \times 133\text{kHz}$). The maximum achievable conversion efficiencies and the required cavity parameters in each regime have been summarized in Table 7.1. We first note that although unit conversion efficiency is achievable with a continuous drive, only a maximum conversion efficiency of only $10^{-1.6}$ is achievable in the single photon system. In addition to that we also observed in both the driven case and the non-driven cases above, in the large optical mode volume regime, the maximum conversion efficiency is ~ 2 orders of magnitude lower than the strong cavity regime.

Starting with the microwave cavity requirements we observe that non zero conversion efficiency is possible in only the small cavity mode volume regime: $g_\mu >> \Gamma_s$. This results in a mode volume requirement of $V_\mu = 10^{-10}(\lambda_b/n)^3$. In the driven case, for a unit conversion

	Max $T^{B}_{\mu\to o}$	**Optical Cavity**	**Microwave Cavity**
	Continuous Drive		
Small Mode Volume ($g_o = 100\Gamma_e$, $g_\mu = 100\Gamma_s$)	10^{0}	$Q_o \sim 10^6 - 10^7$, $V_o = 0.65(\lambda_a/n)^3$	$Q_\mu \sim 10^2 - 10^4$, $V_\mu = 10^{-10}(\lambda_b/n)^3$
Large Mode Volume ($g_o = 0.01\Gamma_e$, $g_\mu = 100\Gamma_s$)	$10^{-2.3}$	$Q_o \sim 10^8 - 10^9$, $V_o = 6.5 \times 10^7(\lambda_a/n)^3$	$Q_\mu \sim 10^2 - 10^3$, $V_\mu = 10^{-10}(\lambda_b/n)^3$
	Single Photon		
Small Mode Volume ($g_o = 100\Gamma_e$, $g_\mu = 100\Gamma_s$)	$10^{-1.6}$	$Q_o \sim 10^6 - 10^7$, $V_o = 0.65(\lambda_a/n)^3$	$Q_\mu \sim 10^2 - 10^3$, $V_\mu = 10^{-10}(\lambda_b/n)^3$
Large Mode Volume ($g_o = 0.01\Gamma_e$, $g_\mu = 100\Gamma_s$)	$10^{-3.8}$	$Q_o \sim 10^8 - 10^9$, $V_o = 6.5 \times 10^7(\lambda_a/n)^3$	$Q_\mu \sim 10^2 - 10^3$, $V_\mu = 10^{-10}(\lambda_b/n)^3$

Table 7.1: Summary of the conversion efficiency, $T^{B}_{\mu\to o}$, and the corresponding optical and microwave cavity parameters for the continuous drive and single photon regimes($\Gamma_e = 2\pi \times 13.3$MHz and $\Gamma_s = 2\pi \times 21.2$Hz).

efficiency, the decay rate of the microwave cavity is required to be $\kappa_\mu \sim g_\mu - 10^2 g_\mu$. This corresponds to a quality factor of $Q_\mu \sim 10^2 - 10^4$. In the single photon regime the we observe a similar requirement in the microwave cavity quality factors, albeit resulting in a lower conversion efficiency.

Now with the optical cavity requirements as we have seen above, non zero conversion efficiency is possible with both the small and large cavity mode volumes. This results in a mode volume requirements of $V_o = 0.65(\lambda_a/n)^3$ and $V_o = 6.5 \times 10^7$ respectively. With $g_o = 100\Gamma_e$, for maximum unit conversion the decay rate of the optical cavity is required to be, $\kappa_o \sim 10^{-1} g_o - g_o$, which corresponds to a quality factor of $Q_o \sim 10^6 - 10^7$. With $g_o = 0.01\Gamma_e$, for maximum conversion efficiency the decay rate of the optical cavity is required to be, $\kappa_o \sim 10 g_o - 10^2 g_o$ corresponding to a quality factor of $Q_o \sim 10^8 - 10^9$. Once again we see a similar trend that we noted in the previous chapter wherein that in order to achieve maximum conversion efficiency in each of the regimes listed in Table 7.1, the optical cavity is required to have a strong temporal confinement whilst the microwave cavity is required to have a strong spatial confinement.

7.3.3 Design Considerations

For optical cavities, there are several potential platforms that can be explored. These include fiber based cavities [116], whispering gallery resonators [122], H0 photonic crystal cavities [123] and cross beam cavities [124, 125], the quality factors and mode volumes of which have been summarized in Table 7.3. As seen in Table 7.3, although the fiber based microcavity fulfills the requirements for efficient inter-photon conversion, integration of a fiber based cavity with a microwave cavity might prove to be difficult. For the purpose of photon conversion, the cross beam cavities would be especially interesting platform to explore due to the availability for the spatial separation of the optical photons from the optical cavity and the optical Rabi drive. Cross-beam photonic crystal cavities are a variation of the photonic crystal nano-beam cavities wherein two orthogonal nano-beams, each with a different photonic bandgap, intersect [125]. These cross beam photonic crystal have been demonstrated to reach Q-factors of up to 10^6. In Reference [49], a variation of a cross beam cavity was demonstrated with a nano-diamond containing an NV center positioned in the intersection of the cross-beams. In the cavity design presented in Refernce [49], a waveguide orthogonal to the photonic crystal cavity was used for above resonant excitation of NV center while the cavity was used to couple the fluorescence from the NV center with a demonstrated quality factor of $\sim 10^3$. In a similar fashion the cross-beam photonic rystal cavity can be used in the frequency conversion design wherein the orthongal waveguide can be used for the Rabi drive Ω, while the optical photons are coupled to the cavity. With the ongoing research improvements can be made to improve the Q-factors of these cross beam cavities by two orders of magnitude [49] to the demonstrated design. Furthermore several experiments in recent times have shown the coupling of single NV centers to optical cavities [126, 127, 116] which is a promising step forward in implementing single NV centers for use in microwave to optical domain conversion.

However when coupling single NV centers to microwave cavities the requirements are little bit more restrictive due to the tighter mode volume requirements for strong coupling. This is due to the small dipole moment in NV center between the $|g\rangle$ and $|s\rangle$ states, and the large coupling strength requirement identified in the analysis. In the past few years there have been several demonstrations showing the coupling of high-Q and low mode volume Coplanar Waveguide (CPW) resonators to spin ensembles NV centers in diamonds [129, 130, 131, 132] reaching Q-factors of up to $Q \sim 10^6$ with ensemble with mode volumes reaching as low as of $V \sim 10^{-6}(\lambda/n)^3$. In an ensemble of N emitters, the coupling strength scales as $\sqrt{N}$ permitting the system to achieve strong coupling regimes [130] thus coupling strength between ensemble NV centers and microwave cavities can be increased by increasing the density of NV centers. However considerable experimental

Cavity Type	**Quality Factor**	**Mode Volume**
Crossbeam Photonic Crystal	$Q \sim 1.9 \times 10^4$ [124, 125]	$V = 0.25(\lambda/n)^3$ [124, 125]
Photonic Crystal Nanobeams	$Q \sim 13 \times 10^3$ [88]	$V = 3.7(\lambda/n)^3$ [88]
Toroid Microcavity	$Q \sim 4 \times 10^8$ [128]	$V = 1.6 \times 10^2(\lambda/n)^3$ [128]
H0 Photonic Crystal Cavity	$Q \sim 6 \times 10^3$ [126]	$V = 0.74(\lambda/n)^3$[126]
Whispering Gallery Microresonator	$Q \sim 10^9$ [122]	$V = 0.65(\lambda/n)^3$ [122]
Fiber Based Microcavity	$Q \sim 10^9$ [116]	$V = 2.4(\lambda/n)^3$ [116]

Table 7.2: Summary of optical cavity parameters from literature.

Cavity Type	**Quality Factor**	**Mode Volume**
Crossbeam Photonic Crystal	$Q \sim 1.9 \times 10^4$	$V = 0.25(\lambda/n)^3$
Photonic Crystal Nanobeams	$Q \sim 13 \times 10^3$	$V = 3.7(\lambda/n)^3$
H0 Photonic Crystal Cavity	$Q \sim 6 \times 10^3$	$V = 0.74(\lambda/n)^3$
Whispering Gallery Microresonator	$Q \sim 10^9$	$V = 0.65(\lambda/n)^3$
Fiber Based Microcavity	$Q \sim 10^9$	$V = 2.4(\lambda/n)^3$

Table 7.3: Summary of optical cavity parameters from literature.

progress still need to be done in the coupling of CPW resonators to single NV centers [133] as the demonstrated coupling of single NV centers to microwave cavities have been in the weak coupling regime with coupling strength of $g \sim 65$Hz which is well below the required coupling strength. However Reference [134] provides a proposal of using a hybrid spin-electromechanical resonator wherein the coupling between a single NV center and the CPW cavity is achieved through phonon mediated coupling resulting in cavity Q-factors of $Q \sim 10^6$ and an effective coupling strength of $g \sim 2\pi \times 10$kHz. Furthermore in the approach presented in Reference [134], the diamond is only required to be placed above the CPW without the requirement to be integrated with the coupling capacitor, thus alleviating some of the system integration concerns.

7.4 Future Work

From this point on this work opens up several avenues which can be further investigated. One of the first approaches that can be explored would be to incorporate the use of phonon assisted microwave cavity coupling, discussed in Reference [76], into the Hamiltonian used in this study to understand how the conversion efficiency compares to the work investigated here. To do this, improvements need to be made to the NV center model presented here. For our purpose we assumed one vibrational state $|g'\rangle$ which was at the same energy level as the ground state $|g\rangle$. However in an NV center there are multiple vibrational states, in the vibronic band, each at a different energy level above the ground state $|g\rangle$ which decay to the ground state with different phonon decay rates. This subtle difference will become much more important when working with phonon assisted coupling. Secondly, more research should be done into designing microwave cavities that are able to achieve small mode volumes, as this is a primary requirement for efficient conversion between the microwave and optical regimes. Furthermore, as the NV centers offer also provide other level schemes, such as a 4 level diamond system, the potential of using the 4 level diamond scheme in single NV centers to convert between microwave and optical photons can be explored [135] in a similar manner as presented above. Furthermore, in this work we have looked at a small scope of optimizing over the rich parameter space available to us. One could potentially devise a much more efficient way of optimizing over the several parameters available to identify the required cavity characteristics to maximize conversion between the microwave and optical photons. Finally, another aspect in which progress has to be made is to identifying an efficient way in which the optical and microwave cavities can be integrated together. As the simulations we performed assumed a complete mode overlap between the optical and microwave modes, this would require that optical and microwave cavities to be tightly confined. Some progress should be made via FDTD simulations in devising an efficient way of integrating the optical and microwave cavities to achieve maximum mode overlap between the NV center and the cavities.

Chapter 8

Conclusion

8.1 Directional Control of NV Center Emission

In Part I of this we thesis we saw a study on using an inverse design tool, known as adjoint optimization, to design a 2D subwavelength structure that would be able to control the emission pattern from NV centers embedded in diamonds. In Chapter 3 we looked at how two level quantum emitters can be modelled as a classical electric dipole using the Local Density of state formalism. Since quantum emitters can be modelled as dipoles, we looked at the use of antenna design parameters such as directivity and gain to study the emission pattern from emitters. In Chapter 4 we looked at the theoretical derivation of adjoint optimization as a tool for nanophotonic device design. We observed that by using adjoint optimization over brute force methods the number of required simulations per iteration can be reduced from $N + 1$ simulations to just 2 simulations. In Chapter 5 we looked the use of adjoint optimization for the design of a subwavelength structure that would be able to control the emission profile of the NV centers. The use of adjoint optimization approach also has the added advantage of mode profile shaping which allows for direct coupling NV center emission to a free standing fiber without any additional optical elements. We saw that the adjoint optimization designed structure has a maximum upward directivity of 7.3dB with the upward emission confined within upper half angle of 45^o(NA $= 0.7$). We also saw the confocal microscope setup assembled in the lab to observe fluorescence from NV centers with some preliminary images from the microscope. Unfortunately a lot of the planned work towards an experimental realisation of the designed structure was impossible due to the quarantine measures placed in early 2020 due to the COVID situation.

8.2 Microwave to Optical Transducer

In Part II of the thesis we investigated the potential of using the Λ system in single NV centers coupled to microwave and optical cavities for efficient conversion between the microwave and optical regimes. In Chapter 6 we first started by looking at the proposed model for inter-photon conversion. We then defined the conversion efficiency of the system with two definitions. The intrinsic conversion efficiency of the system was defined as the ratio between the output optical photons and the microwave photons in the microwave cavity. We performed analytical studies with the ground state and first manifold of the system to intuitively understand the steady state performance of the system large and small optical cavity mode volumes. We then performed Monte-Carlo simulations with a continuous drive and in the single photon regimes to observe the required cavity parameters for maximum conversion efficiency (see Table 6.2 for cavity parameters summary). We continued our investigation in Chapter 7 where we explored the extrinsic conversion efficiency. The extrinsic conversion efficiency was defined as the ratio between the output optical photons and the microwave photons incident on the microwave cavity. We performed a similar analysis to the previous chapter to identify the required cavity parameters for maximum conversion efficiency (see Table 7.1 for cavity parameters summary). We first observe that a fundamental requirement for non-zero conversion efficiency, we require the microwave cavity to have small mode volumes. Furthermore, we observe that in both the continuous drive and the single photon system, maximum conversion efficiency is achieved with small optical cavity mode volumes, $g_o >> \Gamma_e$. Although unit extrinsic conversion efficiency ($T^B_{\mu\to o}$) is achievable in the continuous drive system, a maximum conversion efficiency of only $10^{-1.6}$ is achievable in the single photon system. The primary reason for this would be the low fraction of optical emission into the Zero Phonon Line (ZPL). However the method of analysis presented in this thesis can be easily adapted to investigate other potential three level Λ systems. Although there currently exist different optical cavities that satisfy the requirements of the system to achieve maximal conversion efficiency, further research needs to be done in microwave cavity design to satisfy the requirement for strong coupling between individual NV centers and the microwave cavity.

References

[1] Katja Beha, Helmut Fedder, Marco Wolfer, Merle C. Becker, Petr Siyushev, Mohammad Jamali, Anton Batalov, Christopher Hinz, Jakob Hees, Lutz Kirste, Harald Obloh, Etienne Gheeraert, Boris Naydenov, Ingmar Jakobi, Florian Dolde, Sébastien Pezzagna, Daniel Twittchen, Matthew Markham, Daniel Dregely, Harald Giessen, Jan Meijer, Fedor Jelezko, Christoph E. Nebel, Rudolf Bratschitsch, Alfred Leitenstorfer, and Jörg Wrachtrup. Diamond nanophotonics. *Beilstein J. Nanotechnology*, 3:895–908, dec 2012.

[2] C Santori, P E Barclay, K-M C Fu, R G Beausoleil, S Spillane, and M Fisch. Nanophotonics for quantum optics using nitrogen-vacancy centers in diamond. *Nanotechnology*, 21(27):274008, jun 2010.

[3] Christopher G. Yale, F. Joseph Heremans, Brian B. Zhou, Adrian Auer, Guido Burkard, and David D. Awschalom. Optical manipulation of the berry phase in a solid-state spin qubit. *Nature Photonics*, 10(3):184–189, feb 2016.

[4] Charles Santori, Philippe Tamarat, Philipp Neumann, Jörg Wrachtrup, David Fattal, Raymond G. Beausoleil, James Rabeau, Paolo Olivero, Andrew D. Greentree, Steven Prawer, Fedor Jelezko, and Philip Hemmer. Coherent population trapping of single spins in diamond under optical excitation. *Physical Review Letters*, 97(24), dec 2006.

[5] R. W. Andrews, R. W. Peterson, T. P. Purdy, K. Cicak, R. W. Simmonds, C. A. Regal, and K. W. Lehnert. Bidirectional and efficient conversion between microwave and optical light. *Nature Physics*, 10(4):321–326, mar 2014.

[6] Alfredo Rueda, Florian Sedlmeir, Michele C. Collodo, Ulrich Vogl, Birgit Stiller, Gerhard Schunk, Dmitry V. Strekalov, Christoph Marquardt, Johannes M. Fink, Oskar Painter, Gerd Leuchs, and Harald G. L. Schwefel. Efficient microwave to optical photon conversion: an electro-optical realization. *Optica*, 3(6):597, jun 2016.

[7] Linran Fan, Chang-Ling Zou, Risheng Cheng, Xiang Guo, Xu Han, Zheng Gong, Sihao Wang, and Hong X. Tang. Superconducting cavity electro-optics: A platform for coherent photon conversion between superconducting and photonic circuits. *Science Advances*, 4(8):eaar4994, aug 2018.

[8] J. P. Hadden, J. P. Harrison, A. C. Stanley-Clarke, L. Marseglia, Y.-L. D. Ho, B. R. Patton, J. L. O'Brien, and J. G. Rarity. Strongly enhanced photon collection from diamond defect centers under microfabricated integrated solid immersion lenses. *Applied Physics Letters*, 97(24):241901, dec 2010.

[9] J. J. Longdell, E. Fraval, M. J. Sellars, and N. B. Manson. Stopped light with storage times greater than one second using electromagnetically induced transparency in a solid. *Physical Review Letters*, 95(6), aug 2005.

[10] Alain Aspect, Philippe Grangier, and Gérard Roger. Experimental tests of realistic local theories via bell's theorem. *Physical Review Letters*, 47(7):460–463, 1981.

[11] Lilian Childress and Ronald Hanson. Diamond NV centers for quantum computing and quantum networks. *MRS Bulletin*, 38(2):134–138, feb 2013.

[12] D. Leibfried, R. Blatt, C. Monroe, and D. Wineland. Quantum dynamics of single trapped ions. *Reviews of Modern Physics*, 75(1):281–324, mar 2003.

[13] Jeremy L. O Brien, Akira Furusawa, and Jelena Vučković. Photonic quantum technologies. *Nature Photonics*, 3(12):687–695, dec 2009.

[14] Christian Kurtsiefer, Sonja Mayer, Patrick Zarda, and Harald Weinfurter. Stable solid-state source of single photons. *Physical Review Letters*, 85(2):290–293, jul 2000.

[15] Gopalakrishnan Balasubramanian, I. Y. Chan, Roman Kolesov, Mohannad Al-Hmoud, Julia Tisler, Chang Shin, Changdong Kim, Aleksander Wojcik, Philip R. Hemmer, Anke Krueger, Tobias Hanke, Alfred Leitenstorfer, Rudolf Bratschitsch, Fedor Jelezko, and Jörg Wrachtrup. Nanoscale imaging magnetometry with diamond spins under ambient conditions. *Nature*, 455(7213):648–651, oct 2008.

[16] Graciana Puentes, Gerald Waldherr, Philipp Neumann, Gopalakrishnan Balasubramanian, and Jörg Wrachtrup. Efficient route to high-bandwidth nanoscale magnetometry using single spins in diamond. *Scientific Reports*, 4(1):4677–4677, 2015.

[17] R. Hanson, F. M. Mendoza, R. J. Epstein, and D. D. Awschalom. Polarization and readout of coupled single spins in diamond. *Physical Review Letters*, 97(8):87601–87601, 2006.

[18] P. Neumann, R. Kolesov, B. Naydenov, J. Beck, F. Rempp, M. Steiner, V. Jacques, G. Balasubramanian, M. L. Markham, D. J. Twitchen, S. Pezzagna, J. Meijer, J. Twamley, F. Jelezko, and J. Wrachtrup. Quantum register based on coupled electron spins in a room-temperature solid. *Nature Physics*, 6(4):249–253, feb 2010.

[19] P. Neumann, N. Mizuochi, F. Rempp, P. Hemmer, H. Watanabe, S. Yamasaki, V. Jacques, T. Gaebel, F. Jelezko, and J. Wrachtrup. Multipartite entanglement among single spins in diamond. *Science*, 320(5881):1326–1329, 2008.

[20] E. Togan, Y. Chu, A. S. Trifonov, L. Jiang, J. Maze, L. Childress, M. V. G. Dutt, A. S. Sørensen, P. R. Hemmer, A. S. Zibrov, and M. D. Lukin. Quantum entanglement between an optical photon and a solid-state spin qubit. *Nature*, 466(7307):730–734, aug 2010.

[21] Ze Liang Xiang, Sahel Ashhab, J. Q. You, and Franco Nori. Hybrid quantum circuits: Superconducting circuits interacting with other quantum systems. *Reviews of Modern Physics*, 85(2):623–653, 2013.

[22] Mahdi Hosseini, Ben M. Sparkes, Gabriel Hétet, Jevon J. Longdell, Ping Koy Lam, and Ben C. Buchler. Coherent optical pulse sequencer for quantum applications. *Nature*, 461(7261):241–245, sep 2009.

[23] Morgan P. Hedges, Jevon J. Longdell, Yongmin Li, and Matthew J. Sellars. Efficient quantum memory for light. *Nature*, 465(7301):1052–1056, jun 2010.

[24] Patange, Om. On an instrument for the coherent investigation of nitrogen-vacancy centres in diamond, 2013.

[25] Charles Santori, Paul E. Barclay, Kai-Mei C. Fu, and Raymond G. Beausoleil. Vertical distribution of nitrogen-vacancy centers in diamond formed by ion implantation and annealing. *Physical Review B*, 79(12), mar 2009.

[26] Bernhard Grotz, Moritz V. Hauf, Markus Dankerl, Boris Naydenov, Sébastien Pezzagna, Jan Meijer, Fedor Jelezko, Jörg Wrachtrup, Martin Stutzmann, Friedemann Reinhard, and Jose A. Garrido. Charge state manipulation of qubits in diamond. *Nature Communications*, 3(1), jan 2012.

[27] Lilian Isabel Childress. Coherent manipulation of single quantum systems in the solid state. *Thesis*, (March):188, 2007.

[28] Gopalakrishnan Balasubramanian, Philipp Neumann, Daniel Twitchen, Matthew Markham, Roman Kolesov, Norikazu Mizuochi, Junichi Isoya, Jocelyn Achard, Johannes Beck, Julia Tissler, Vincent Jacques, Philip R. Hemmer, Fedor Jelezko, and Jörg Wrachtrup. Ultralong spin coherence time in isotopically engineered diamond. *Nature Materials*, 8(5):383–387, apr 2009.

[29] J. M. Taylor, P. Cappellaro, L. Childress, L. Jiang, D. Budker, P. R. Hemmer, A. Yacoby, R. Walsworth, and M. D. Lukin. High-sensitivity diamond magnetometer with nanoscale resolution. *Nature Physics*, 4(10):810–816, sep 2008.

[30] Dominik B. Bucher, Diana P. L. Aude Craik, Mikael P. Backlund, Matthew J. Turner, Oren Ben Dor, David R. Glenn, and Ronald L. Walsworth. Quantum diamond spectrometer for nanoscale NMR and ESR spectroscopy. *Nature Protocols*, 14(9):2707–2747, aug 2019.

[31] G. D. Fuchs, V. V. Dobrovitski, D. M. Toyli, F. J. Heremans, and D. D. Awschalom. Gigahertz dynamics of a strongly driven single quantum spin. *Science*, 326(5959):1520–1522, nov 2009.

[32] J. Meijer, B. Burchard, M. Domhan, C. Wittmann, T. Gaebel, I. Popa, F. Jelezko, and J. Wrachtrup. Generation of single color centers by focused nitrogen implantation. *Applied Physics Letters*, 87(26):261909, dec 2005.

[33] S. Sangtawesin, T. O. Brundage, Z. J. Atkins, and J. R. Petta. Highly tunable formation of nitrogen-vacancy centers via ion implantation. *Applied Physics Letters*, 105(6):063107, aug 2014.

[34] J. R. Maze, P. L. Stanwix, J. S. Hodges, S. Hong, J. M. Taylor, P. Cappellaro, L. Jiang, M. V. Gurudev Dutt, E. Togan, A. S. Zibrov, A. Yacoby, R. L. Walsworth, and M. D. Lukin. Nanoscale magnetic sensing with an individual electronic spin in diamond. *Nature*, 455(7213):644–647, oct 2008.

[35] Francesco Casola, Toeno van der Sar, and Amir Yacoby. Probing condensed matter physics with magnetometry based on nitrogen-vacancy centres in diamond. *Nature Reviews Materials*, 3(1), jan 2018.

[36] F. Dolde, H. Fedder, M. W. Doherty, T. Nöbauer, F. Rempp, G. Balasubramanian, T. Wolf, F. Reinhard, L. C. L. Hollenberg, F. Jelezko, and J. Wrachtrup. Electric-field sensing using single diamond spins. *Nature Physics*, 7(6):459–463, apr 2011.

[37] M. P. Ledbetter, K. Jensen, R. Fischer, A. Jarmola, and D. Budker. Gyroscopes based on nitrogen-vacancy centers in diamond. *Physical Review A*, 86(5), nov 2012.

[38] Jörg Wrachtrup and Fedor Jelezko. Processing quantum information in diamond. *Journal of Physics: Condensed Matter*, 18(21):S807–S824, may 2006.

[39] L. Childress, J. M. Taylor, A. S. Sørensen, and M. D. Lukin. Fault-tolerant quantum communication based on solid-state photon emitters. *Physical Review Letters*, 96(7), feb 2006.

[40] H. J. Kimble. The quantum internet. *Nature*, 453(7198):1023–1030, jun 2008.

[41] M. V. G. Dutt, L. Childress, L. Jiang, E. Togan, J. Maze, F. Jelezko, A. S. Zibrov, P. R. Hemmer, and M. D. Lukin. Quantum register based on individual electronic and nuclear spin qubits in diamond. *Science*, 316(5829):1312–1316, jun 2007.

[42] J H N Loubser and J A van Wyk. Electron spin resonance in the study of diamond. *Reports on Progress in Physics*, 41(8):1201–1248, aug 1978.

[43] D. A. Redman, S. Brown, R. H. Sands, and S. C. Rand. Spin dynamics and electronic states of n-vcenters in diamond by EPR and four-wave-mixing spectroscopy. *Physical Review Letters*, 67(24):3420–3423, dec 1991.

[44] Neil B. Manson, Xing-Fei He, and Peter T. H. Fisk. Raman heterodyne detected electron-nuclear-double-resonance measurements of the nitrogen-vacancy center in diamond. *Optics Letters*, 15(19):1094, oct 1990.

[45] E van Oort, N B Manson, and M Glasbeek. Optically detected spin coherence of the diamond n-v centre in its triplet ground state. *Journal of Physics C: Solid State Physics*, 21(23):4385–4391, aug 1988.

[46] N. B. Manson, J. P. Harrison, and M. J. Sellars. Nitrogen-vacancy center in diamond: Model of the electronic structure and associated dynamics. *Physical Review B*, 74(10), Sep 2006.

[47] F. Jelezko, I. Popa, A. Gruber, C. Tietz, J. Wrachtrup, A. Nizovtsev, and S. Kilin. Single spin states in a defect center resolved by optical spectroscopy. *Applied Physics Letters*, 81(12):2160–2162, sep 2002.

[48] Daniel Riedel, Immo Söllner, Brendan J. Shields, Sebastian Starosielec, Patrick Appel, Elke Neu, Patrick Maletinsky, and Richard J. Warburton. Deterministic enhancement of coherent photon generation from a nitrogen-vacancy center in ultrapure diamond. *Physical Review X*, 7(3), sep 2017.

[49] Konstantin G. Fehler, Anna P. Ovvyan, Nico Gruhler, Wolfram H. P. Pernice, and Alexander Kubanek. Efficient coupling of an ensemble of nitrogen vacancy center to the mode of a high-q, si3n4 photonic crystal cavity. *ACS Nano*, 13(6):6891–6898, jun 2019.

[50] Elke Neu, Patrick Appel, Marc Ganzhorn, Javier Miguel-Sánchez, Margarita Lesik, Vianney Mille, Vincent Jacques, Alexandre Tallaire, Jocelyn Achard, and Patrick Maletinsky. Photonic nano-structures on (111)-oriented diamond. *Applied Physics Letters*, 104(15):153108, apr 2014.

[51] C. G. Yale, B. B. Buckley, D. J. Christle, G. Burkard, F. J. Heremans, L. C. Bassett, and D. D. Awschalom. All-optical control of a solid-state spin using coherent dark states. *Proceedings of the National Academy of Sciences*, 110(19):7595–7600, apr 2013.

[52] Jin-Hui Wu, G. C. La Rocca, and M. Artoni. Controlled light-pulse propagation in driven color centers in diamond. *Physical Review B*, 77(11), mar 2008.

[53] D. Andrew Golter, Thein Oo, Mayra Amezcua, Ignas Lekavicius, Kevin A. Stewart, and Hailin Wang. Coupling a surface acoustic wave to an electron spin in diamond via a dark state. *Physical Review X*, 6(4), dec 2016.

[54] P. C. Maurer, G. Kucsko, C. Latta, L. Jiang, N. Y. Yao, S. D. Bennett, F. Pastawski, D. Hunger, N. Chisholm, M. Markham, D. J. Twitchen, J. I. Cirac, and M. D. Lukin. Room-temperature quantum bit memory exceeding one second. *Science*, 336(6086):1283–1286, jun 2012.

[55] E. D. Herbschleb, H. Kato, Y. Maruyama, T. Danjo, T. Makino, S. Yamasaki, I. Ohki, K. Hayashi, H. Morishita, M. Fujiwara, and N. Mizuochi. Ultra-long coherence times amongst room-temperature solid-state spins. *Nature Communications*, 10(1), aug 2019.

[56] Amila Ariyaratne, Dolev Bluvstein, Bryan A. Myers, and Ania C. Bleszynski Jayich. Nanoscale electrical conductivity imaging using a nitrogen-vacancy center in diamond. *Nature Communications*, 9(1), jun 2018.

[57] N. Bar-Gill, L.M. Pham, A. Jarmola, D. Budker, and R.L. Walsworth. Solid-state electronic spin coherence time approaching one second. *Nature Communications*, 4(1), apr 2013.

[58] M. Minsky. Memoir on inventing the confocal scanning microscope. *Scanning*, 10(4):128–138, 1988.

[59] Lukas Novotny and Bert Hecht. Optical interactions. In *Principles of Nano-Optics*, pages 224–281. Cambridge University Press.

[60] Palash Bharadwaj, Bradley Deutsch, and Lukas Novotny. Optical antennas. *Advances in Optics and Photonics*, 1(3):438, aug 2009.

[61] E. M. Purcell, H. C. Torrey, and R. V. Pound. Resonance absorption by nuclear magnetic moments in a solid. *Physical Review*, 69(1-2):37–38, jan 1946.

[62] Alexander E. Krasnok, Alexey P. Slobozhanyuk, Constantin R. Simovski, Sergei A. Tretyakov, Alexander N. Poddubny, Andrey E. Miroshnichenko, Yuri S. Kivshar, and Pavel A. Belov. An antenna model for the purcell effect. *Scientific Reports*, 5(1), aug 2015.

[63] Itzik Malkiel, Michael Mrejen, Achiya Nagler, Uri Arieli, Lior Wolf, and Haim Suchowski. Plasmonic nanostructure design and characterization via deep learning. *Light: Science & Applications*, 7(1), sep 2018.

[64] Mahdad Mansouree, Hyounghan Kwon, Ehsan Arbabi, Andrew McClung, Andrei Faraon, and Amir Arbabi. Multifunctional 25d metastructures enabled by adjoint optimization. *Optica*, 7(1):77, jan 2020.

[65] Christopher M. Lalau-Keraly, Samarth Bhargava, Owen D. Miller, and Eli Yablonovitch. Adjoint shape optimization applied to electromagnetic design. *Optics Express*, 21(18):21693, sep 2013.

[66] Owen D. Miller. Photonic design: From fundamental solar cell physics to computational inverse design, 2013.

[67] Haskell B. Curry. The method of steepest descent for non-linear minimization problems. *Quarterly of Applied Mathematics*, 2(3):258–261, oct 1944.

[68] Shun Lien Chuang, Nasser Peyghambarian, and Stephan Koch. Physics of optoelectronic devices. *Physics Today*, 49(7):62–62, jul 1996.

[69] Stanley Osher and Ronald Fedkiw. Particle level set method. In *Applied Mathematical Sciences*, pages 79–86. Springer New York, 2003.

[70] Thomas M. Babinec, Birgit J. M. Hausmann, Mughees Khan, Yinan Zhang, Jeronimo R. Maze, Philip R. Hemmer, and Marko Lončar. A diamond nanowire single-photon source. *Nature Nanotechnology*, 5(3):195–199, feb 2010.

[71] S. Ali Momenzadeh, Rainer J. Stöhr, Felipe Favaro de Oliveira, Andreas Brunner, Andrej Denisenko, Sen Yang, Friedemann Reinhard, and Jörg Wrachtrup. Nanoengineered diamond waveguide as a robust bright platform for nanomagnetometry using shallow nitrogen vacancy centers. *Nano Letters*, 15(1):165–169, dec 2014.

[72] Jennifer T. Choy, Birgit J. M. Hausmann, Thomas M. Babinec, Irfan Bulu, Mughees Khan, Patrick Maletinsky, Amir Yacoby, and Marko Lončar. Enhanced single-photon emission from a diamond–silver aperture. *Nature Photonics*, 5(12):738–743, oct 2011.

[73] D. Riedel, D. Rohner, M. Ganzhorn, T. Kaldewey, P. Appel, E. Neu, R. J. Warburton, and P. Maletinsky. Low-loss broadband antenna for efficient photon collection from a coherent spin in diamond. *Physical Review Applied*, 2(6), dec 2014.

[74] Tim Schröder, Friedemann Gädeke, Moritz Julian Banholzer, and Oliver Benson. Ultrabright and efficient single-photon generation based on nitrogen-vacancy centres in nanodiamonds on a solid immersion lens. *New Journal of Physics*, 13(5):055017, may 2011.

[75] L. Marseglia, J. P. Hadden, A. C. Stanley-Clarke, J. P. Harrison, B. Patton, Y.-L. D. Ho, B. Naydenov, F. Jelezko, J. Meijer, P. R. Dolan, J. M. Smith, J. G. Rarity, and J. L. O'Brien. Nanofabricated solid immersion lenses registered to single emitters in diamond. *Applied Physics Letters*, 98(13):133107, mar 2011.

[76] Luozhou Li, Edward H. Chen, Jiabao Zheng, Sara L. Mouradian, Florian Dolde, Tim Schröder, Sinan Karaveli, Matthew L. Markham, Daniel J. Twitchen, and Dirk Englund. Efficient photon collection from a nitrogen vacancy center in a circular bullseye grating. *Nano Letters*, 15(3):1493–1497, mar 2015.

[77] M. Davanço, M. T. Rakher, D. Schuh, A. Badolato, and K. Srinivasan. A circular dielectric grating for vertical extraction of single quantum dot emission. *Applied Physics Letters*, 99(4):041102, jul 2011.

[78] Mark Y. Su and Richard P. Mirin. Enhanced light extraction from circular bragg grating coupled microcavities. In *2006 Conference on Lasers and Electro-Optics and 2006 Quantum Electronics and Laser Science Conference*. IEEE, 2006.

[79] M. Lesik, J.-P. Tetienne, A. Tallaire, J. Achard, V. Mille, A. Gicquel, J.-F. Roch, and V. Jacques. Perfect preferential orientation of nitrogen-vacancy defects in a synthetic diamond sample. *Applied Physics Letters*, 104(11):113107, mar 2014.

[80] Julia Michl, Tokuyuki Teraji, Sebastian Zaiser, Ingmar Jakobi, Gerald Waldherr, Florian Dolde, Philipp Neumann, Marcus W. Doherty, Neil B. Manson, Junichi Isoya, and Jörg Wrachtrup. Perfect alignment and preferential orientation of nitrogen-vacancy centers during chemical vapor deposition diamond growth on (111) surfaces. *Applied Physics Letters*, 104(10):102407, mar 2014.

[81] William M. J. Green, Jacob Scheuer, Guy DeRose, and Amnon Yariv. Vertically emitting annular bragg lasers using polymer epitaxial transfer. *Applied Physics Letters*, 85(17):3669–3671, oct 2004.

[82] D. Taillaert, W. Bogaerts, P. Bienstman, T.F. Krauss, P. Van Daele, I. Moerman, S. Verstuyft, K. De Mesel, and R. Baets. An out-of-plane grating coupler for efficient butt-coupling between compact planar waveguides and single-mode fibers. *IEEE Journal of Quantum Electronics*, 38(7):949–955, jul 2002.

[83] Jennifer T. Choy, Irfan Bulu, Birgit J. M. Hausmann, Erika Janitz, I-Chun Huang, and Marko Lončar. Spontaneous emission and collection efficiency enhancement of single emitters in diamond via plasmonic cavities and gratings. *Applied Physics Letters*, 103(16):161101, oct 2013.

[84] Christopher M. Lalau-Keraly. Continuous adjoint optimization wrapper for lumerical, 2019.

[85] Jacques Arnaud. Representation of gaussian beams by complex rays. *Applied Optics*, 24(4):538, feb 1985.

[86] Lin He, Zhongzheng Lin, Yuanhui Wen, Yujie Chen, and Siyuan Yu. An inverse design method combining particle swarm optimization and wavefront matching method for multiplane light conversion. In *Frontiers in Optics / Laser Science*. OSA, 2020.

[87] Birgit Judith Maria Hausmann. Nanophotonics in diamond. *Doctoral dissertation, Harvard University*, 2013.

[88] B. J. M. Hausmann, B. J. Shields, Q. Quan, Y. Chu, N. P. de Leon, R. Evans, M. J. Burek, A. S. Zibrov, M. Markham, D. J. Twitchen, H. Park, M. D. Lukin, and M. Loncăr. Coupling of NV centers to photonic crystal nanobeams in diamond. *Nano Letters*, 13(12):5791–5796, nov 2013.

[89] Mariusz Radtke, Richard Nelz, Abdallah Slablab, and Elke Neu. Reliable nanofabrication of single-crystal diamond photonic nanostructures for nanoscale sensing. *Micromachines*, 10(11):718, oct 2019.

[90] Srivatsa Chakravarthi, Pengning Chao, Christian Pederson, Sean Molesky, Andrew Ivanov, Karine Hestroffer, Fariba Hatami, Alejandro W. Rodriguez, and Kai-Mei C. Fu. Inverse-designed photon extractors for optically addressable defect qubits. *Optica*, 7(12):1805, dec 2020.

[91] Raymond A. Wambold, Zhaoning Yu, Yuzhe Xiao, Benjamin Bachman, Gabriel Jaffe, Shimon Kolkowitz, Jennifer T. Choy, Mark A. Eriksson, Robert J. Hamers, and Mikhail A. Kats. Adjoint-optimized nanoscale light extractor for nitrogen-vacancy centers in diamond. *Nanophotonics*, 10(1):393–401, nov 2020.

[92] L. DiCarlo, J. M. Chow, J. M. Gambetta, Lev S. Bishop, B. R. Johnson, D. I. Schuster, J. Majer, A. Blais, L. Frunzio, S. M. Girvin, and R. J. Schoelkopf. Demonstration of two-qubit algorithms with a superconducting quantum processor. *Nature*, 460(7252):240–244, jun 2009.

[93] L. DiCarlo, M. D. Reed, L. Sun, B. R. Johnson, J. M. Chow, J. M. Gambetta, L. Frunzio, S. M. Girvin, M. H. Devoret, and R. J. Schoelkopf. Preparation and measurement of three-qubit entanglement in a superconducting circuit. *Nature*, 467(7315):574–578, sep 2010.

[94] Jeff T. Hill, Amir H. Safavi-Naeini, Jasper Chan, and Oskar Painter. Coherent optical wavelength conversion via cavity optomechanics. *Nature Communications*, 3(1), jan 2012.

[95] S. A. McGee, D. Meiser, C. A. Regal, K. W. Lehnert, and M. J. Holland. Mechanical resonators for storage and transfer of electrical and optical quantum states. *Physical Review A*, 87(5), may 2013.

[96] Amir H Safavi-Naeini and Oskar Painter. Proposal for an optomechanical traveling wave phonon–photon translator. *New Journal of Physics*, 13(1):013017, jan 2011.

[97] Joerg Bochmann, Amit Vainsencher, David D. Awschalom, and Andrew N. Cleland. Nanomechanical coupling between microwave and optical photons. *Nature Physics*, 9(11):712–716, sep 2013.

[98] V.S. Ilchenko, A.A. Savchenkov, A.B. Matsko, and L. Maleki. Sub-microwatt photonic microwave receiver. *IEEE Photonics Technology Letters*, 14(11):1602–1604, nov 2002.

[99] D. V. Strekalov, H. G. L. Schwefel, A. A. Savchenkov, A. B. Matsko, L. J. Wang, and N. Yu. Microwave whispering-gallery resonator for efficient optical up-conversion. *Physical Review A*, 80(3), sep 2009.

[100] Kerry Vahala. Cavity optomechanics. In *Conference on Lasers and Electro-Optics/International Quantum Electronics Conference*. OSA, 2009.

[101] Xavier Fernandez-Gonzalvo, Yu-Hui Chen, Chunming Yin, Sven Rogge, and Jevon J. Longdell. Coherent frequency up-conversion of microwaves to the optical telecommunications band in an er:YSO crystal. *Physical Review A*, 92(6), dec 2015.

[102] Lewis A. Williamson and et al. Magneto-optic modulator with unit quantum efficiency. *Physical Review Letters*, 113(20), 2014.

[103] Christopher O'Brien, Nikolai Lauk, Susanne Blum, Giovanna Morigi, and Michael Fleischhauer. Interfacing superconducting qubits and telecom photons via a rare-earth-doped crystal. *Physical Review Letters*, 113(6), aug 2014.

[104] John G. Bartholomew, Jake Rochman, Tian Xie, Jonathan M. Kindem, Andrei Ruskuc, Ioana Craiciu, Mi Lei, and Andrei Faraon. On-chip coherent microwave-to-optical transduction mediated by ytterbium in YVO4. *Nature Communications*, 11(1), jun 2020.

[105] Jingshan Han, Thibault Vogt, Christian Gross, Dieter Jaksch, Martin Kiffner, and Wenhui Li. Coherent microwave-to-optical conversion via six-wave mixing in rydberg atoms. *Physical Review Letters*, 120(9), mar 2018.

[106] M. Hafezi, Z. Kim, S. L. Rolston, L. A. Orozco, B. L. Lev, and J. M. Taylor. Atomic interface between microwave and optical photons. *Physical Review A*, 85(2), feb 2012.

[107] J.R. Johansson, P.D. Nation, and Franco Nori. QuTiP: An open-source python framework for the dynamics of open quantum systems. *Computer Physics Communications*, 183(8):1760–1772, aug 2012.

[108] J.R. Johansson, P.D. Nation, and Franco Nori. QuTiP 2: A python framework for the dynamics of open quantum systems. *Computer Physics Communications*, 184(4):1234–1240, apr 2013.

[109] Daniel Adam Steck. *Quantum and Atom Optics*. 2007.

[110] Klaus Mølmer, Yvan Castin, and Jean Dalibard. Monte carlo wave-function method in quantum optics. *Journal of the Optical Society of America B*, 10(3):524, mar 1993.

[111] M.S.Zubairy M.Scully. *Quantum Optics*. Cambridge University Press, 1997.

[112] P.R Rice and R.J Brecha. Cavity induced transparency. *Optics Communications*, 126(4-6):230–235, may 1996.

[113] S. E. Harris, J. E. Field, and A. Imamoğlu. Nonlinear optical processes using electromagnetically induced transparency. *Physical Review Letters*, 64(10):1107–1110, mar 1990.

[114] Jinjin Du, Wenfang Li, and Michal Bajcsy. Deterministic single-photon subtraction based on a coupled single quantum dot-cavity system. *Optics Express*, 28(5):6835, feb 2020.

[115] D. Bothner, T. Gaber, M. Kemmler, D. Koelle, and R. Kleiner. Improving the performance of superconducting microwave resonators in magnetic fields. *Applied Physics Letters*, 98(10):102504, mar 2011.

[116] Roland Albrecht, Alexander Bommer, Christian Deutsch, Jakob Reichel, and Christoph Becher. Coupling of a single nitrogen-vacancy center in diamond to a fiber-based microcavity. *Physical Review Letters*, 110(24), jun 2013.

[117] M Bajcsy and et al. Photon blockade with a four-level quantum emitter coupled to a photonic-crystal nanocavity. *New Journal of Physics*, 15(2), 2013.

[118] P. A. M. Dirac. The quantum theory of the emission and absorption of radiation. In *Special Relativity and Quantum Theory*, pages 157–179. Springer Netherlands, 1988.

[119] Yiwen Chu and Mikhail D. Lukin. *Quantum optics with nitrogen-vacancy centres in diamond*. Oxford University Press, aug 2017.

[120] Howard Carmichael. *An Open Systems Approach to Quantum Optics*. Springer Berlin Heidelberg, 1993.

[121] C. W. Gardiner and M. J. Collett. Input and output in damped quantum systems: Quantum stochastic differential equations and the master equation. *Physical Review A*, 31(6):3761–3774, jun 1985.

[122] Peng-Bo Li, Shao-Yan Gao, and Fu-Li Li. Quantum-information transfer with nitrogen-vacancy centers coupled to a whispering-gallery microresonator. *Physical Review A*, 83(5), may 2011.

[123] Masahiro Nomura, Katsuaki Tanabe, Satoshi Iwamoto, and Yasuhiko Arakawa. High-q design of semiconductor-based ultrasmall photonic crystal nanocavity. *Optics Express*, 18(8):8144, apr 2010.

[124] Kelley Rivoire, Sonia Buckley, and Jelena Vučković. Multiply resonant photonic crystal nanocavities for nonlinear frequency conversion. *Optics Express*, 19(22):22198, oct 2011.

[125] Sonia Buckley. Engineering photonic crystal cavities in iii-vsemiconductors for $\chi^{(2)}$ frequency conversion. *Thesis*, page 188, 2014.

[126] Dirk Englund, Brendan Shields, Kelley Rivoire, Fariba Hatami, Jelena Vuckovic, Hongkun Park, and Mikhail D. Lukin. Deterministic coupling of a single nitrogen vacancy center to a photonic crystal cavity. *Nano Letters*, 10(10):3922–3926, oct 2010.

[127] T. Schröder, M. Walsh, J. Zheng, S. Mouradian, L. Li, G. Malladi, H. Bakhru, M. Lu, A. Stein, M. Heuck, and D. Englund. Scalable fabrication of coupled NV center - photonic crystal cavity systems by self-aligned n ion implantation. *Optical Materials Express*, 7(5):1514, apr 2017.

[128] T. J. Kippenberg, S. M. Spillane, and K. J. Vahala. Demonstration of ultra-high-q small mode volume toroid microcavities on a chip. *Applied Physics Letters*, 85(25):6113–6115, dec 2004.

[129] D. I. Schuster, A. P. Sears, E. Ginossar, L. DiCarlo, L. Frunzio, J. J. L. Morton, H. Wu, G. A. D. Briggs, B. B. Buckley, D. D. Awschalom, and R. J. Schoelkopf. High-cooperativity coupling of electron-spin ensembles to superconducting cavities. *Physical Review Letters*, 105(14), sep 2010.

[130] Y. Kubo, F. R. Ong, P. Bertet, D. Vion, V. Jacques, D. Zheng, A. Dréau, J.-F. Roch, A. Auffeves, F. Jelezko, J. Wrachtrup, M. F. Barthe, P. Bergonzo, and D. Esteve.

Strong coupling of a spin ensemble to a superconducting resonator. *Physical Review Letters*, 105(14), sep 2010.

[131] Y. Kubo, C. Grezes, A. Dewes, T. Umeda, J. Isoya, H. Sumiya, N. Morishita, H. Abe, S. Onoda, T. Ohshima, V. Jacques, A. Dréau, J.-F. Roch, I. Diniz, A. Auffeves, D. Vion, D. Esteve, and P. Bertet. Hybrid quantum circuit with a superconducting qubit coupled to a spin ensemble. *Physical Review Letters*, 107(22), nov 2011.

[132] R. Amsüss, Ch. Koller, T. Nöbauer, S. Putz, S. Rotter, K. Sandner, S. Schneider, M. Schramböck, G. Steinhauser, H. Ritsch, J. Schmiedmayer, and J. Majer. Cavity QED with magnetically coupled collective spin states. *Physical Review Letters*, 107(6), aug 2011.

[133] Chang-Hao Li and Peng-Bo Li. Coupling a single nitrogen-vacancy center with a superconducting qubit via the electro-optic effect. *Physical Review A*, 97(5), may 2018.

[134] Peng-Bo Li, Yong-Chun Liu, S.-Y. Gao, Ze-Liang Xiang, Peter Rabl, Yun-Feng Xiao, and Fu-Li Li. Hybrid quantum device based onNVCenters in diamond nanomechanical resonators plus superconducting waveguide cavities. *Physical Review Applied*, 4(4), oct 2015.

[135] Bo Li, Peng-Bo Li, Yuan Zhou, Sheng-Li Ma, and Fu-Li Li. Quantum microwave-optical interface with nitrogen-vacancy centers in diamond. *Physical Review A*, 96(3), sep 2017.

[136] J. Flannery. *Optical resonators integrated into a hollow core photonic crystal fiber for enhanced light-matter interactions.* PhD Thesis, 2019.

APPENDICES

Appendix A

Fabrication of Photonic Crystal Membranes for Hollow-Core Fiber Integrated Cavities

This work was done together with Supratik Sarkar, and Dr. Rubayet Al Maruf with guidance from Dr. Jeremy Flannery.

The fabrication was done with by following the recipe developed by Dr. Jeremy Flannery in Referece [136] detailed in Figure A.1.

1. We began with a silicon wafer which had SiN deposited on it with a layer of PMMA protective coating. The PMMA was removed by sonicating the chip in Remover PG at 80^{o}C for 15 minutes. Then the SiN layer was etched down to the required thickness of 400nm by Reactive Ion Etching(RIE)(Oxford Instruments ICP380) with a mixture of C_4F_8 at 130 SCCM, and SF_6 at 60 SCCM with a pressure of 10mTorr, RF power of 1000W ICP, and platen RF powe of 30W. The thickness of the SiN layer was characterized with reflectometry (Filmetrics F40) before and after etching to determine the etch rate.

2. **Al Deposition:** A hardmask of Aluminium was deposited on to the sample with a E-beam Physical Vapour Deposition (Intlvac Nanochrome II).

3. **ZEP:** A 450nm later of ZEP520A(positive resist) was deposited on the Aluminium with a spincoater(3000RPM for 60s with a 3000RPM/s ramp) and developed on a hotplate at 180^{o}C for 2 minutes.

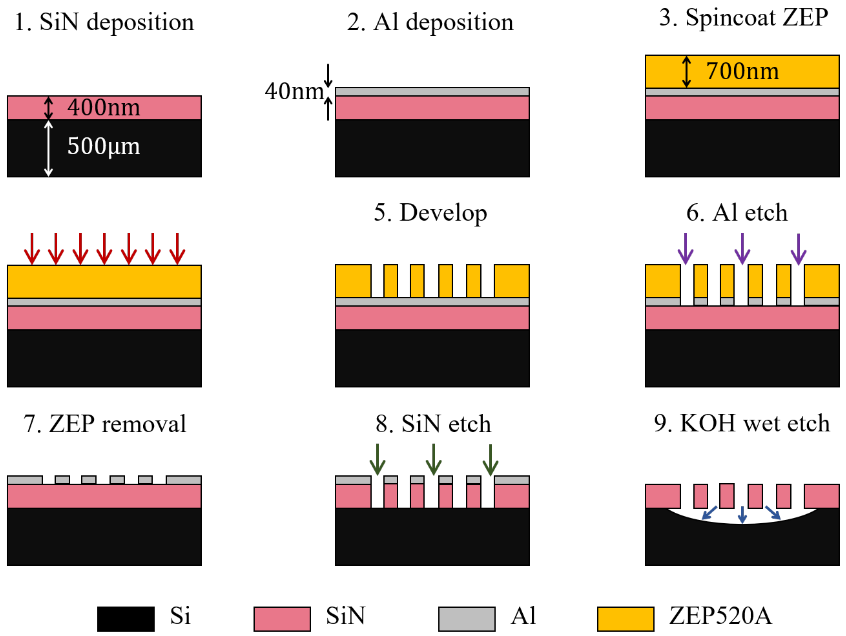

Figure A.1

4. **E-beam Lithography(EBL):** The photonic crystal pattern was then transferred to the ZEP with EBL(JEOL JBX-6300FS) at 100keV and developed with amyl-acetate.
5. **Aluminium Etch:** The Aluminium hardmask was etched with RIE. Any oxidation layer was first removed with a mixture of Cl_2 at 10SCCM, BCl_3 at 40SCCM, and N_2 at 50SCCM, with a pressure of 5mTorr, ICP power of 800W, and HF power of 150W for 8s. The Aluminium was then etched with a mixture of Cl_2 at 40SCCM, BCl_3 at 10SCCM, and N_2 at 50SCCM, with a pressure of 5mTorr, ICP power of 800W, and HF power of 120W for 10s.
6. **ZEP Removal:** The ZEP layer was removed by sonication in Remover PG at 80^{o}C for 15 minutes.
7. **SiN Etch:** The same recipe from Step 1 was used to etch the SiN. The etching was done for 1.5 times the SiN thickness to ensure that the holes was etched all the way through.
8. **KOH Wet Etch:** This step was performed by Rubayet Al Maruf. The Si substrate was undercut with KOH wet etching by immersing the chip in 45% concentration of

KOH for 1 hour at 80^oC followed by two baths in deinonized water for 5 minutes each at 80^oC. After that the chips were immersed in two IPA baths for for 5 minutes each.

Appendix B

Inverse Design Setup Codes

This work was done in collaboration with Supratik Sarkar.

B.1 Lumerical Intial Structure Setup File (.lsf)

```
switchtolayout;
selectall;
delete;

## SIM PARAMS
opt_size_x = 3.0e-6;
opt_size_y = 3.0e-6;
opt_size_z = 300e-9;

fiber_rad = 700e-9;

dist_to_source = 200e-9;
dist_to_fiber = 2e-6;

grating_thickness = 300e-9;

size_x = opt_size_x + 1.5e-6;
size_y = opt_size_y + 1.5e-6;
size_z_min = - (grating_thickness/2 + dist_to_source + 50e-9);
size_z_max = grating_thickness/2 + dist_to_fiber + 50e-9;

wavelength = 680e-9;
```

```
diamond_index = 2.41;
fiber_index = 1.44;
air_index = 1;

dx = 20e-9;

# DIAMOND SAMPLE
addrect;
set(’name’,’diamond sample’);
set(’x’,0);
set(’x span’,2*opt_size_x);
set(’y’,0);
set(’y span’,2*opt_size_y);
set(’z max’,grating_thickness/2);
set(’z min’,-grating_thickness/2 - 1e-6);
set(’index’,diamond_index);

# OUTPUT FIBER
addcircle;
set(’name’,’output fiber top’);
set(’x’,0);
set(’y’,0);
set(’radius’,fiber_rad);
set(’z min’,grating_thickness/2 + dist_to_fiber);
set(’z max’,grating_thickness/2 + dist_to_fiber + 5e-6);
set(’index’,fiber_index);

# NV CENTER SOURCE
adddipole;
set(’x’,0);
set(’y’,0);
set(’z’,-grating_thickness/2 - dist_to_source);
set(’amplitude’,1);
set(’center wavelength’,wavelength);
set(’wavelength span’,0);
set(’theta’,90);

# FDTD
addfdtd;
set(’dimension’,’3D’);
set(’background index’,air_index);
set(’mesh accuracy’,3); #< To increase this, we also need to refine the optimization mesh below 20nm
set(’x min’,-size_x/2);
```

```
set('x max',size_x/2);
set('y min',-size_y/2);
set('y max',size_y/2);
set('z min',size_z_min - 0.5e-6);
set('z max',size_z_max);
set('y min bc','Symmetric');
set('x min bc','Anti-Symmetric');
set('auto shutoff min',1e-7);

# OPTIMIZATION FIELDS MONITOR IN OPTIMIZABLE REGION
addpower;
set('name','opt_fields');
set('monitor type','3D');
set('x',0);
set('x span',opt_size_x);
set('y',0);
set('y span',opt_size_y);
set('z',0);
set('z span',opt_size_z);

# FOM
addpower;
set('name','fom');
set('monitor type','2D Z-normal');
set('x',0);
set('x span',fiber_rad * 2.1);
set('y',0);
set('y span',fiber_rad * 2.1);
set('z',grating_thickness/2 + dist_to_fiber);

# FOR LATER VISUALIZATION
addindex;
set('name','global_index');
set('monitor type','3D');
set('x min',-size_x/2);
set('x max',size_x/2);
set('y min',-size_y/2);
set('y max',size_y/2);
set('z min',-opt_size_z/2);
set('z max',opt_size_z/2);
set('enabled',true);

# INITIAL BULLSEYE GEOMETRY
addstructuregroup;
set('name','initial_guess');
```

```
mesh_order = 2;
gradient_factor = 0.1;
period = wavelength/diamond_index; #< Second order Bragg grating
    criterion
radius = 2* period;
ridge_width = period/2;

for (0; (2*(radius + ridge_width)) < (opt_size_x) ; 0) {
    addring;
    set('name','etch_ring');
    set('x',0);
    set('y',0);
    set('inner radius',radius);
    set('outer radius',radius + ridge_width);
    set('z',0);
    set('z span',grating_thickness);
    set('material','etch');
    addtogroup('initial_guess');
    radius = radius + (2 * ridge_width);
}
```

B.2 Python Adjoint Optimization Code

```

# General purpose imports
import numpy as np
import os
import sys
import scipy as sp

# Uncomment the next two lines if using Linux
#import imp
#lumapi = imp.load_source("lumapi", "/opt/lumerical/2019b/api/python/
    lumapi.py")

# Optimization specific imports
from lumopt import CONFIG
from lumopt.geometries.topology import TopologyOptimization2D,
    TopologyOptimization3DLayered
from lumopt.utilities.load_lumerical_scripts import load_from_lsf
from lumopt.figures_of_merit.modematch import ModeMatch
from lumopt.optimization import Optimization
from lumopt.optimizers.generic_optimizers import ScipyOptimizers
from lumopt.utilities.wavelengths import Wavelengths
```

```

# DEFINE BASE SIMULATION #
def runSim(params, eps_air, eps_diamond, x_pos, y_pos, z_pos, size_x, filter_R):

    # DEFINE A 3D TOPOLOGY OPTIMIZATION REGION #
    geometry = TopologyOptimization3DLayered(params=params, eps_min=eps_air, eps_max=eps_diamond, x=x_pos, y=y_pos, z=z_pos, filter_R=filter_R)

    # DEFINE FIGURE OF MERIT #
    # The base simulation script defines a field monitor named 'fom' at the point where we want to modematch to the fundamental TE mode
    fom = ModeMatch(monitor_name = 'fom', mode_number = 'Fundamental TE mode', direction = 'Forward', norm_p = 2)

    # DEFINE OPTIMIZATION ALGORITHM #
    optimizer = ScipyOptimizers(max_iter=40, method='L-BFGS-B', scaling_factor=1, pgtol=1e-6, ftol=1e-4, scale_initial_gradient_to=0.25)

    # LOAD TEMPLATE SCRIPT AND SUBSTITUTE PARAMETERS #
    script = load_from_lsf(os.path.join(CONFIG['root'], 'examples/NV_grating/dipole_source.lsf'))

    wavelengths = Wavelengths(start = 680e-9, stop = 680e-9, points = 1)
    opt = Optimization(base_script=script, wavelengths = wavelengths, fom=fom, geometry=geometry, optimizer=optimizer, use_deps=False, hide_fdtd_cad=True, plot_history=False, store_all_simulations=False)

    # RUN THE OPTIMIZER #
    opt.run()

if __name__ == '__main__':
    size_x = 3000
    size_y = 3000
    size_z = 300

    filter_R = 400e-9

    # Permittivity of diamond and air
    eps_diamond = 2.41**2
    eps_air = 1**2

    if len(sys.argv) > 2 :
```

```
        size_x = int(sys.argv[1])
        filter_R = int(sys.argv[2])*1e-9
        print(size_x,filter_R)

    x_points = int(size_x/20) + 1
    y_points = int(size_y/20) + 1
    z_points = int(size_z/20) + 1

    x_pos = np.linspace(-size_x/2*1e-9,size_x/2*1e-9,x_points)
    y_pos = np.linspace(-size_y/2*1e-9,size_y/2*1e-9,y_points)
    z_pos = np.linspace(-size_z/2*1e-9,size_z/2*1e-9,z_points)


    ## Initialization tests
    paramList=[None,                               #< Use the structure defined in the project file as initial condition
               np.ones((x_points,y_points)),       #< Start with the domain filled with eps_diamond
               0.5*np.ones((x_points,y_points)),   #< Start with the domain filled with (eps_diamond+eps_air)/2
               np.zeros((x_points,y_points)),      #< Start with the domain filled with eps_air
               ]

    for curParams in paramList:
        runSim(curParams, eps_air, eps_diamond, x_pos, y_pos, z_pos, size_x*1e-9, filter_R)
```

Appendix C

Galvo Control Circuit

This work was done in collaboration with Supratik Sarkar

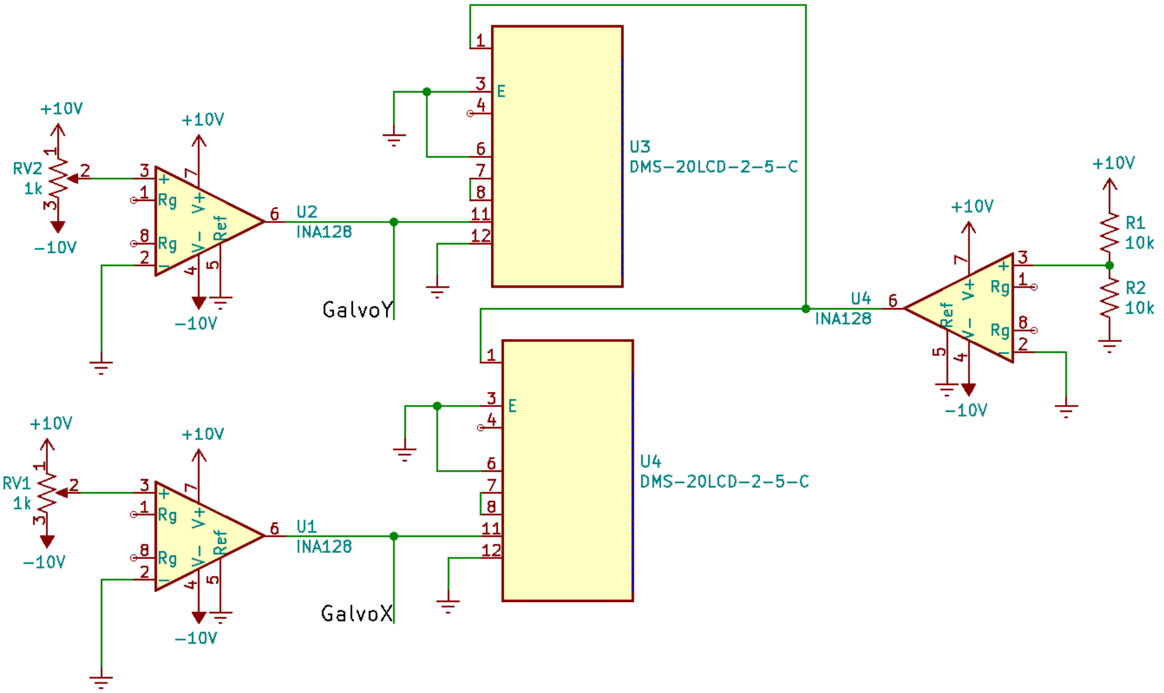

Figure C.1

Appendix D

Gaussian Beam Waist Calculation

This work was done in collaboration with Supratik Sarkar

D.1 Mathematica Code

```
Lens[f_] := {{1, 0}, {-1/f, 1}};
Air[d_] := {{1, d}, {0, 1}};

(*The ray vectors at z=0*)6Xi[ wavelength_ , w0_] := {{0}, {wavelength
    /(Pi*w0)}};
Eta[w0_] := {{w0}, {0}};
WInit = 1.4*2;
Lambda = 532*(10^ -9);
f1 = 100;f2 = 200;f3 = 200;

d1 = ((f1^2)/f2) + f1 - (d3*((f1/f2)^2));d2 = f1 + f2;
d3 = 150;d4 = f3;

(* Propagation through air*)16M1 = Air[z];
Eta1 = M1.Eta[WInit];
Xi1   = M1.Xi[Lambda , WInit];
R1 = Sqrt[Eta1 [[1]]^2 + Xi1 [[1]]^2];

(* Propagation through lens*)
M2   = Air[z - d1].Lens[f1].Air[d1];
Eta2 = M2.Eta[WInit];
Xi2   = M2.Xi[Lambda , WInit];
```

```
R2 = Sqrt[Eta2 [[1]]^2 + Xi2 [[1]]^2];

(* Propagation through air*)28M3 = Air[z - d1 - d2].Lens[f2].Air[d2].
   Lens[f1].Air[d1];
Eta3 = M3.Eta[WInit];
Xi3   = M3.Xi[Lambda , WInit];
R3 = Sqrt[Eta3 [[1]]^2 + Xi3 [[1]]^2];

(* Propagation through lens*)34M4 = Air[z - d1 - d2 - d3].Lens[f3].Air[
   d3].Lens[f2].Air[d2].Lens[35f1].Air[d1];
Eta4 = M4.Eta[WInit];
Xi4   = M4.Xi[Lambda , WInit];
R4 = Sqrt[Eta4 [[1]]^2 + Xi4 [[1]]^2];

Plot[Piecewise [{{R1 , z < d1}, {R2 ,41d1 < z < (d2 + d1)}, {R3 , (d1 +
   d2 + d3) > z > (d2 + d1)}, {R4 ,42z > (d1 + d2 + d3)}}], {z, 0, d1 +
   d2 + d3 + d4 + 180},43AxesLabel -> {"z", "Beam radius"}]
```

Appendix E

Microwave to Optical Domain Converison Codes

E.1 Analytical Approximation Codes

E.1.1 Analytical Approximation for Constant κ_o or κ_μ

```
#Import necessary libraries to run the Conversion Efficiency Codes
import matplotlib.pyplot as plt
import numpy as np
from pylab import *
from scipy import arange, conj, prod
import scipy.sparse as sp
from mpl_toolkits.mplot3d import Axes3D
from mpl_toolkits.axes_grid1 import make_axes_locatable
from math import sqrt
import matplotlib
matplotlib.use("TKAGG")
import matplotlib.pyplot as pyplot
import mpl_toolkits.mplot3d
import matplotlib as mpl

fact = (1E9)
wa = 2*pi*470*(10**12)/(fact) #optical cavity frequency
wb = 2*pi*2.88*(10**9)/(fact) #microwave cavity frequency
wl = wa-wb #coherent drive frequency

```

```

#Defining the decay rates corresponding to NV center
gammaE = 2*pi*13.3*1E6/(fact)
gamma_31 = 2*pi*0.35*1E6/(fact) #ZPL
gamma_32 = 0.2*gammaE
gamma_34 = gammaE - gamma_31 - gamma_32
gamma_21 = 2*pi*21.2/(fact)

#Coherence Decay Rates
gamma_a = 2*pi*66.3/(fact)
gamma_b = 2*pi*15.9*1E6/(fact)

#Optical and Microwave cavity coupling strengths
g_o = gammaE*(0.01)
#g_o = gammaE*(100) #Uncomment for strong optical coupling
g_mu = gamma_21*100

#Detuning list to loop over
det_list = linspace(-3*g_mu,3*g_mu,50)

# #################################################################################

#Loop over the microwave cavity paramters with a constant kappa_a
#Defining the list of optical and microwave cavity decay rates to loop over
kappa_a = g_o
kappa_b_list = linspace(-2,2,3)
kappa_b_list = [(10**x)*g_mu for x in kappa_b_list]

T1_o_list = np.zeros([len(kappa_b_list),l,l])

#Loop over the microwave cavity paramters with a constant kappa_a
for kappa_b in kappa_b_list:

    Omega_list = linspace((10**-4)*g_o,(10**-0.5)*g_o,l)
    i= 0;j =0;

    T1_o = np.zeros([l,l])
    T1_m = np.zeros([l,l])

    for Omega in Omega_list:
        for det in det_list:
            #Linear set of equations defining the zeroth and first manifold of the system analytically
```

```
            A =  np.array([[-(gamma_a*1j + det), 0, g_o, Omega],
                           [0, -(kappa_b*1j + det), 0, g_mu],
                           [g_o, 0, -(kappa_a*1j + det ), 0],
                           [Omega, g_mu, 0, -(gamma_b*1j + det)]]);
            b = np.array([0, -epsilon, 0, 0]);

            C = np.linalg.solve(A, b);
            c2 = C[1]
            c3 = C[2]

            #Save conversion efficiency values in a 2D array
            T1_o[i][j] = (c3*(c3.conjugate()))*(kappa_a)/(epsilon) # Conversion Efficiency Definition A
            #T1_o[i][j] = (c3*(c3.conjugate()))*(kappa_a)*(kappa_b)/(epsilon**2) #Conversion Efficiency Definition B

            i = i+1;
            if (i ==l):
                i = 0;
        j = j+1

    temp_min = min(map(min, T1_o))
    if (min_value > temp_min):
        min_value = temp_min

    temp_max = max(map(max, T1_o))
    if (max_value<temp_max):
        max_value = temp_max

    T1_o_list[kappa_b_list.index(kappa_b)] = T1_o


OMEGA,DET = np.meshgrid(Omega_list,det_list);
normi = mpl.colors.Normalize(vmin = log10(min_value/max_value),vmax = 0);


fig = plt.figure(figsize = (8,10))
ax = fig.gca(projection='3d')
cset0 = ax.contourf(log10(OMEGA/g_o), DET/g_mu, log10(T1_o_list[0]), zdir='z', offset=off[0],levels = 20,norm = normi)
cset1 = ax.contourf(log10(OMEGA/g_o), DET/g_mu, log10(T1_o_list[1]), zdir='z', offset=off[1],levels = 20,norm = normi)
cset2 = ax.contourf(log10(OMEGA/g_o), DET/g_mu, log10(T1_o_list[2]), zdir='z', offset=off[2],levels = 20,norm = normi)

```

```
ax.set_xlabel(r'$log10(\Omega / g_o)$',fontsize = 20, linespacing=3)
ax.set_ylabel(r'$\Delta / g_\mu$',fontsize =20, linespacing=3)
ax.set_zlabel(r'$log_{10}(\kappa_\mu / g_\mu) $',fontsize =20, linespacing=5)
ax.tick_params(axis='x', pad=-0.1)
ax.tick_params(axis='y', pad=-0.1)

ax.xaxis.labelpad=10
ax.yaxis.labelpad=10
ax.zaxis.labelpad=25

ax.tick_params(axis='z', pad=10)

ax.set_zlim(-2,2)

fig.colorbar(cset0,fraction = 0.04, pad = 0.1)
plt.show()

# ################################################################################
#Looping over optical cavity paramters with a constant kappa_b
#Detuning list to loop over
det_list = linspace(-3*g_mu,3*g_mu,50)

#Defining the list of optical and microwave cavity decay rates to loop over
kappa_b = g_mu
kappa_b_list = linspace(-2,2,3)
kappa_b_list = [(10**x)*g_mu for x in kappa_b_list]

l = 50;
T1_m_list = np.zeros([len(kappa_a_list),l,l])

#Loop over the optical cavity paramters with a constant kappa_b
for kappa_a in kappa_a_list:

    Omega_list = linspace((10**-4)*g_o,(10**-0.5)*g_o,l)
    i= 0;j =0;

    T1_m = np.zeros([l,l])
    T1_m = np.zeros([l,l])

    for Omega in Omega_list:
        for det in det_list:
```

```
            #Linear set of equations defining the zeroth and first manifold of the system analytically
            A =  np.array([[-(gamma_a*1j + det), 0, g_o, Omega],
                           [0, -(kappa_b*1j + det), 0, g_mu],
                           [g_o, 0, -(kappa_a*1j + det ), 0],
                           [Omega, g_mu, 0, -(gamma_b*1j + det)]]);
            b = np.array([0, -epsilon, 0, 0]);

            C = np.linalg.solve(A, b);
            c2 = C[1]
            c3 = C[2]

            #Save conversion efficiency values in a 2D array
            T1_m[i][j] = (c3*(c3.conjugate()))*(kappa_a)/(epsilon) # Conversion Efficiency Definition A
            #T1_m[i][j] = (c3*(c3.conjugate()))*(kappa_a)*(kappa_b)/(epsilon**2) #Conversion Efficiency Definition B

            i = i+1;
            if (i ==l):
                i = 0;
        j = j+1

    temp_min = min(map(min, T1_m))
    if (min_value > temp_min):
        min_value = temp_min

    temp_max = max(map(max, T1_m))
    if (max_value<temp_max):
        max_value = temp_max

    T1_m_list[kappa_a_list.index(kappa_a)] = T1_m


OMEGA,DET = np.meshgrid(Omega_list,det_list);
normi = mpl.colors.Normalize(vmin = log10(min_value/max_value),vmax = 0);

fig = plt.figure(figsize = (8,10))
ax = fig.gca(projection='3d')
cset0 = ax.contourf(log10(OMEGA/g_o), DET/g_mu, log10(T1_m_list[0]), zdir='z', offset=off[0],levels = 20,norm = normi)
cset1 = ax.contourf(log10(OMEGA/g_o), DET/g_mu, log10(T1_m_list[1]), zdir='z', offset=off[1],levels = 20,norm = normi)
cset2 = ax.contourf(log10(OMEGA/g_o), DET/g_mu, log10(T1_m_list[2]), zdir='z', offset=off[2],levels = 20,norm = normi)
```

```

ax.set_xlabel(r’$log10(\Omega / g_o)$’,fontsize = 20, linespacing=3)
ax.set_ylabel(r’$\Delta / g_\mu$’,fontsize =20, linespacing=3)
ax.set_zlabel(r’$log_{10}(\kappa_\mu / g_\mu) $’,fontsize =20,
    linespacing=5)
ax.tick_params(axis=’x’, pad=-0.1)
ax.tick_params(axis=’y’, pad=-0.1)

ax.xaxis.labelpad=10
ax.yaxis.labelpad=10
ax.zaxis.labelpad=25

ax.tick_params(axis=’z’, pad=10)

ax.set_zlim(-2,2)

fig.colorbar(cset0,fraction = 0.04, pad = 0.1)
plt.show()
```

E.1.2 Analytical approximation sweeping over κ_μ and κ_o with system on resonance

```

#Import necessary libraries to run the Conversion Efficiency Codes
import matplotlib.pyplot as plt
import numpy as np
from pylab import *
from scipy import arange, conj, prod
import scipy.sparse as sp
from mpl_toolkits.mplot3d import Axes3D
from mpl_toolkits.axes_grid1 import make_axes_locatable
from math import sqrt
import matplotlib
matplotlib.use("TKAGG")
import matplotlib.pyplot as pyplot
import mpl_toolkits.mplot3d
import matplotlib as mpl

fact = (1E9)
wa = 2*pi*470*(10**12)/(fact) #optical cavity frequency
wb = 2*pi*2.88*(10**9)/(fact) #microwave cavity frequency
wl = wa-wb #coherent drive frequency


#Defining the decay rates corresponding to NV center
```

```
gammaE = 2*pi*13.3*1E6/(fact)
gamma_31 = 2*pi*0.35*1E6/(fact) #ZPL
gamma_32 = 0.2*gammaE
gamma_34 = gammaE - gamma_31 - gamma_32
gamma_21 = 2*pi*21.2/(fact)

#Coherence Decay Rates
gamma_a = 2*pi*66.3/(fact)
gamma_b = 2*pi*15.9*1E6/(fact)

#Optical and Microwave cavity coupling strengths
g_o = gammaE*(0.01)
#g_o = gammaE*(100) #Uncomment for strong optical coupling
g_mu = gamma_21*100

#Detuning list to loop over
det_list = linspace(-3*g_mu,3*g_mu,50)

#Defining the list of optical and microwave cavity decay rates to loop over
kappa_a_list = linspace(-3,3,50)
kappa_a_list = [(10**x)*g_o for x in kappa_a_list]

kappa_b_list = linspace(-3,3,50)
kappa_b_list = [(10**x)*g_mu for x in kappa_b_list]


#Defining the Rabi drive list and microwave cavity drive terms where epsilon -> 0
Omega_list = linspace(g_o,200*g_o,7)
eps_b = (1E-4)*g_mu
Omega_list = linspace((10**-4)*g_o,(10**4)*g_o,l)

l = 50
det_list = linspace(0,0,1)*g_mu# Detuning values to loop through (running system on resonance)
#Defining empty arrays to fill with the maximum photon values
max_list = np.zeros([len(kappa_a_list),len(kappa_b_list)])
max_Omega_list = np.zeros([len(kappa_a_list),len(kappa_b_list)])
max_det_list = np.zeros([len(kappa_a_list),len(kappa_b_list)])
max_x=0
max_y=0

for kappa_a in kappa_a_list:
    for kappa_b in kappa_b_list:
```

```

        T1_o = np.zeros([l,l])
        T1_m = np.zeros([l,l])

        for Omega in Omega_list:
            for det in det_list:
                #Linear set of equations defining the zeroth and first manifold of the system analytically
                A =  np.array([[-(gamma_a*1j + det), 0, g_o, Omega,0],
                               [0, -(kappa_b*1j + det), 0, g_mu,0],
                               [g_o, 0, -(kappa_a*1j + det ), 0,epsilon],
                               [Omega, g_mu, 0, -(gamma_b*1j + det),0],
                              [0, 0, epsilon,0, -(kappa_b*1j+ kappa_a*1j + (2*det))]]);
                b = np.array([0, -epsilon, 0, 0,0]);

                C = np.linalg.solve(A, b);
                c2 = C[1]
                c3 = C[0]

                T1_o[i][j] = (c3*(c3.conjugate()))*(kappa_a)/(epsilon) #Conversion Efficiency Definition A
                #T1_o[i][j] = (c3*(c3.conjugate()))*(kappa_a)*(kappa_b)/(epsilon**2) #Conversion Efficiency Definition B

                i = i+1;
                if (i ==l):
                    i = 0;
            j = j+1

        #Pick the maximum value for conversion efficiency term from the list of conversion values.
        photon_out = max(map(max, T1_o))
        if (photon_out >= 1):
            photon_out = 1

        #Store max values in a 2D array
        max_list[kappa_a_list.index(kappa_a)][kappa_b_list.index(kappa_b)] = photon_out
        max_Omega_list[kappa_a_list.index(kappa_a)][kappa_b_list.index(kappa_b)] = Omega_list[unravel_index(T1_o.argmax(), T1_o.shape)[1]]


KAPPA_A,KAPPA_B = np.meshgrid(kappa_a_list,kappa_b_list)

```

```
KAPPA_A = KAPPA_A.transpose()
KAPPA_B = KAPPA_B.transpose()

plt.rcParams.update({'font.size': 20})
fig,ax=plt.subplots(figsize=(8,6))

#plot Maximum Conversion Efficiency Values
max_conversion_plt = plt.contourf(log10(KAPPA_A/g_o),log10(KAPPA_B/g_mu),
    log10(max_list),levels = 30)
plt.colorbar(max_conversion_plt)
plt.xlabel(r'$log_{10}(\kappa_o / g_o)$',fontsize = 25)
plt.ylabel(r'$log_{10}(\kappa_\mu / g_\mu)$',fontsize =25)
plt.show()

fig,ax=plt.subplots(figsize=(8,6))

#plot corresponding Rabi Drive Strength Values
max_omega_plt = plt.contourf(log10(KAPPA_A/g_o),log10(KAPPA_B/g_mu),log10
    (max_Omega_list/g_o),levels = 30)
plt.colorbar(max_omega_plt)
plt.xlabel(r'$log_{10}(\kappa_o / g_o)$',fontsize = 25)
plt.ylabel(r'$log_{10}(\kappa_\mu / g_\mu)$',fontsize =25)
plt.show()
```

E.2 Python Qutip Monte Carlo Solver Code for Continuous Drive

```
#Import necessary libraries to run the Conversion Efficiency Codes
from qutip import *
import matplotlib.pyplot as plt
import numpy as np
from pylab import *
from scipy import arange, conj, prod
import scipy.sparse as sp
from qutip.qobj import Qobj
from qutip.operators import destroy, jmat
from qutip.tensor import tensor
from mpl_toolkits.mplot3d import Axes3D
import time
from scipy.constants import *
import qutip.settings
from qutip.ipynbtools import HTMLProgressBar

ntraj = 500
```

```
sampls=10000
t=10000
tlist=np.linspace(0,t,sampls)

#atom operators
N = 7 #number of mnaifolds in system
sigma11=tensor(qeye(N),qeye(N),basis(4,0)*(basis(4,0).dag()))
sigma22=tensor(qeye(N),qeye(N),basis(4,1)*(basis(4,1).dag()))
sigma33=tensor(qeye(N),qeye(N),basis(4,2)*(basis(4,2).dag()))
sigma44=tensor(qeye(N),qeye(N),basis(4,3)*(basis(4,3).dag())) #virtual state


sigma32 = tensor(qeye(N),qeye(N),basis(4,2)*(basis(4,1).dag()))
sigma23 = tensor(qeye(N),qeye(N),basis(4,1)*(basis(4,2).dag()))
sigma21 = tensor(qeye(N),qeye(N),basis(4,1)*(basis(4,0).dag()))
sigma12 = tensor(qeye(N),qeye(N),basis(4,0)*(basis(4,1).dag()))
sigma31 = tensor(qeye(N),qeye(N),basis(4,2)*(basis(4,0).dag()))
sigma13 = tensor(qeye(N),qeye(N),basis(4,0)*(basis(4,2).dag()))
sigma43 = tensor(qeye(N),qeye(N),basis(4,3)*(basis(4,2).dag()))
sigma34 = tensor(qeye(N),qeye(N),basis(4,2)*(basis(4,3).dag()))
sigma14 = tensor(qeye(N),qeye(N),basis(4,0)*(basis(4,3).dag()))

#a - annihilation operator on optical field
#b - annihilation operator on microwave field
a = tensor(destroy(N),qeye(N),qeye(4))
b = tensor(qeye(N),destroy(N),qeye(4))


def evolve_sys_int(kappa_a,kappa_b,Omega):
    #function defining the evolution of the system
    a_outint = zeros(len(tlist))
    b_outint = zeros(len(tlist))
    a_int = zeros(len(tlist))
    b_int=zeros(len(tlist))

    #initial wavefunction setup with atom initialized to ground state and with no photons in the microwave/optical cavities
    #For non-driven case with one photon in microwave cavity set psi0=tensor(basis(N,0),basis(N,1),basis(4,0))
    psi0=tensor(basis(N,0),basis(N,0),basis(4,0))

    #defining the Hamiltonian of the system
    H0 = det_su*sigma22 + det_Omega*sigma33 + det_Omega*(a.dag()*a) + det_bu*(b.dag()*b)
```

```
 #H0 = wb*sigma22 + wb*sigma33 + wb*(a.dag()*a) + wb*(b.dag()*b) # uncomment for non-driven case
 Hint = g_mu*(b*sigma21 + b.dag()*sigma12) + g_o*(a*sigma31 + a.dag()*sigma13) + Omega*(sigma32+sigma23)
 Hdrive = eps_b*(b+b.dag())
 #Hdrive = 0  #For non-driven case

 H = H0+Hint+Hdrive

 #Defining the collapse operators of the system
 C_1= np.sqrt(kappa_a)*a
 C_2= np.sqrt(kappa_b)*b
 C_3= np.sqrt(gamma_31) * sigma13
 C_4 = np.sqrt(gamma_32) * sigma23
 C_5 = np.sqrt(gamma_21)* sigma12
 C_6 = np.sqrt(gamma_34) * sigma43
 C_7 = np.sqrt(gamma_2)*(sigma22)
 C_8 = np.sqrt(gamma_3)*(sigma33)
 C_9 = np.sqrt(gamma_41)*sigma14

 c_ops = [C_1,C_2,C_3,C_5,C_4,C_6,C_7,C_8,C_9]

 #Evolve system with the Qutip Monte-Carlo Solver
 result=mcsolve(H,psi0,tlist,c_ops,[sigma11,sigma22,sigma33,a.dag()*a,b.dag()*b,C_1.dag()*C_1,C_2.dag()*C_2],ntraj=ntraj,progress_bar=HTMLProgressBar(),map_func=parallel_map)

 #Expectation values of the photon number operators
 a_cav = result.expect[3]
 b_cav = result.expect[4]
 aout=result.expect[5]
 bout=result.expect[6]

 #Integral of the photon number operators
 for i in range(1,len(tlist)):
     a_int[i] = (a_cav[i]*((t)/sampls)+a_int[i-1])
     b_int[i] = (b_cav[i]*((t)/sampls)+b_int[i-1])
     a_outint[i]=(aout[i]*((t)/sampls)+a_outint[i-1])
     b_outint[i]=(bout[i]*((t)/sampls)+b_outint[i-1])

 a_out = a_outint[-1]
 b_out = b_outint[-1]

 return a_out, b_out, a_int[-1], b_int[-1]

```

```


#GHz
fact = 1E13
wa = 2*pi*470*(10**12)/(fact) #optical cavity frequency
wb = 2*pi*2.88*(10**9)/(fact) #microwave cavity frequency
wl = wa-wb #coherent drive frequency

#Defining the decay rates corresponding to NV center
gammaE = 2*pi*13.3*1E6/(fact)
gamma_31 = 2*pi*0.35*1E6/(fact) #ZPL
gamma_32 = 0.2*gammaE
gamma_34 = gammaE - gamma_31 - gamma_32
gamma_21 = 2*pi*21.2/(fact)
gamma_41 =  2*pi*66*1E12/(fact)

#Transverse Decay rate
gamma_a = 2*pi*66.3/(fact)
gamma_b = 2*pi*15.9*1E6/(fact)

#Pure Decay rates
gamma2 = gamma_a - (gammaE/2)
gamma3 = gamma_b - (gamma_21/2)



#Optical and Microwave cavity coupling strengths
g_o = gammaE*(0.01)
#g_o = (1/(12*(1E-9)*(fact)))*(100) #Uncomment for strong optical
    coupling
g_mu = gamma_21*100


#Defining the list of optical and microwave cavity decay rates to loop
    over
kappa_a_list = linspace(-3,3,5)
kappa_a_list = [(10**x)*g_o for x in kappa_a_list]

kappa_b_list = linspace(-3,3,5)
kappa_b_list = [(10**x)*g_mu for x in kappa_b_list]

#Defining the Rabi drive list and microwave cavity drive terms where
    epsilon -> 0
Omega_list = linspace(g_o,200*g_o,7)
eps_b = (1E-4)*g_mu
```

```
det_list = linspace(0,0,1)*g_mu # Detuning values to loop through (running system on resonance)

transmission_a =[]
transmission_b = []
transmission_a_cav = []
transmission_b_cav =[]

#Defining empty arrays to fill with the maximum photon values
max_list = np.zeros([len(kappa_a_list),len(kappa_b_list)])
max_list_b = np.zeros([len(kappa_a_list),len(kappa_b_list)])
max_list_a_cav = np.zeros([len(kappa_a_list),len(kappa_b_list)])
max_list_b_cav = np.zeros([len(kappa_a_list),len(kappa_b_list)])
max_Omega_list = np.zeros([len(kappa_a_list),len(kappa_b_list)])


#Looping over the cavity decay paramters and the rabi drive strength terms
for kappa_a in kappa_a_list:
    for kappa_b in kappa_b_list:
        for Omega in Omega_list:
            for det in det_list:
                det_Omega = det
                det_su =det
                det_bu = det


                A_out,B_out, A_cav, B_cav = evolve_sys_int(kappa_a,kappa_b,Omega)


                fexpt_a = (A_out*kappa_b/(eps_b**2)) #Conversion efficiency B Definition
                #fexpt_a = (A_out/(eps_b**2)) #Conversion efficiency A Definition

                fexpt_b = (B_out/(eps_b**2))
                fexpt_a_cav = (A_cav)
                fexpt_b_cav = (B_cav)

                transmission_a.append(fexpt_a)
                transmission_b.append(fexpt_b)
                transmission_a_cav.append(fexpt_a_cav)
                transmission_b_cav.append(fexpt_b_cav)

```

```
        #Pick the maximum value for conversion efficiency term from the list of conversion values.
        photon_out = max( transmission_a)

        print('Conversion Efficiency max = %.0e \n kappa_a=%1.3fg_o kappa_b=%1.3fg_mu '%(photon_out,kappa_a/g_o,kappa_b/g_mu))

        max_list[kappa_a_list.index(kappa_a)][kappa_b_list.index(kappa_b)] = photon_out
        max_list_b[kappa_a_list.index(kappa_a)][kappa_b_list.index(kappa_b)] = transmission_b[transmission_a.index(max(transmission_a))]
        max_list_a_cav[kappa_a_list.index(kappa_a)][kappa_b_list.index(kappa_b)] = transmission_a_cav[transmission_a.index(max(transmission_a))]
        max_list_b_cav[kappa_a_list.index(kappa_a)][kappa_b_list.index(kappa_b)] = transmission_b_cav[transmission_a.index(max(transmission_a))]
        max_Omega_list[kappa_a_list.index(kappa_a)][kappa_b_list.index(kappa_b)] = Omega_list[transmission_a.index(max(transmission_a))]

        transmission_a =[]
        transmission_b = []
        transmission_a_cav = []
        transmission_b_cav =[]

KAPPA_A,KAPPA_B = np.meshgrid(kappa_a_list,kappa_b_list)
KAPPA_A = KAPPA_A.transpose()
KAPPA_B = KAPPA_B.transpose()

#Save the Maximum Converion Efficiency values with the corresponding parameters
np.savez('Conversion_Efficiency.npz',kappa_a=KAPPA_A,kappa_b=KAPPA_B, max_list = max_list,max_list_b=max_list_b, max_list_a_cav=max_list_a_cav,max_list_b_cav=max_list_b_cav, max_Omega_list = max_Omega_list )

#plot Maximum Conversion Efficiency Values
max_conversion_plt = plt.contourf(log10(KAPPA_A/g_o),log10(KAPPA_B/g_mu),log10(max_list),levels = 50)
plt.colorbar(max_conversion_plt)
plt.title(r'Maximum "Conversion Efficiency" of First Microwave to Optical Photon / $log_{10}$',fontsize = 22)
plt.xlabel(r'$log_{10}(\kappa_a / g_o)$',fontsize = 22)
plt.ylabel(r'$log_{10}(\kappa_b / g_\mu)$',fontsize =22)
plt.show()
```

```

#plot corresponding Rabi Drive Strength Values
max_omega_plt = plt.contourf(log10(KAPPA_A/g_o),log10(KAPPA_B/g_mu),log10
    (max_Omega_list/g_o),levels = 50)
plt.colorbar(max_omega_plt)
plt.title(r'$\Omega/g_{o}$ for Max Conversion/ $log_{10}$',fontsize = 22)
plt.xlabel(r'$log_{10}(\kappa_a / g_o)$',fontsize = 22)
plt.ylabel(r'$log_{10}(\kappa_b / g_\mu)$',fontsize =22)
plt.show()
```

E.3 Python Qutip Monte Carlo Solver Code for Source Cavity Case

```
#Import necessary libraries to run the Conversion Efficiency Codes
%matplotlib inline
import matplotlib.pyplot as plt
import numpy as np
from qutip import*
from pylab import*
from scipy import arange, conj,prod
import scipy.sparse as sp
from qutip.qobj import Qobj
from qutip.operators import destroy,jmat
from qutip.tensor import tensor
import time
from scipy.constants import *
import qutip.settings
from qutip.ipynbtools import HTMLProgressBar

ntraj = 500 #number of trajectories taken in the monte carlo solver
sampls=10000 #no of samples to consider
t=10000 #total time the solver is evolved for
tlist=np.linspace(0,t,sampls)

#atom operators
N = 7
#(source_cavity, optical, microwave,atom)
sigma11=tensor(qeye(N),qeye(N),qeye(N),basis(4,0)*(basis(4,0).dag()))
sigma22=tensor(qeye(N),qeye(N),qeye(N),basis(4,1)*(basis(4,1).dag()))
sigma33=tensor(qeye(N),qeye(N),qeye(N),basis(4,2)*(basis(4,2).dag()))
sigma44=tensor(qeye(N),qeye(N),qeye(N),basis(4,3)*(basis(4,3).dag()))

sigma32 = tensor(qeye(N),qeye(N),qeye(N),basis(4,2)*(basis(4,1).dag()))
sigma23 = tensor(qeye(N),qeye(N),qeye(N),basis(4,1)*(basis(4,2).dag()))
```

```
sigma21 = tensor(qeye(N),qeye(N),qeye(N),basis(4,1)*(basis(4,0).dag()))
sigma12 = tensor(qeye(N),qeye(N),qeye(N),basis(4,0)*(basis(4,1).dag()))
sigma31 = tensor(qeye(N),qeye(N),qeye(N),basis(4,2)*(basis(4,0).dag()))
sigma13 = tensor(qeye(N),qeye(N),qeye(N),basis(4,0)*(basis(4,2).dag()))
sigma43 = tensor(qeye(N),qeye(N),qeye(N),basis(4,3)*(basis(4,2).dag()))
sigma34 = tensor(qeye(N),qeye(N),qeye(N),basis(4,2)*(basis(4,3).dag()))

#a - annihilation operator on optical field
#b - annihilation operator on microwave field
#b_s - annihilation operator on microwave field from source cavity
b_s = tensor(destroy(N),qeye(N),qeye(N),qeye(4))
a = tensor(qeye(N),destroy(N),qeye(N),qeye(4))
b = tensor(qeye(N),qeye(N),destroy(N),qeye(4))


def evolve_single_photon(kappa_a,kappa_b,Omega):
    #function defining the evolution of the system
    a_outint = zeros(len(tlist))
    b_outint = zeros(len(tlist))


    #initial wavefunction setup with atom initialized to ground state and with one photon in the microwave source cavity
    psi0=tensor(basis(N,1),basis(N,0),basis(N,0),basis(4,0))

    det_Omega = wb #if system is on resonance
    H0 = wb*sigma22 + det_Omega*sigma33 + det_Omega*(a.dag()*a) + wb*(b.dag()*b)
    Hint = g_mu*(b*sigma21 + b.dag()*sigma12) + g_o*(a*sigma31 + a.dag()*sigma13) + Omega*(sigma32+sigma23)
    Hsource = wb*(b_s.dag()*b_s)
    H1 = (1j/2)*(np.sqrt(kappa_b*kappa_s)*b_s.dag()*b) - (1j/2)*(np.sqrt(kappa_b*kappa_s)*b.dag()*b_s)
    H = H0+Hint+Hsource+H1

    #Defining the collapse operators for the system
    C_1= np.sqrt(kappa_a)*a
    C_2= np.sqrt(kappa_s)*b_s + np.sqrt(kappa_b)*b
    C_3= np.sqrt(gamma_31) * sigma13
    C_4 = np.sqrt(gamma_32) * sigma23
    C_5 = np.sqrt(gamma_21)* sigma12
    C_6 = np.sqrt(gamma_34) * sigma43
    C_7 = np.sqrt(gamma_2)*(sigma22)
    C_8 = np.sqrt(gamma_3)*(sigma33)
    C_9 = np.sqrt(gamma_41)*sigma14
```

```
    c_ops = [C_1,C_2,C_3,C_5,C_4,C_6,C_7,C_8,C_9]

    #Evolve system with the Qutip Monte-Carlo Solver
    result=mcsolve(H,psi0,tlist,c_ops,[sigma11,sigma22,sigma33,a.dag()*a,b.dag()*b,b_s.dag()*b_s,C_1.dag()*C_1,C_2.dag()*C_2],ntraj=ntraj,progress_bar=HTMLProgressBar(),map_func=parallel_map)

    aout=result.expect[6]
    bout=result.expect[7]

    for i in range(1,len(tlist)):
        a_outint[i]=(aout[i]*((t)/sampls)+a_outint[i-1])
        b_outint[i]=(bout[i]*((t)/sampls)+b_outint[i-1])

    return  a_outint[-1],b_outint[-1]


fact = 1E13
wa = 2*pi*470*(10**12)/(fact) #optical cavity frequency
wb = 2*pi*2.88*(10**9)/(fact) #microwave cavity frequency
wl = wa-wb #coherent drive frequency

#Defining the decay rates corresponding to NV center
gammaE = 2*pi*13.3*1E6/(fact)
gamma_31 = 2*pi*0.35*1E6/(fact) #ZPL
gamma_32 = 0.2*gammaE
gamma_34 = gammaE - gamma_31 - gamma_32
gamma_21 = 2*pi*21.2/(fact)
gamma_14 =  2*pi*66*1E12/(fact)

#Transverse Decay rate
gamma_a = 2*pi*66.3/(fact)
gamma_b = 2*pi*15.9*1E6/(fact)

#Pure Decay rates
gamma2 = gamma_a - (gammaE/2)
gamma3 = gamma_b - (gamma_21/2)


#Optical and Microwave cavity coupling strengths
g_o = gammaE*(0.01)
#g_o = (1/(12*(1E-9)*(fact)))*(100) #Uncomment for strong optical coupling
g_mu = gamma_21*100
```

```



#Defining the list of optical and microwave cavity decay rates to loop over
kappa_a_list = linspace(-3,3,5)
kappa_a_list = [(10**x)*g_o for x in kappa_a_list]

kappa_b_list = linspace(-3,3,5)
kappa_b_list = [(10**x)*g_mu for x in kappa_b_list]

#Defining the Rabi drive list and microwave cavity drive terms where epsilon -> 0
Omega_list = linspace(g_o,200*g_o,7)
eps_b = (1E-4)*g_mu
det_list = linspace(0,0,1)*g_mu # Detuning values to loop through (running system on resonance)

transmission_a =[]
transmission_b = []
transmission_a_cav = []
transmission_b_cav =[]

#Defining empty arrays to fill with the maximum photon values
max_list = np.zeros([len(kappa_a_list),len(kappa_b_list)])
max_list_b = np.zeros([len(kappa_a_list),len(kappa_b_list)])
max_Omega_list = np.zeros([len(kappa_a_list),len(kappa_b_list)])

for kappa_a in kappa_a_list:
    for kappa_b in kappa_b_list:
        for Omega in Omega_list:

            kappa_s = kappa_b # Setting source cavity decay rate to microwave cavity decay rate
            A_out,B_out = evolve_single_photon(kappa_a,kappa_b,Omega)

            transmission_a.append(A_out)
            transmission_b.append(B_out)

        #Pick the maximum value for conversion efficiency term from the list of conversion values.
        photon_out_a = max(transmission_a)
        print(’Conversion Efficiency max = %.0e \n kappa_a=%1.3fg_mu kappa_b=%1.3fg_mu ’%(photon_out_a,kappa_a/g_o,kappa_b/g_mu))

```

```
        #Store the maximum conversion values in a 2 dimenisonal array
        max_list[kappa_a_list.index(kappa_a)][kappa_b_list.index(kappa_b)] = photon_out_a
        max_Omega_list[kappa_a_list.index(kappa_a)][kappa_b_list.index(kappa_b)] = Omega_list[transmission_a.index(max(transmission_a))]

        transmission_a = []
        transmission_b = []

    j = -1;


KAPPA_A,KAPPA_B = np.meshgrid(kappa_a_list,kappa_b_list)
KAPPA_A = KAPPA_A.transpose()
KAPPA_B = KAPPA_B.transpose()

#Save the Maximum Converion Efficiency values with the corresponding parameters
np.savez('Conversion_Efficiency_withSourceCavity.npz',kappa_a=KAPPA_A,kappa_b=KAPPA_B,max_list = max_list,max_Omega_list = max_Omega_list )

#plot Maximum Conversion Efficiency Values
max_conversion_plt = plt.contourf(log10(KAPPA_A/g_o),log10(KAPPA_B/g_mu),log10(max_list),levels = 50)
plt.colorbar(max_conversion_plt)
plt.title(r'Maximum Conversion Efficiency of First Microwave to Optical Photon / $log_{10}$',fontsize = 22)
plt.xlabel(r'$log_{10}(\kappa_a / g_o)$',fontsize = 22)
plt.ylabel(r'$log_{10}(\kappa_b / g_\mu)$',fontsize =22)
plt.show()

#plot corresponding Rabi Drive Strength Values
max_omega_plt = plt.contourf(log10(KAPPA_A/g_o),log10(KAPPA_B/g_mu),log10(max_Omega_list/g_mu),levels = 50)
plt.colorbar(max_omega_plt)
plt.title(r'$\Omega/g_{o}$ for Max Conversion/ $log_{10}$',fontsize = 22)
plt.xlabel(r'$log_{10}(\kappa_a / g_o)$',fontsize = 22)
plt.ylabel(r'$log_{10}(\kappa_b / g_\mu)$',fontsize =22)
plt.show()
```